A combined immersed boundary/phase-field method for simulating two-phase pipe flows

A thesis submitted for the Degree of
Doctor of Philosophy of the Imperial College London
and the
Diploma of Imperial College London

by

Christos Argyropoulos

Department of Chemical Engineering
Imperial College London
London, SW7 2AZ, UK
March 2015

Declaration of Originality

I hereby declare that the work presented in this thesis is my own and any published or unpublished work used from other authors has been cited and acknowledged appropriately.

Christos D. Argyropoulos
London, 05 March 2015

To my family and Alexia

Abstract

The investigation of the flow in a pipe is a major issue for the pipeline capacity but also plays an important role for the control and prevention of phenomena that could damage the pipe, such as corrosion, erosion, and the potential formation of wax or their deposits. Therefore, the characterization of the flow patterns is also a major issue for the prediction of the distribution over the cross-section of the pipe, in order to understand any problems that may interrupt or shut down the operation of the production line.

The main purpose of the present effort is to develop an appropriate numerical method for simulating two-phase pipe flows. Advanced Computational Fluid Dynamics (CFD) methods are employed as Navier-Stokes solver, while a Phase-Field method is used to simulate the interfacial region between the two fluids. A Ghost-Cell Immersed Boundary Method (GCIBM) was developed and implemented for the reconstruction of smooth rigid boundaries (pipe wall) based on the work of Tseng and Ferziger (2003). The method was also modified in order to incorporate appropriate boundary conditions for coupling the Phase-Field and Navier-Stokes solvers for two-phase pipe flows. Tseng and Ferziger (2003) used the GCIBM for turbulent single-phase flows; the present modified version comprises a continuation of the method for handling two-phase pipe flows. The computational model is capable of handling large density and viscosity ratios with good accuracy.

The developed GCIBM algorithm was validated against analytical solutions for single- and two-phase pipe flow, presenting very good agreement. The computational model was compared to available experimental data from the literature for single rising bubbles and bubble coalescence in vertical pipe also with good agreement. The numerical method was used to investigate the lateral wall effects of a 3-D single bubble in a viscous liquid for

different pipe diameters and bubble flow regimes. The dynamics of 3-D Taylor bubbles was also examined in vertical pipes for different properties of fluids (e.g. air-water system) and dimensionless parameters relevant to the problem (e.g. Re_B, Eo, Mo). The numerical results were compared with available experimental and numerical data from the literature, presenting good agreement.

Acknowledgments

Before proceeding with the acknowledgments, I would like to mention that this PhD thesis was conducted by the author without any supervision during the course of his PhD studies in the Department of Chemical Engineering of Imperial College London. The author takes full responsibility of the content.

The accomplishment of writing this thesis seemed, at times, to be like walking in a desert without hope for your final destination. This voyage was a long one, full of adventure and discovery, but also full of pain and suffering.

I was fortunate to have with me at this long period of time a number of friends and colleagues, who helped me to deal with these difficulties and challenges with a spirit of creativity and support. Without the patience, help and support of the following people, this thesis would not have been accomplished.

First and foremost, I would like to express my deepest gratitude to my parents, Dimitrios Argyropoulos and Antonia Rontou, who have always supported me both moral and financial, encouraged and believed in me, in all my endeavours throughout all these years of my studies.

In particular, I would like to extend my thanks to Dr. Edo Boek, who spent a fair amount of time proofreading the present manuscript, as well as my collaborating academic Prof. Serafim Kalliadasis for his useful comments and advice during my PhD.

My friend and colleague, Dr. Roman Zhvansky for his endless support, patience, invaluable help and continuous advice during the course of the present research work.

Many thanks to my brother Athanasios Argyropoulos and my friends Dr. Vicky Skoulou, Dr. Anastasia Sivena, Dr. Eirini Velliou, Dr. Stavros Karabelas, Dr. Alexandros

Avdis and Dr. Ioannis Zacharoudiou for their continuous support.

I would like also to express my sincere gratitude to the examination committee of my PhD viva, Professor Omar Matar and Professor Christopher P. Thompson for their useful comments and corrections.

Last but not least, I would like to thank Alexia Demenopoulou, my girlfriend. I do not know how I would have finished this thesis without her endless love, utterly care, continuous encouragement and the countless hours that she spent to listen my thoughts and worries, when I was discouraged by the difficulties posed by this challenge.

This work has been undertaken within the Joint Project on Transient Multiphase Flows and Flow Assurance. The author wishes to acknowledge the contributions made to this project by the UK Engineering and Physical Sciences Research Council (EPSRC) and the following: ASCOMP, GL Noble Denton, BP Exploration, CD adapco, Chevron, ConocoPhillips, ENI, ExxonMobil, FEESA, FMC Technologies, IFP Energies nouvelles, Granherne, Institutt for Energiteknikk, Kongsberg Oil and Gas Technologies, MSi Kenny, PDVSA (INTEVEP), Petrobras, PETRONAS, SPT Group, Shell, SINTEF, Statoil and TOTAL. The author wishes to express his sincere gratitude for this support.

Christos D. Argyropoulos
London, 05 March 2015

Θερμοπύλες[1]

Τιμή σ΄ εκείνους όπου στην ζωή των
ώρισαν και φυλάγουν Θερμοπύλες.
Ποτέ από το χρέος μη κινούντες·
δίκαιοι κ΄ ίσιοι σ΄ όλες των τες πράξεις,
αλλά με λύπη κιόλας κ΄ ευσπλαχνία·
γενναίοι οσάκις είναι πλούσιοι, κί όταν
είναι πτωχοί, πάλ΄ εις μικρόν γενναίοι,
πάλι συντρέχοντες όσο μπορούνε·
πάντοτε την αλήθεια ομιλούντες,
πλην χωρίς μίσος για τους ψευδομένους.

Και περισσότερη τιμή τούς πρέπει
όταν προβλέπουν (και πολλοί προβλέπουν)
πώς ο Εφιάλτης θα φανεί στο τέλος,
κ΄ οι Μήδοι επί τέλους θα διαβούνε.

Κωνσταντίνος Π. Καβάφης, (1863-1933)

---

[1] Από τα Ποιήματα 1897-1933, Ίκαρος 1984

Thermopylae[2]

Honour to those who in their lives have fixed
and guard strait passes of Thermopylae.
They from the path of duty never stray;
upright and scrupulous in every act,
but tolerant withal and merciful;
generous when possessed of affluence,
and still in small things generous when poor -
still helping to the utmost of their power;
speaking the truth despite all hindrances,
without ill-will, however, for the liars.

And greater honour is well due to them
when they foresee (and many of them foresee)
that in the end Ephialtes will appear,
that after all the Persian shall break through.

Constantine P. Cavafy, (1863-1933)

---

[2] Poems by C.P. Cavafy. Translated, from the Greek, by J.C. Cavafy. Ikaros, 2003

Contents

List of Figures

List of Tables

Chapter 1

Introduction

1.1 Background

According to Brennen (2005), a multiphase flow is defined as any fluid flow consisting of more than one phase (e.g. gas, liquid and solid). Such flows occur in the petrochemical industry, environment and biological systems, heat and mass transfer processes, among others (Ishii and Takashi, 2010; Yeoh and Tu, 2010). It is obvious that the prediction of the flow behaviour on the aforementioned types of flow is of high importance for the efficiency and optimization of those processes.

Over the past decades, the oil and gas sectors have presented significant progress, developing new technologies and cost-effective solutions, in order to face the new challenges of petroleum and gas production processes. This progress was achieved by the latest advancements in the field of multiphase flows. It is well known that many, if not most, flows are a form of multiphase flow which indicates their importance, almost at any aspect of engineering systems, especially for optimum design, cost reduction, safety and efficient operations.

In general, the physical mechanisms that govern the multi-phase flows are characterised by great complexity and the derivation of the appropriate equations for their description is more sophisticated than single-phase flows. The configuration of multiple interfacial regions with or without moving boundaries, along with the presence of discontinuities across the interfacial region due to fluid properties, are only some of the great challenges facing the field of multi-phase flows.

Intensive research has been conducted by many scientists and engineers for the investigation and prediction of multi-phase flows, many times with satisfactory results. Notwithstanding the great progress in the field of multi-phase flows, it is recognized that fundamental research is still required in order to address many open technological problems (e.g. deep-water fields). The solutions to these open problems are neither straightforward, as they depend upon a large number of constraints, nor are they, for most of the time, economical and technological feasible. On the other hand, multi-phase transportation of fluids are preferable not only for economical reasons, but because they are also the only technologically feasible means. For instance, multi-phase transportation of fluids with ice conditions or in very deep waters are characterised by great difficulties and technological challenges, which pose great demands for engineers and scientists.

The most common category of multi-phase flows are two-phase flows and may be divided, regarding the combination of the two phases, in the following subcategories: gas-liquid flows (e.g. oil-gas mixture transportation), gas-solid flows (e.g. fluidized beds), liquid-solid flows (e.g. slurry transportation) and liquid-liquid flows (e.g oil-water transportation). Information for problems involving multiphase flows, is provided in detail in the textbook by Yeoh and Tu (2010).

Two-phase flow may also be categorised as separated, dispersed and mixed or transitional flow, regarding the interfacial configuration (Ishii and Takashi, 2010). Each of the aforementioned categories may also be classified in more subcategories. According to Figure 1.1, the separated flows can also be grouped into film, annular and jet flows, regarding the phase configuration. Similarly, mixed or transitional flows may also be described by five different flow regimes such as bubbly-annular flow, droplet-annular flow, bubbly droplet-annular flow, and cap, slug or Churn-turbulent flow. Finally, dispersed flows can also be categorized in bubbly, droplet and particulate flows, based on the geometry of the interfacial region. All the subcategories along with their configurations are illustrated in Figure 1.1.

In this study, particular emphasis is given to the gas-liquid flows and liquid-liquid flows. Gas-liquid flows are the most complex among the two-phase flows, primarily due to the compressibility effect of one of the phases and deformation of interfacial region.

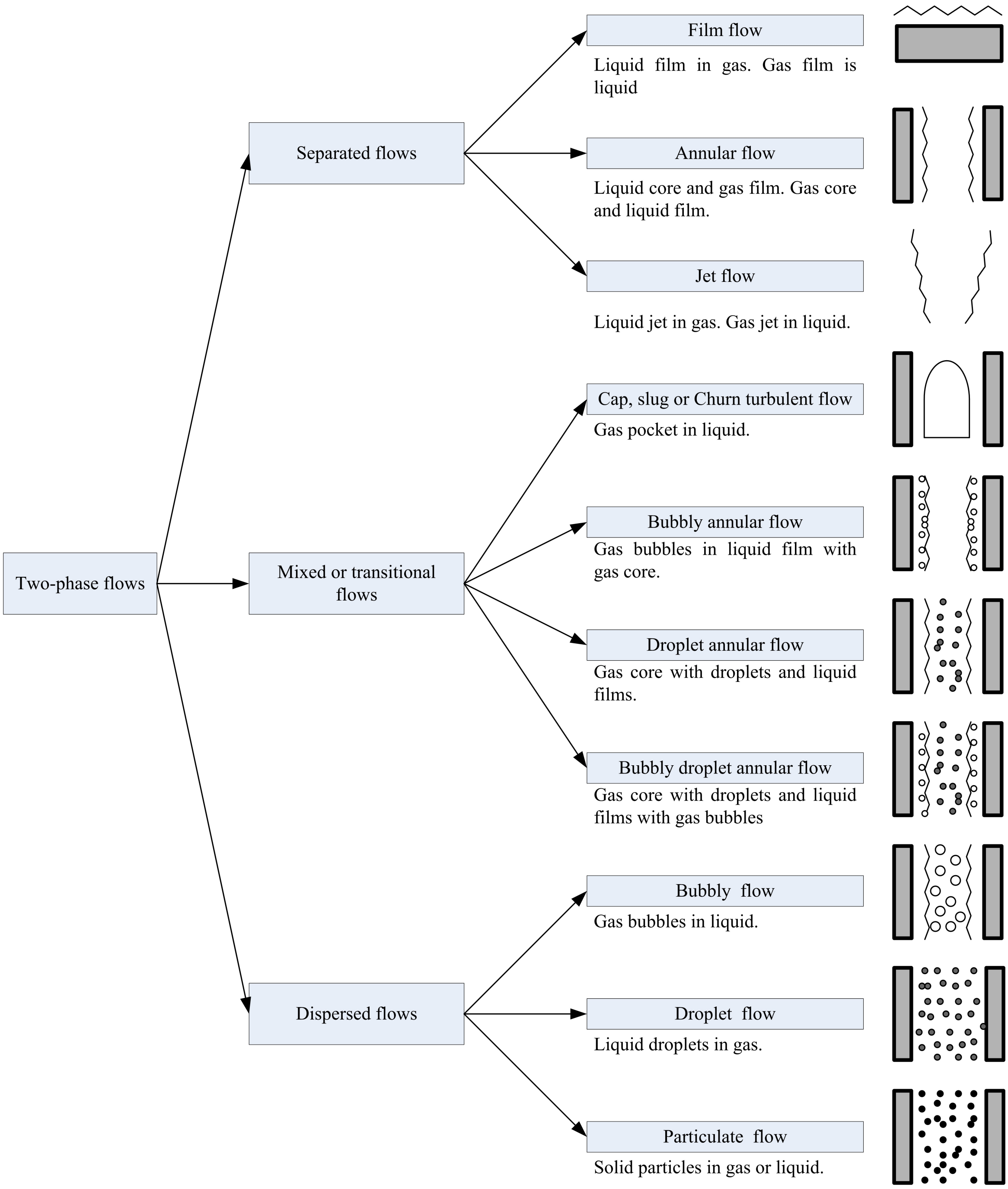

Figure 1.1: Categories of two-phase flows. Redrawn from the work of Ishii and Takashi (2010).

1.1.1 Flow patterns in horizontal pipes

The characterisation of the flow patterns is also a major issue for the prediction of the distribution over the cross section of the pipe, in order to understand any problem that may interrupt, delay or shut down the operation of the production line. However, without the determination of the flow regimes, it is not possible to calculate other parameters of engineering significance, such as heat transfer and pressure drop. It is also worth mentioning that flow regimes depend on many parameters such as inclination of the pipe or tube, geometry and pressure (Argyropoulos, 2011).

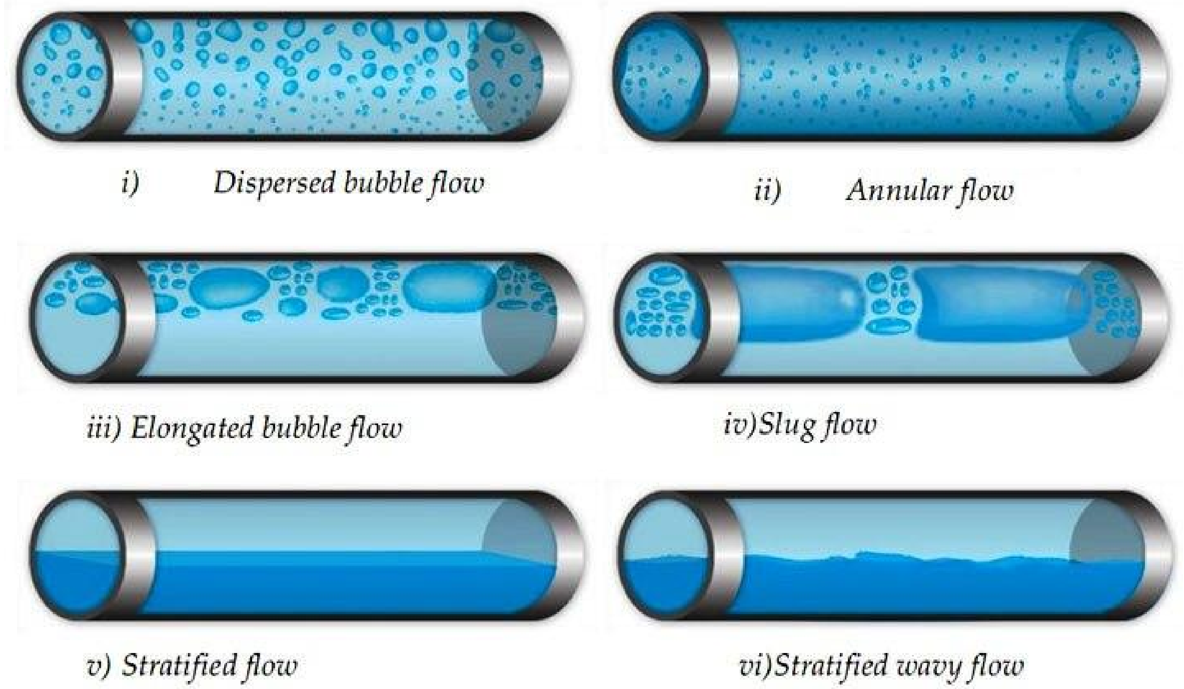

Figure 1.2: Gas-liquid flow regimes in horizontal pipes. From the work of Bratland (2010), reproduced with the author's permission.

In Figure 1.2, it is seen the flow patterns for horizontal gas-liquid flow. According to Azzopardi (2006) and Bratland (2010) the flow patterns are specified as follows:

Dispersed bubble flow: In this flow regime, the gas bubbles are dispersed in the continuous liquid phase. In the case of high liquid velocity, a significant increase of turbulence intensity takes place in the flow. As a result the bubbles are dispersed in the cross-section of the pipe and with the gravity effect are concentrated on the upper part of the pipe.

Stratified flow: In this flow pattern, the flow is separated by a smooth interface. The liquid phase is situated on the bottom of the pipe (under normal gravity conditions) with the gas above it. Subsequently, this flow pattern is characterised by two regimes; a stratified smooth and a stratified wavy. The difference between them is based on the interface at stratified flow. Thus, at low gas velocities the flow regime is stratified smooth. On the other hand, when the gas velocity is increased, waves are propagated on the interfacial region in the direction of the flow.

Plug or elongated bubble flow: This flow regime is defined as the formation of plugs of gas in liquid phase. Thus, the plug flow regime appears a similar behaviour to the bubble flow at low flow rates and moderate liquid rate.

Slug flow: This flow pattern is intermittent, similarly to plug flow. In stratified flow with the increase of gas velocity, the formation and propagation of waves take place and may reach the upper part of the pipe. In this case, the gas is throttled or even blocked instantly and as a result this flow discontinuity is responsible for the formation of elongated bubbles or slugs (Bratland, 2010).

Annular flow: This flow regime is characterised by a continuous gas core with a wall film. Subsequently, liquid may be entrained in the form of drops inside the gas core. The configured film under the gravity effect is thicker on the bottom of the pipe but as the gas velocity is increased the film becomes peripherally more uniform (Azzopardi, 2006).

During the course of this study, a substantial number of numerical simulations were performed for liquid-liquid and gas-liquid horizontal pipe flows in order to test the developed in house code but also investigate different types of flow. More specifically, single- and two-phase Poiseuille flow, droplet coalescence, single droplet and interfacial waves in pipe flows are some of the considered flows, which were investigated for different fluid properties, as a part of the validation process for the developed numerical method. More details will be presented in the next chapters.

1.1.2 Flow patterns in vertical pipes

Similar to the above Section 1.1.1, Figure 1.3 depicts the gas-liquid flow regimes in vertical pipes (Bratland, 2010). The flow regimes in vertical pipes appear great similarities with those in horizontal pipes but also a great difference is the absence of stratified flow. For more information the interested reader is directed to the works of Hewitt (1982), Dukler and Taitel (1986) and Whalley (1987). According to Figure 1.3 the flow patterns can be defined as:

Dispersed bubble flow: In this flow regime, similar to horizontal pipes, a number of bubbles is dispersed in the continuous liquid phase.

Slug flow: This flow regime is characterised by the formation of large bubbles approaching in diameter the equivalent pipe diameter, as a result of the coalescence of smaller bubbles.

Churn flow: In this flow pattern, the produced bubbles from slug flow fragment to a thick and unstable oscillating liquid film. This type of flow is characterised by chaotic behaviour which makes very difficult its investigation.

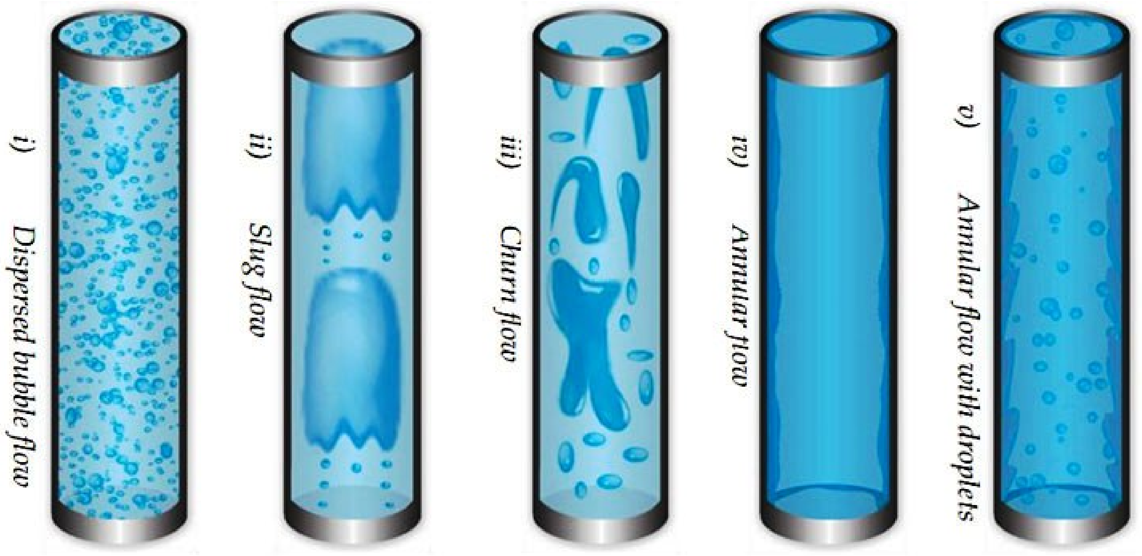

Figure 1.3: Gas-liquid flow regimes in vertical pipes. From the work of Bratland (2010), reproduced with the author's permission.

Annular flow: This flow regime is characterised by the presence of a liquid film in the vicinity of pipe wall, whilst the gas phase is situated in the core.

Wispy annular flow or annular flow with droplets: In this flow pattern, the gas core is comprised by drops which their number is increased by the high rate of liquid flow. As a result, large streaks (wisps) of liquid are formed.

In this study, a number of different gas-liquid flows were investigated in vertical pipes, such as rising of single spherical bubbles and Taylor bubbles.

1.2 Objectives of the research

The investigation of the pipe flow is a major issue for the pipelines capacity but also plays an important role for the control and prevention of phenomena that could damage the pipe, such as corrosion, erosion and the potential formation of wax or other deposits. Thus, the pipe flow simulations are very useful for the design, monitoring, operational support, sizing and optimization of the pipeline network (Bratland, 2009).

In this study, the main interest is concentrated mainly on the gas-liquid and less on the liquid-liquid pipe flows. This forms a major challenge as it requires one to incorporate with large μ and ρ ratios and achieve a real accurate resolution for simulating the interface and the interactions between the mechanisms which are important for the study of the physical problem. A Finite Difference Method (FDM) is employed while a phase-field method is adopted for simulating the interface based on the work of Ding et al. (2007). The computational model is extended to handle pipe flows by using a Ghost Cell Immersed Boundary Method (GCIBM) based on the work of Tseng and Ferziger (2003). The combination of the aforementioned methods is implemented for first time in order to investigate 3-D pipe flows, according to the author's knowledge.

The main goals of the present study are specified as follows:

1. Develop and demonstrate a computational 3-D two-phase model for the description of two-phase pipe flows.
2. Achieve laminar two-phase pipe flows with accurate simulation of the gas-liquid and liquid-liquid interface, following the topological changes.

3. Validate and compare the numerical results with available experimental and analytical data from the literature.
4. Investigate the wall effects of 3-D single bubble rising in a vertical pipe.
5. Study of a single 3-D Taylor bubble rising in a vertical pipe.

The study of three-dimensional Taylor bubbles and the wall effects on a three-dimensional buoyant bubble in a pipe is motivated by their high importance in many industrial applications and physiological systems. This type of flows, for instance, is present in oil and gas extraction, fluid transport in pipelines, nuclear reactor cooling and drilling systems (Lu and Prosperetti, 2009), as well as in blood vessels and veins.

Under special circumstance, Taylor bubbles are formed as “sausage” shape (Cavanagh and Eckmann, 1999) in human blood vessels known as gas embolism (Mukundakrishnan et al., 2007). This disorder occurs frequently in divers. The formation of air bubbles in the bloodstream can lead to pulmonary barotrauma or Decompression Sickness (DCS) and may cause unanticipated consequences for the divers health, as well as stroke or thrombosis.

Many studies have been devoted to investigate numerically the dynamics of Taylor bubbles, but mainly limited in axisymmetric simulations using VOF (Bugg and Saad, 2002) and Front Tracking (Kang et al., 2010) methods for tracking the interfacial region. In the present study, for first time fully three-dimensional numerical simulations were conducted using a combined ghost cell immersed boundary/phase-field method with large density ratio (e.g. 1000). As a result, a full parametric study for different properties of fluid was performed for the formation of a Taylor bubble, such as viscosity and density ratio, Eotvos number, Morton number and buoyancy Reynolds number. Three-dimensional numerical simulations were also conducted for studying the cylindrical wall effects on a single rising bubble in a pipe. The implementation of the proposed numerical method for the aforementioned physical problems has not been reported in the literature, according to the author’s knowledge. In both cases, the numerical predictions were compared with available experimental results, presenting good agreement.

1.3 Structure of the thesis

In the remainder of this thesis: Chapter 2 illustrates the majority of the Immersed Boundary (IB) methods with particular emphasis on Ghost-Cell Immersed Boundary Method (GCIBM) in Chapter 3, a detailed literature review is presented of the Interface tracking and capturing methods for the simulation of the interfacial region between two immiscible fluids, with the main focus on phase-field method; in Chapter 4, the mathematical formulation and the numerical method are exhibited; in Chapter 5, the validation of the developed in house code is outlined; in Chapters 6 and 7 the wall effects of a single bubble rising in vertical pipe and the dynamics of Taylor bubbles were examined and the numerical results are presented and discussed, respectively; finally in Chapter 8, the main conclusions from the present study are outlined and some general considerations for turbulent two-phase pipe flows are presented, as well as future directions for the implementation and improvement of the proposed numerical method.

This study concludes with three Appendices, which consist of the non-dimensional analysis for the Navier-Stokes and continuity equations along with the derivation of analytical solution for single- and two-phase pipe flows, and a review paper respectively.

Chapter 2

Immersed boundary methods

2.1 Introduction

This chapter aims primarily at presenting a comprehensive review of the available Immersed Boundary (IB) methods in the literature. A large number of relatively recent studies were considered, together with reference to the classical detailed review papers by Iaccarino and Verzicco (2003) and Mittal and Iaccarino (2005). Also the work of Bandringa (2010) is very interesting, including extensive comparisons of several IB methods and for this is also highly recommended.

For completeness, a brief discussion of the classification of the methods along with the advantages and disadvantages of each method are also presented and discussed. Special emphasis is given to the Ghost-Cell Immersed Boundary Method (GCIBM) and its improvements, since it is the selected method for the numerical simulations in the present study.

2.2 Definition and classification of immersed boundary methods

The use of Computational Fluid Dynamics (CFD) has helped engineers and scientists to confront complex phenomena in order to analyze and understand the physical mechanisms governing them. For simple geometries such as cube and channel domains the grid generation is usually trivial, on the other hand for complex geometries such as reactors, vehicles and heat exhangers, the mesh generation poses great difficulties along with high demand in time. Moreover, the use of turbulence modelling combined with moving boundaries and high Reynolds number flows can make the problem even worse.

Given the above mentioned circumstances the use of a body conforming grid is not always the best choice. In view of these difficulties, an alternative is the use of the immersed boundary method which allows the physical boundary to cut a grid volume.

The origin of the term “Immersed boundary method” comes from the work of Peskin (1972). The method was introduced by Peskin in order to investigate the blood flow in heart valves, assuming 2-D geometry and low-Re number for the blood flow (Peskin, 1972, 1977, 1982). The main idea behind this method is that the computational grid does not have to conform to the shape of the geometry (e.g. heart) and allows with the appropriate forcing conditions the discretization of the motion equations on a Cartesian grid. In order to enforce the desired boundary conditions it will be needed to modify the motion equations in the vicinity of the boundary, by adding a forcing function.

The type of grid that is often associated with the IB method is the Cartesian grid combined often with a Finite Difference Method (FDM). In the literature, IB methods have also been applied with Finite Element Method (FEM) (Bramble and King, 1996) and Finite Volume Method (FVM)(Ye et al., 1999). In the present study, an IB method with a FDM is adopted, which often is considered to be easier in programming than FVM or FEM. However, the best selection is dependent on the physics of the problem and may be also made by guiding the available studies in the literature. The selection of a Cartesian grid is preferable because it is not difficult to derive and requires less time and effort.

One of the main advantages of the IB method is the simple way of grid generation. The IB method can deal with almost any arbitrary body shape and appears to save memory and CPU time (Tseng and Ferziger, 2003). Another advantage is that IB method can also handle very well cases with moving boundaries (e.g. fluid-structure interactions) which require a new mesh at each time step along with an efficient algorithm to project the solution for the new mesh. On the other hand, the IB methods suffer from imposing the appropriate boundary conditions and in some cases this could be a very difficult task. Other issues are the accuracy of the boundary representation and the efficiency of the numerical schemes (Mittal and Iaccarino, 2005).

The selected forcing approach for imposing the desired boundary conditions in the vicinity of the boundary is very important for the characterisation of the proposed IB method among the other types, but it also determines the accuracy of the type.

Considering the unsteady incompressible flow for a Newtonian fluid, the governing equations can be written as:

$$\nabla \cdot \mathbf{u} = 0 \tag{2.1}$$

$$\frac{\partial \mathbf{u}}{\partial t} + \mathbf{u} \cdot \nabla \mathbf{u} = -\frac{1}{\rho}\nabla p + \frac{\mu}{\rho}\nabla^2 \mathbf{u} + \mathbf{g} \tag{2.2}$$

where $\mathbf{u}$ is the velocity of fluid flow, ρ the density, p the pressure, $\mathbf{g}$ the gravity acceleration and μ the viscosity.

According to Mittal and Iaccarino (2005), there are two alternatives for the selection of the appropriate force function, $\mathbf{f_{IB}}$. The first is the “continuous forcing approach” and the second is the “discrete forcing approach”. The main difference between the two approaches is the way that the forcing term is incorporated in the Navier-Stokes equations (2.1) and (2.2), leading to the following equations (2.3)-(2.5).

$$\nabla \cdot \mathbf{u} = 0, \quad in \quad \Omega_{fluid} \cup \Omega_{solid} \tag{2.3}$$

$$\frac{\partial \mathbf{u}}{\partial t} + \mathbf{u} \cdot \nabla \mathbf{u} = -\frac{1}{\rho}\nabla p + \frac{\mu}{\rho}\nabla^2 \mathbf{u} + \mathbf{g} + \mathbf{f_{IB}} \tag{2.4}$$

$$\mathbf{u} = \mathbf{u}_{\Gamma_{IB}}, \quad at\ \Gamma_{IB} \tag{2.5}$$

where Ω_{fluid} and Ω_{solid} denote the fluid and solid domain, respectively. Γ_{IB} is the interface between the solid and fluid domain. The set of the above equations (2.3-2.5) is well-known as standard formulation of IB method (Kang et al., 2009).

In the "continuous forcing approach", the forcing term is introduced before the discretization of the governing equations. In these methods, a Dirac delta function is often adopted (Peskin, 1982) in order to have a non-zero force function. On the other hand, the methods fall to the "discrete forcing approach" using an implicit forcing term, which is never computed in practice (Tseng and Ferziger, 2003; Mohd-Yusof, 1997). More details for both categories will be presented in the next subsections.

2.2.1 Continuous forcing approach

This class includes a substantial number of methods that introduce a continuous forcing approach in order to enforce the desired boundary conditions for the boundary representation, including methods for treating elastic and rigid boundaries.

One of the advantages of these methods is that they are independent of the discretisation process due to the fact that the forcing function is implemented before the process starts. The approach is characterised by simplicity and it is easy for implementing to an existing Navier-Stokes solver.

The use of smooth functions for the reconstruction of immersed boundary is not recommended for high Reynolds number flows, because they fail to represent the immersed boundary with high accuracy. The more the Reynolds number increases, the more the number of grid nodes increases inside the immersed boundary.

2.2.1.1 Methods for elastic boundaries

The IB method was first proposed by Peskin (1982, 2002) with the aim of modelling and predicting the low-*Re* blood flow in human cardiovascular system. The key idea behind this method is the reconstruction of the immersed boundary using a set of massless points for tracking the set of elastic fibers and the introduction of a Dirac delta function, as a force term. The solution of the governing equations is obtained by using a stationary Cartesian grid. However, problems appear with the fibers locations and the nodal points of the grid. As a result, the Dirac function is replaced by a smooth distribution function which is preferable for a discrete Cartesian grid. The appropriate selection of the distribution function is of high importance for the method and several have been proposed over the years (Beyer and Leveque, 1992; Saiki and Biringen, 1996; Lai and Peskin, 2000).

Many scientists and engineers have contributed to the extension and improvement of the method. Improvements of the method are mainly focused on accuracy (Li and Lai, 2001; Xu and Wang, 2006) and stability (Tu and Peskin, 1992; Stockie and Wetton, 1999).

2.2.1.2 Methods for solid boundaries

The first attempts for implementing the IB method to problems with solid boundaries were performed by Briscolini and Santangelo (1989) and Goldstein et al. (1993).

Briscolini and Santangelo (1989) developed a mask method[1] for investigating 2-D incompressible flows. Numerical results for 2-D driven cavity and flow around a cylinder at various Reynolds numbers were presented and discussed. The numerical results were compared with available numerical data, presenting satisfactory agreement.

Goldstein et al. (1993) used a similar IB method to Peskin's method for modelling 2-D flow around a circular cylinder, 3-D turbulent channel flow and ribbed turbulent channel flow. This IB method introduces a force function which expresses the force on the element of surface and x_s is a boundary point:

$$f(x_s, t) = \alpha \int_0^t U(x_s, t')\, dt' + \beta U(x_s, t) \tag{2.6}$$

where α and β are negative constants. This feedback forcing approach was designed with the aim of controlling the velocity close to the surface region. Numerical results were presented for flow around a cylinder at low Reynolds number and compared with

---

[1] IBM referred as "mask method".

available numerical data exhibiting fair agreement. The main disadvantage of the method is that the values of α and β are required to be large enough for accurate predictions. The large values also create limitations to the time step resulting in numerical stability problems, in particular for unsteady flows (Mittal and Iaccarino, 2005).

Saiki and Biringen (1996) investigated the uniform flow on stationary and moving cylinders. In this study, the method of Goldstein et al. (1993) was employed using fourth order FDM. The use of FDM was selected in order to minimize the development of parasitic or spurious oscillations caused by the forcing term, in contrast to Goldstein's method. Both methods implement forcing terms in Navier-Stokes equations for enforcing the fluid velocity to be zero at the desired points which represent the solid boundary.

A similar approach is the penalty method or fictitious domain method (Iaccarino and Verzicco, 2003). The method was developed by Angot et al. (1999) and Khadra et al. (2000). The key idea behind the method is that the immersed boundary is assumed to be a porous medium and solved using the Navier-Stokes/Brinkman equations. The difference with the ordinary Navier-Stokes equations is an additional term. This term is known as Darcy drag and expresses the porous medium on the flow. Accordingly, the forcing function can be written in the following form:

$$\mathbf{f} = \frac{\nu(\mathbf{u} - \mathbf{V}_S)}{\rho Da K} \tag{2.7}$$

where $Da = \dfrac{K_0}{L^2}$ is the Darcy number, K_0 the permeability of the medium, L the characteristic length, K the new free parameter, and $\mathbf{V}_S$ the desired velocity distribution.

The method suffers from weaknesses such as the parameter K and the time step restriction. As a result, a compromise is required for specifying the rigid boundary and at the same time preserving a numerically stable scheme with affordable computational cost.

2.2.2 Discrete forcing approach

This category includes the methods for which the imposition of the desired immersed boundary condition is enforced without computing or inserting any forcing term. The forcing term is not computed, because an implicit forcing technique is adopted (Kang et al., 2009).

The key idea behind this approach is the enforcement of the desired velocity V_{Bi} at each time step. Hence, the governing equations (2.3)-(2.5) can be discretised as:

$$\frac{u_i^{n+1} - u_i^n}{\Delta t} = RHS_i + f_i \tag{2.8}$$

where RHS_i includes the viscous and convective terms and the pressure gradient. In order for the forcing term to enforce the immersed boundary condition for the velocity at every time step, the forcing term must give $u_i^{n+1} = {V_{Bi}}^{n+1}$. Accordingly, the forcing term, f_i, is given by:

$$f_i = -RHS_i + \frac{{V_{Bi}}^{n+1} - u_i^n}{\Delta t} \tag{2.9}$$

Thus, the forcing term in Eq. (2.4) can be written as:

$$\begin{aligned}
\mathbf{f_{IB}} &= \frac{({V_{Bi}}^{n+1} - u_i^n)}{\Delta t} + \mathbf{u} \cdot \nabla \mathbf{u} + \frac{1}{\rho}\nabla p - \frac{\mu}{\rho}\nabla^2 \mathbf{u} - \mathbf{g} \quad at\ \Gamma_{IB} \\
\mathbf{f_{IB}} &= 0 \quad elsewhere
\end{aligned}$$

The above form of forcing term is satisfactory when the grid is coincided with the boundary. In the case of solid interface which does not coincide with the grid, the computation of the forcing term is obtained by using several techniques which belong in the class of discrete forcing approach such as the direct forcing technique or the ghost-cell technique. The implementation algorithm for the direct forcing technique may be found in the work of Balaras (2004). The ghost-cell algorithm will be presented in detail in Section 4.4.2 (Chapter 4).

The aforementioned forcing formulation has the advantage of not suffering from user-defined parameters or any stability constraints to the time step. However, this approach depends strongly on the adopted discretisation algorithm for the governing equations (Mittal and Iaccarino, 2005).

2.2.2.1 Direct forcing

This approach was first proposed by Mohd-Yusof (1997). The spectral method of Mohd-Yusof uses the forcing term to mirror the values of the velocity field across the immersed boundary. However, the method suffers from mass conservation problems in the boundary cells and its accuracy is dependent on the adopted interpolation scheme. The method was implemented for simulating 3-D laminar ribbed channel flow, presenting substantial improvements compared to previous studies.

Fadlun et al. (2000) developed a numerical method for simulating incompressible flows with second order accuracy. This method interprets a combination of immersed boundary and finite difference method with satisfactory results for flows such as the formation of a vortex ring from a curvilinear nozzle, flow around a sphere and a motored IC piston/cylinder assembly. The proposed method is an extended version of Mohd-Yusof (1997) for 3-D FDM and the difference between the two methods is that the Fadlun et al. (2000) method does not mirror the velocity field across the immersed boundary compared to the Mohd-Yusof (1997) method.

Further improvements of the aforementioned method were presented by Balaras (2004) and Gilmanov et al. (2003) with satisfactory results. The first case is restricted to 2-D and axisymmetric geometries, while the latter case is applied only for stationary bodies of simple (convex) shape. The overall accuracy for the proposed methodology of Gilmanov et al. (2003) is second order and tested for laminar flow around a sphere.

Gilmanov and Sotiropoulos (2005) proposed a new hybrid 3-D IB method, called as Hybrid Cartesian Immersed Boundary (HCIB). The method was tested for cases such as flow past a planktonic copenod and flow past an undulating fish-like body. The numerical results obtained appeared to be in good agreement with available numerical and experimental data. However, difficulties arise from high Reynolds flows, which might be treated by using local or adaptive grid refinement in the vicinity of immersed boundary.

Recently, Ge and Sotiropoulos (2007) presented a continuation of the work of Gilmanov and Sotiropoulos (2005) by extending the HCIB approach to curvilinear coordinates. Numerical results were exhibited for physiological flow through a mechanical heart valve and compared with experimental data, appearing a reasonable agreement. Similar to the above studies, Choi et al. (2007) developed a more general IB method capable for high Reynolds number and suitable for arbitrary grid topologies. The proposed method was examined for five different problems such as flow over a circular cylinder, sphere, NACA 0012 airfoil and stationary mannequin.

There are more studies with IB methods that follow the direct forcing approach but it is not possible to describe all of them, due to space limitations. However, the interested reader may find more information concerning comparisons of the IB methods for mass conservation, numerical schemes, among others, in the work of Bandringa (2010) and review paper by Mittal and Iaccarino (2005).

2.2.2.2 Ghost-cell approach

Tseng and Ferziger (2003) extended the studies of Fadlun et al. (2000) and Verzicco et al. (2000), by using a ”ghost cell“ technique (Majumdar et al., 2001) for enforcing the desired boundary conditions on the IB. The ghost cells are determined as the cells in the solid region which have at least one fluid neighbour cell in the fluid region (Mittal and Iaccarino, 2005). The desired boundary conditions in the IB are obtained by using an interpolation scheme (e.g. linear, bilinear, quadratic) in order to evaluate the ghost cell values. The accuracy of the method is based on the selection of the interpolation scheme. The proposed method was implemented for flow past a circular cylinder, Large Eddy Simulation (LES) over a wavy surface and geophysical flow over a 3-D bump. The numerical results were validated with available experimental and numerical data, exhibiting good agreement. The method is characterised by no additional CPU time since there are no new terms to calculate. The programming of the method is relatively simple and can be added very easily to existing codes, as a separate module.

An improved version of Fadlun’s method was developed by Gao et al. (2007). In this approach, the treatment of ghost cell points is handled by replacing the polynomial function with second order Taylor series expansions. As a result, the method employs an inverse distance weighting (IDW) interpolation and avoids the inverse matrix problems which can be created using polynomial functions. The numerical methods was tested for cases such as flow past a circular cylinder, a sphere, two cylinders and an array of 18 staggered cylinders. According to the numerical results, an overall second order accuracy was achieved.

Major improvements of the method were also presented by Mittal et al. (2008). The proposed sharp interface IB method based on the ghost cell approach with particular emphasis on fast, accurate and efficient solutions for flows with 3-D moving boundaries. The method satisfies with high accuracy the representation of immersed boundary. Numerical results obtained were validated for flow past a circular cylinder, airfoil, sphere and accelerated bodies, presenting good results against available numerical and experimental data from the literature.

Berthelsen and Faltinsen (2008) presented an IB method via a ghost cell approach for irregular bodies. The key idea of the method is to obtain the local ghost cell value by extrapolating (one-dimensional) the solution smoothly across the boundary in the same direction as the adopted discretisation approach. The temporal discretisation is achieved by using a second order Runge-Kutta method, while in the spatial discretisation a FDM is employed with local refinement in the vicinity of the immersed boundary. In addition, the convective terms are approximated by a weighted essentially non-oscillatory (WENO) scheme and the rest terms with central schemes. Overall the method preserves second order accuracy. The method was validated against various flow problems such as flow past a circular cylinder and objects with sharp corners (e.g facing square, chamfered plate).

Pan and Shen (2009) presented an improved version of the Tseng and Ferziger (2003) method by solving the Navier-Stokes equation with an implicit pressure correction approach along with local refinement. The stability and convergence of the solution obtained is satisfied for velocity and pressure using multigrid methods. Numerical simulations were performed for different flow problems (flow past circular cylinder and sphere) in order to validate the method and the numerical results compared with available experimental and numerical data.

Shinn et al. (2009) presented an IB method based on a ghost cell approach. Their method is focused on the treatment of mass continuity on the ghost cells. In order to achieve that they solve the mass continuity on the ghost cells together with the pressure equations, in a similar way to the work of Mark and van Wachem (2008). As a result, the method conserves mass continuity at any ghost cell with improved accuracy at the boundaries. Numerical results were presented and discussed for shear and buoyancy driven flows such as triangular and sinusoidal cavity and natural convection in square cavity.

2.2.2.3 Cut-cell finite-volume approach

Beside the above studies, there is another technique for developing IB methods, namely cut-cell (Clarke et al., 1986). The main advantage of this approach compared to the aforementioned is the capability to conserve locally the mass and the momentum using a finite volume approach (Mittal and Iaccarino, 2005). The cut-cell technique was first presented by Clarke et al. (1986) for investigating inviscid flows using Cartesian grids.

Some years later, the technique was extended for allowing the motion of immersed boundaries (Ye et al., 1999; Udaykumar et al., 2001). The method has also been implemented for various flow problems, such as flow induced vibrations (Mittal et al., 2003), objects in free fall through a fluid (Mittal et al., 2004) and many others.

Batty et al. (2007) proposed a new novel approach for accurate solid fluid coupling. The new method provides robustness and accurate solution on relatively coarse Cartesian meshes, with major improvements in the time consumption. A new variational interpretation of the pressure equation was introduced for coupled fluids. As a result, the pressure was viewed as a function that decreases the kinetic energy of the system.

Ikeno and Kajishima (2007) presented an IB method which satisfies the consistency with a desired wall velocity. This difficulty arises from the inability of pressure with the velocity to represent the solid wall, which does not coincide with the computational mesh. To cope with this drawback, a pressure solver with the necessary modifications was proposed. The method was implemented for LES of a plane channel, pipe and nuclear rod bundle.

2.3 Chapter summary

In the present Chapter, an attempt was made to present the main categories of IB methods and classify them, regarding the selected force function for enforcing the desired boundary conditions, known as “continuous forcing approach” and “discrete forcing approach”.

The main advantages and disadvantages of “continuous forcing approach” can be summarised as (Mittal and Iaccarino, 2005):

1. Attractive for flows with moving elastic boundaries.
2. Easy implementation.
3. Independent of the discretisation process due to the fact that the force function is introduced before the start of process.
4. Lack of representing a smooth immersed boundary.
5. No need for pressure boundary condition.
6. User-defined parameters may cause numerical stability problems.
7. The more the Reynolds number increases, the more the required number of nodes increases inside the immersed body.

The main advantages and disadvantages of “discrete forcing approach” can be summarised as (Mittal and Iaccarino, 2005):

1. Smooth representation of the immersed boundary.
2. Control of the solver properties (numerical stability and accuracy).
3. No need for user-defined parameters or constraints for time step.
4. Attractive for flows with high Reynolds number.
5. Dependent on the discretisation process.
6. Not attractive for flows with moving boundaries.
7. Imposition of a pressure boundary condition for the immersed boundary.

In the present study, a GCIBM was selected for the numerical simulations based on the work of Tseng and Ferziger (2003). This method was particularly chosen because of its simplicity to be implemented in existing numerical codes as a separate module and at the same time allows the preserving of the second order accuracy near the boundary for the Navier-Stokes solver. The GCIBM is capable of handling Dirichlet and Neumann boundary conditions, as well as rigid or moving boundary. Finally, the method was further extended to incorporate the appropriate boundary condition for the phase-field method which is the simulation method for the interfacial region. More details for the selected phase-field method will be presented in the next Chapter.

For more details on the evaluation of IB methods regarding mass conservation, turbulent flows by means of Large Eddy Simulation (LES), compressible flows, among others, the interested reader is directed to the works of (Mittal and Iaccarino, 2005; Iaccarino and Verzicco, 2003) and Bandringa (2010).

Chapter 3

Interface tracking and capturing methods

3.1 Introduction

The present chapter presents a review of the available numerical techniques for simulating the interfacial region between two immiscible fluids. A substantial number of studies were considered for a number of interface-tracking and capturing methods.

Details for the main characteristics of the methods such as advantages and drawbacks, as well as the key ideas of each method are presented and discussed. Special attention is given to the Phase-Field, since it is the selected technique for the simulation of the interfacial region.

In the remainder of this section, a number of the better-established and most promising versions of the methods, according to the present author opinion, along with some recently developed ones, will be presented and discussed.

3.2 Categories of interface tracking and capturing methods

The numerical simulation of discontinuous fronts and interface regions between two immiscible fluids may be accomplished by using several interface tracking or capturing methods.

The main categories for the computation of free surfaces and fluid interfaces can be divided in two classes (Gopala and van Wachem, 2008; Yeoh and Tu, 2010): a) surface methods (e.g. Front Tracking method, Level-Set method) and b) volume methods (e.g. Marker Particle method, Volume of Fluid). The first category includes methods of which the interfacial region is tracked by a large number of special marker points and the latter class comprises methods that represent the interface by an indicator function or massless particles. The first type of methods allows the precise representation (geometry and location) of the interface. The second class of methods uses specific advection schemes in order to preserve and reconstruct the interfacial region.

The advantages of the first class of methods are that the position of the interfacial region is known and maintain a sharp profile during the simulation, as well as they are the simplest to implement. On the other hand, they appear difficult to simulate coalescence and break up phenomena.

The main advantage of the volume methods is accurate mass conservation during the simulation. However, they are unable to prescribe the position of the interface and as a result numerical techniques are adopted for the reconstruction of the interfacial region. A more detailed discussion of the above mentioned methods is given below.

3.2.1 Volume of fluid methods

The volume of fluid (VOF) method falls in the class of volume methods and is based on the simple approach of the volume fraction. The method is characterised by simplicity, mass conservation between phases and satisfactory accuracy but also by increasing computational complexity. The VOF method tracks the interfacial region by computing the fractional volume of each material occupied in each computational cell (Hyman, 1984). In VOF methods, a scalar indicator function, C, known as volume fraction or color function is adopted. The value of C is associated with the region of each fluid and interface. Thus, $C = 0$ (no material) and $C = 1$ (full of material), while $0 < C < 1$ if the interfacial region cut the computational cell. At every time step the interfacial region reconstruction is achieved by using the cell volume fraction and its nearest neighbours cells accordingly, by means of FDM or other more complicated numerical methods. The reconstructed interfacial region is characterised as sharp. However, special attention is needed for the case of $0 < C < 1$, because of the developed numerical errors for computing the fluxes which may lead to unrealistic values of volume fraction C according to Scardovelli and Zaleski (1999).

Over the years, several versions of the method have been developed by many engineers and scientists. The first version of the method known as Simple Line Interface Calculation (SLIC) VOF was introduced by Noh and Woodward (1976) and later followed by the Donor-Acceptor technique of Hirt and Nichols (1981). These two types express the simplest versions of the method, but with the least accuracy. The main difference between these two methods is that they use different technique for the reconstruction of the interfacial region. The first algorithm adopts a piecewise constant approximation, while the latter algorithm uses a piecewise constant/stair-stepped approximation (Rider and Kothe, 1998).

A large number of studies have been devoted to improve the accuracy of the above mentioned techniques for the reconstruction of the interfacial region. Chorin (1980) improved SLIC-VOF method with a multidimensional algorithm for the interface reconstruction. Other more accurate schemes have been proposed, such as the Flux Corrected Transport (FCT) by Boris and Book (1973), Zalesak (1979) and Rudman (1997), the Flux Line-segment model for Advection and Interface Reconstruction (FLAIR) by Ashgriz and Poo (1991), the SURFER by Lafaurie et al. (1994), the Compressive Interface Capturing Scheme Arbitrary Meshes (CICSAM) by Ubbink (1997), the Lagrangian - PLIC by Van Wachem and Schouten (2002), among others.

A significant improvement of VOF methods was the introduction of Piecewise Linear Interface Calculation (PLIC) VOF by Youngs (1982). The Young's method presents robustness and efficiency but is limited to only first order of accuracy. Improvements and extensions of Young's method were developed by many researchers. Puckett and Saltzman (1992) extended the PLIC-VOF by using an adaptive mesh refinement (AMR) technique. Kothe et al. (1996) enhanced the method by combining a second order Runge-Kutta method along with structured and unstructured grid.

Van Sint Annaland et al. (2005) developed a 3-D VOF method based on Young's method. The 3-D VOF method was implemented for investigating rising bubbles in quiescent liquids. The numerical results obtained were compared to experimental data from the bubble diagram of Grace (1973), presenting good agreement.

Another problem of the VOF methods is the implementation of surface tension to the interfacial region. The problem is getting even worse with the computation of surface tension in systems of high density ratio. As a result, an inaccurate calculation of the surface tension at the interface creates ”parasitic or spurious currents” (Lafaurie et al., 1994). Serious attempts to face this problem were presented by Francois et al. (2006), Popinet (2009), among others.

Francois et al. (2006) proposed a numerical approach combining the VOF method with surface tension models. They employ the Continuum Surface Force (CSF) and Sharp Surface Force (SSF) models with the aim to identify any notable differences. The main difference between the aforementioned surface tension models was the implementation of the pressure jump condition across the interfacial region. However, both techniques suffer from the presence of parasitic or spurious currents.

Popinet (2009) presented a novel technique for modelling two-phase flows based on the VOF method. The technique is characterised by an adaptive quad/octree spatial discretization for surface tension driven flows. The numerical results obtained showed good agreement for the test case of capillary wave oscillations and for the case of a stationary droplet.

Despite all the aforementioned improvements and extensions of VOF methods, there are still limitations (Sethian, 1999). These methods are characterised by inaccurate reconstruction of the interfacial region and as a result it is required to have a substantial number of cells in order to obtain a reasonable representation of the interface. Computation of the normal and curvature from volume fraction may lead to lack of accuracy. Furthermore, the use of high-order discretization schemes for the reduction of numerical diffusion requires a considerable amount of work and time. More information for VOF methods is provided in detail in the review paper by Scardovelli and Zaleski (1999).

Recently, Dyadechko and Shashkov (2005) developed the Moment of Fluid (MOF) method which may be characterised as a generalisation of the VOF method. Jemison et al. (2013) claim that the MOF method gives better results for deforming boundaries with corners or thin filaments compared to VOF methods, LS methods or CLSVOF methods (Wang et al., 2012; Cervone et al., 2009). Application of the method for the free-surface dam-break and the Rayleigh-Taylor problems can be found in the work of Ahn and Shashkov (2009).

3.2.2 Marker particle methods

A standard approach for modelling interfaces is the Marker Particle (MP) method (Harlow and Welch, 1965). In this method, the interfacial region is reconstructed by a set of marker particles at any time (Sethian, 1999). This method is known as MP method, as well as under the names, string methods and nodal methods. In 2-D problems, line segments are commonly used for the interface representation, while in 3-D problems, triangles are preferable.

MP methods are characterised by high degree of accuracy, robustness and account for substantial topology changes in interface. However, these methods are computationally expensive, in particular for 3-D problems. More difficulties arise with merging, break up and shrinking of the interface, resulting in additional marker particles requirements during the simulation (Scardovelli and Zaleski, 1999; Van Sint Annaland et al., 2005, 2006; Gopala and van Wachem, 2008).

The first MP method known as Marker and Cell (MAC) was presented by Harlow and Welch (1965) at the Los Alamos National Laboratory. Significant refinement and optimization of the method was made by Amsden and Harlow (1970) and renamed as the Simplified Marker and Cell (SMAC) method.

Chen et al. (1991) improved the older version of SMAC method with reference to the computational cost and mass storage for transient flows, by using new marker movements and cell reflagging techniques. The improved version of the method is known as Simplified Marker (SM) method. Numerical results for SMAC and SM methods were obtained for three different problems (e.g. broken dam problem, cavity in horizontal and vertical plane) and comparisons made between the solutions.

Some years later, Chen et al. (1997) presented the Surface Marker and Micro Cell (SMMC), which is an improved version of SM method. The main advantage of the new method is that it can track the interfacial region much faster compared to previous versions of the method. Subsequently, numerical results were validated with experimental data for water sloshing in a tank, presenting good agreement between the shapes and the locations of the free surfaces.

3.2.3 Level set methods

Notable among the surface methods is the Level-Set (LS) method (Osher and Sethian, 1988; Sethian and Straint, 1992; Sussman et al., 1994, 1999; Sethian, 1999; Chang et al., 1996; Sussman and Smereka, 1997; Sussman and Fatemi, 1999; Osher and Fedkiw, 2001). The main idea behind of this method is the introduction of a distance or level set function ϕ. The distance function ϕ corresponds to one fluid with positive value ($\phi > 0$) and negative for the other fluid ($\phi < 0$). For the interfacial region, ϕ is equal to zero. The equation which expresses the advection of the distance function with the local fluid velocity is defined as:

$$\frac{\partial \phi}{\partial t} + U_i \frac{\partial \phi}{\partial x_i} = 0 \tag{3.1}$$

LS methods are characterised by simplicity and easy implementation. The LS methods fall in the sharp interface methods and give results with high accuracy when the interface is advected parallel to one of the co-ordinate axis (Gopala and van Wachem, 2008; Van Sint Annaland et al., 2005). However, the main disadvantage of this class of methods is the mass loss, where the interfacial region shows significant deformations.

Improvements and modifications of the LS methods are many, with probably the most important being the works of Sussman and Fatemi (1999), Enright et al. (2002) and Menard et al. (2007).

Sussman and Fatemi (1999) introduced an improved LS method with better accuracy and efficiency. The novel part of the technique is the implementation of a 'constraint' along with high-order discretization schemes. The numerical results obtained were compared with available experimental and theoretical data. It was concluded that the method presented better representation of the interfacial region with smaller mass loss.

Enright et al. (2002) proposed a novel technique in order to improve the mass conservation of the LS method. Lagrangian marker particles were used to reconstruct the level set in regions that are under-resolved. The numerical results appeared to be in satisfactory agreement regarding the conservation mass compared to VOF method and the Lagrangian schemes for the interfacial region.

Yu and Fan (2008) performed numerical simulations with a 3-D LS method for investigating the shape and terminal velocity of bubbles rising in liquid. The numerical results were compared with experimental data from the work of Grace (1973), exhibiting good agreement. Further results for bubble coalescence were also presented.

For more details of the LS method, the interested reader is directed to the review paper of Sethian and Smereka (2003) and to the classical textbook by Sethian (1999).

3.2.4 Front tracking methods

Another 'successful' class of methods and also widely used is the Front Tracking (FT) methods. Early attempts of the FT methods were presented by Glimm's group (Glimm et al., 1981, 1986, 1998, 2001) and by Tryggvason's group (Unverdi and Tryggvason, 1992a,b; Tryggvason et al., 2001).

The main concept of the method is to retain a sharp interfacial region between the two fluids, by using massless marker particles for the interface reconstruction. The main advantage of the method is the high accuracy of the interfacial region but it is also rather difficult to implement. The difficulty arises from the use of an additional grid for tracking the interfacial region, whilst a fixed or Eulerian grid is adopted for solving the Navier-Stokes equations.

Van Sint Annaland et al. (2006) performed numerical simulations for investigating the dynamics of rising bubbles in quiescent liquids. The proposed model was able to simulate systems (e.g. air-water) with large viscosity and density ratio. The numerical results appeared to be in a good agreement with experimental data from the work of Grace (1973).

The study of Van Sint Annaland et al. (2006) was continued by Dijkhuizen et al. (2010) by using an improved version of the FT method. The method has been improved for simulating flows with very small bubbles and high surface tension. As a result, effects concerning the mass loss and the presence of spurious or parasitic currents have been almost eliminated. Numerical results for stationary bubble and oscillating droplet with viscous damping were compared with available experimental and analytical data, presenting satisfactory agreement.

Hua and Lou (2007) developed an improved FT method for modelling bubbles rising in quiescent liquids. The proposed method preserves the bubble volume by introducing a volume correction procedure. Parametric analysis was performed for air-water systems in order to investigate the effects of Reynolds number, Bond number, density ratio, viscosity ratio and initial bubble shape. The numerical results predicted with satisfactory agreement the bubble shape and terminal velocity compared to experimental data.

Extension of the previous study is the work of Hua et al. (2008) with the simulation of 3-D bubbles rising in water. An adaptive mesh refinement (AMR) technique is adopted for simulating the interfacial region with high resolution. The numerical results were compared with available experimental data, regarding the bubble terminal velocity and shape.

3.2.5 Phase-field methods or Diffusive Interface methods

Phase-Field (PF) or Diffusive-Interface (DI) methods belong to the large category of interface capturing methods. This class of methods is very attractive as they do not seem to be affected by problems such as mass conservation or the accurate computation of surface tension. The key idea behind the phase-field method is the description of the system by an order parameter (Qin and Bhadeshia, 2010). The order parameter may be expressed by the difference between the concentrations of the two mixtures or the relative mass density, or even with a phase indicator function.

The interfacial region between two immiscible fluids may be characterised as a very narrow region in which the phase field variables vary gradually. Accordingly, the interface position is implicitly captured by the phase-field variable. The idea for this class of methods was proposed by Van der Waals (1979) many years ago, but it has been applied for modelling two-phase flows relatively recently.

An important advantage of PF methods is the implicit tracking of the interfacial region. There is no need for any a priori knowledge of the location of the interfacial region. As a result, any topology alterations are treated without the need of mathematical equations. On the other hand, PF methods require high grid resolution, in particular for three dimensional problems in order to keep the interfacial region extremely thin and the correct value of the adjustable parameter for the interface width.

There are many phase field models for simulating two-phase flows such as the Cahn-Hilliard-van der Waals (CHW) model (Jacqmin, 1999), the Cahn-Hilliard (CH) model (Cahn and Hilliard, 1958), the Model H (Hohenberg and Halperin, 1977; Starovoitov, 1994; Gurtin et al., 1996; Jasnow and Vinals, 1996; Badalassi et al., 2003), among others.

Lowengrub and Truskinovsky (1998) developed a quasi-incompressible Euler-Cahn-Hilliard (ECH) model for the case of fluids with different densities. They implemented the model for investigating the annihilation of a spherical droplet. It was found that the ECH model can predict the topological transitions smoothly without any topological singularities, in contrast to the sharp interface models.

Jacqmin (1999) presented numerical simulation by using the Cahn-Hilliard-van der

Waals (CHW) model in order to calculate the phase-field convection with less than two cells wide. He tested the CHW model for linear capillary waves and Rayleigh-Taylor instabilities. One year later, Jacqmin (2000) investigated with CHW model the moving contact line problem with promising results.

Badalassi et al. (2003) performed numerical simulations based on the Model H in order to investigate multi-phase flows. The numerical results appeared to be in a fair agreement with analytical solutions and scaling laws, and for the 3-D applications in the presence of shear, reveal rich and complex structure, including strings.

Ding et al. (2007) performed numerical simulation for incompressible two-phase flows with large density ratios based on a modified Model H. Numerical results were compared with cases of axisymmetric bubble and Rayleigh-Taylor instability. Subsequently, results for the head-on droplet collision and the onset of droplet entrainment in stratified flow were also presented.

Recently, phase-field methods have been used for a variety of applications such as droplet collision (Yue et al., 2004), moving contact lines (Seppecher, 1996; Jacqmin, 2000), vesicle dynamics (Biben et al., 2005) and droplet coalescence involving four different phases (Kim et al., 2009). The reader interested in more details is addressed to the review papers by Anderson et al. (1998), Qin and Bhadeshia (2010) and the recent one by Kim (2012).

3.2.6 Hybrid methods

As mentioned before all the available tracking and capturing interface methods have advantages and drawbacks. In order to surmount the weaknesses of the above methods, a number of hybrid methods has been proposed. Hybrid methods combine the advantages of two or more of the above mentioned methods in one.

The most well-known and widely used of this category is the Coupled Level Set Volume of Fluid (CLSVOF). The main idea of CLSVOF is to combine the VOF with LS for preserving the mass conservation. The method was initially proposed by Bourlioux (1995) and further improved by Sussman and Puckett (2000). Some years later, Sussman

(2003) presented a second order accurate version of the method for modelling vapor bubbles.

Son (2003) further improved the method by replacing the two pressure equations of Sussman and Puckett (2000) method with one and by using a high order advection scheme for the momentum equation, namely Cubic-Interpolated Propagation scheme (Takewaki and Yabe, 1987).

Chakraborty et al. (2013) performed numerical simulations by using the CLSVOF method for investigating the dynamics of axisymmetric bubbles rising in quiescent liquid. The numerical results obtained were compared with experimental data from Bhaga and Weber (1981) and Hnat and Buckmaster (1976), exhibiting good agreement.

Aulisa et al. (2003) presented a new method, combining mixed markers and VOF algorithm for the reconstruction and advection of interface, in order to model two-phase and free boundary flows. Many two-dimensional cases were tested, showing good accuracy and mass conservation. Finally, the MP method has been extended by using the characteristic Galerkin finite element method (FEM) for metal forming by Yamada and Matsui (2008) with interesting results.

Menard et al. (2007) performed numerical simulations for investigating the dense zone of a spray. The proposed methodology is a combination of LS, VOF and Ghost Fluid Method (GFM). The LS method is adopted for tracking interfacial region and GFM for capturing precisely sharp discontinuities for pressure, viscosity and density, while the VOF method is used for mass conservation. The numerical results were compared with 2-D and 3-D test cases.

Wang et al. (2012) developed a hybrid level set-volume constraint (HLSVC) method for modelling deforming boundaries. The numerical results obtained were compared with numerical data from the CLSVOF method. The main advantage of the HLSVC method is the mass conservation and relatively easy implementation. Numerical results for various applications were validated against on a number of benchmark problems (e.g. Rayleigh capillary instability, rising bubble, break-up of a liquid jet, liquid jet flow in a gas cross-flow).

Recently, Jemison et al. (2013) proposed a Coupled Level Set-Moment of Fluid Method (CLSMOF) for incompressible flows. The key idea behind the hybrid method is the combination of the level-set function, the volume of function and the reference centroid for the reconstruction of interfacial region. Numerical results for two- and three-dimensional flow problems such as bubbles, jets, waves and drops are presented and discussed.

3.3 Chapter summary

In the present Chapter, an attempt was made to briefly review the state of the art of the main interface tracking and capturing methods. One of the differences between VOF and LS methods is that the first category adopts a discontinuous function for the interface reconstruction, while the latter class of methods expresses the interface reconstruction by a contour of smooth function.

The first type of methods suffers from inaccurate representation of the interfacial region but at the same time preserves exactly the mass of each fluid volume. On the other hand, the use of a smooth function for the interface reconstruction allows numerical results with better accuracy.

In Lagrangian methods, the interfacial region is explicitly tracked by using a set of marker particles or a moving mesh. These methods suffer from weakness when applied to interfaces with large deformations or topological alterations, along with the surface tension effect. However, the application of this class of methods is accompanied by highly accurate computations.

Phase-Field or Diffusive-Interface methods handle naturally the topology changes or large deformations of the interface without any a priori knowledge of the location or tracking of the interface. This is very useful for visualizing microstructural flows and phenomena such as coalescence and morphology changes. On the other hand, the main disadvantage is the value of interface width which is an adjustable parameter and sometimes may lead to unrealistic values.

In the present study, the Phase-Field method is the adopted technique for the simulation of the interfacial region because of its aforementioned advantages for the investigation of physical problems with topology changes and coalescence, such as the dynamics of Taylor bubbles rising in pipes, wall effects of single bubble rising in stagnant liquids, dynamics of bubble swarms and droplets, among others.

Table 3.1: Advantages and disadvantages of interface and capturing methods.

Method	Advantages	Drawbacks
SLIC VOF	Easy implementation Mass conservation Extension to 3-D Automatic merging and breakage of interfacial region	Limited accuracy Numerical diffusion
PLIC VOF	Accurate and relatively simple Mass conservation Automatic merging and breakage of interfacial region	Difficult for 3-D flows Difficult with boundary fitted grids
Front Tracking (FT)	Extremely accurate Robust Accounts for substantial topology changes in interface	Dynamic re-meshing Mapping of interface mesh onto Eulerian mesh
Marker Particle (MP)	Extremely accurate Robust Accounts for substantial topology changes in interface	High computational cost Marker particle redistribution
Level Set (LS)	Easy implementation Simple	Limited accuracy Mass loss
Phase Field (PF)	Visualization of microstructural development Naturally handled with topology changes and coalescence	Interface width (adjustable parameter) Challenging for large computational domain
Hybrid	High accuracy Mass conservation	Computational cost Complex implementation

Table 3.1 illustrates the main advantages and drawbacks of the aforementioned methods. Due to space limitations, the interested reader is directed to the review paper by Scardovelli and Zaleski (1999), for VOF methods. Information for the currently widely used LS methods may be found in Sussman et al. (1994), Sethian (1999) and Sussman and Smereka (1997). More details for the development and progress of Phase-Field methods can be found in the review papers by Anderson et al. (1998), Qin and Bhadeshia (2010) and Kim (2012).

Chapter 4

Mathematical formulation and numerical methods

4.1 Introduction

A numerical methodology is presented for simulating laminar two-phase pipe flows of separated phases with an interfacial region. The set of the 3-D model partial-differential equations with their dimensionless form, along with the appropriate auxiliary relations and boundary conditions, have been solved by means of a Finite Difference Method.

A uniform staggered grid was selected for the numerical simulations, while a projection method was adopted for coupling the continuity and momentum equations. In momentum equations, an Adams-Bashforth was employed to discretise the diffuse term and the treatment of the viscous term was obtained by a Crank-Nicolson scheme. Central finite differences were used for the spatial discretisation. The interface simulation was achieved by using a phase-field method based on the Cahn-Hilliard equation. The convective Cahn-Hilliard equation was descretised by using a fifth-order WENO scheme.

Two immersed boundary algorithms were developed for the representation of the rigid boundaries (pipe wall). The first IB method based on a penalty technique and the latter is known as Ghost Cell Immersed Boundary Method and is based on the ghost cell technique.

4.2 Governing differential equations

4.2.1 Phase-field modelling

The modelling of interface region between two immiscible fluids can be accomplished by using several interface methods. In the present study, a phase-field method was selected for the computation of the interface between the two fluids. The interfacial region between two immiscible fluids may be characterised as very narrow region in which the phase field variables is gradually vary.

In the past few decades, phase-field models have gained great popularity for the investigation of interfacial phenomena and the micro-structure evolution during solidification. The key idea behind the phase-field method is the description of the system by an order parameter (Qin and Bhadeshia, 2010). The order parameter may be expressed as the difference between the concentrations of the two mixtures or the relative mass density, or even with a phase indicator function.

In the present formulation, the flow of two incompressible immiscible fluids (A and B) with variable density and viscosity is considered. Every control volume in the domain may contain a part of the phases A and B, and the amount of phase A or B (state of the system) can be determined by the volume fraction, C, of one of the fluids (i.e. A). The volume fraction, C $(0 \leq C \leq 1)$ is a function of the position vector and represents the order parameter for the phase-field model (Argyropoulos, 2011).

According to C the local properties such as viscosity (μ) and density (ρ), are specified as follows:

$$\rho = (1 - C)\rho_A + C\rho_B \tag{4.1}$$

$$\mu = (1 - C)\mu_A + C\mu_B \tag{4.2}$$

where ρ_A and ρ_B are the bulk densities for phases A and B, respectively. Similarly, μ_A and μ_B are the bulk viscosities for phases A and B, respectively. The above formulation indicates that the density and the viscosity are linearized with C field in order to avoid the discontinuities across the interfacial region.

The governing equation for the description of the phase-field is the convective Cahn-Hilliard equation:

$$\frac{\partial C}{\partial t} + \mathbf{u} \cdot \nabla C - \nabla \cdot j = 0 \tag{4.3}$$

where $\mathbf{u}$ is the velocity field and j denotes the volumetric diffuse flow rate of phase A (j_A) but it will be referred to as j in order to simplify the notation, defined as:

$$j = M(C)\nabla\phi \tag{4.4}$$

where ϕ is the chemical potential and is defined by the variation of the free energy with respect to the volume fraction C and $M(C) > 0$ is the mobility (diffusion parameter). From equations 4.3 and 4.4, it follows that the convective Cahn-Hilliard equation can be written as:

$$\frac{\partial C}{\partial t} + \mathbf{u} \cdot \nabla C = \nabla \cdot (M(C)\nabla\phi) \tag{4.5}$$

It is also worth mentioning regarding equation 4.5 that C on the left-hand side represents a different function, depending on the selected interface method. Thus, for the level-set method, the interface is characterised by a continuous function ϕ, representing the distance to the interface which is set to zero on the interface, is positive on one side and negative on the other. In VOF approach, C expresses the volume fraction of the fluid (Lakehal, 2010).

According to the literature, many scientists have proposed various formulations for the mobility. Jacqmin (1999) selected a mobility profile dependent on the interface width and obtained by the following expression, $M = O(\varepsilon^{\delta}), 1 \leq \delta < 2$. Badalassi et al. (2003) used a phase-field dependent mobility, $M(\phi) = M_c(1-\gamma\phi^2)$, following the work of Langer et al. (1975).

Borcia and Bestehorn (2003) introduced the following expression for the mobility, $M(C) = 1$, while Kim (2007) and Ding et al. (2007) used a mobility profile $M(C) = C(1 - C)$. In the present work was adopted the last formulation of mobility by Kim (2007) and Ding et al. (2007). This formulation is characterised by lower levels of long-range diffusion across the bulk regions (Kim, 2007).

The dynamics of C can be obtained from a free-energy density model for immiscible isothermal two-phase fluids according to Van der Waals (1979):

$$f = 0.5\alpha \left|\nabla C\right|^2 + \beta\psi(C) \tag{4.6}$$

where α and β are positive constants, $\psi(C)$ the bulk energy density and f the free energy density. The bulk energy density is given by the following expression:

$$\psi(C) = 0.25C^2(1-C)^2 \tag{4.7}$$

In general, the available free energy density models can be classified as singular or non-singular according to their behaviour (Jacqmin, 1999). The simplest non-singular model with two equal minima at $C = \pm 0.5$ is $\psi(C) = (C+0.5)^2(C-0.5)^2$ (Jacqmin, 1999). On the other hand, singular free energy density models with interesting properties are the $\psi(C) = \left|C-0.5\right|^{1.5}\left|C+0.5\right|^{1.5}$ and the double obstacle energy model which was used by Nochetto et al. (1996) and Oono and Puri (1988). More details for the characteristics of the above mentioned free energy density models may be found in the work of Jacqmin (1999).

The chemical potential or partial molar free energy, ϕ, is defined as the partial derivative of Gibbs free energy with respect to C:

$$\phi = \frac{\delta F}{\delta C} = \beta\psi'(C) - \alpha\nabla^2 C \tag{4.8}$$

From equations (4.6), (4.7) and (4.8), it follows that ϕ is equal to

$$\phi = \beta(C^3 - 1.5C^2 + 0.5C) - \alpha\nabla^2 C \tag{4.9}$$

The interface profile in equilibrium may be derived by equating the right hand side of equation (4.9) to zero. Hence, if the z-axis is normal to the interface yields:

$$\frac{d^2C}{dz^2} - \frac{\beta}{\alpha}(C^3 - 1.5C^2 + 0.5C) = 0 \tag{4.10}$$

The two positive constants α and β affect the surface tension (σ) and the interface thickness (ε). The solution of the equation (4.10) yields the equilibrium profile of C, normal to z-axis:

$$C(z) = 0.5 + 0.5\tanh\left(0.5\sqrt{\frac{\beta}{\alpha}}z\right) \tag{4.11}$$

where $z = 0$ at the interface for $C = 0.5$. The interface thickness (ε) is specified as follows:

$$\varepsilon = \sqrt{\frac{\alpha}{2\beta}} \tag{4.12}$$

In our case the volume fraction varies from $C = 0.05$ to $C = 0.95$ and this variation defines a equilibrium interface thickness of 8.328ε.

For an isothermal system of fluids in equilibrium the surface tension is defined as the integral of the free energy density along the surface area and is given by the following equation (Bray, 1994):

$$\sigma = \alpha \int_{-\infty}^{+\infty} \left(\frac{\mathrm{dC}}{\mathrm{dz}}\right)^2 \mathrm{d}z = \frac{1}{6}\sqrt{\alpha\beta} \tag{4.13}$$

From equations (4.12) and (4.13) the chemical potential ϕ can be written as:

$$\phi = -6\sqrt{2}\varepsilon\sigma\nabla^2 C + 6\sqrt{2}\frac{1}{\varepsilon}\sigma(C^3 - 1.5C^2 + 0.5C) \tag{4.14}$$

where ε is the interface thickness and σ the surface tension.

Substituting the above equation (4.14) for ϕ in equation (4.5) the Cahn-Hilliard equation can be written:

$$\frac{\partial C}{\partial t} + \mathbf{u}\cdot\nabla C = \nabla\cdot(C(1-C)\nabla(-6\sqrt{2}\varepsilon\sigma\nabla^2 C + 6\sqrt{2}\frac{1}{\varepsilon}\sigma(C^3 - 1.5C^2 + 0.5C)) \tag{4.15}$$

4.2.2 Equations of the fluid motion

The system of partial differential equations for the incompressible two-component flows can be expressed as follows:

Continuity equation:

$$\nabla\cdot\mathbf{u} = 0 \tag{4.16}$$

where $\mathbf{u}$ is the velocity of fluid flow.

Navier-Stokes equations:

$$\rho\left(\frac{\partial \mathbf{u}}{\partial t} + \mathbf{u}\cdot\nabla\mathbf{u}\right) = -\nabla p + \nabla\cdot[\mu(\nabla\mathbf{u} + \nabla\mathbf{u}^T)] + \phi\nabla C + \rho\mathbf{g} + \mathbf{f_{IB}} \tag{4.17}$$

where ρ is the density, p the pressure, μ the viscosity, ϕ the chemical potential, $\mathbf{f_{IB}}$ the forcing term for the immersed boundary and $\mathbf{g}$ the gravitation acceleration. The superscript T denotes the transpose operator.

In the case of a single-phase flow the above equations are the same excluding that the density and viscosity are now functions of the composition. According to the work of Hohenberg and Halperin (1977), the set of equations (4.15)-(4.17) comprises the modified model H. As mentioned earlier, the proposed numerical methodology does not rely on the reconstruction of the interface for the calculation of the surface tension. The surface tension is specified as a function of the concentration field.

4.2.3 Non-dimensionalisation

Considering the above equations (4.15)-(4.17), it is more convenient to express them in dimensionless form as numerically are solved in the developed in house code. The following variables and dimensionless numbers are introduced in order to derive the dimensionless form of the governing equations. The variables with the asterisk are the dimensionless variables and with the subscript c are the characteristic variables. The dimensionless variables and parameters can be defined as:

$$u^* \equiv \frac{u}{u_c}, \qquad t^* \equiv t\frac{u_c}{L_c}, \qquad x^* \equiv \frac{x_c}{L_c}, \qquad p^* \equiv \frac{p}{\rho_A u_c^2}$$

$$M^* \equiv \frac{M}{M_c}, \qquad \phi^* \equiv \frac{\phi}{\phi_c}, \qquad g^* \equiv \frac{g}{g_c}, \qquad \nabla^* \equiv L_c^{-1}\nabla$$

where L_c is the characteristic length scale, u_c the characteristic velocity, u is the velocity, t is the time, p is the pressure, M is the mobility, M_c is the characteristic mobility, ϕ is the chemical potential, ϕ_c is the characteristic chemical potential, g is the gravitational acceleration and g_c is the characteristic gravitational acceleration.

It is important to mention that the characteristic velocity, u_c, is equal to u_p for pressure driven flows and u_b for gravity driven flows in the present study. The u_p based on the pressure gradient and the u_b based on the gravity acceleration, respectively. The aforementioned terms are defined as:

$$u_p = \sqrt{\left|\frac{\partial p}{\partial z}\right| \frac{L_c}{\rho_A}} \qquad\qquad u_b = \sqrt{gL_c}$$

the selected characteristic length scale (L_c) is the pipe diameter (D_p). The dimensionless form for the viscosity and density is:

$$\rho^* \equiv \frac{\rho}{\rho_A} = (1-C) + r_d C \qquad \mu^* \equiv \frac{\mu}{\mu_A} = (1-C) + r_v C$$

where C is the volume fraction, ρ_A the density of fluid A, μ_A the viscosity of fluid A, r_d the ratio density and r_v the ratio viscosity.

The necessary dimensionless numbers for the description of the pressure driven flows in this study are the pressure gradient-based Reynolds number, Peclet number, Capillary number and Froude number, respectively.

$$Re_p \equiv \frac{\rho_A u_p D_p}{\mu_A}, \qquad Pe_p \equiv \frac{D_p u_p}{M_c \phi_c}, \qquad Ca_p \equiv \mu_A \frac{u_p}{\sigma}, \qquad Fr_p \equiv \frac{u_p}{\sqrt{g D_p}}$$

Accordingly, with the asterisks omitted henceforth for simplicity, the equations (4.15)-(4.17) can be written as:

Cahn-Hilliard equation:

$$\frac{\partial C}{\partial t} + \mathbf{u} \cdot \nabla C = \frac{1}{Pe_p} \nabla \cdot M \nabla \phi \tag{4.18}$$

Continuity equation:

$$\nabla \cdot \mathbf{u} = 0 \tag{4.19}$$

Navier-Stokes equations:

$$\rho\left(\frac{\partial \mathbf{u}}{\partial t} + \mathbf{u} \cdot \nabla \mathbf{u}\right) = -\nabla p + \frac{1}{Re_p} \nabla \cdot [\mu(\nabla \mathbf{u} + \nabla \mathbf{u}^T)] + \frac{\phi \nabla C}{Re_p Ca_p} + \frac{\rho}{Fr_p^2} \mathbf{g} + \mathbf{f_{IB}} \tag{4.20}$$

The above equations (4.18) and (4.20) represent the Cahn-Hilliard and Navier-Stokes equations for pressure driven flows with gravity. In the case of gravity driven flows (i.e. rising single bubbles, bubble swarms, Taylor bubble) the continuity equation is identical, while the equations (4.18) and (4.20) take the following form:

$$\frac{\partial C}{\partial t} + \mathbf{u} \cdot \nabla C = \frac{1}{Pe_b} \nabla \cdot M \nabla \phi \tag{4.21}$$

$$\rho\left(\frac{\partial \mathbf{u}}{\partial t} + \mathbf{u} \cdot \nabla \mathbf{u}\right) = -\nabla p + \frac{1}{Re_b} \nabla \cdot [\mu(\nabla \mathbf{u} + \nabla \mathbf{u}^T)] + \frac{\phi \nabla C}{Eo} + \frac{\rho}{Fr_b^2} \mathbf{g} + \mathbf{f_{IB}} \tag{4.22}$$

where the gravity gradient-based Reynolds number, Peclet number, Froude number and Eotvos number are defined as:

$$Re_b \equiv \frac{\rho_A u_b D_p}{\mu_A}, \qquad Pe_b \equiv \frac{D_p u_b}{M_c \phi_c}, \qquad Fr_b \equiv \frac{u_b}{\sqrt{g D_p}}, \qquad Eo \equiv \frac{\rho_A g D_p^2}{\sigma}$$

4.3 Boundary conditions

The boundary conditions for the numerical simulations are specified as follows. At the inlet the velocity and pressure are set to zero. Periodic boundary conditions for pressure and velocity are imposed on the domain in the flow direction as follows:

$$\mathbf{u}(x_0)\Big|_{(x_0=L_x)} = \mathbf{u}(x_0)\Big|_{(x_0=0)} \tag{4.23}$$

$$p(x_0)\Big|_{(x_0=L_x)} = p(x_0)\Big|_{(x_0=0)} + L_x \frac{\partial p}{\partial x} \tag{4.24}$$

where L_x is the length of the computational domain and $\frac{\partial p}{\partial x}$ is the pressure gradient.

4.4 Immersed boundary methods

The imposition of the desired boundary conditions on the immersed boundary method is of vital importance for the construction of the appropriate IB algorithm, but also characterizes the type of the proposed IB method among the other types and its accuracy. In order to handle the immersed boundary for solid boundaries, the governing equations should be modified properly to ensure the imposition of boundary conditions in the vicinity of the boundary. Therefore, a forcing term $\mathbf{f_{IB}}$ is introduced in Navier-Stokes equations (4.20) to specify the boundary reconstruction at the fluid/body interface for the pipe geometry.

The forcing term is equal to zero in the fluid domain and non zero in the solid or interface domain. In that case, where the forcing term is non zero, a smooth Dirac delta function is often used for the determination of the forcing term for some types of IB methods. On the other hand, for types of IB methods such as the ghost-cell immersed boundary method (GCIBM) (Tseng and Ferziger, 2003) the forcing term is treated implicitly and as a result is not calculated. The boundary is represented by a ghost cell technique inside the body (Majumdar et al., 2001). More details for the developed GCIBM based on the idea of Tseng and Ferziger (2003) are presented and discussed below.

4.4.1 IBM based on the penalty technique

The solid boundary which represents the pipe geometry does not conform with the structure of the computational grid. Consequently for the imposition of boundary conditions on immersed boundaries, it will be necessary to modify the momentum equations in the vicinity of the boundary. More specifically, the forcing term is added to the momentum equations in order to achieve at the desired points the fluid velocity equal to zero. Considering the following equation which expresses the forcing term, $\mathbf{f_{IB}}$,

$$\mathbf{f_{IB}} = -\frac{\mathbf{u}}{C_{IB}} \tag{4.25}$$

where $\mathbf{u}$ is the velocity of fluid flow and C_{IB} the user define parameter and is taken to be equal to 0.0001 for the considered cases. The selection of the appropriate value for the C_{IB} parameter was obtained by comparing the numerical results with analytical solutions. Two cases are herein considered to validate and investigate the performance of the proposed 1st order IB method, a single-phase and a two-phase annular pipe flow. Before presenting the numerical results for the above mentioned test cases, it is necessary to express some general observations for the user define parameter C_{IB}.

When the parameter $C_{IB} \to \infty$, the forcing term ($\mathbf{f_{IB}}$) vanishes and the equation returns again to the previous status of Navier-Stokes equations. On the contrary, when $C_{IB} \to 0$, the forcing term ($\mathbf{f_{IB}}$) gives $\mathbf{u} = \mathbf{V_s}$, where $\mathbf{V_s}$ is the velocity distribution over the boundary. This behaviour has main effects in numerical simulations, because the value of C_{IB} can be neither 0 or ∞. Thus, the solid and fluid regions are estimated by finite, user defined values. The problem is getting worse when the values of C_{IB} are set to be very small. It is observed the increase of stiffness in the numerical system and as a result affects the convergence of the solution.

The solution in this situation can be obtained by ensuring a value of C_{IB} which compromises the need of approximating solid boundaries and the preservation of the numerical stability at a reasonable computational cost. Subsequently, a partial improvement to the stability of the method may be achieved by treating the forcing term implicitly which helps the alleviation of the severe time step limitation of a fully explicit approach (Iaccarino and Verzicco, 2003).

The aforementioned IBM is characterized by simply grid generation, easy implementation and is very attractive for applications with immersed elastic boundaries, such as biological and multi-phase flows. However, the proposed method has also drawbacks especially for flows with rigid bodies. As mentioned earlier, the parameter that introduced in these approaches appears stability and accuracy problems. In addition, the smoothing of forcing function in order to avoid the above mentioned problems has effect in the representation of immersed boundary which in cases of turbulent flows with high Reynolds numbers is undesirable. It is worth mentioning that imposition of the appropriate boundary condition is also required for the pressure solver, depending on the particular implementation.

4.4.2 The proposed Ghost-cell immersed boundary method

The current section is focused on the development of a modified ghost cell immersed boundary method based on the idea of Tseng and Ferziger (2003). A boundary forcing term, f_i, is imposed implicitly through a ghost-cell technique and is only active on the boundary according to the Equations (2.8) and (2.9) in Chapter 2.

In this section, we present the proposed GCIBM in two dimensions for the sake of clarity, even though the method has been implemented for the 3-D case. The proposed IB method based on the ghost cell technique (see Figure 4.1). In this technique, the values of the local field variable (ϕ) inside the body or outside of the fluid domain for a steady boundary are unalterable at every time step. This is achieved by mirroring the values of the image points and the values on the immersed boundary by satisfying the following equality:

$$\phi_G = 2\phi_B - \phi_I \tag{4.26}$$

where ϕ_G is the value of the variable ϕ at the ghost cell, ϕ_I is the value of the variable ϕ at the image point and ϕ_B is the value of the variable ϕ at the boundary. It is interesting to point out that the image point (I_1) intersects the immersed boundary (B_1), while the boundary is located between the image point and the ghost cell. The value of the local flow variable (ϕ) (i.e velocity components, pressure and volume fraction) at the image point ϕ_I is computed by using an interpolation scheme and taking advantage of the nearby adjacent fluid points, while the accuracy of the scheme is dependent on the polynomial degree. Herein, three interpolation construction schemes were used, namely linear, bilinear and quadratic.

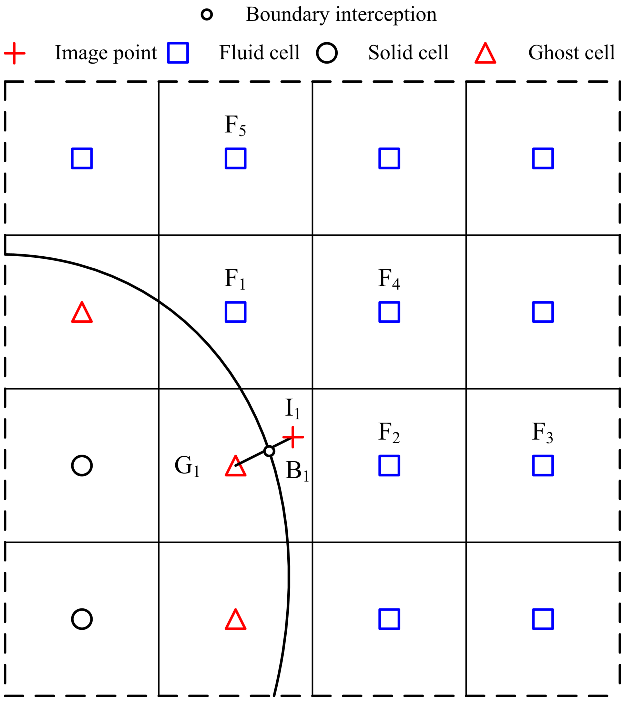

Figure 4.1: Description of the proposed GCIBM.

Another issue of the method is the unknown value of the pressure at the immersed boundary. Therefore, an appropriate boundary condition is needed to be imposed. A Neumann boundary condition is adopted for the pressure which imposes a zero wall normal derivative.

$$\begin{aligned}&\frac{\partial P}{\partial n} = 0 \Leftrightarrow \\ &\frac{\partial P}{\partial n} = \frac{\partial P}{\partial x}\hat{n}_x + \frac{\partial P}{\partial y}\hat{n}_y\end{aligned} \tag{4.27}$$

where $\hat{n}_x$ and $\hat{n}_y$ are the x and y directions of the unit vector normal to the boundary, respectively. It is also worth noting that the method is also capable to handle moving boundary with the constraint that the points where the imposition of the boundary conditions takes place must be recalculated at every time step.

The proposed GCIBM can be described by the following steps:
(a) Identification of the fluid and solid cells: In the present case the specification of the fluid and solid cells are based on the radius of the pipe. Hence, a cell is identified as "fluid cell" if the distance between the cell center and pipe center is less than the pipe radius, otherwise the cell is identified as "solid cell".
(b) Identification of the ghost cells: These cells are located close to the boundary region and have at least one fluid neighbour cell in the fluid region. The value at the ghost cells is obtained by satisfying the mirroring condition (Eq. 4.26).
(c) Identification of the neighbour cells and the intersection point: According to Figure 4.1, the ghost cell ($G_1 = (x_{G_1}, y_{G_1})$ has an image point ($I_1 = (x_{I_1}, y_{I_1})$ and the intersection point $B_1 = (x_{B_1}, y_{B_1})$ is the midpoint between G_1 and I_1. The relation of the above points, regarding the coordinates of image point can be written as:

$$(x_{I_1}, y_{I_1}) = (x_{B_1} - [x_{G_1} - x_{B_1}], y_{B_1} - [y_{G_1} - y_{B_1}]) \tag{4.28}$$

The image points are determined in the flow region and the value of the local flow variable (ϕ) at image point can be presented by using an interpolation scheme in terms of the neighbour cells. Thus, for the selected linear interpolation scheme, the value of ϕ at the image point can be specified as follows:

$$\phi(x_i, y_j) = \alpha_B + \alpha_1 x_i + \alpha_2 y_j \tag{4.29}$$

The coefficients are computed from the values at F_1, F_2 (two neighbour cells) and B_1 (see

Fig. 4.1). According to the three points, the coefficients can be expressed as:

$$\alpha = D^{-1}\phi \tag{4.30}$$

where α is the vector with the unknown coefficient, D is a 3x3 matrix for the linear interpolation scheme and ϕ is the vector expressing the values of the two neighbour points and intersection point.

$$\alpha = \begin{bmatrix} \alpha_B \\ \alpha_1 \\ \alpha_2 \end{bmatrix}, \qquad D = \begin{bmatrix} 1 & x_B & y_B \\ 1 & x_1 & y_1 \\ 1 & x_2 & y_2 \end{bmatrix}, \qquad \phi = \begin{bmatrix} \phi_B \\ \phi_1 \\ \phi_2 \end{bmatrix} \tag{4.31}$$

In the case of a bilinear interpolation scheme, equation 4.29 is replaced by:

$$\phi(x_i, y_j) = \alpha_B + \alpha_1 x_i + \alpha_2 y_j + \alpha_3 x_i y_j \tag{4.32}$$

while for a quadratic interpolation scheme takes the following form:

$$\phi(x_i, y_j) = \alpha_B + \alpha_1 x_i + \alpha_2 y_j + \alpha_3 x_i^2 + \alpha_4 x_i y_j + \alpha_5 y_j^2 \tag{4.33}$$

Equation 4.30 holds as it is for both interpolation schemes, but α and ϕ vectors together with the matrix D are different for each interpolation scheme. For bilinear interpolation scheme yields:

$$\alpha = \begin{bmatrix} \alpha_B \\ \alpha_1 \\ \alpha_2 \\ \alpha_3 \end{bmatrix}, \qquad D = \begin{bmatrix} 1 & x_B & y_B & x_B y_B \\ 1 & x_1 & y_1 & x_1 y_1 \\ 1 & x_2 & y_2 & x_2 y_2 \\ 1 & x_3 & y_3 & x_3 y_3 \end{bmatrix}, \qquad \phi = \begin{bmatrix} \phi_B \\ \phi_1 \\ \phi_2 \\ \phi_3 \end{bmatrix} \tag{4.34}$$

while for a quadratic interpolation scheme the above can be written as:

$$\alpha = \begin{bmatrix} \alpha_B \\ \alpha_1 \\ \alpha_2 \\ \alpha_3 \\ \alpha_4 \\ \alpha_5 \end{bmatrix}, \qquad D = \begin{bmatrix} 1 & x_B & y_B & x_B^2 & x_B y_B & y_B^2 \\ 1 & x_1 & y_1 & x_1^2 & x_1 y_1 & y_1^2 \\ 1 & x_2 & y_2 & x_2^2 & x_2 y_2 & y_2^2 \\ 1 & x_3 & y_3 & x_3^2 & x_3 y_3 & y_3^2 \\ 1 & x_4 & y_4 & x_4^2 & x_4 y_4 & y_4^2 \\ 1 & x_5 & y_5 & x_5^2 & x_5 y_5 & y_5^2 \end{bmatrix}, \qquad \phi = \begin{bmatrix} \phi_B \\ \phi_1 \\ \phi_2 \\ \phi_3 \\ \phi_4 \\ \phi_5 \end{bmatrix} \tag{4.35}$$

(d) Calculating the values of the local flow variable (ϕ) at ghost cells: Once coefficients values are computed from equation 4.30, then the values at image point can be calculated from equation 4.29. Accordingly, the values of ϕ at ghost cells are worked out using the mirror condition (see equation 4.26).

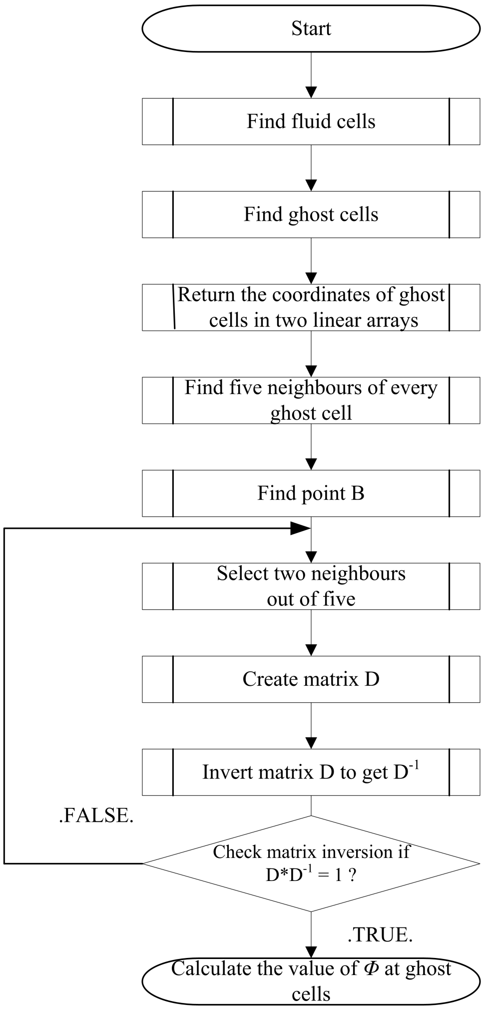

Figure 4.2: The proposed ghost-cell immersed boundary method.

It is important to mention that the first three steps take place only once because the proposed GCIBM is implemented for smooth rigid boundary (e.g. pipe geometry). In the case of deformable or moving boundaries the aforementioned steps must be repeated at every time step. Figure 4.2 depicts the algorithm for the proposed IBM.

As mentioned earlier, for the calculation of the unknown pressure and volume fraction on the boundary a Neumann boundary condition is essential to be imposed. Then, the form of matrix D is required to modify in order to accommodate the desired changes. Hence, for the linear, bilinear and quadratic interpolation scheme the matrix D takes the following forms, respectively:

$$D = \begin{bmatrix} 0 & -sin(\theta_B) & cos(\theta_B) \\ 1 & x_1 & y_1 \\ 1 & x_2 & y_2 \end{bmatrix} \tag{4.36}$$

$$D = \begin{bmatrix} 1 & -sin(\theta_B) & cos(\theta_B) & cos(\theta_B)x_B - sin(\theta_B)y_B \\ 1 & x_1 & y_1 & x_1y_1 \\ 1 & x_2 & y_2 & x_2y_2 \\ 1 & x_3 & y_3 & x_3y_3 \end{bmatrix} \tag{4.37}$$

$$D = \begin{bmatrix} 1 & -sin(\theta_B) & cos(\theta_B) & -2sin(\theta_B)x_B & cos(\theta_B)x_B - sin(\theta_B)y_B & 2cos(\theta_B)y_B \\ 1 & x_1 & y_1 & x_1^2 & x_1y_1 & y_1^2 \\ 1 & x_2 & y_2 & x_2^2 & x_2y_2 & y_2^2 \\ 1 & x_3 & y_3 & x_3^2 & x_3y_3 & y_3^2 \\ 1 & x_4 & y_4 & x_4^2 & x_4y_4 & y_4^2 \\ 1 & x_5 & y_5 & x_5^2 & x_5y_5 & y_5^2 \end{bmatrix} \tag{4.38}$$

where $tan(\theta_B)$ is the slope of the normal at the surface B. Accordingly, equation 4.30 for the coefficients of pressure and volume fraction is expressed as:

$$\begin{bmatrix} \alpha_B \\ \alpha_1 \\ \cdots \\ \alpha_m \end{bmatrix} = D^{-1} \begin{bmatrix} \frac{\partial P_B}{\partial n} \\ P_1 \\ \cdots \\ P_m \end{bmatrix}, \qquad \begin{bmatrix} \alpha_B \\ \alpha_1 \\ \cdots \\ \alpha_m \end{bmatrix} = D^{-1} \begin{bmatrix} \frac{\partial C_B}{\partial n} \\ C_1 \\ \cdots \\ C_m \end{bmatrix} \tag{4.39}$$

where m is equal to two for the linear interpolation scheme, three for the bilinear interpolation scheme and five for the quadratic interpolation scheme. $\frac{\partial P_B}{\partial n}$ and $\frac{\partial C_B}{\partial n}$ are the Neumann boundary conditions for pressure and volume fraction, respectively.

4.5 Method of solution

The set of model partial-differential equations along with the appropriate boundary conditions have been solved by means of the FDM. A staggered grid (Figure 4.3) was employed to discretise equations (4.18-4.22). The velocity components (u, v and w) are defined in the centres of the faces of the mass control volumes, while all the dependent variables (pressure and volume fraction) are defined in the centre of each control volume.

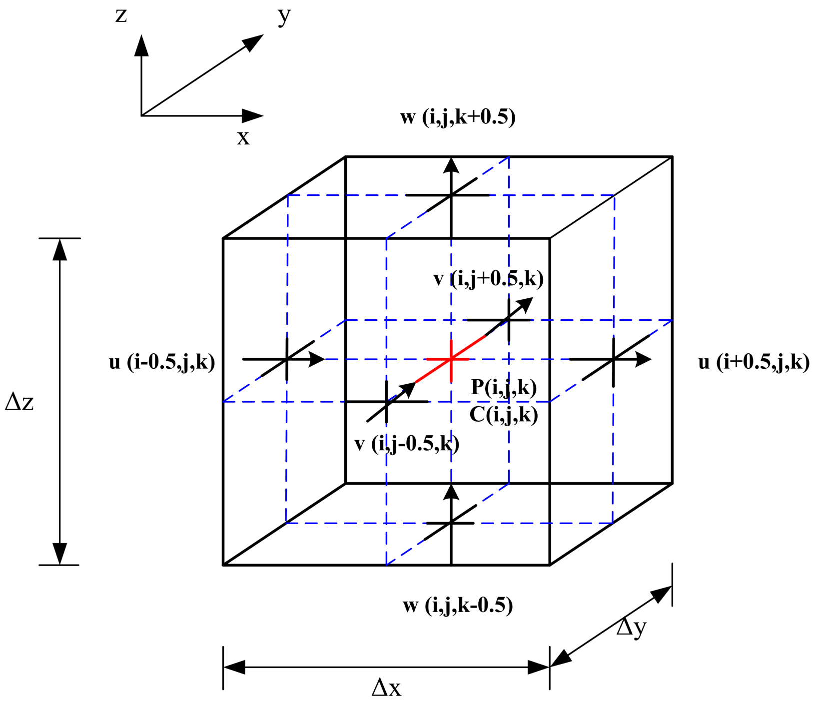

Figure 4.3: 3-D staggered grid.

The numerical solution of the continuity and Navier-Stokes equations is achieved by using a classical projection method (Chorin, 1967, 1968; Temam, 1968). The projection method is based on the Helmholtz decomposition and constituted by two steps. The former is the calculation of an intermediate velocity at every time step and the latter is the projection of the intermediate velocity on the solenoid space in order to satisfy the divergence-free (incompressibility) constrain.

The intermediate velocity is obtained by using the explicit Adams-Bashforth (Bashforth and Adams, 1883) scheme for the convective term and the implicit Crack-Nicholson

(Crank and Nicolson, 1947) scheme for the viscous term of Navier-Stokes equations. The update of the velocity field is achieved by using a first order Euler method at every time step.

A time-split semi-implicit scheme was employed for the solution of the Cahn-Hilliard equation based on the work of Badalassi et al. (2003). The details of this method along with the aforementioned will be briefly presented in the next two sections.

4.5.1 Temporal discretisation

The numerical solution for the Cahn-Hilliard and Navier-Stokes equations from t^n to t^{n+1} are specified as follows:

Step 1: Compute the volume fraction, C, by solving the Cahn-Hilliard equation 4.21, using the velocity field, $\mathbf{u}$, at time step n.

Step 2: Calculate the surface tension force, $\frac{\phi \nabla C}{Eo}$ at time step $n + 1/2$ by using the averaged volume fraction, C, at time step n and $n + 1$, respectively.

Step 3: Solving the momentum equations (4.22) and continuity equation (4.19) simultaneously and update the velocity field, $\mathbf{u}$, at time step $n + 1$

The time split semi-implicit method based on treating the first term of the right hand side of equation (4.40) implicitly and the rest terms explicitly. As a result, semi-implicit discretisation approaches can be created and solved efficiently with reasonable computational cost (Badalassi et al., 2003).

Following the above mentioned steps, the volume fraction, C at time step t^{n+1} is calculated from

$$\begin{aligned}\frac{1.5C^{n+1} - 2C^n + 0.5C^{n-1}}{t^{n+1} - t^n} &= \frac{1}{Pe}(\alpha_1 \nabla^2 C^{n+1} - \alpha_2 \nabla^4 C^{n+1}) \\ &+ 2\Big\{\frac{1}{Pe}[\nabla \cdot (M \nabla \phi) - (\alpha_1 \nabla^2 C^n - \alpha_2 \nabla^4 C^n)] - \nabla \cdot (\mathbf{u}^n C^n)\Big\} \\ &- \frac{1}{Pe}[\nabla (M \nabla \phi) - (\alpha_1 \nabla^2 C^{n-1} - \alpha_2 \nabla^4 C^{n-1})] \\ &- \nabla \cdot (\mathbf{u}^{n-1} C^{n-1}) \end{aligned} \tag{4.40}$$

where α_1 and α_2 are defined as the approximate values for the nonlinear mobility.

The solution for the Navier-Stokes is achieved by using a standard Euler first-order in time projection method. An intermediate velocity, u^*, is introduced by splitting the momentum equations in two parts such that:

$$\mathbf{u}^{n+1} - \mathbf{u}^n = \mathbf{u}^{n+1} - \mathbf{u}^* + \mathbf{u}^* - \mathbf{u}^n \tag{4.41}$$

In the first part (predictor step), the intermediate velocity is obtained by working out the viscous term with an implicit Crank-Nicolson scheme (Crank and Nicolson, 1947) and an explicit Adams-Bashforth (Bashforth and Adams, 1883) scheme for the advective term. Then, the predictor step without any pressure effects is

$$\frac{\mathbf{u}^* - \mathbf{u}^n}{\Delta t} = \frac{1}{\rho^{n+1/2}}\Big\{ - \Big[\frac{3}{2}\hat{H}(\mathbf{u}^n) - \frac{1}{2}\hat{H}(\mathbf{u}^{n-1})\Big] + \frac{1}{2}Re^{-1}[\hat{L}(\mathbf{u}^*, \mu^{n+1}) + \hat{L}(\mathbf{u}^n, \mu^n)] + \mathbf{f_{ST}} + \mathbf{f_{IB}}\Big\} \tag{4.42}$$

where $\hat{H}$ and $\hat{L}$ are the discrete operators for the convection and diffusion, respectively. The term $\mathbf{f_{ST}}$ represents the dimensionless interfacial and body forces, while $\mathbf{f_{IB}}$ expresses the force function for the IBM. Then a correction step is followed, where the pressure gradient is introduced:

$$\frac{\mathbf{u}^{n+1} - \mathbf{u}^*}{\Delta t} = -\frac{\nabla p^{n+1/2}}{\rho^{n+1/2}} \tag{4.43}$$

The determination of the pressure is specified by the fulfillment of the divergence free constraint at the new time step by the velocity:

$$\nabla \cdot \mathbf{u}^{n+1} = 0 \tag{4.44}$$

Accordingly, the equation for the pressure is

$$\nabla \cdot \left(\frac{\nabla p^{n+1/2}}{\rho^{n+1/2}}\right) = \frac{\nabla \cdot \mathbf{u}^*}{\Delta t} \tag{4.45}$$

4.5.2 Spatial discretisation

The selection of the appropriate spatial discretisation scheme is based on the compromise between accuracy, stability and computation complexity. A central finite difference scheme was employed for the spatial discretisation of Navier-Stokes and continuity equations. The used central-difference formulas of order $O(h^2)$ for first and second derivative are expressed as follows:

$$\phi'(x_0) \approx \frac{\phi_1 - \phi_{-1}}{2h}, \qquad \phi''(x_0) \approx \frac{\phi_1 - 2\phi_0 + \phi_{-1}}{h^2} \tag{4.46}$$

Central finite difference scheme was also employed for the discretisation in space for the Laplace operator in diffusive terms, while for the advection term in the Cahn-Hilliard equation a fifth-order weighted essentially non-oscillatory (WENO) scheme was selected. The WENO scheme is described in detail in the works of (Jiang and Shu, 1996; Zhang and Jackson, 2009; Shu, 2009), we briefly outline it below.

The reconstruction of a function ϕ where ϕ is the velocity components u_i in the Cahn-Hilliard equation, can be expressed as follows:

$$\hat{\phi}_{i+1/2} = \sum_{m=1}^{3} \omega_m \bar{\phi}^{(m)}_{i+1/2} \tag{4.47}$$

where ω_m are the non-linear weights and $\hat{\phi}_{i+1/2}$ is the polynomial reconstruction of ϕ on the mth set of stencils,

$$\omega_m = \frac{\hat{\omega}_m}{\sum_{l=1}^{3} \hat{\omega}_l}, \qquad \hat{\omega}_l = \frac{\gamma_l}{(\epsilon + \beta_l)^2} \tag{4.48}$$

If $u_i \geq 0$ then $\gamma_1 = 0.3$, $\gamma_2 = 0.6$, $\gamma_3 = 0.1$ and the calculation of $\hat{\phi}_{i+1/2}$ is obtained by the following equations:

$$\begin{aligned}
\hat{\phi}^1_{i+1/2} &= \frac{1}{3}\phi_i + \frac{5}{6}\phi_{i+1} - \frac{1}{6}\phi_{i+2} \\
\hat{\phi}^2_{i+1/2} &= -\frac{1}{6}\phi_{i-1} + \frac{5}{6}\phi_i - \frac{1}{3}\phi_{i+1} \\
\hat{\phi}^3_{i+1/2} &= -\frac{1}{3}\phi_{i-2} - \frac{7}{6}\phi_{i-1} - \frac{11}{6}\phi_{i+2}
\end{aligned} \tag{4.49}$$

while the smoothness indicators β_l are estimated as:

$$\begin{aligned}
\beta_1 &= \frac{13}{12}(\phi_i - 2\phi_{i+1} + \phi_{i+2})^2 + 0.25(3\phi_i - 4\phi_{i+1} + \phi_{i+2})^2 \\
\beta_2 &= \frac{13}{12}(\phi_{i-1} - 2\phi_i + \phi_{i+1})^2 + 0.25(\phi_{i-1} - \phi_{i+1})^2 \\
\beta_3 &= \frac{13}{12}(\phi_{i-2} - 2\phi_{i-1} + \phi_i)^2 + 0.25(\phi_{i-2} - 4\phi_{i-1} + 3\phi_i)^2
\end{aligned} \tag{4.50}$$

If $u_i < 0$ then $\gamma_1 = 0.1$, $\gamma_2 = 0.6$, $\gamma_3 = 0.3$ and the calculation of $\hat{\phi}_{i+1/2}$ is obtained by the following equations:

$$\begin{aligned}
\hat{\phi}^1_{i+1/2} &= \frac{11}{6}\phi_{i+1} - \frac{7}{6}\phi_{i+2} - \frac{1}{3}\phi_{i+3} \\
\hat{\phi}^2_{i+1/2} &= -\frac{1}{3}\phi_i + \frac{5}{6}\phi_{i+1} - \frac{1}{6}\phi_{i+2} \\
\hat{\phi}^3_{i+1/2} &= -\frac{1}{6}\phi_{i-1} + \frac{5}{6}\phi_i + \frac{1}{3}\phi_{i+1}
\end{aligned} \tag{4.51}$$

while the smoothness indicators β_l are estimated as:

$$\begin{aligned}
\beta_1 &= \frac{13}{12}(\phi_{i+1} - 2\phi_{i+2} + \phi_{i+3})^2 + 0.25(3\phi_{i+1} - 4\phi_{i+2} + \phi_{i+3})^2 \\
\beta_2 &= \frac{13}{12}(\phi_i - 2\phi_{i+2} + \phi_{i+1})^2 + 0.25(\phi_i - \phi_{i+2})^2 \\
\beta_3 &= \frac{13}{12}(\phi_{i-1} - 2\phi_i + \phi_{i+1})^2 + 0.25(\phi_{i-1} - 4\phi_i + 3\phi_{i+1})^2
\end{aligned} \tag{4.52}$$

Accordingly, the gradients of the convective terms are given by

$$\frac{\partial \phi}{\partial \eta} = \frac{\hat{\phi}_{i+1/2} - \hat{\phi}_{i-1/2}}{h} \tag{4.53}$$

where h is defined as the distance between the nodes.

4.5.3 Numerical solver

The numerical solution of the governing equations is achieved by a Gauss-Seidel Successive Over Relaxation (SOR) method. The method introduces a parameter into the iterative procedure and then attempts to optimise it in order to increase the convergence rate.

The convergence rate is dependent on the largest eigenvalue of the iteration matrix. Thus, the objective of the method is to minimise the largest eigenvalue as much as possible. This method is described in detail in many numerical textbooks (Press et al., 2007; Moin, 2010); we briefly present it here.

A system of equation can be expressed as: $Ax = b$ and $A = A_1 - A_2$, resulting in the following equation:

$$A_1 x = A_2 x + b \tag{4.54}$$

From equation 4.54 is created the following iterative relationship:

$$A_1 x^{m+1} = A_2 x^m + b \tag{4.55}$$

where $m = 0, 1, 2, \cdots$ is the iteration index. Let us define as $A_1 = D - L$ and $A_2 = U$ where D is the diagonal matrix with the diagonal elements of matrix A, U is the upper triangular matrix consisting of the negative of the upper triangular elements of matrix A, and L is the lower triangular matrix consisting of the negative of the upper triangular elements of matrix A.

According to the above relationship, we have

$$(D - L)\phi^{m+1} = U\phi^{(m)} + b \tag{4.56}$$

Let express $d = \phi^{(m+1)} - \phi^{(m)}$ as the change between two successive iteration, such that

$$\phi^{(m+1)} = d + \phi^{(m)} \tag{4.57}$$

If we introduce a parameter ω in order to increase the change between two successive iteration, then we have the following equation:

$$\phi^{(m+1)} = \omega d + \phi^{(m)} \tag{4.58}$$

where $\omega > 1$ is the relaxation parameter. If ω is equal to one the Gauss-Siedel method is retrieved. In SOR, the first step based on the Gauss-Siedel is to obtain an intermediate solution $\tilde{\phi}$

$$D\phi^{(\tilde{m}+1)} = L\phi^{(m+1)} + U\phi^{(m)} + b \tag{4.59}$$

Finally, the SOR solution at the next iteration is given by the following expression:

$$\phi^{(m+1)} = \phi^{(m)} + \omega(\phi^{(\tilde{m}+1)} - \phi^{(m)}) \tag{4.60}$$

4.5.4 Implementation of the numerical model

The numerical model was implemented in a CFD code developed in house. The existing CFD code was written in Fortran 90/95 and initially parallelised with Open

Multi-Processing (OMP). However, the parallelisation with OMP is inefficient when a large number of processors is used. Therefore, the CFD code was also parallelised with Message Passing Interface (MPI) in order to accommodate the increasing complexity of calculations. This improvement helped to speed up the calculations and increase the grid resolution in order to obtain fast results with high accuracy. An adaptive time step technique was also implemented for helping to quicken the solution procedure. Figure 4.4 illustrates the solution algorithm for the current study.

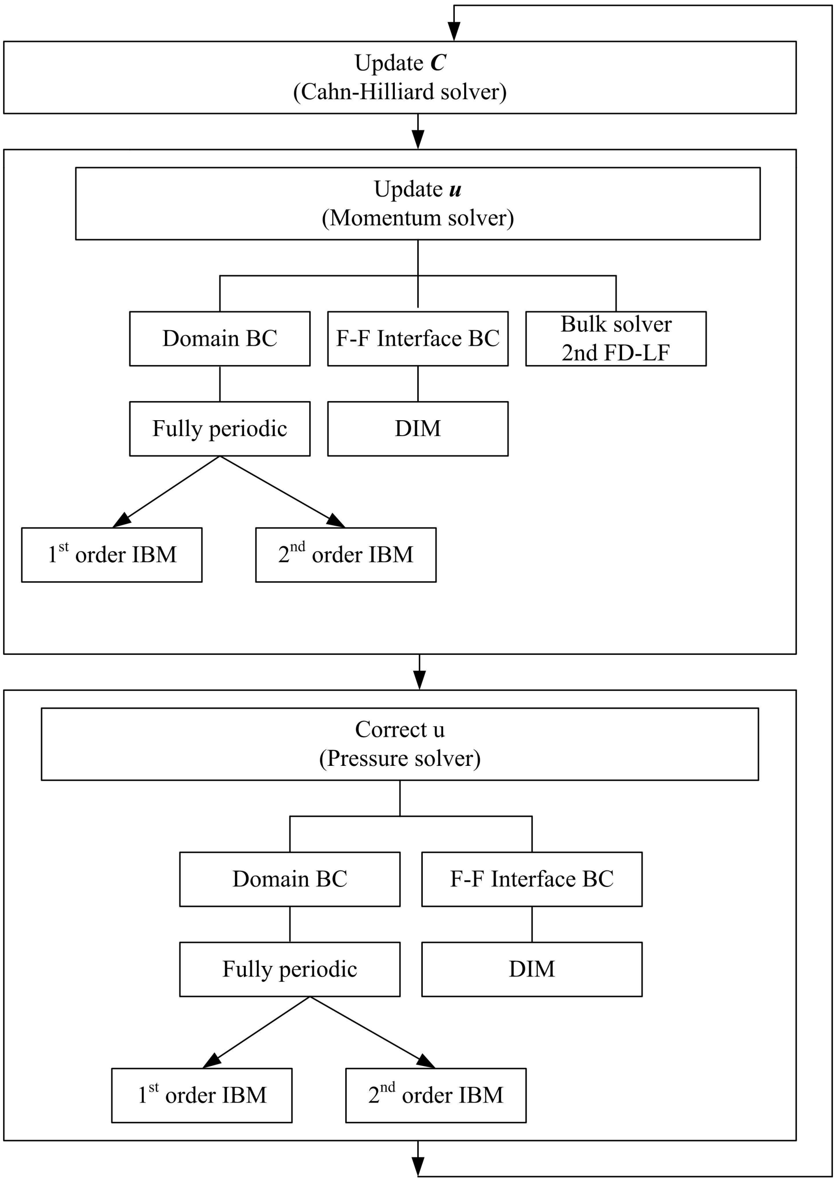

Figure 4.4: Solution procedure algorithm.

4.6 Chapter summary

In this Chapter, the mathematical formulation and the numerical methods for the solution procedure were presented and discussed in detail. The governing equations consisting by the continuity, Navier-Stokes and Cahn-Hilliard equations along with the appropriate boundary condition and the auxiliary relations have been resolved by means of the finite difference method. The solution of the governing equations was obtained using an iterative algorithm, namely Gauss-Seidel Successive Over Relaxation (SOR). Two different immersed boundary algorithms for the representation of the pipe geometry were presented and discussed.

Chapter 5

Validation of the numerical method

5.1 Introduction

An attempt was made to validate the results of the developed IB algorithms, regarding velocity profile, with data from analytical solutions. The single- and two-phase Poiseuille flow were selected for evaluating the accuracy of the developed IB algorithms. The numerical method was verified and validated with available experimental data from the literature.

The classical test case of a single bubble rising in a liquid-filled vertical pipe has been investigated for different selections of Eotvos, Morton and Reynolds numbers. The numerical results for the shape and terminal velocity, drag coefficient along with the instantaneous Reynolds number were compared with experimental data from the literature.

Numerical simulations were performed for investigating the presence of parasitic or spurious currents and their dependency with the interface thickness. Volume conservation tests were conducted for investigating the mass conservation of bubble flows. The numerical code was also tested for bubble coalescence with encouraging agreement against experimental data.

5.2 Validation of IB algorithm based on the penalty technique

5.2.1 Single-phase Poiseuille flow

Numerical simulations were performed at $Re_p = 20$ and pipe diameter $D_p = 1$. Three different grids were selected for the validation of the proposed IB algorithm and compared with those of analytical solution for single-phase Poiseuille flow. The coarse grid of 14x30x30, the medium grid of 14x60x60 and the fine grid of 14x120x120. A cross section of the computational domain is depicted in Figure 5.1.

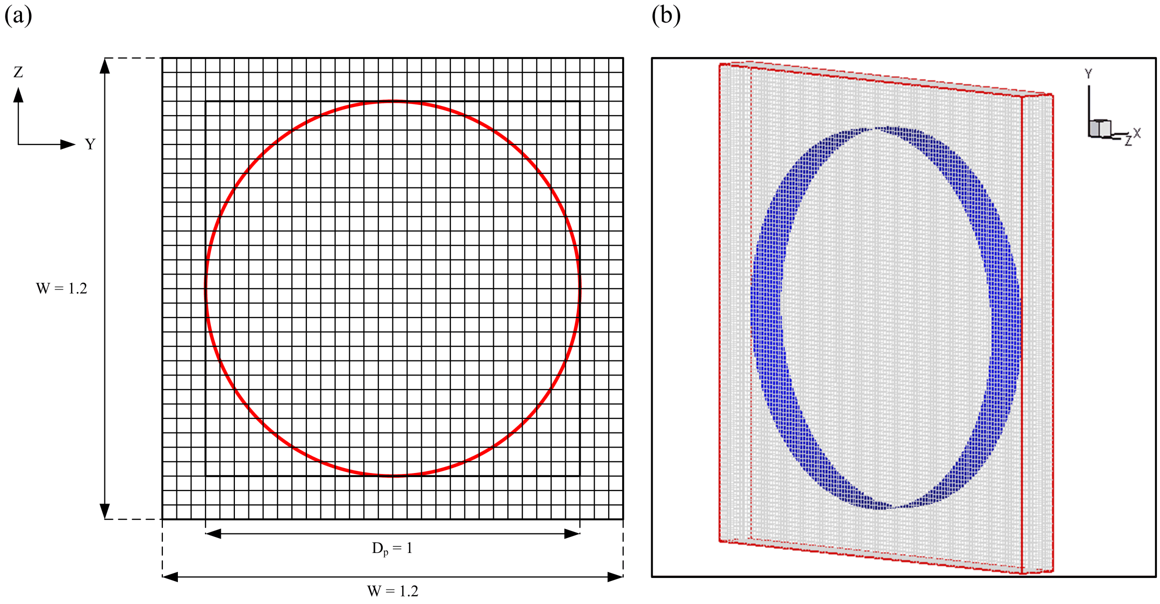

Figure 5.1: Representation of the computational domain for single-phase Poiseuille flow: (a) cross section of the geometry and (b) 3-D geometry.

The selection of the appropriate value for the user define parameter C_{IBM} in forcing term, f_i, was made by examining different values for C_{IB} and time step (Δt) until the code crashes. The final value was determined by the calculation of the % error regarding the dimensionless maximum velocity. The analytical solution of u-velocity component for a steady state pipe flow is given by the following equation in dimensionless form:

$$u_z^* = \frac{Re_p}{16}\left(1 - \frac{r^2}{R^2}\right) \tag{5.1}$$

where r is the radius and R the pipe radius. The dimensionless maximum velocity is expressed as $u_{max}^* = Re_p/16$ and is equal to 1.25 for $Re_p = 20$. For simplicity the asterisk which denotes the dimensionless form is dropped. The full derivation of the analytical solution is presented in Appendix B.

In Figure 5.2, it is shown that among the three grids with $C_{IB} = 0.0001$ the finer gives the best prediction for the velocity profile compared to the analytical solution.

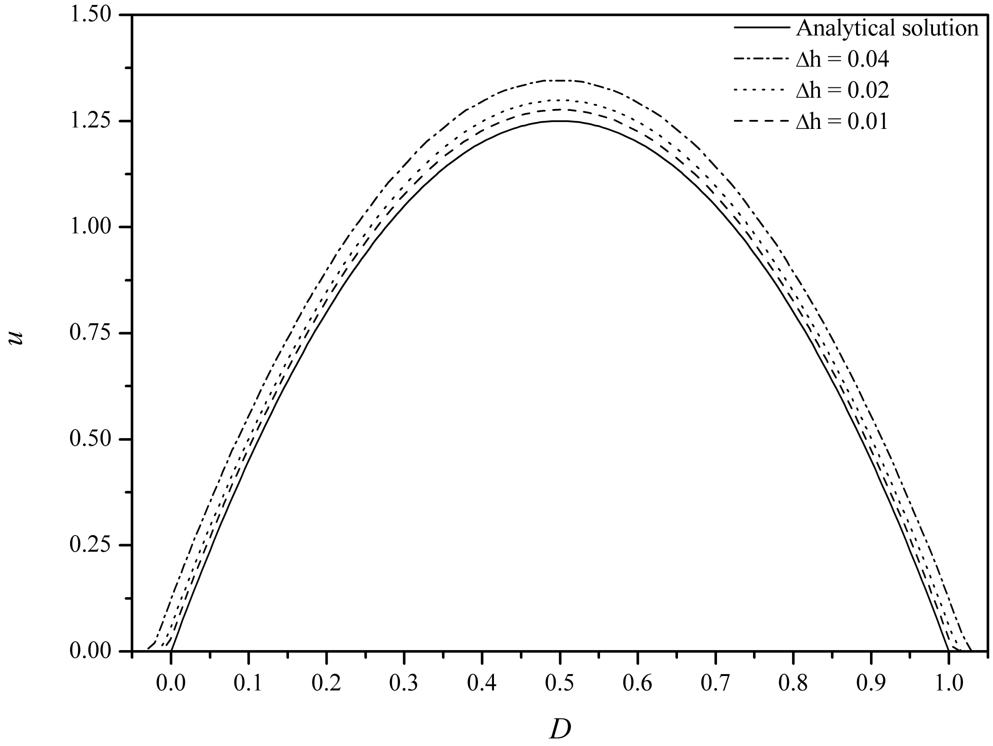

Figure 5.2: Comparison of the velocity profiles for $C_{IB} = 0.0001$, $Re_p = 20$ and various grids with the analytical solution.

Figure 5.3 illustrates the % error of maximum velocity (u_{max}) with respect to the computational grid. The lower the value of user define parameter C_{IB}, the higher accuracy for the representation of the pipe wall (smooth rigid) is achieved. It is noticed that the best selection for the value of C_{IB} is 0.0001 due to the minimum % error compared to the other values, while the accuracy of the method approaches the first order. The u_{max} % error for the coarse, medium and fine grid is 7.74%, 3.90% and 2.11%, respectively, when the C_{IB} is equal to 0.0001. For $C_{IB} = 0.0002$ the % error is 7.82%, 4.04% and 2.33%. In the case of $C_{IB} = 0.0003$ the % error of u_{max} is equal to 7.90%, 4.15% and 2.52%. Finally, the % error of u_{max} is 7.96%, 4.26% and 2.70%, respectively, for the three selected grids and $C_{IB} = 0.0004$.

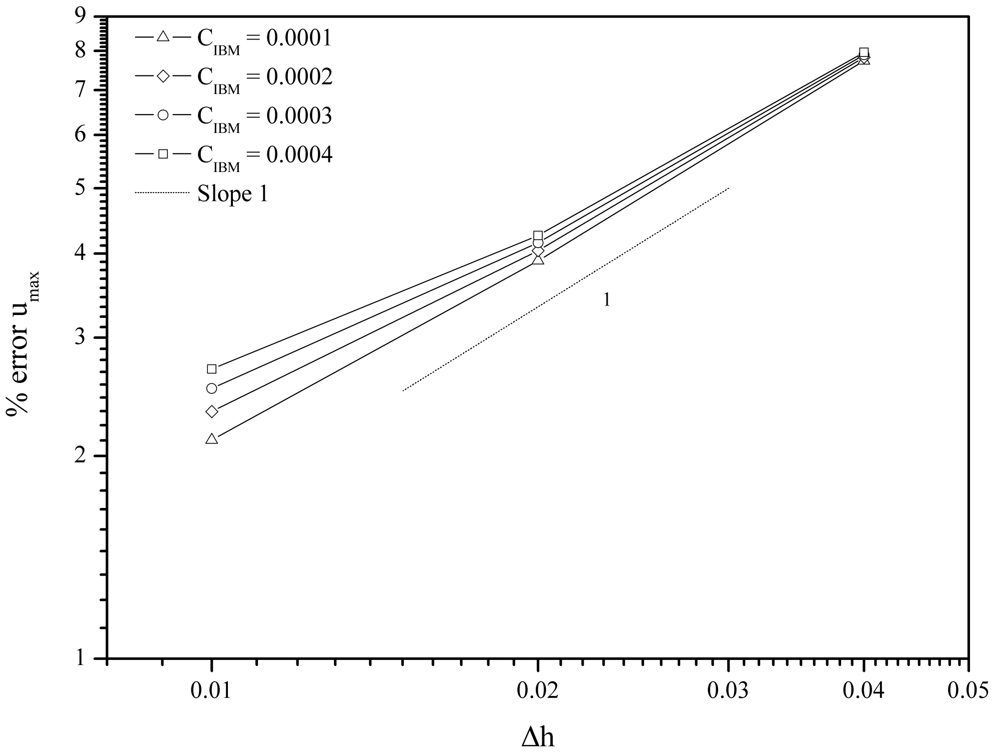

Figure 5.3: % error of the u_{max} vs. the grid size for various values of C_{IB}.

It is concluded that the combination of the minimum value of C_{IB} (=0.0001) with the fine grid (14x120x120) is the best selection in order to obtain the highest accuracy for steady state single-phase Poiseuille flow. It is also worth noting that for all the numerical cases considered, the steady state status was achieved after the period of six dimensionless time units. Finally, it is observed that for the specific time step ($\Delta t = 0.0001$), the grid of 14x120x120 and values of parameter C_{IB} for lower to 0.0001 and higher to 0.005, the method is not working.

5.2.2 Laminar two-phase annular pipe flow

In the previous section, validation of the numerical results with the analytical solution for laminar single-phase Poiseuille flow was presented and discussed. Herein, in order to demonstrate the validation of the proposed IBM, numerical simulations have been conducted to investigate the laminar two-phase annular pipe flow between a heavy fluid (A) on top of a lighter fluid (B), $\frac{\mu_A}{\mu_B} = 0.1$. Numerical simulations are performed at $Re_p = 200$ and compared with the steady state analytical solution for the velocity profile. In the present case the surface tension is zero and the Cahn-Hilliard equation is employed for the interface tracking only. Figure 5.4 illustrates the cross section of the computational domain for the two-phase numerical simulations.

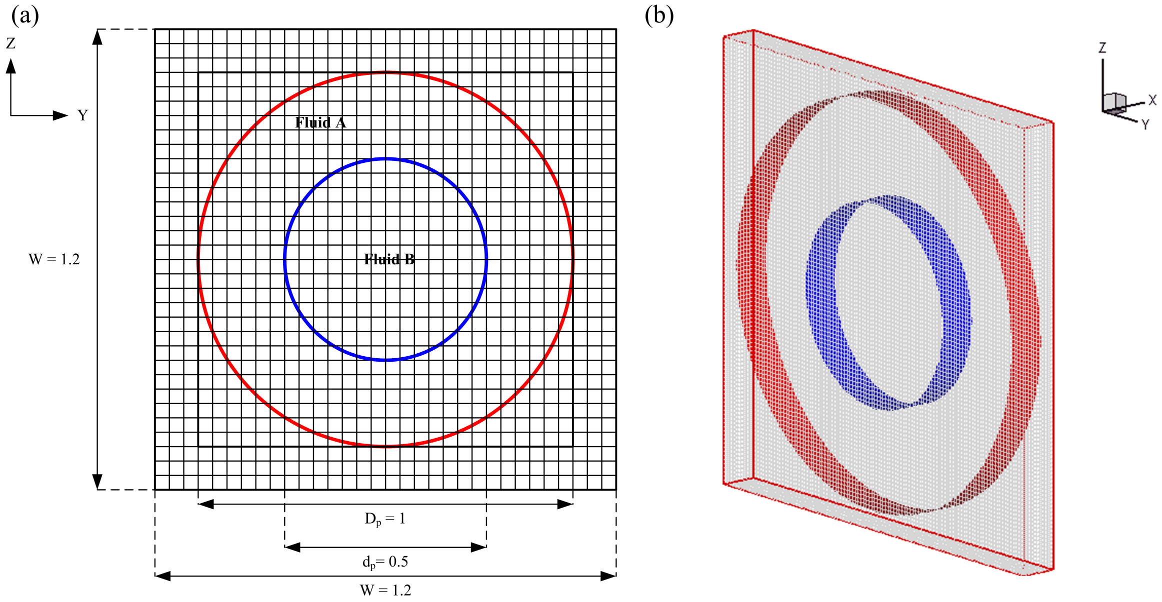

Figure 5.4: Representation of the computational domain for two-phase annular flow: (a) cross section of the geometry and (b) 3-D geometry.

Various grids and values of parameter C_{IB} were examined in order to select the appropriate value for the parameter of the present flow problem. The final selection of C_{IB} was obtained by the comparison of the numerical results with those of analytical solution. The analytical solution for the velocity profile is defined by the following equations in dimensionless form:

$$u_z^* = -\frac{Re_p}{16}\frac{r^2}{R^2} - \frac{Re_p}{16}\left(k^2\left(\frac{\mu_A}{\mu_B} - 1\right) - \frac{\mu_A}{\mu_B}\right), \qquad if \quad 0 \leq r \leq kR \tag{5.2}$$

and,

$$u_z^* = \frac{Re_p}{16}\frac{\mu_A}{\mu_B}\left(1 - \frac{r^2}{R^2}\right), \qquad if \quad kR \leq r \leq R \tag{5.3}$$

According to equation 5.2 the maximum velocity is equal to 4.0625. The full derivation of the aforementioned equations is presented in Appendix B2.

Figure 5.5 presents the velocity profile for the coarse, the medium and the fine grid, while C_{IB} is taken to be equal to 0.0001. It is observed that the velocity profile with the fine grid is much closer to the analytical velocity profile.

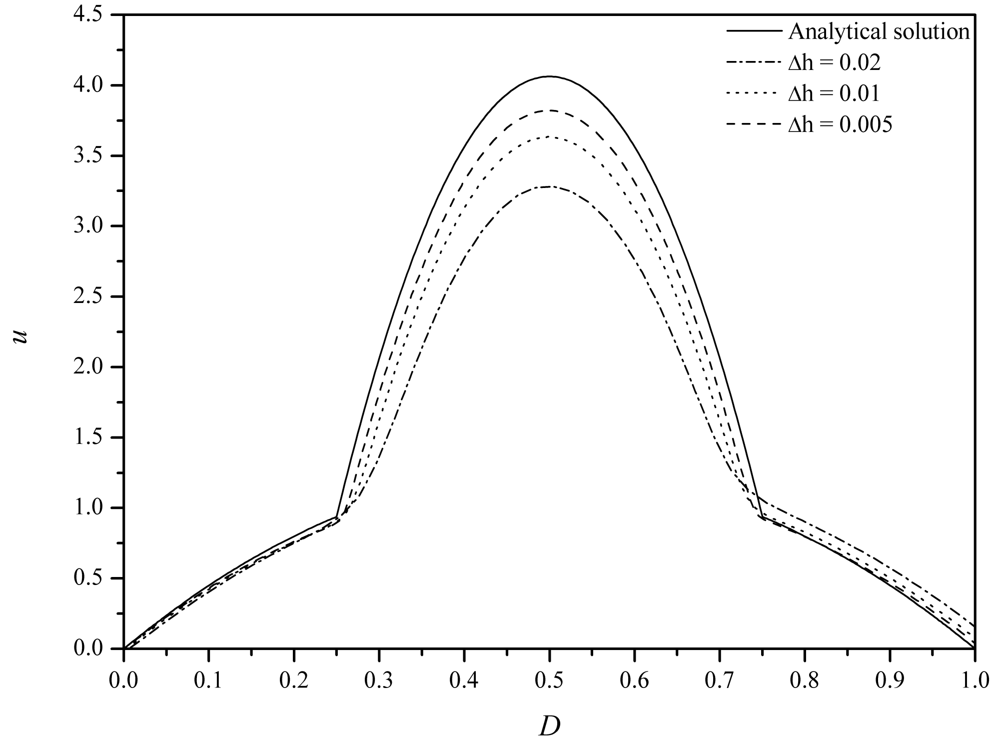

Figure 5.5: Velocity profiles for different grid resolutions compared to the analytical solution at $C_{IB} = 0.0001$ and $Re_p = 200$.

Table 5.1 presents the overall characteristics of all scenarios with the value of parameter C_{IB} which considered for the present numerical simulations. It is seen that the results for the fine grid appear the minimum % error compared to the analytical solution. It is noticed that the accuracy of the method is close to first order. It is also worth mentioning that for the case with the fine grid (14x240x240) other three values of C_{IB} = 0.0002, 0.0003 and 0.001 were examined. Even though the % error for maximum velocity appears slightly lower values compared to the case for $C_{IB} = 0.0001$. However, the numerical results for the velocity profile with C_{IB} = 0.0002, 0.0003 and 0.001 are not captured the vicinity of the pipe wall, in contrast to the scenario for $C_{IB} = 0.0001$. Therefore, the value of 0.0001 is adopted as the best selection for this case.

Table 5.1: Cases considered for the appropriate selection of C_{IB}.

Grid	Δh	C_{IB}	u_{max}	% error
14x60x60	0.020	0.0001	3.2891	19.03
14x120x120	0.010	0.0001	3.6363	10.49
14x120x120	0.010	0.0010	3.6501	10.15
14x240x240	0.005	0.0001	3.8221	5.92
14x240x240	0.005	0.0002	3.8259	5.82
14x240x240	0.005	0.0003	3.8266	5.81
14x240x240	0.005	0.0010	3.8370	5.55

5.3 Validation of the GCIBM

5.3.1 Single-phase Poiseuille flow

Similar to Section 5.2.1, numerical simulations were conducted to evaluate the accuracy of the developed Ghost-Cell Immersed Boundary Method (GCIBM) at $Re_p = 20$ for single-phase Poiseuille flow. Three different interpolation schemes (LI, BI and QI) are examined for the GCIBM algorithm. The selection of the appropriate interpolation scheme prescribes the desired level of accuracy.

The numerical results obtained were compared with those of the analytical solution according to equation 5.1. Table 5.2 lists the parameters for the considered test cases, including the grid size, the values of the maximum velocity (u_{max}) and the percentage error of u_{max} for each of the selected interpolation reconstruction scheme.

Table 5.2: Cases examined for GCIBM with different interpolation reconstruction schemes.

Grid	Δh	u^{LI}_{max}	$\%\ error^{LI}$	u^{BI}_{max}	$\%\ error^{BI}$	u^{QI}_{max}	$\%\ error^{QI}$
14x30x30	0.040	1.2692	1.536	1.2746	1.968	1.2701	1.608
14x60x60	0.020	1.2628	1.024	1.2631	1.048	1.2654	1.232
14x120x120	0.010	1.2564	0.512	1.2563	0.504	1.2567	0.536
14x240x240	0.005	1.2521	0.168	1.2519	0.152	1.2517	0.136

LI: Linear interpolation scheme.

BI: Bilinear interpolation scheme.

QI: Quadratic interpolation scheme.

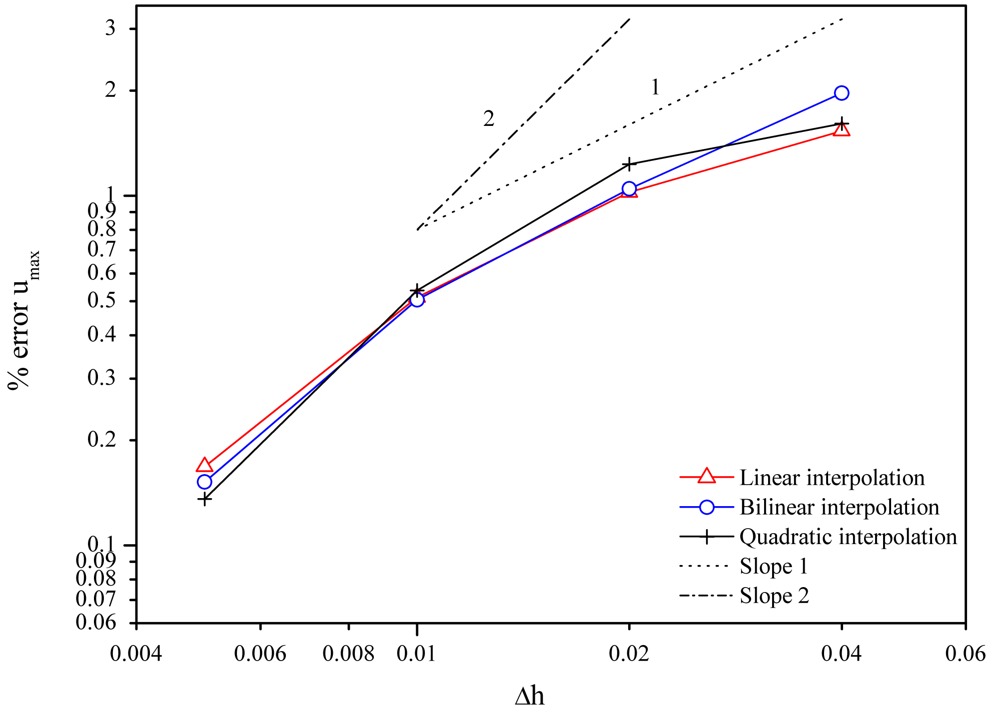

Figure 5.6: The percentage error of u_{max} vs. the grid size for different interpolation schemes for $Re_p = 20$.

Figure 5.6 illustrates the percentage error of u_{max} versus grid resolution for the three selected interpolation reconstruction schemes. It is noted that the accuracy is slightly better for the high order interpolation schemes along with the finer grids, while for the coarser mesh sizes the difference is almost negligible for linear and bilinear interpolation schemes. It is also worth mentioning that the accuracy of the method is around to the second order, as it can be seen from the curves for the finer mesh sizes which approach a slope of two (Figure 5.6). It should be noted that the error of u_{max} is not exclusively due to the representation of the wall but also due to truncation errors in the finite difference approximation of the Navier Stokes equations which are, in principle, second order for single-phase flows.

It is observed that the minimum value of the u_{max} percentage error is obtained for the case of $\Delta h = 0.005$ with the QI scheme and is equal to 0.136. For coarser grids the QI scheme is not supported by the same superiority compared to the LI and BI schemes. The GCIBM with the QI scheme provides slightly higher accuracy compared to BI and LI schemes for fine grid resolution, but it is also more demanding in CPU time.

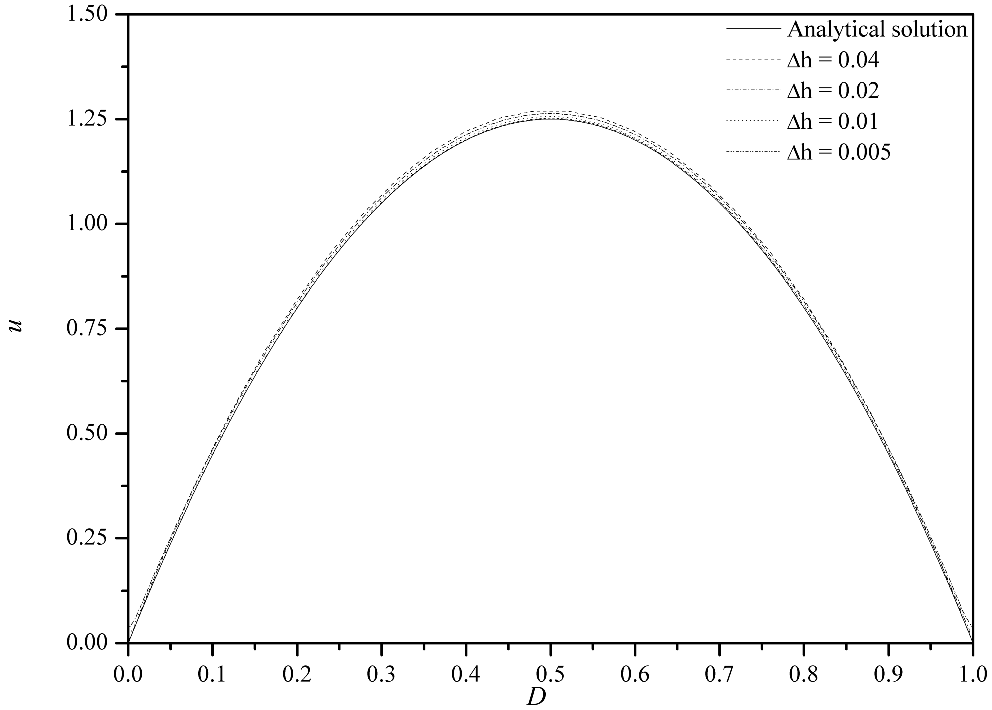

Figure 5.7: Comparison of the velocity profiles for LI reconstruction scheme and various mesh resolutions with the analytical velocity profile for $Re_p = 20$.

Figure 5.7 presents the parabolic velocity profiles for four different mesh sizes compared to the analytical velocity profile for single-phase Poiseuille flow. It is observed that for Δh = 0.01 and 0.005 the difference with the analytical solution is almost negligibly, while for the cases of Δh = 0.04 and 0.02 there is a very small deviation from the analytical solution. Similar results were obtained for the cases of BI and QI schemes.

Figure 5.8 depicts the relation of u_{max} vs. dimensionless time t. It is shown that for the finer mesh resolution Δh = 0.005, the u_{max} is much closer to the analytical solution compared to the other cases. It is worth noting that for all cases considered, the steady state status is achieved after the period of six time units. The horizontal line represents the analytical solution and its value is equal to 1.25.

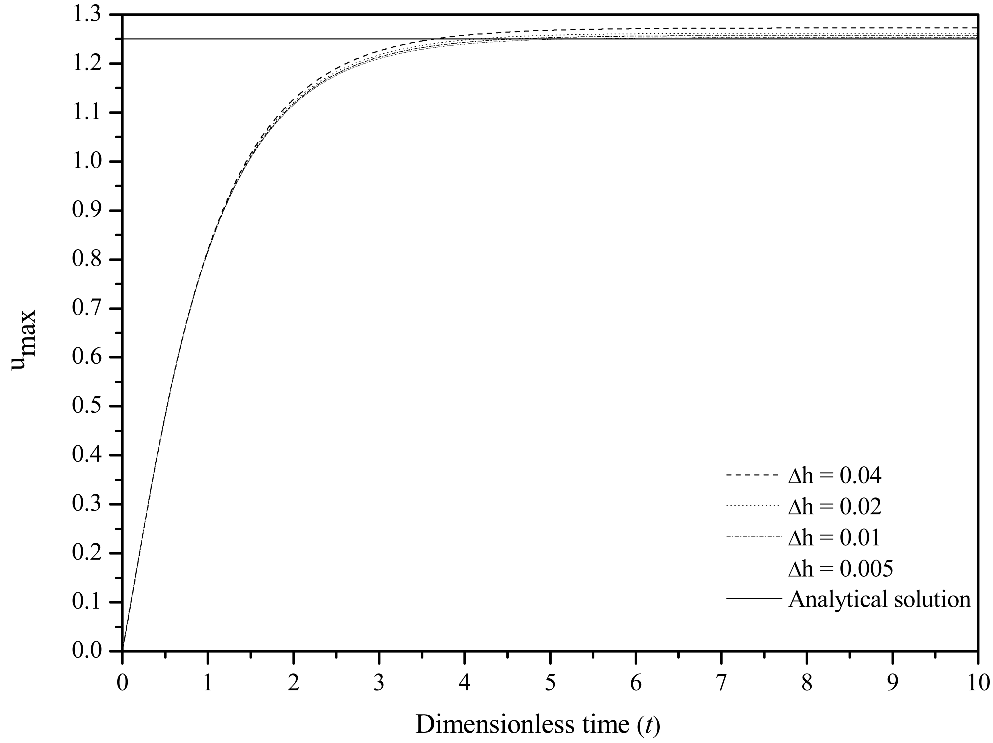

Figure 5.8: u_{max} vs. dimensionless time (t) for four different grids and QI scheme.

In Figure 5.9, it is illustrated the u-velocity contours for Δh = 0.04 and 0.005. The value of the u-velocity in the centre of the pipe is the maximum as expected and also the smooth rigid boundary reconstruction is well configured for all cases. The black circle is the ideal boundary of the pipe and the velocity on the boundary is zero. The Figure

5.9(a) has a grid resolution ($\Delta h = 0.04$) and represents the LI scheme. The Figure 5.9 (b) illustrates the distribution of u-velocity for $\Delta h = 0.005$ and QI reconstruction scheme. Similar distributions of u-velocity were obtained for the rest cases. All the values of u_{max} along with the percentage errors for each case are included in Table 5.2.

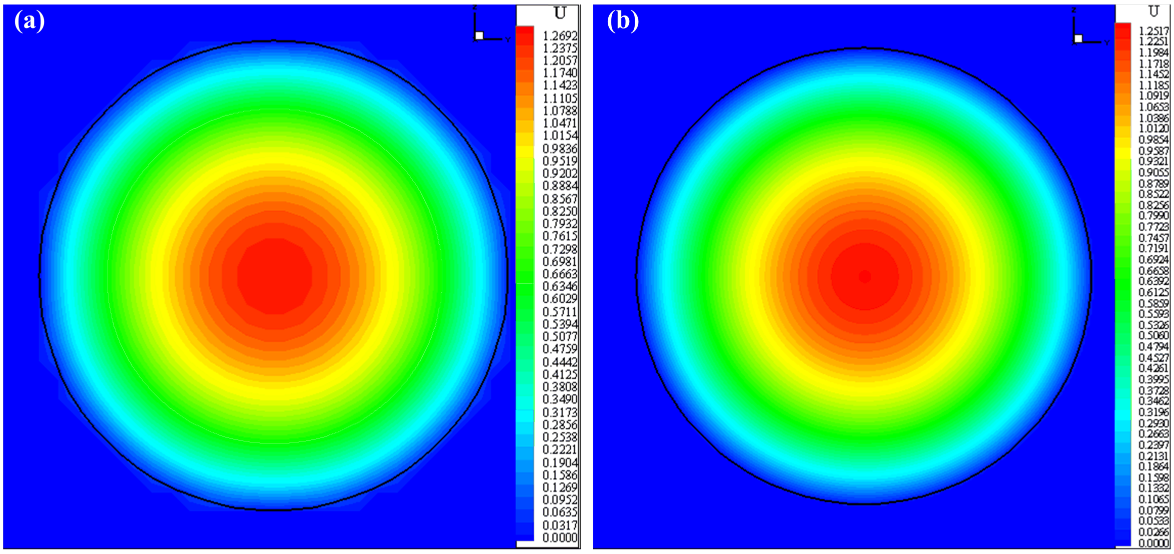

Figure 5.9: Contours of u velocity for: (a) LI and $\Delta h = 0.04$ and (b) QI and $\Delta h = 0.005$.

5.3.2 Laminar two-phase annular pipe flow

Numerical simulations conducted for laminar two-phase annular pipe flows, in order to evaluate the developed GCIBM. The computational domain, the boundary conditions and the properties of fluids are selected to be identical, according to Section 5.2.2.

Table 5.3 presents the test cases for the GCIBM performance for different grid resolutions and interpolation schemes. The difference of u_{max} percentage error for the same grid resolution and different interpolation schemes is very small and for some cases negligible, while the results for the finer grids display the lower levels of u_{max} percentage error (Figure 5.10). The minimum percentage error of u_{max} is equal to 4.79 and occurs for the case with $\Delta h = 0.005$ and QI reconstruction scheme.

It is important to note that the Cahn-Hilliard equation is employed only for the interface tracking. Even though with the above assumption, the proposed analytical

Table 5.3: GCIBM cases examined for different reconstruction schemes

Grid	Δh	u_{max}^{LI}	$\%\ error^{LI}$	u_{max}^{BI}	$\%\ error^{BI}$	u_{max}^{QI}	$\%\ error^{QI}$
14x30x30	0.040	2.8706	29.34	2.8977	28.67	2.8704	29.34
14x60x60	0.020	3.4006	16.29	3.3538	17.45	3.3558	17.39
14x120x120	0.010	3.6548	10.04	3.6548	10.04	3.6584	9.94
14x240x240	0.005	3.8292	5.74	3.8489	5.25	3.8678	4.79

LI: Linear interpolation scheme.

BI: Bilinear interpolation scheme.

QI: Quadratic interpolation scheme.

solution gives some confidence for the accuracy of the present GCIBM on the boundary. Unfortunately, there is not any other available analytical solution in order to compare the results for two-phase pipe flows.

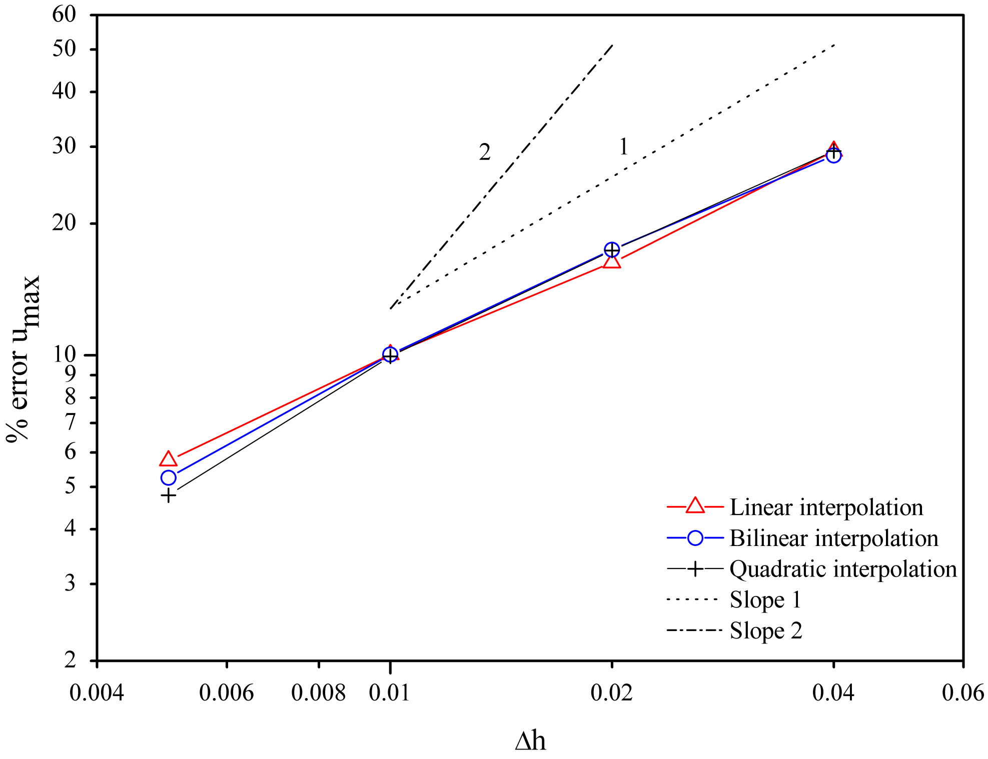

Figure 5.10: The percentage error of u_{max} vs. the grid size for different interpolation schemes for $Re_p = 200$.

The aforementioned assumptions along with the inadequate grid resolution for two-phase flows may explain the behaviour of percentage error for u_{max} (Figure 5.10).

In Figure 5.11, it is observed that when the value of the pipe diameter (D) is between 0 and 0.25 and between 0.75 and 1.0 the more viscous fluid is present, while the less viscous fluid is located between 0.25 and 0.75. As a result, the velocity values for the less viscous are higher compared to the more viscous fluid. It is also indicated that the maximum velocity occurs with the finer grid resolution $\Delta h = 0.005$ and the velocity profile approaches closer to the analytical velocity profile compared to the rest cases. Herein, the coarse grid with resolution $\Delta h = 0.04$ displays the lower velocity and diverses from the analytical velocity profile, especially in the vicinity of the interfacial region at D = 0.25 and 0.75 between the two fluids.

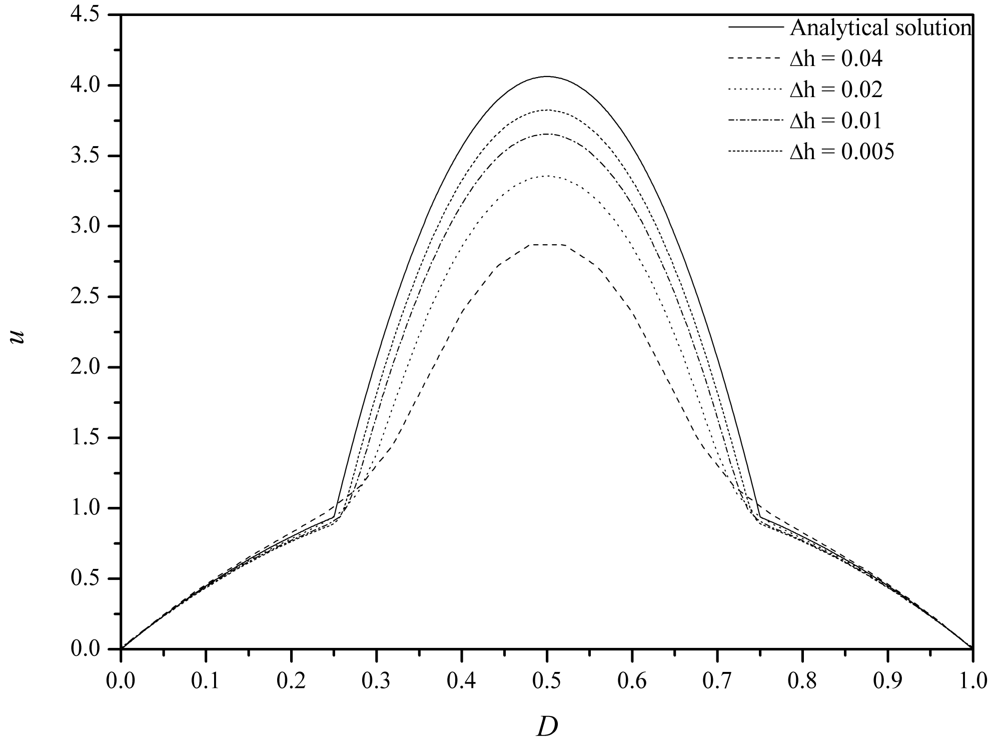

Figure 5.11: Comparison of the velocity profiles for LI scheme and various grid resolutions with the analytical solution at $Re_p = 200$.

Figure 5.12 depicts the maximum velocity with the dimensionless time for grid resolution $\Delta h = 0.04$, 0.02, 0.01 and 0.005. It is seen that the steady state status is obtained for LI reconstruction scheme after the period of 12 time units.

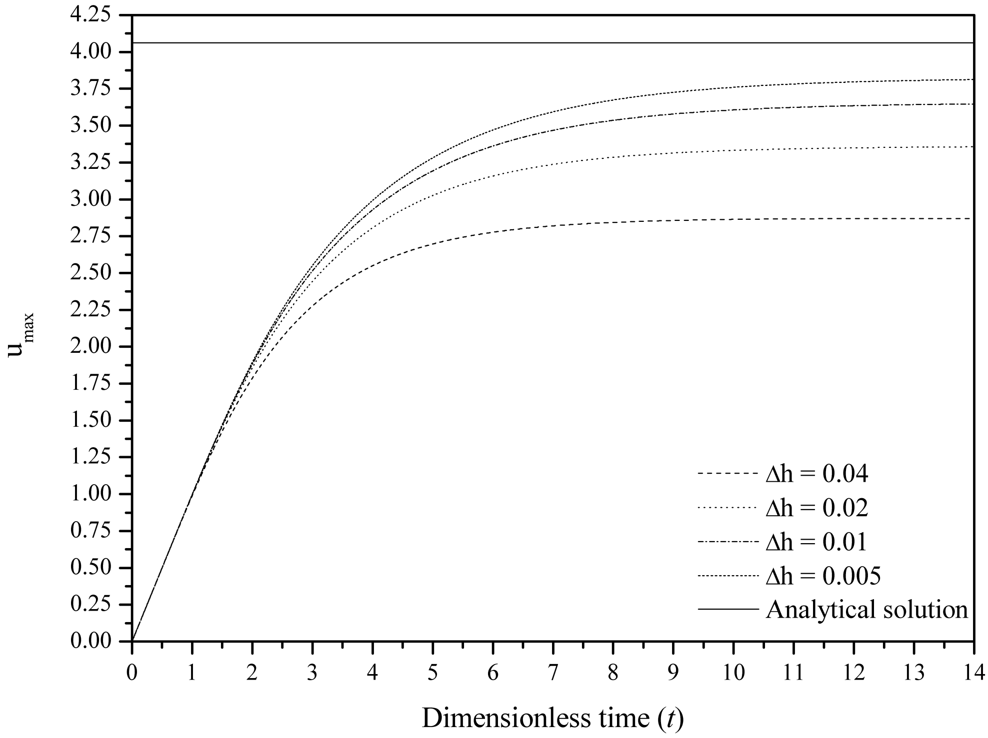

Figure 5.12: u_{max} vs. dimensionless time t for the LI scheme and different grid resolutions.

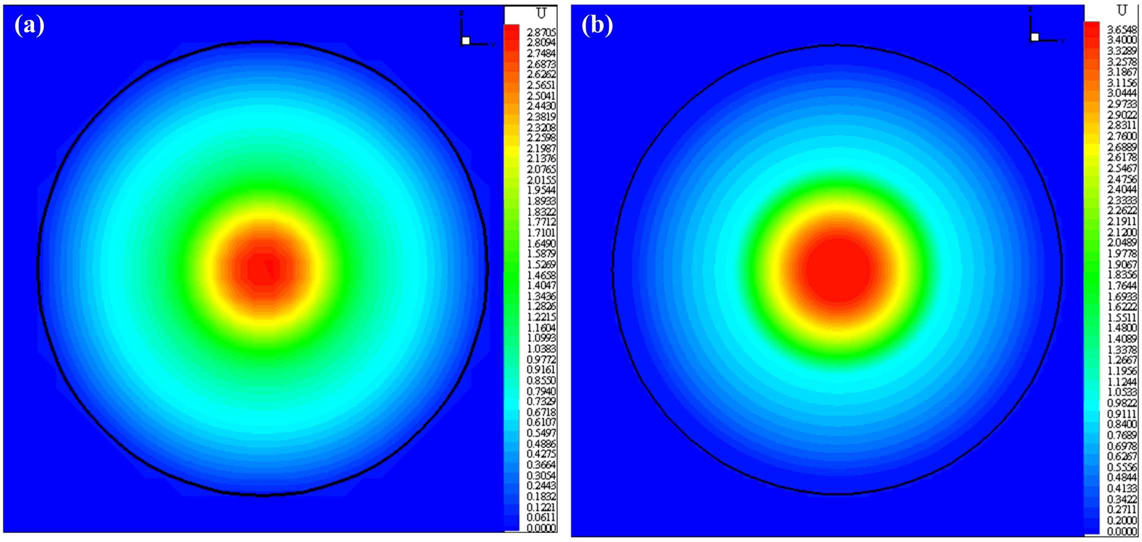

Figure 5.13: Contours of u velocity for: (a) LI and $\Delta h = 0.04$, and (b) LI and $\Delta h = 0.01$.

The contours of u velocity for LI reconstruction scheme and two different grid resolutions are shown in Figure 5.13. It is observed that the maximum value of u velocity occurs for the fine grid resolution $\Delta h = 0.01$, while the accuracy of GCIBM for the boundary representation (pipe geometry) is higher for the finer mesh size.

Figures 5.14 (a) and (b) illustrate velocity and volume fraction contours. These figures show clearly the way the flow develops (magnitude and direction) and the location of the highest velocities.

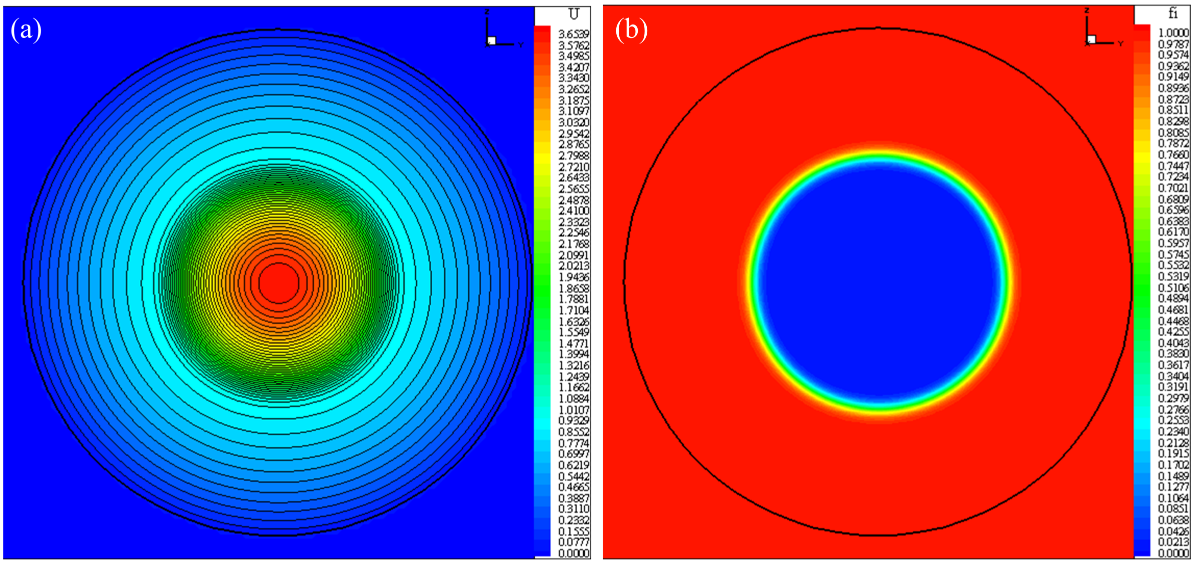

Figure 5.14: For grid resolution $\Delta h = 0.01$ and LI reconstruction scheme: (a) Contours of velocity and volume fraction, and (b) volume fraction.

5.4 Validation of the numerical method with experimental data

5.4.1 A single rising bubble in a vertical pipe

Bubble flows play a vital role in many chemical and metallurgical processes, as well as in operations such as boiling, fermentation, purification, distillation, cavitation, among others. Over the past decades, extensive investigation has been conducted by many researchers for understanding the flow behaviour and the characteristics of a single rising bubble in a pipe with quiescent viscous liquid (Wegener and Parlange, 1973). A substantial amount of experimental (Grace, 1973; Clift et al., 1978; Bhaga and Weber, 1981; Stewart, 1995; Takemura and Magnaudet, 2003; Dijkhuizen et al., 2010), numerical (Krishna and Baten, 1999; Van Sint Annaland et al., 2005, 2006; Yu and Fan, 2008; Hua et al., 2008; Chakraborty et al., 2013) and theoretical (Davies and Taylor, 1950; Moore, 1959; Taylor and Acrivos, 1964) studies have been devoted to identify the physical mechanisms that govern the phenomenon.

The free motion of a gravity driven single bubble in an infinite liquid medium depends on the sum of the forces acting on the bubble and obeys Newton' s second law. The forces acting on a single bubble rising in a pipe are the gravitational force, the resistance (drag) force and the buoyancy force. However, the gravitational force often is assumed to be unimportant due to the negligible air density. The drag force expresses the bubble resistance in the liquid and is dependent on the bubble shape. F_D is defined as:

$$F_D = \frac{1}{8} C_D \rho_l U_T^2 \pi d_e^2 \tag{5.4}$$

where C_D is the drag coefficient, U_T is the terminal velocity of the rising bubble and $d_e = \left(\frac{6V}{\pi}\right)^{1/3}$ is the volume-equivalent bubble diameter. The terminal velocity is defined as the steady state velocity at which the bubble reaches when the force balance of buoyancy and drag is equal. On the other hand, the buoyancy force is given by the following equation:

$$F_B = -\frac{\pi}{6} g(\rho_l - \rho_g) d_e^3 \tag{5.5}$$

The rise of a single bubble in an infinite liquid is caused by the buoyancy force. As a result, the onset of the surrounding liquid motion takes place, along with the shape deformation of the bubble. These shape deformations and rising velocity are highly dependent on the ratio viscosity and density, surface tension and the surrounding flow field. As mentioned above, the bubble achieves a terminal velocity when $F_D = F_B$. As a result, the drag coefficient of the bubble, C_D, can be estimated by the following equality:

$$\begin{aligned} F_D &= F_B \Leftrightarrow \\ \frac{1}{2} C_D \rho_l U_T^2 \pi \frac{d_e^2}{4} &= \frac{\pi}{6} g(\rho_l - \rho_g) d_e^3 \Leftrightarrow \\ C_D &= \frac{4}{3} \frac{(\rho_l - \rho_g) g d_e}{\rho_l U_T^2} \end{aligned} \tag{5.6}$$

According to the dimensional analysis and the use of $\Pi-$theorem, the physical problem may be characterised by the following five dimensionless parameters (Grace, 1973):

$$r_v = \frac{\mu_l}{\mu_g}, \qquad r_d = \frac{\rho_l}{\rho_g}, \qquad Re_T = \frac{\rho_l U_T d_e}{\mu_l}, \qquad Mo = \frac{g \mu_l^4}{\rho_l \sigma^3}, \qquad Eo = \frac{g \rho_l d_e^2}{\sigma}$$

where r_v is the viscosity ratio, r_d the density ratio, Re_T the bubble Reynolds number, Mo the Morton number and Eo the Eotvos number, respectively. The Re number expresses the ratio of inertial forces to viscous forces, the Mo number represents the ratio of gravitational and viscous force to surface tension and determines the bubble shape, and Eo number reflects the buoyancy force to surface tension and characterize the bubble shape. Other useful dimensionless parameters which may be used in place of Eotvos number is the bubble Weber number (We_T) or Bond number (Bo). The latter dimensionless number is exactly the same as Eo number. Another useful dimensionless parameters are the Froude number (Fr) and the buoyancy Reynolds number (Re_B). It is also worth mentioning that Mo number can be written as a combination of the dimensionless parameters Eo and Re_B, as well as We_T number along with Re, Mo and Eo numbers, respectively:

$$We_T = \frac{\rho U_T^2 d_e}{\sigma} = \frac{Re_T^2 Mo^{0.5}}{Eo^{0.5}}, \qquad Mo = \frac{Eo^3}{Re_B^4}, \qquad Fr_T = \frac{U_T}{\sqrt{g d_e}}, \qquad Re_B = \frac{\rho_l g^{0.5} d_e^{1.5}}{\mu_l}$$

The values of Mo and Eo numbers are usually known, while the values of Re_T, We_T and Fr_T numbers required the definition of U_T. In addition, it is preferable only one of the dimensionless parameters to include the bubble terminal velocity and the rest to depend only on the gravity acceleration and fluids properties. A well-known relation from the literature for the definition of terminal velocity is given by:

$$U_T = \sqrt{g d_e} \tag{5.7}$$

Grace (1973) conducted a large number of experiments for single rising bubbles in 21 different infinite liquids for investigating the bubble shape deformation. According to these experimental data, he created a generalized bubble regime map based on the Reynolds, Morton and Eotvos numbers. According to this graph, the bubble shape may be categorized in the following three types: spherical, ellipsoidal and spherical cap. An improved version of the Grace' s graph was presented by Clift et al. (1978) with additional bubble shapes (i.e. wobbling shape, spherical-cap, the skirted and the dimpled ellipsoidal-cap).

Some years later, Bhaga and Weber (1981) extended the graph of Grace by adding more subcategories for the the spherical cap regime. The subcategories are the oblate ellipsoidal cap, spherical cap closed, spherical cap open, skirted with smooth skirt (steady) and skirted with wavy skirt (unsteady), respectively. They also investigated the wake formation and size of the bubble.

In the present section, the numerical method is tested for a single rising bubble in a pipe and the obtained results are compared with experimental data from the work of Bhaga and Weber (1981).

5.4.1.1 Selection of the appropriate pipe length

For investigating the behaviour and characteristics of the bubble flow under infinite medium conditions is necessary to specify the suitable computational domain (pipe length and diameter) for the numerical simulations. The computational domain was selected to be large enough in order to minimise the effect by the pipe geometry and at the same time to be affordable in computational cost and time. The selection criteria for the assessment of the appropriate computational domain are the terminal rising bubble velocity and the terminal bubble shape.

Herein, the ratio of the pipe length to the diameter of the initially spherical bubble is specified as $L_p^* = \dfrac{L_p}{d_e}$, while the ratio of the pipe diameter to the diameter of the initially spherical bubble is defined as $D_p^* = \dfrac{D_p}{d_e}$. Numerical simulations were performed for $Re_B = 79.88$, $Eo = 32.2$ and $Mo = 8.2 \cdot 10^{-4}$ which represent a rising bubble with an oblate ellipsoidal disk shape and $Re_{T_{exp}} = 55.3$, according to the work of Bhaga and Weber (1981). Three additional dimensionless parameters are required to be specified for the numerical simulations, namely ratio viscosity (r_v), ratio density (r_d) and the instantaneous Reynolds number (Re_{inst}). The r_v and the r_d were set to 100 and 1000, respectively. Following the work of Chakraborty et al. (2013), the Re_{inst} is defined as:

$$Re_{inst} = \frac{\rho_l d_e U_{inst}}{\mu_l}, \qquad U_{inst} = \frac{1}{n_{cells}} \sum_{n=1}^{n_{cells}} C_n u_n \tag{5.8}$$

where C_n is the gas fraction in cell n and u_n is the flow velocity of cell n. A constant grid resolution, $\Delta h = 0.004$, was adopted for the numerical simulations.

Table 5.4: Selection of the appropriate pipe length for single rising bubble.

Cases	Grid	Δh	L_p^*	D_p^*	$U_{T_{sim}}$	$Re_{T_{sim}}$	$Re_{T_{exp}}$	% error
(1)	214x262x262	0.004	6	7	0.277	58.54	55.3	5.85
(2)	286x262x262	0.004	8	7	0.266	56.11	55.3	1.47
(3)	358x262x262	0.004	10	7	0.265	56.02	55.3	1.31
(4)	428x262x262	0.004	12	7	0.265	55.97	55.3	1.21

Table 5.4 presents the cases considered for the pipe length sensitivity analysis along with the L_p^*, D_p^*, grid resolution (Δh), terminal bubble velocity (U_T), simulated terminal Reynolds number ($Re_{T_{sim}}$), experimental terminal Reynolds number ($Re_{T_{exp}}$), percentage error between the simulated and experimental terminal Reynolds numbers. It is observed that when the L_p^* increases from 6 to 8 bubble diameters the effects on the terminal bubble shape (Figure 5.15) and rising velocity are very small, while for pipe length more than 8 bubble diameters the pipe wall effects are negligible.

Figure 5.15: Effects on the terminal bubble shape for $L_p^* = 6$, 8, 10 and 12.

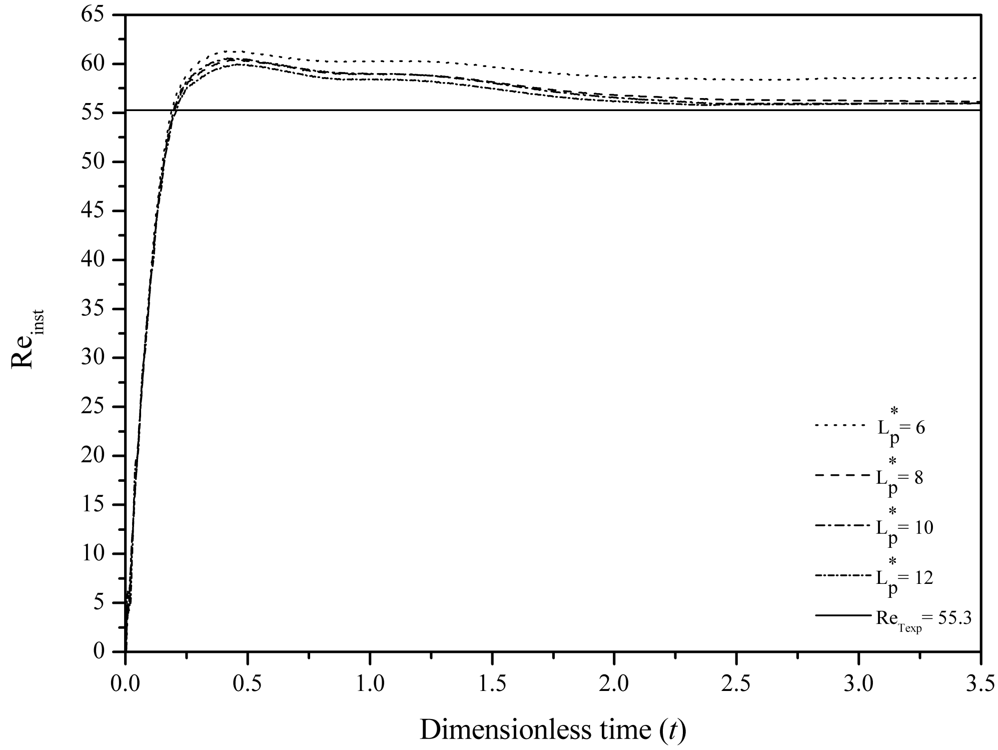

Figure 5.16: The Re_{inst} of the single rising bubble vs. t for $L_p^* = 6$, 8, 10 and 12.

Figure 5.16 illustrates the Re_{inst} with the dimensionless time. It is seen that the Re_{inst} is become almost identical for the cases (2-4) when the flow achieves steady state status after $t = 2.6$. Hence, the difference for the simulated terminal Reynolds number ($Re_{T_{sim}}$) for cases (2-4) is almost negligible. It is concluded that a pipe length more than 8 bubble diameters is sufficient for the numerical simulations. This finding is in agreement with the works of Mukundakrishnan et al. (2007) and Hua et al. (2008). In the present study, a pipe length equal to 10 bubble diameters was adopted for all the numerical simulations involving single rising bubbles.

5.4.1.2 Selection of the appropriate pipe diameter

Similar to the above Section 5.4.1.1, sensitivity analysis was performed for the appropriate selection of the pipe diameter. Therefore, four cases with different values for D_p^*, namely 5, 6, 7 and 8, were examined.

From Table 5.5 and Figures 5.17, for the D_p^*, it is shown that for values more than 6 bubble diameters the difference for the simulated Reynolds number and terminal bubble shape are almost negligible, while for values less than 6 bubble diameters the difference is considerable for U_T and $Re_{T_{sim}}$.

Table 5.5: Selection of the appropriate pipe diameter for single rising bubble.

Cases	Grid	Δh	L_p^*	D_p^*	U_T	$Re_{T_{sim}}$	$Re_{T_{exp}}$	% error
(1)	358x193x193	0.004	10	5	0.296	62.50	55.3	13.01
(2)	358x226x226	0.004	10	6	0.275	58.10	55.3	5.07
(3)	358x262x262	0.004	10	7	0.265	56.02	55.3	1.31
(4)	358x298x298	0.004	10	8	0.265	55.96	55.3	1.20

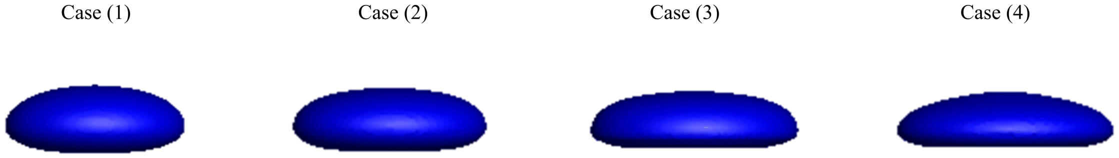

Figure 5.17: Effects on the terminal bubble shape for D_p^* equal to 5, 6, 7 and 8.

In Figure 5.18, it is observed that the instantaneous Reynolds number for the cases with D_p^*= 7 and 8 displays almost negligible values after t = 2.75, while for values less than 6 bubble diameters there are significant differences.

According to the numerical results, the selection of a pipe diameter more than 6 bubble diameters should be sufficient for minimising the pipe wall effects. This is supported by the numerical study of Mukundakrishnan et al. (2007), which indicates that for $D_p^* \geq 6$ the rise of a single bubble corresponds to minimum wall effects.

Hua et al. (2008) claims that for a pipe diameter more than 6 bubble diameters there is no significant changes to terminal bubble velocity and shape, while for pipe diameter between 8 to 10 bubble diameters the terminal bubble velocity differs only around 1 %. Their numerical results agree with the experimental findings of Krishna et al. (1999), which demonstrate that a pipe diameter equal to 8 bubble diameters or larger satisfies the infinite medium conditions for a single rising bubble. In the present study, the pipe diameter was selected to be equal to 7 instead of 8 bubble diameters due to negligible difference for $Re_{T_{sim}}$ and to maintain an affordable computational time.

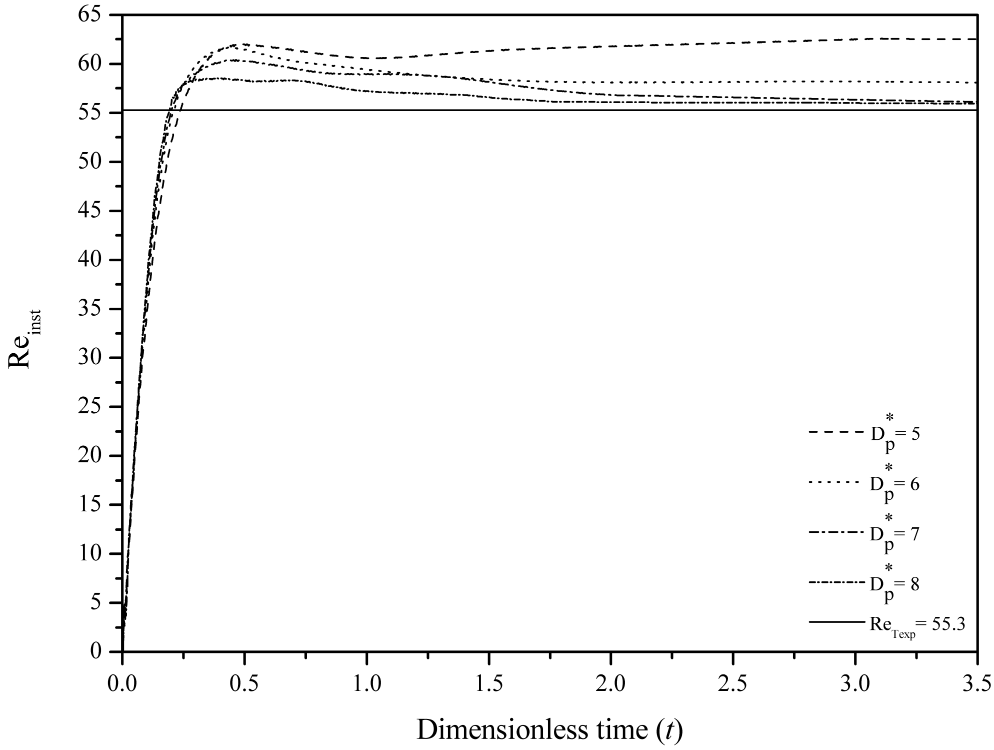

Figure 5.18: The Re_{inst} of the single rising bubble with t for D_p^* equal to 5, 6, 7 and 8.

5.4.1.3 Grid sensitivity analysis

A uniform Cartesian grid was selected for the numerical simulations based on a grid sensitivity analysis among various grids with resolution of 0.006, 0.005, 0.004, 0.0035 and 0.003, respectively. The parameters for the numerical simulation are identical to the above sections.

Table 5.6 presents the cases for the grid sensitivity analysis along with all the appropriate parameters considered. An important issue for the numerical simulation of a single rising bubble is the number of cells for the bubble. Regarding the selection of the grid resolution for each simulation a number of cell per bubble was devoted. In Figure 5.19, it is observed that the final bubble shape for cases (1) and (2) with 24 and 29 cells per bubble, respectively, is slightly different in shape. For cases (3-5) the effects on the terminal bubble shape is almost negligible, as well as on the terminal velocity, the instantaneous and simulated Reynolds number.

Table 5.6: Grid independence for single rising bubble.

Cases	Grid	Δh	cell/bub.	L_p^*	D_p^*	U_T	$Re_{T_{sim}}$	$Re_{T_{exp}}$	% error
(1)	238x175x175	0.0060	24	10	7	0.279	58.91	55.3	6.54
(2)	286x210x210	0.0050	29	10	7	0.274	57.83	55.3	4.58
(3)	358x262x262	0.0040	36	10	7	0.265	56.02	55.3	1.31
(4)	408x300x300	0.0035	41	10	7	0.265	55.98	55.3	1.24
(5)	476x350x350	0.0030	48	10	7	0.264	55.90	55.3	1.09

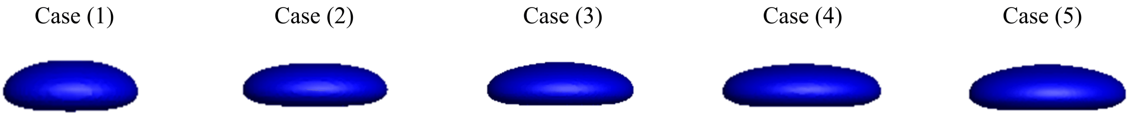

Figure 5.19: Effects on the terminal bubble shape for different grid resolution.

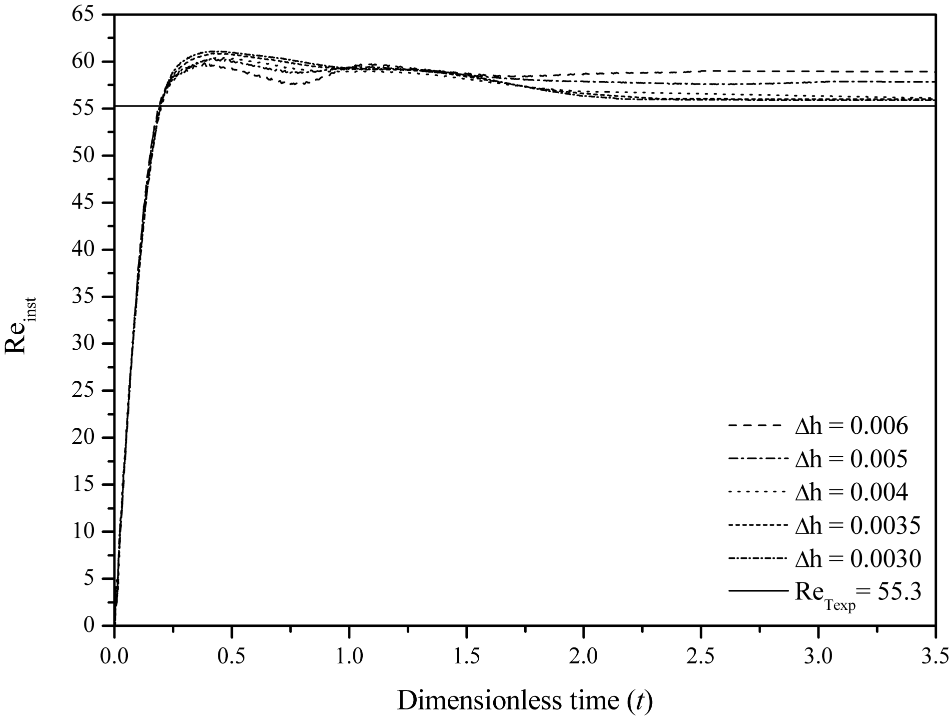

Figure 5.20: Re_{inst} of the single rising bubble t for different grid resolution (Δh).

In the present simulations for single rising bubble, the finest grid with resolution 0.0030 was selected, even though the difference among the finer grids (cases 3-5) are almost negligible. This selection was made in order to achieve the highest accuracy from the adopted phase field or diffusion interface method for validation compromising with the available computer sources, as well as for the test cases in Section 5.4.1.6.

5.4.1.4 Volume conservation test

Another important issue for successful numerical simulations of two-phase flows is the requirement of the volume conservation between the two phases. This requirement is one of the advantages of some of the most well known interface tracking and capturing methods such as VOF, but also the disadvantage of other methods such as the level-set.

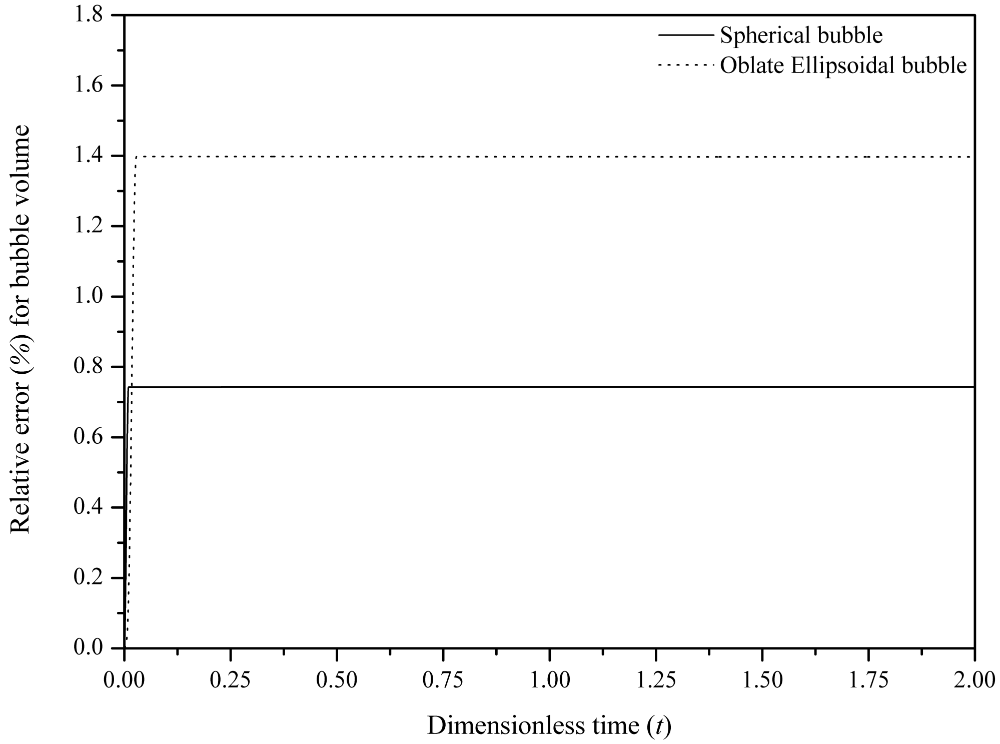

Figure 5.21: The percentage bubble volume error as a function of the dimensionless time.

The satisfaction of the aforementioned condition is presented by displaying the bubble volume percentage error for a spherical and an oblate ellipsoidal bubble. The relative error of bubble volume is computed for a specific time and compared to the initial bubble volume for a spherical shape bubble. The dimensionless parameters for the case of spherical bubble are $\frac{\mu_l}{\mu_g} = 100$, $\frac{\rho_l}{\rho_g} = 1000$, $Eo = 0.5$ and $Mo = 10^{-6}$, while for the oblate ellipsoidal bubble are $\frac{\mu_l}{\mu_g} = 100$, $\frac{\rho_l}{\rho_g} = 100$, $Eo = 10$ and $Mo = 0.1$. In Figure 5.21, it is observed that the value of relative error is less than 1% for the spherical regime and less than 1.4% which indicate that the volume of rising bubble is satisfactory conserved.

5.4.1.5 Presence of parasitic or spurious currents

One major issue of the classical interface tracking and capturing methods is the accurate computation of surface tension. The most widely used technique for modelling surface forces on the interfacial region is the Continuum Surface Force (CSF) by Brackbill et al. (1992), but its performance is affected by the presence of parasitic or spurious currents. According to Lafaurie et al. (1994), parasitic or spurious currents are defined as the "small amplitude velocity field due to the slight unbalance between the stresses at the sites in the interfacial region".

Harvie et al. (2006) claim that the parasitic or spurious current magnitude associated with the surface tension force. Hence, the increase of surface tension is followed by an increase of the parasitic currents magnitude. Their findings support that the parasitic currents are not decreased in magnitude with the decrease of time step or mesh refinement. The produced oscillations from the parasitic currents can be strong enough and usually resulting to misprediction of the flow field velocities or deform the interfacial region (Popinet and Zaleski, 1999).

Evidence of these parasitic or spurious currents has been reported by many scientists and engineers, despite the fact that new numerical techniques for simulating the interfacial region are used. Among them are the SURFER Lafaurie et al. (1994), CSF (Brackbill et al., 1992), VOF (Hirt and Nichols, 1981), front-tracking method (Tryggvason et al., 2001), and the second-gradient method (Jamet et al., 2002).

In the present study, a static bubble is considered as a test case for the presence of parasitic currents on the interfacial region. The main reason for the generation of the parasitic currents is the incorrect computation of the surface tension on the interface.

The magnitude of the parasitic currents can be calculated by measuring the maximum velocities during the time of the simulation. The selected parameters for the current simulations are, $D_p^* = 7$, $L_p^* = 10$, $Mo = 36.3$, $Eo = 240$ and $\frac{\rho_l}{\rho_g} = 1000$ and $\frac{\mu_l}{\mu_g} = 50$.

Figure 5.22 illustrates the maximum spurious velocity vs. dimensionless time for interfacial thickness equal to $\varepsilon = 0.5\Delta h$, which is the selected interfacial thickness for the bubble rise simulations.

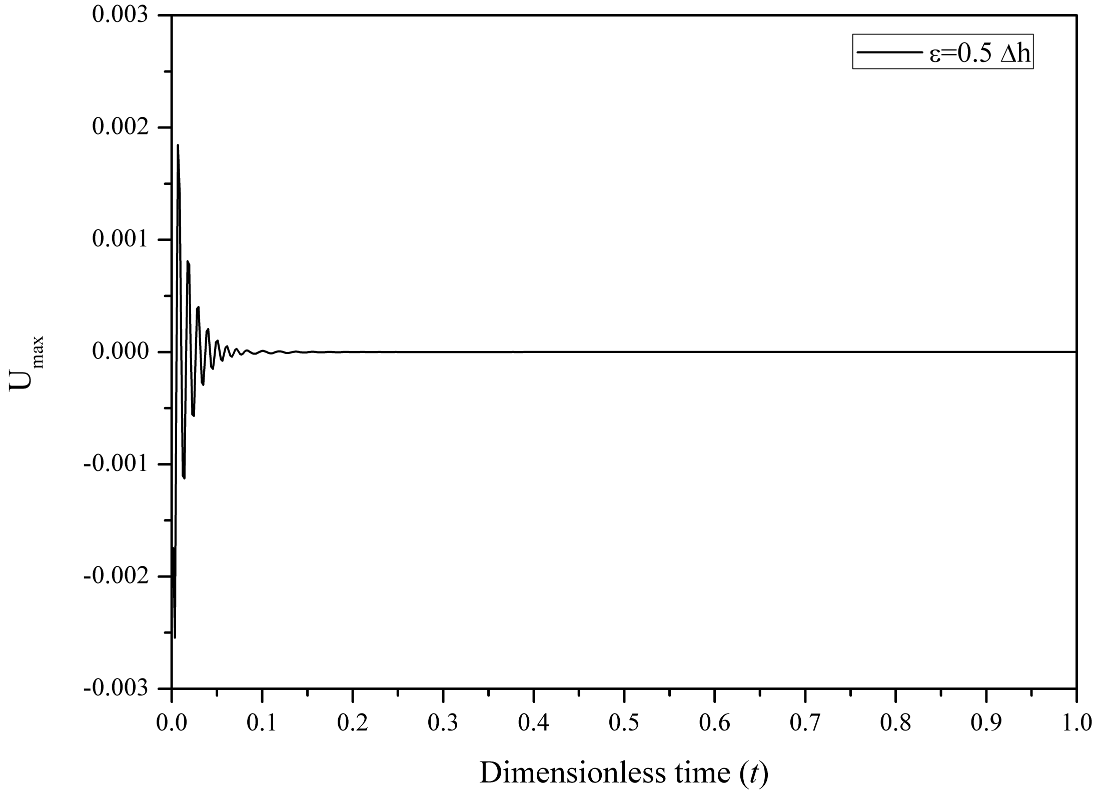

Figure 5.22: The maximum spurious velocity as a function of dimensionless time for $Mo = 36.3$, $Eo = 240$, $\rho_g = 1000$ and $\frac{\mu_l}{\mu_g} = 50$.

The appropriate value of interface thickness was selected by comparing the U_{max} for different values of ε (Table 5.7) after one time step. The magnitude of terminal spurious velocity is in the range of $1.48 \cdot 10^{-6} \leq \varepsilon \leq 1.8 \cdot 10^{-6}$ for $0.4\Delta h \leq \varepsilon \leq 0.6\Delta h$. It is observed that for $\epsilon = 0.5\Delta h$ displays the minimum value for the spurious velocity.

Table 5.7: The maximum velocity for different values of interface thickness

Interface thickness (ϵ)	U_{max}
$0.40 \cdot \Delta h$	$1.48 \cdot 10^{-6}$
$0.45 \cdot \Delta h$	$1.27 \cdot 10^{-6}$
$0.50 \cdot \Delta h$	$1.25 \cdot 10^{-6}$
$0.55 \cdot \Delta h$	$1.39 \cdot 10^{-6}$
$0.60 \cdot \Delta h$	$1.82 \cdot 10^{-6}$

5.4.1.6 Test cases

In the present section, four different test cases for single rising bubbles were examined for validating the numerical method. Four numerical simulation selected for four different flow regimes, namely spherical, oblate ellipsoidal, oblate ellipsoidal disk and oblate ellipsoidal cap. The flow regimes obey the flow regime map of a bubble rising in quiescent viscous liquids according to the work of Bhaga and Weber (1981), Grace (1973) and Clift et al. (1978). The numerical results obtained were compared to available experimental data from the aforementioned studies. The comparison is focused on the terminal bubble shape and the simulated terminal Reynolds number ($Re_{T_{sim}}$).

Table 5.8 presents the parameters for the current simulations such as the Eotvos number (Eo), the Morton number (Mo), the simulated terminal Reynolds number ($Re_{T_{sim}}$), the experimental terminal Reynolds number ($Re_{T_{exp}}$), as well as the relative error between simulated and experimental terminal Reynolds numbers. In this section, all the numerical simulations performed for$D_p^* = 7$, $L_p^* = 10$, $\Delta h = 0.0030$, $\frac{\rho_l}{\rho_g} = 1000$ and $\frac{\mu_l}{\mu_g} = 100$.

Table 5.8: Parameters for the considered test cases.

Shape	Eo	Mo	$Re_{T_{sim}}$	$Re_{T_{exp}}$	% error
Spherical	0.5	$1.25 \cdot 10^{-6}$	14.5	12	20
Oblate ellipsoidal	10	0.01	11.7	11.0	6.36
Oblate ellipsoidal disk	32.2	$8.20 \cdot 10^{-4}$	55.9	55.3	1.09
Oblate ellipsoidal cap	116	1.31	21.9	20.4	7.2

Figure 5.23(a) illustrates the evolution of the 3-D terminal bubble shape for the spherical regime. It is also observed that the terminal bubble shape is identical to that specified from the regime map of the work of Bhaga and Weber (1981), indicating a well predicted terminal shape for the spherical regime. However, the deviation between the simulated terminal Reynolds number ($Re_{T_{sim}}$) and the experimental terminal Reynolds number ($Re_{T_{exp}}$) is 20%. This behaviour can be explained by the small size of the domain and/or by the low rise velocity where the percentage error will be high even for small absolute errors, but without change in the simulation accuracy (Hua et al., 2008).

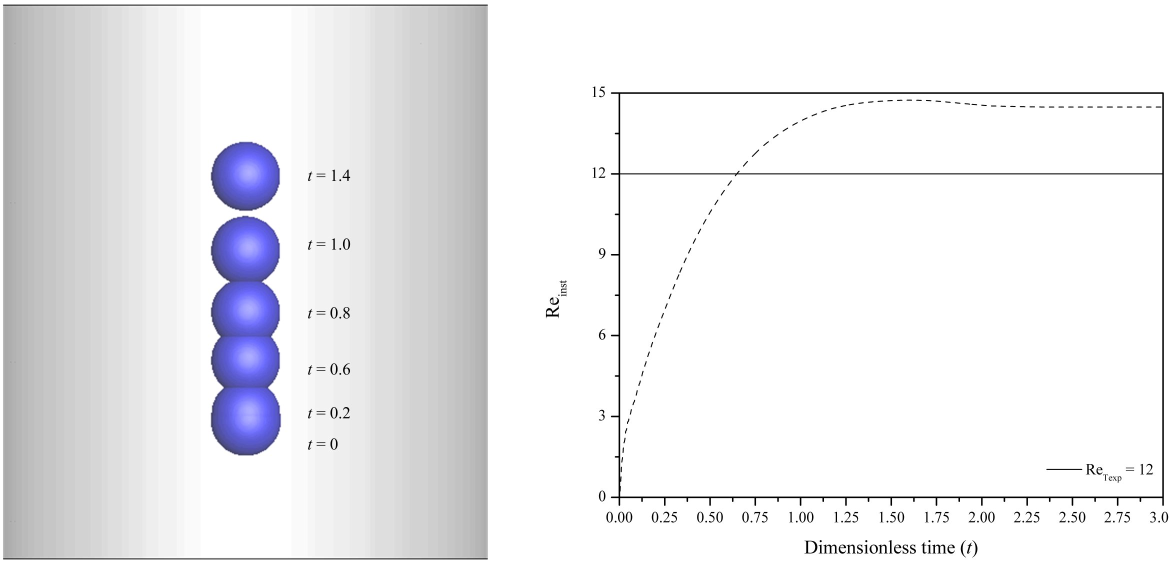

(a) (b)

Figure 5.23: Spherical shape: (a) Evolution of the terminal bubble shape and (b) the Re_{inst} versus the dimensionless time.

Figure 5.24(a) depicts the rising of an oblate ellipsoidal bubble until to reach the terminal bubble shape. It is also observed that the obtained terminal oblate ellipsoidal bubble shape predicts very well terminal bubble shape according to the regime maps of Clift et al. (1978) and Bhaga and Weber (1981). The $Re_{T_{sim}}$ is compared against the $Re_{T_{exp}}$, presenting satisfactory agreement, while Figure 5.24(b) presents the instantaneous Reynolds number versus dimensionless time. The relative error is calculated around to 6.4%.

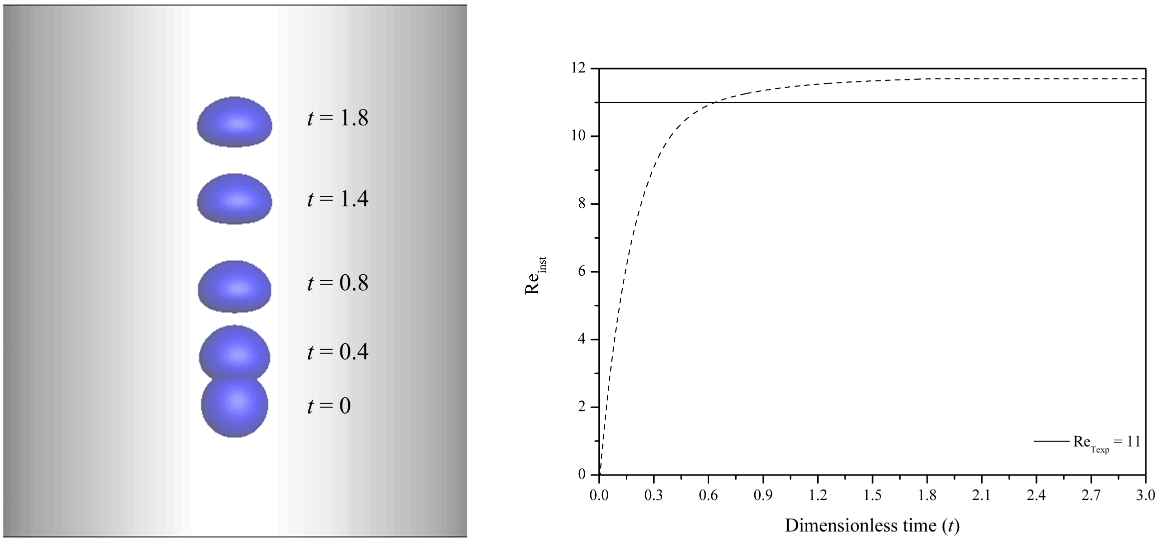

(a) (b)

Figure 5.24: Oblate ellipsoidal shape: (a) Evolution of the terminal bubble shape and (b) the Re_{inst} versus the dimensionless time.

The next test case is the simulation of an oblate ellipsoidal disk rising in infinite liquid. Figure 5.25(a) illustrates the rising bubble which maintains an oblate ellipsoidal shape and concludes to the terminal disk shape. The obtained terminal bubble shape presents very good agreement compared to the identical case from the work of Bhaga and Weber (1981), as shown in Figures 5.26(a) and 5.26(b). Figure 5.25(b) exhibits the instantaneous Reynolds number relate to dimensionless time. It is observed that Reynolds number reaches to the terminal phase after three dimensionless time units. The obtained $Re_{T_{sim}}$ yields a value of 55.9 which deviates only 1.09% from the $Re_{T_{exp}} = 55.3$.

The fourth test case is the bubble rising in the oblate ellipsoidal cap regime. Figure 5.27(a) exhibits the changes on the bubble shape during the simulation, while Figure 5.27(b) depicts the Re_{inst} during the simulation time period, up to the point at which the Re_{inst} achieves a terminal value.

In Figures 5.28(a) and 5.28(b), it is observed that the predicted terminal bubble shape exhibits an oblate ellipsoidal cap shape very similar to the experimental terminal bubble shape of Bhaga and Weber (1981). The relative error between the $Re_{T_{sim}}$ and $Re_{T_{exp}}$ is

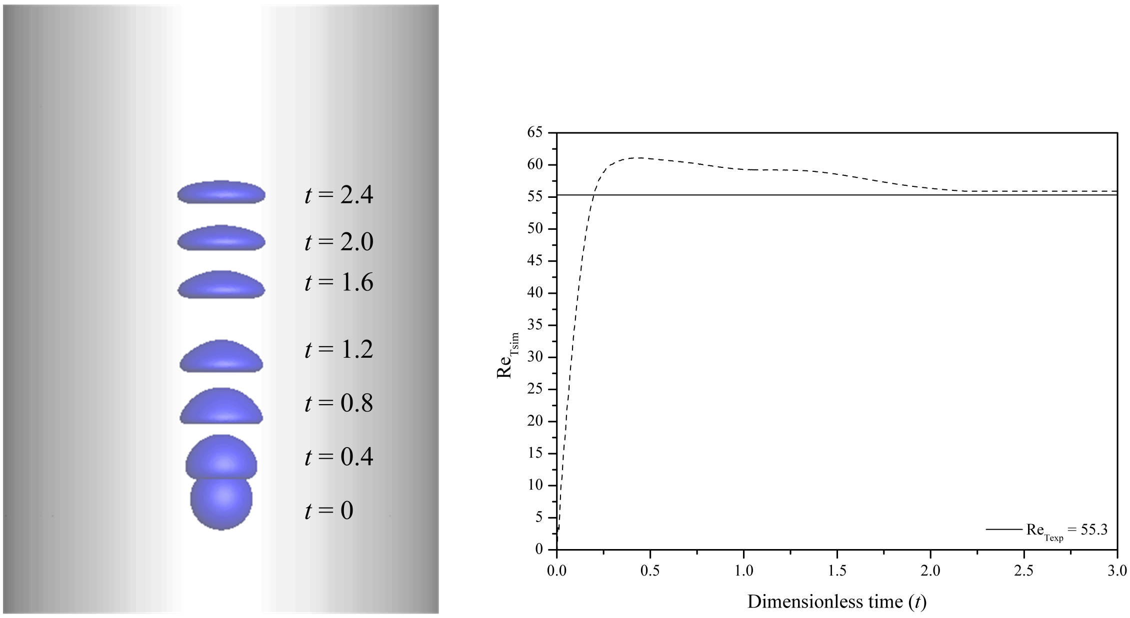

(a) (b)

Figure 5.25: Oblate ellipsoidal disk shape: (a) Evolution of the terminal bubble shape and (b) the Re_{inst} versus the dimensionless time.

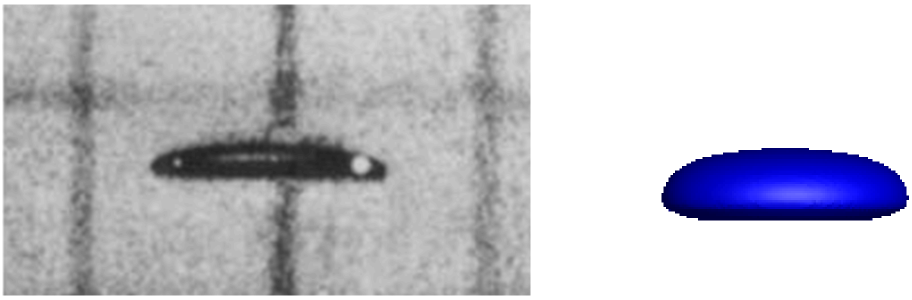

(a) (b)

Figure 5.26: (a) Comparison of the experimental terminal bubble shape according to the work of Bhaga and Weber (1981) with the numerical predicted bubble shape (b).

equal to 7.2%, as shown in Table 5.8.

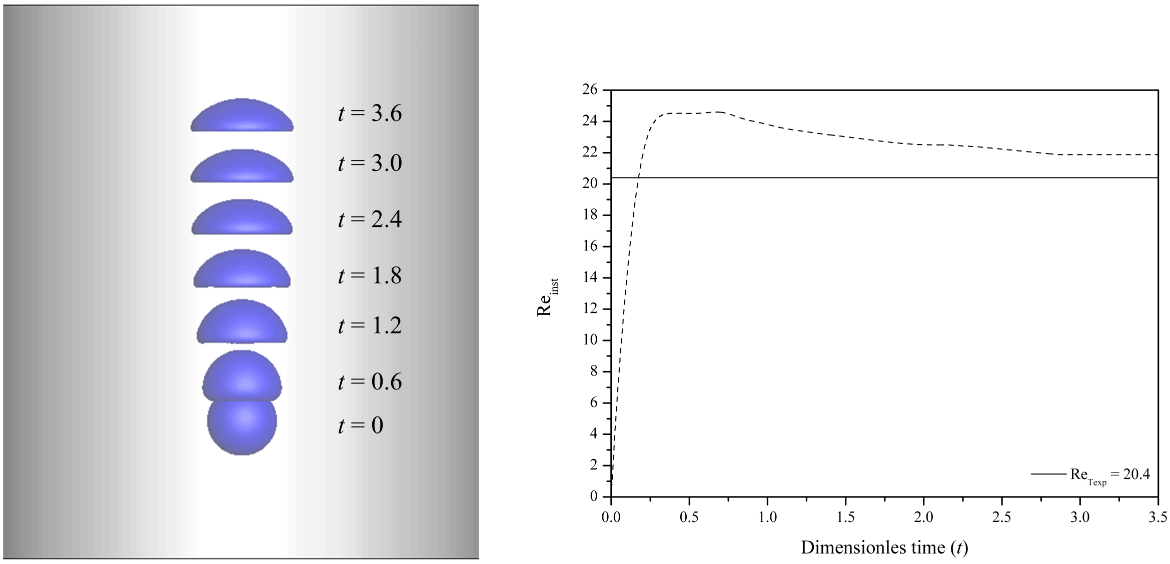

(a) (b)

Figure 5.27: Oblate ellipsoidal cap shape: (a) Evolution of the terminal bubble shape and (b) the Re_{inst} versus the dimensionless time.

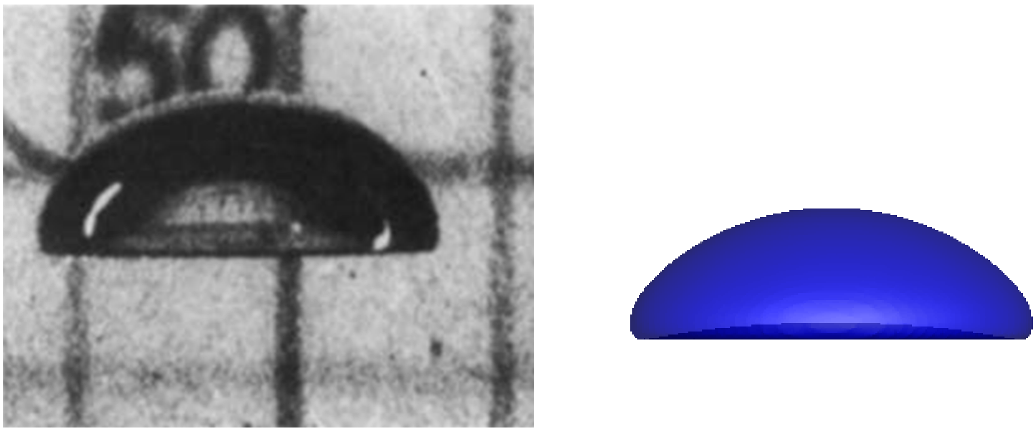

(a) (b)

Figure 5.28: (a) Comparison of the experimental terminal bubble shape according to the work of Bhaga and Weber (1981) with the numerical predicted bubble shape (b).

5.4.1.7 Comparison of drag coefficients

In this section, an attempt was made to compare the numerical results for the computation of drag coefficient with the obtained correlation from the experimental study of Bhaga and Weber (1981):

$$C_D = [(2.67)^{0.9} + (16/Re)^{0.9}]^{1/0.9} \tag{5.9}$$

For Morton numbers more than $4 \cdot 10^{-3}$ the above correlation behaves very well for high-Mo liquids and is dependent only from the Reynolds number. The Reynolds number in our study is the simulated terminal Reynolds number which is obtained from the numerical simulation. The selected parameters for the present numerical simulations are $D_p^* = 7$, $L_p^* = 10$, $Eo = 10$, $\frac{\rho_l}{\rho_g} = 1000$, $\frac{\mu_l}{\mu_g} = 100$ and $Mo = 5.48 \cdot 10^{-3}$, 0.01 and 0.1. A grid of 476x350x350 with resolution of 0.003 was selected for the simulations.

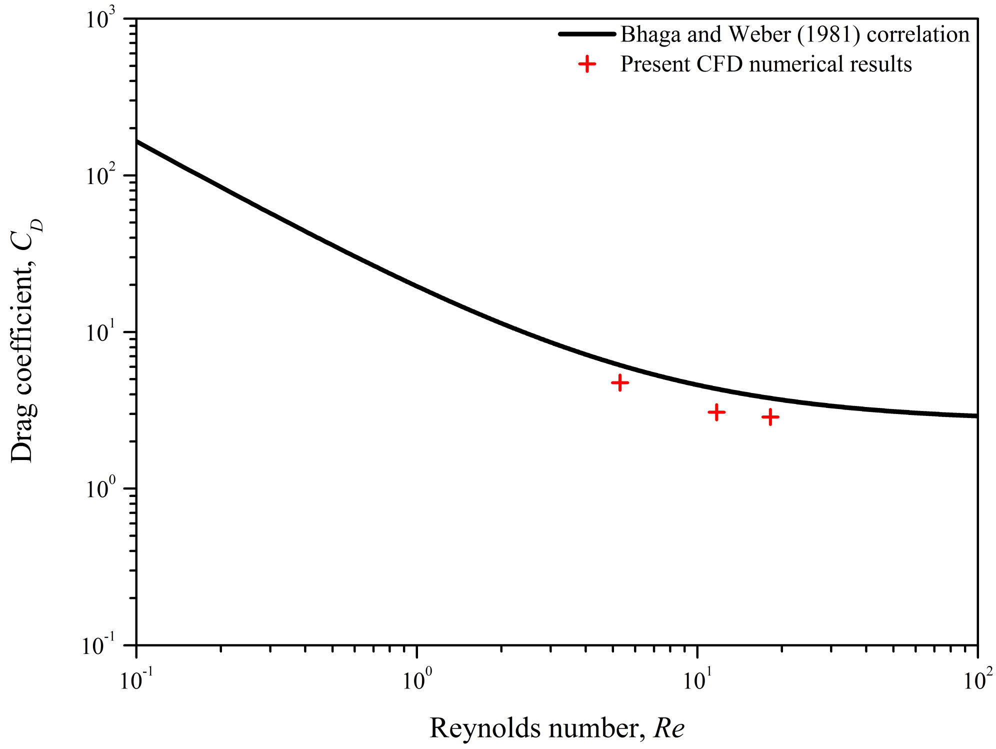

Figure 5.29: Comparison of the numerical results for the relationship drag coefficient vs. Reynolds number with the correlation of Bhaga and Weber (1981).

Figure 5.29 presents the computed drag coefficients as a function of the Reynolds number according to the equation (5.9) and the computed drag coefficients from the numerical results according to equation (5.6).

The numerical predictions present small deviation from the correlation of Bhaga and Weber (1981), especially for $Re > 10$. Small deviation is also seen for the numerical predictions of Yu and Fan (2008) and Chakraborty et al. (2013), at $Re > 10$. In the study of Chakraborty et al. (2013), it is mentioned that the small deviation may be explained by the the loss of the axisymmetric behaviour of the flow. This claim is also supported by the work of Frank et al. (2006) using Lattice Boltzmann technique, who concluded that the axisymmetric condition is not valid for values of $Re > 1.8$.

In this study, this claim is no longer valid due to the adopted full 3-D simulations. However, the small deviation of the current results may be explained by the numerical error of the method obtained by the second order discretisation in space and first order in time, as well as for the need of a finer grid.

5.4.2 Bubble coalescence

Another classical problem for testing the proposed numerical method is the coalescence of two rising bubbles in a pipe. Two identical bubbles with $d_e = \frac{D_p}{7}$ and a desired distance between their centers equal to 1.5 d_e were selected. A computational domain with dimensions 12.6 d_e x 7 d_e x 7 d_e and a grid of 514x300x300 were adopted for the present simulation. The selected parameters for the simulation are $Eo = 16$, $Mo = 2 \cdot 10^{-4}$, $\frac{\rho_l}{\rho_g} = 1000$ and $\frac{\mu_l}{\mu_g} = 100$.

The numerical results were compared with the experimental data of Brereton and Korotney (1991), presenting good agreement. Particularly, for the case of $t = 1.05$ the deformation shape of the trailing bubble agrees very well with the experimental evolution photograph (4) of the bubble coalescence from the work of Brereton and Korotney (1991). The trailing bubble accelerates due to its entrance in the wake of the leading bubble. As a result, the trailing bubble will merge with the leading bubble, as shown in Figure 5.30. The terminal shape of the leading bubble is oblate ellipsoidal disk, according to the work of Bhaga and Weber (1981).

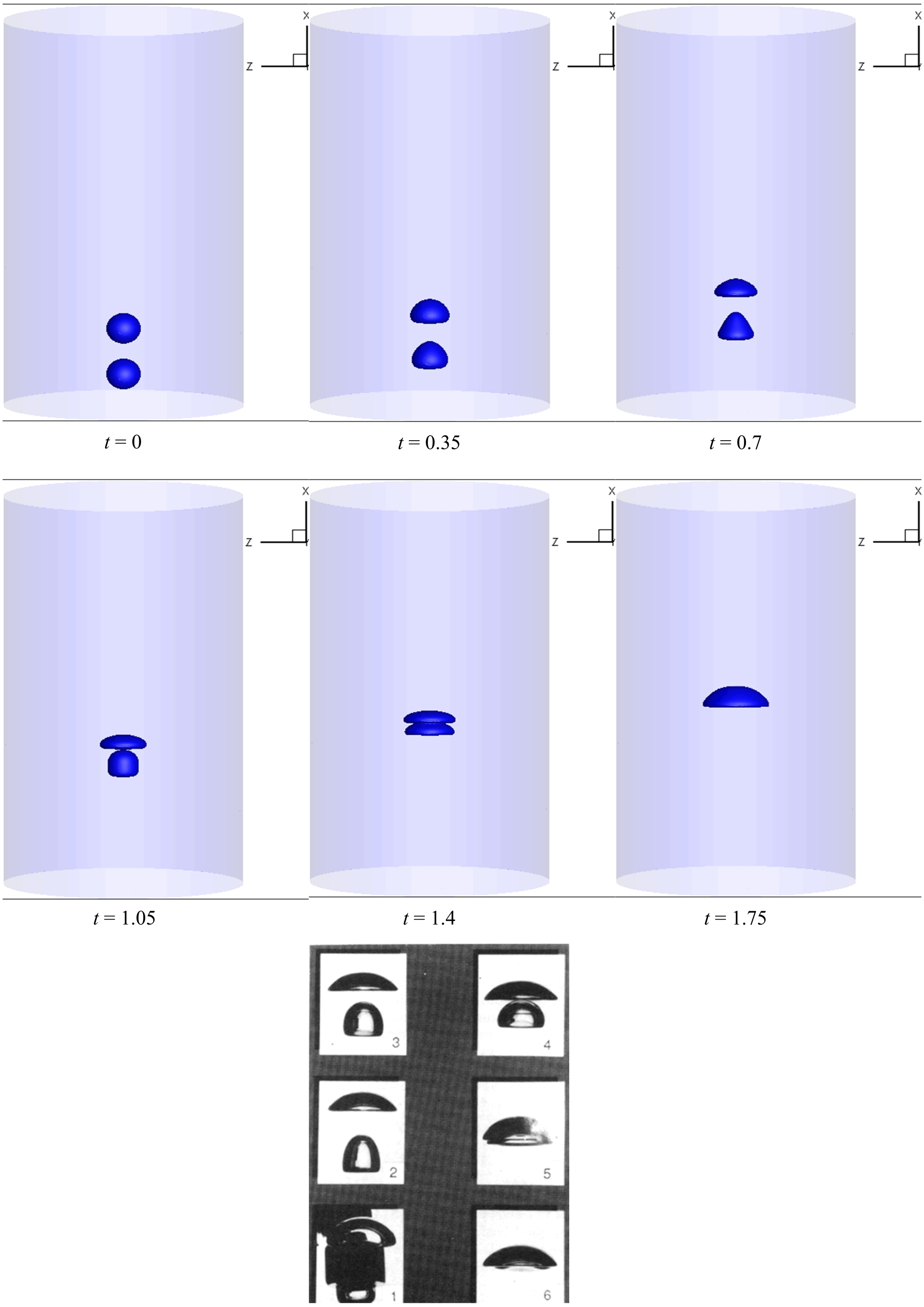

Figure 5.30: Evolution of the present bubble coalescence simulation and comparison with the experimental photograph of Brereton and Korotney (1991).

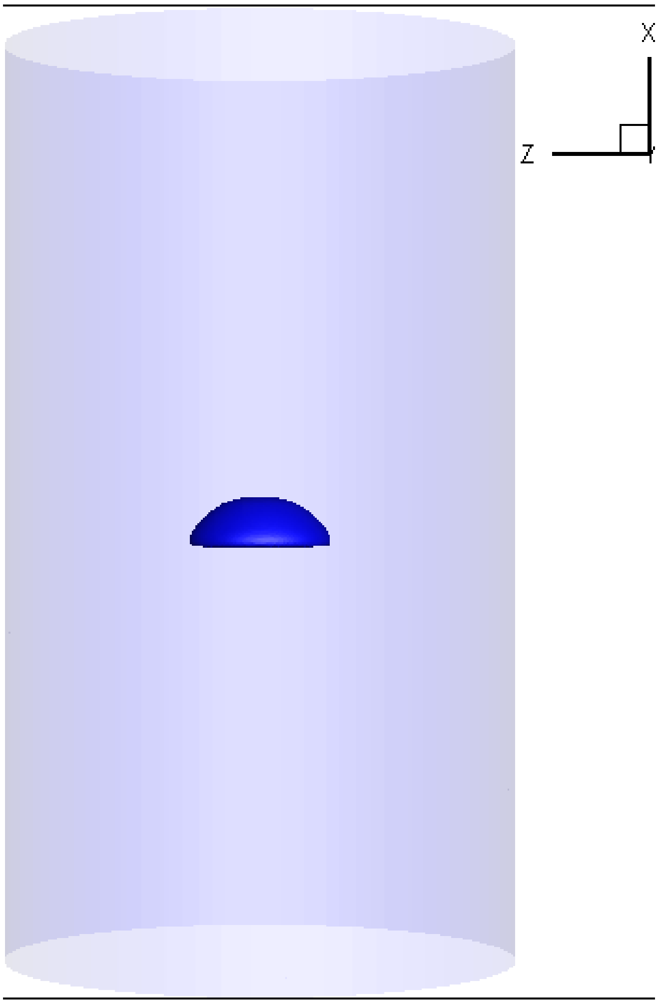

Figure 5.31: Enlarged view (zoom) for the last snapshot at $t = 1.75$.

Figure 5.31 depicts an enlarged view for the last snapshot at which the bubbles merge. It is observed that the bubbles have almost merged but a very small part at the bottom still exist. This observation also exists in photograph six of Figure 5.30 and indicates a good capture of the phenomenon from the present numerical simulation.

Similar simulations have been performed by Van Sint Annaland et al. (2005) with VOF, Yu and Fan (2008) with LS and Chakraborty et al. (2013) with CLSVOF. The numerical studies of Van Sint Annaland et al. (2005) and Yu and Fan (2008) investigated the problem with three-dimensional simulations, while the work of Chakraborty et al. (2013) examined only axisymmetric simulations. In addition, the selected ratios of viscosity and density were equal to 100 and 100, respectively.

It should be noted that interface capturing methods such as the boundary integral and front tracking methods cannot capture the topological change without numerical "treatment" (Sussman and Smereka, 1997; Hua et al., 2008).

5.5 Chapter summary

The purpose of this Chapter is to validate the developed IB algorithms and test the performance of the integrated numerical method for different problems.

Two different IB algorithms based on the penalty technique and ghost-cell technique were validated against analytical solutions, regarding the velocity profile, for the cases of single- and two-phase Poiseuille flow. Both algorithms presented good agreement with the analytical solutions, but the superiority of GCIBM algorithm compared to the IBM algorithm based on the penalty technique is undoubtedly.

A large number of numerical simulations were performed for investigating the performance of the proposed numerical method for classical two-phase flows such as single rising bubbles, toroidal bubbles and bubble coalescence. In the first case, four different bubble regimes were selected from the classical flow regime map of Bhaga and Weber (1981). The numerical predictions were found to be in a good agreement with available experimental data from the work of Bhaga and Weber (1981).

Last but not least, the code was tested for simulating the coalescence of two rising bubbles in a pipe. The numerical results obtained were compared against experimental data from the work of Brereton and Korotney (1991), presenting very good agreement.

Additional effort was also devoted to investigate the performance of the numerical method, regarding the mass conservation, as well as the presence of parasitic or spurious currents and their dependency with the interface thickness.

Chapter 6

Lateral wall effects on a 3-D single rising bubble in viscous liquid

6.1 Introduction

The objective of the present section is to investigate the three-dimensional cylindrical wall effects on a buoyancy single rising bubble in stagnant liquids. Cylindrical wall effects are present in many two-phase industrial applications (e.g. fluid transport in pipelines) and physiological systems (e.g. blood vessels and veins). Three different bubble regimes were considered in this numerical study, namely spherical, ellipsoidal and oblate-ellipsoidal cap. A parametric analysis was performed for investigating the wall effects based on the dimensionless numbers such as Reynolds number (Re), Weber number (We), Morton number (Mo), Eotvos number (Eo) and the ratios of the cylinder diameter and pipe length to the diameter of the initially spherical bubble ($L_p^* = \frac{L_p}{d_e}, D_p^* = \frac{D_p}{d_e}$). The numerical predictions were compared with available experimental data.

It is important to refer that the numerical predictions also examined the performance of the developed GCIBM method, as well as the capability of the phase-field method to capture the topological changes of the interface under the influence of the wall distances.

6.2 Literature survey

Many studies have been devoted to investigate numerically and experimentally the interfacial mechanics of bubbles due to the particular interest in oil and gas extraction, nuclear reactor design, and gas embolism. Uno and Kintner (1956) performed experiments to study the cylindrical wall effects on the rate of rise of single air bubbles. Four different quiescent liquids, namely distilled water, 61% glycerine, diethel glycol, and a solution of a surface-active agent, along with different sizes of vertical tubes were examined. A correlation for the bubble terminal velocity was also proposed as function of the tube size.

Harmathy (1960) investigated the terminal velocity of large bubbles and drops for $Re = 500$ under wall effects. He also proposed empirical and semi-empirical formulas for the terminal velocity of solid spheres in restricted media.

Coutanceau and Thizon (1981) investigated theoretically and experimentally the cylindrical wall effects on the rise of a single bubble for creeping flow. They concluded that the cylindrical wall effects have major impact on the terminal velocity much sooner than the bubble shape. As a result, they observed for a spherical bubble a measured 39% decrease in velocity than the velocity under unbounded medium conditions.

Krishna et al. (1999) conducted a large number of experiments for the investigation of the cylindrical wall effects on the rise velocity of a single bubble in water. They collected measurements for different bubble diameters in a range of $d_b = 3 - 80$mm and different cylindrical column diameters, $D_T = 0.01$, 0.02, 0.03, 0.051, 0.1, 0.174 and 0.63 m. They found that for $\frac{d_b}{D_T} < 0.125$ the wall effects on the rise velocity are negligible, and the bubble velocity obeys with reasonable accuracy the Mendelson (1967) equation. On the other hand for values of $\frac{d_b}{D_T} > 0.125$ the wall effects become significant and the rise velocity of the bubble decreases.

Chen et al. (1999) performed numerical simulations to investigate in a closed vertical cylinder the rise of a single bubble using a VOF method. Governing parameters of the physical problem such as the ratios of viscosity and density, Reynolds number and Bond number were investigated, regarding the bubble shape deformation, break up, joining and cusp formation. They also examined the formation of toroidal bubbles and presented results for two- and three-dimensional coordinate framework, exhibiting reasonable agreement with available experimental data.

Mukundakrishnan et al. (2007) performed axisymmetric numerical simulations for studying the wall effects on the rise of buoyant bubbles in a finite cylinder using front tracking coupled with a level contour reconstruction for the interfacial region. They investigated the influence of dimensionless parameters such as the Morton number, Eotvos number, Reynolds number and Weber number. They also determined the values of ratios $H^* = \frac{H}{d_0} = 8$ and $R^* = \frac{R}{d_0} \geq 3$ at which the rise of a single bubble is independent of any cylindrical wall effects. The numerical results were compared against available experimental data, presenting good agreement.

The present effort is to investigate the pipe wall effects for a three-dimensional single rising bubble in stagnant liquid. The combination of a GCIBM/phase-field method was implemented for first time in order to investigate the current physical problem, according to the author's knowledge. The use of GCIBM for the reconstruction of the pipe wall is characterised by simplicity compared to the use of cylindrical coordinates for full three-dimensional and two-phase flows, as well as without additional difficulties for integrating with the rest modules of the CFD code.

The current study presents numerical simulations regarding the terminal Reynolds number in the range of $20.4 \leq Re_T \leq 1850$ for three bubble regimes. The present range of terminal Reynolds number, especially for the spherical and oblate ellipsoidal bubble regimes are significantly larger compared to the work of Mukundakrishnan et al. (2007) ($0.02 \leq Re_T \leq 70$), and for much smaller value of Morton number $Mo = 2.52 \cdot 10^{-11}$ compared to the Mo = 0.01. It is also important to point out that the present simulations are fully three-dimensional in contrast to the axisymmetric simulations of Mukundakrishnan et al. (2007).

The present work is limited only for two bubble regimes at high terminal Reynolds number and $Re_T < 2000$ due to the high demand of very fine grid (diffusive-interface method (DIM)) for capturing accurately the interfacial region. Another limitation for these types of flows is the very small time step around $10^{-5} - 10^{-6}$, depending on the using numerical method. More details regarding the grid resolution issue will be discussed in the following section.

6.3 Results and discussion

In the present study, three different bubble regimes, namely spherical, oblate ellipsoidal and oblate ellipsoidal cap, were selected for investigating the cylindrical wall effects on the terminal Reynolds number and bubble shape, as well as the characteristics of the flow field regarding the motion of the bubble inside the pipe.

The ratio of the pipe length to the diameter of the initially spherical bubble is specified as $L_p^* = \dfrac{L_p}{d_e}$ and is taken equal to 10, while the ratio of the pipe diameter to the diameter of the initially spherical bubble is defined as $D_p^* = \dfrac{D_p}{d_e}$ and takes the following values 1.2, 1.6, 2, 2.5, 3, 3.5, 4 and 5. The value of d_e is taken to be equal to 0.14286.

The selection of the appropriate values for the ratio of pipe length is based on the previous analysis which performed in Section 5.4.1.1. The values of the dimensionless parameters Morton number (Mo), Eotvos number Eo and experimental terminal Reynolds number ($Re_{T_{exp}}$) considered, with reference to the three bubble regimes, were selected for infinite medium conditions. The density and viscosity ratio for the current simulations are $\frac{\rho_l}{\rho_g} = 1000$ and $\frac{\mu_l}{\mu_g} = 100$, respectively.

Table 6.1 presents the values of the dimensionless parameters Eo, Mo and $Re_{T_{exp}}$ for the three selected bubble regimes. In the present simulations, the grid resolution was selected to be equal to 0.003. The values of the $Re_{T_{exp}}$ were adopted from the regime maps of Bhaga and Weber (1981), Grace (1973) and Clift et al. (1978). The values of Mo number for spherical and oblate ellipsoidal bubble regimes represent air-water properties.

These two cases are real challenge for the present numerical method and for many others in the literature (e.g. L-S, Front-tracking) due to the high demand for very fine grid resolution. According to Bonometti and Magnaudet (2007) a minimum number of 100 grid points per bubble diameter is required, while Magnaudet and Mougin (2007) claim a minimum requirement of five cells within the boundary layer for $Re_T > 2 \cdot 10^3$, which means the grid spacing should be less than 0.01 times the equivalent of bubble radius. Similar studies regarding the investigation of a single rising air bubble in water for infinite medium conditions have proposed different number of cells per bubble diameter, for instance, 20 cells per bubble diameter with $\Delta h = 0.0125$ using front tracking method by Dijkhuizen et al. (2005), 20 cells per bubble diameter with $\Delta h = 0.001$ using front tracking method by Van Sint Annaland et al. (2006) and 20 cells per bubble diameter with $\Delta h = 0.05$ using a 3-D Level-Set method by Yu and Fan (2008). Very accurate simulations for air-water system have been performed by Hua et al. (2008) using the 3-D front tracking method along with an adaptive, unstructured triangular mesh. An improved version of 3-D front tracking method was also presented by Dijkhuizen et al. (2010) with better performance in volume conservation and circumvent problems with surface tension, as well as with high accuracy for small bubble diameters ($d_e = 0.001$, 20 cells/bubble).

In this study, 62 cells per bubble diameter were selected with a grid spacing $\Delta h = 0.0023$. This is the best resolution which could be achieved according to the available computer sources and the domain size.

Table 6.1: Parameters for the considered bubble regimes.

Shape	Eo	Mo	$Re_{T_{exp}}$
Spherical	0.3	$2.52 \cdot 10^{-11}$	570
Oblate ellipsoidal	10	$2.52 \cdot 10^{-11}$	1950
Oblate ellipsoidal cap	116	1.31	20.4

6.3.1 Validation of the model

In this section, we consider a validation case for the cylindrical wall effects on the rise of a single air bubble in water for different pipe diameters, according to the experimental data of Krishna et al. (1999). The corresponding parameters for the numerical simulation of air-water system are $Mo = 2.6 \cdot 10^{-11}$ and $Eo = 11$, while the values of D_p^* are in the range $2 \leq D_p^* \leq 3.34$, according to Mukundakrishnan et al. (2007). The present numerical predictions were compared with their numerical results and the corresponding experimental data of Krishna et al. (1999).

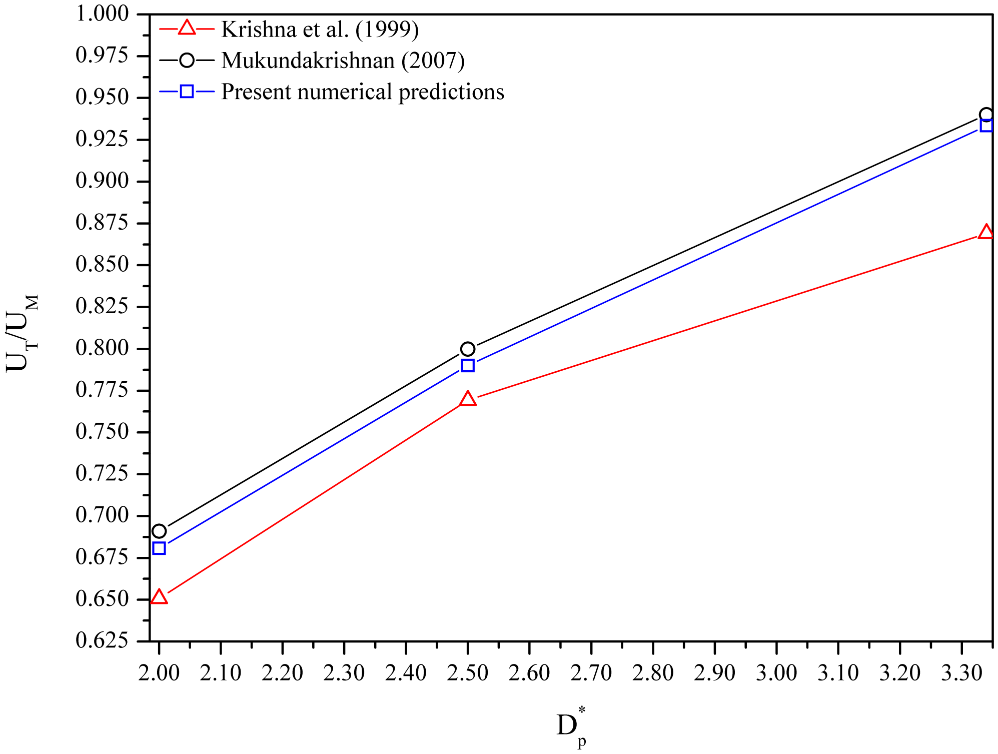

Figure 6.1: Comparison of the present numerical predictions with the available experimental and numerical data from the works of Krishna et al. (1999) and Mukundakrishnan et al. (2007).

Figure 6.1 depicts the present numerical predictions of terminal velocities for air bubble in water along with the available experimental and numerical data of Krishna et al. (1999) and Mukundakrishnan et al. (2007). On the y-axis, we show the ratio of terminal bubble velocity to the velocity by Mendelson (1967) equation:

$$U_M = \sqrt{\frac{2\sigma}{\rho_l d_e} + \frac{g d_e}{2}} \tag{6.1}$$

where σ is the surface tension ($= 0.072\, N/m$), ρ_l is the density of liquid ($= 1000\, kg/m^3$, g is the gravitational constant ($= 9.81\, m/s^2$) and d_e is the bubble diameter. On the x-axis, it is located the ratio of the pipe diameter to the diameter of the initially spherical bubble.

From Figure 6.1, it is also shown that the present numerical predictions display a small variation (around 2%) for the three different dimensionless diameters compared to the numerical data of Mukundakrishnan et al. (2007) and approximately 7% with the experimental data of Krishna et al. (1999). This discrepancy between the experimental data and the present numerical predictions is mainly due to the inadequate grid resolution, as well as the fact that the experimental measurements were collected from very long open cylinders.

The difference between the present numerical predictions and the numerical data of Mukundakrishnan et al. (2007) can be explained by the different adopted numerical methods for the interface simulation and grid resolution, numerical error, as well as on the difference between axisymmetric and three-dimensional simulations.

6.3.2 Bubble simulations

Figure 6.2 illustrates the simulated terminal Reynolds number ($Re_{T_{sim}}$) and the corresponding bubble terminal shapes at $D_p^* = 1.2$, 1.6, 2, 2.5, 3, 3.5, 4 and 5, for various dimensionless wall diameters and three bubble regimes. It is observed that the simulated $Re_{T_{sim}}$ increases gradually with the increase of the wall diameter. It is also important to mention that the bubble terminal shapes at $D_p^* = 5$ are almost identical with the bubble shapes for the infinite medium conditions, according to the works of Yu and Fan (2008) and Bhaga and Weber (1981). On the other hand, the author is not aware for experimental data regarding terminal bubble shapes under lateral wall effects for comparison with the present cases (e.g.$D_p^* < 5$) .

The inertial forces are lower than viscous forces for small pipe diameters and are getting higher for large pipe diameters, as shown in Figure 6.2. After a certain point, the wall distance has only a minimum effect to the value of $Re_{T_{sim}}$ (infinite medium conditions, $D_p^* \geq 6$) and as a result a terminal Reynolds number is obtained.

In the case of spherical regime and $D_p^* = 5$, the bubble deformation is almost negligible, maintaining a spherical shape similar to the terminal bubble shape for infinite medium conditions. The computed values for $Re_{T_{sim}}$ and $We_{T_{sim}}$ were found to be equal to 331.87 and 1.00, respectively. For $1.2 < D_p^* < 5$, a very small shape deformation of bubble takes place on the top surface of the bubble, especially for $D_p^* = 1.2$, while for the rest selected $D_p^* = 2$, 3 and 5 the shape deformation is indistinguishable. The slight deformation for $D_p^* = 1.2$ is located on the top surface of the bubble.

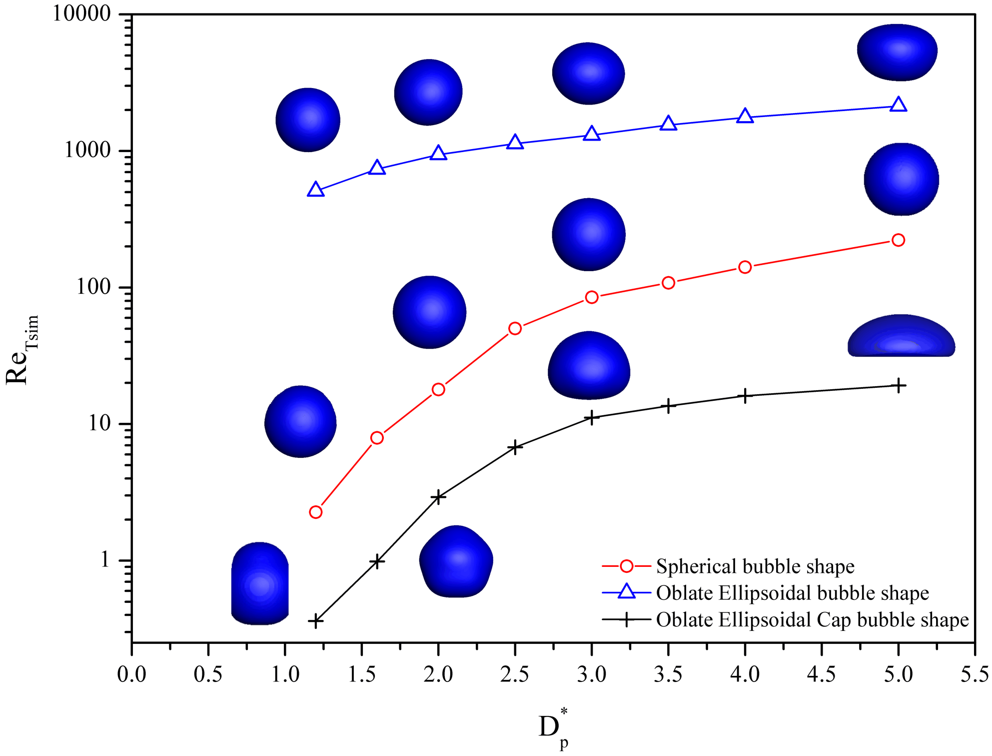

Figure 6.2: Values of the simulated terminal Reynolds number for various dimensionless pipe diameters (D_p^*).

It is also observed that the $Re_{T_{sim}}$ decreases from 331.87 ($D_p^* = 5$) to 2.26 ($D_p^* = 1.2$). The largest decrease rate occurs for $D_p^* < 2.5$. The $We_{T_{sim}}$ also decreases from 1.00 to $4.7 \cdot 10^{-5}$ with decreasing the wall distance from $D_p^* = 5$ to 1.2 on the bubble, as shown in Figures 6.3 and 6.4.

For the ellipsoidal regime and $D_p^* = 5$, the bubble maintains an oblate ellipsoidal shape identical to the terminal bubble shape for infinite medium conditions, while for $1.2 < D_p^* < 3$ the $Re_{T_{sim}}$ presents a further decrease from 1261.62 at $D_p^* = 3$ to 220 at D_p^*

= 1.2, as shown in Figure 6.2. The deformation of the bubble shape maintains almost a spherical shape with a slight flatten in the radial direction. For $D_p^* < 3$, the bubble shape is almost spherical while the $Re_{T_{sim}}$ is decreased gradually.

It should be noted that the bubble in the present case belongs to the ellipsoidal regime according to the classification of Grace (1973), while in Clift et al. (1978)'s diagram belongs to the wobbling regime. Thus, the bubble is characterised by oscillations during its motion in the liquid.

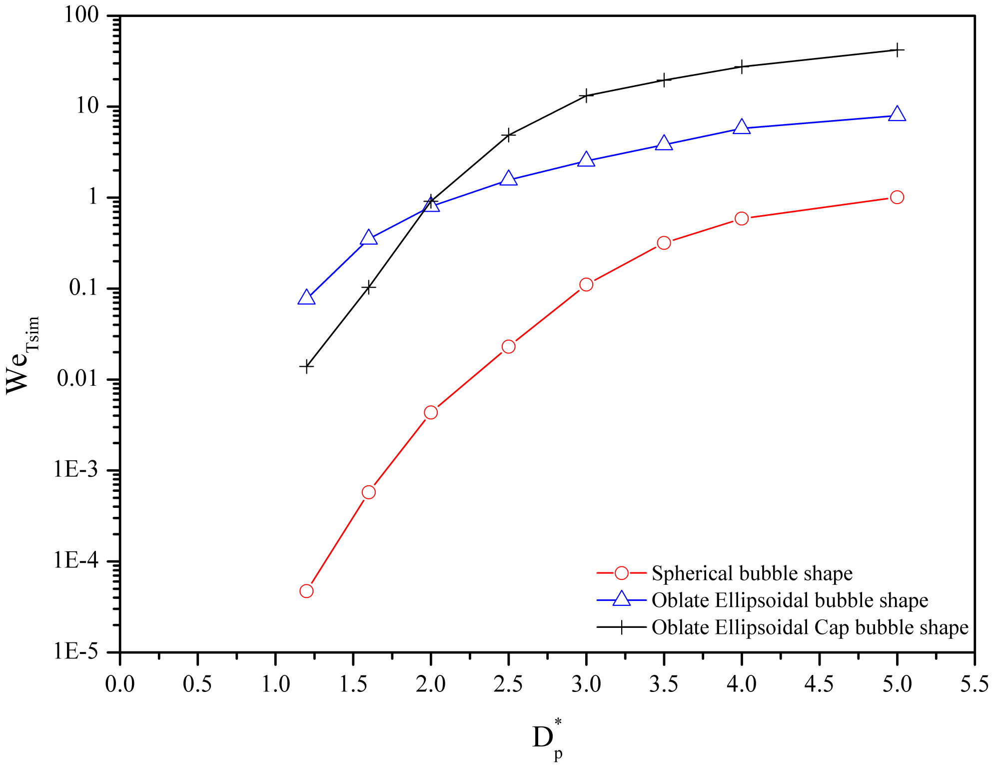

Figure 6.3: Values of the simulated terminal Weber number for various D_p^*.

The $We_{T_{sim}}$ number is characterised by similar behaviour to $Re_{T_{sim}}$ regarding the distance from the pipe wall. In Figure 6.4, it is depicted that the $We_{T_{sim}}$ decreases with small wall diameters (inertial forces lower than surface tension forces) and increases with large wall diameters (inertial forces higher than surface tension forces). As a result, the bubble rising velocity is reduced significantly due to the increase of the drag force with decreasing D_p^*. The final ellipsoidal shape depends on the combined effects of inertial, surface tension and hydrostatic forces for the shape and size characteristics of bubble, such as flattening, elongating and spherical shape. The inertial forces have effect on the flattening, while the bubble elongation is affected by the hydrostatic force. The conservation of the spherical shape (top of the bubble) based on the tension forces (Mukundakrishnan et al., 2007).

In the case of oblate ellipsoidal cap bubble shape and $D_p^* = 5$, the obtained bubble shape holds the same ellipsoidal cap shape with an indentation at the bottom of the bubble (shadowed part, Figure 6.2), as occurs for infinite medium conditions. The computed $Re_{T_{sim}}$ and $We_{T_{sim}}$ are equal to 19.92 and 42.17, respectively. At $D_p^* = 2$, the bubble shape is deformable on the top surface at $Re_{T_{sim}} = 2.93$ and $We_{T_{sim}} = 0.91$, while for $D_p^* = 3$ the bubble shape is nearly spherical, presenting an indentation at the rear of the bubble (shadowed part) at $Re_{T_{sim}} = 11.15$ and $We_{T_{sim}}$ =13.22 .

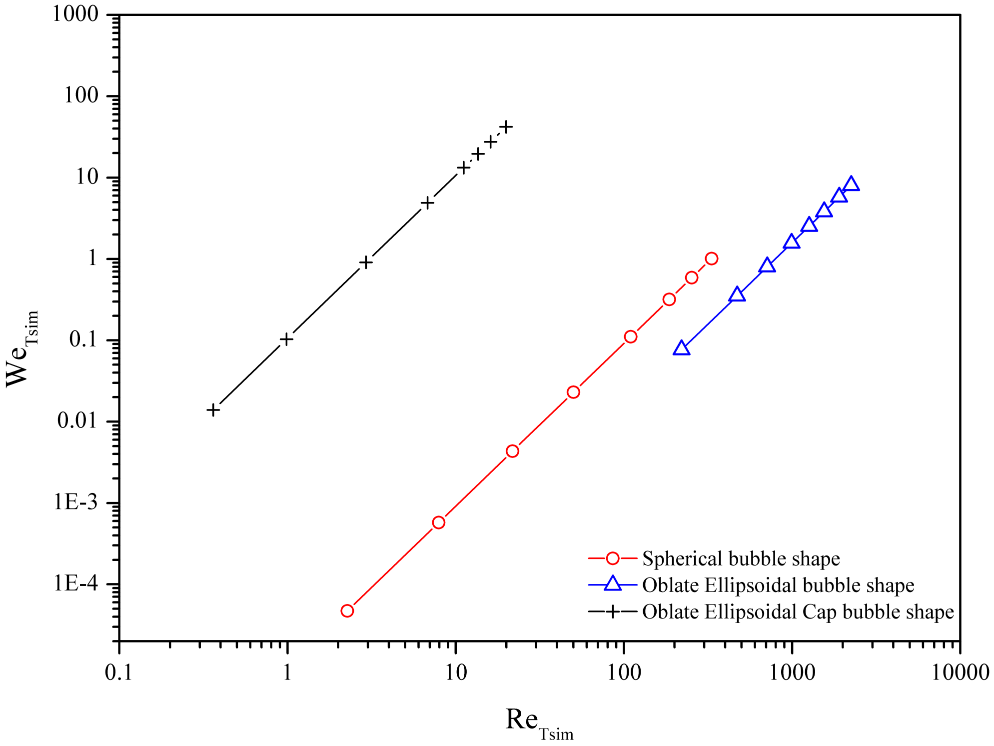

Figure 6.4: Values of the simulated terminal Reynolds number vs. the simulated Weber number.

On the other hand, at $D_p^* = 1.2$ the wall effects are significant and the bubble achieves an elongated cylindrical shape. The simulated $Re_{T_{sim}}$ and $We_{T_{sim}}$ were found to be equal to 0.36 and 0.014, respectively, as shown in Figures 6.2-6.4. The low Weber number is an indication of the surface tension forces dominance compared to the inertial forces.

6.3.3 Terminal velocities and drag coefficients

Figure 6.5 presents the dimensionless terminal velocities (U_T/U_∞) as a function of the dimensionless ratio D_p^*. It can be seen that the values of the U_T/U_∞ at $D_p^* = 1.2$ correspond to spherical, oblate ellipsoidal and oblate ellipsoidal cap, were found to be approximately equal to 0.013, 0.178 and 0.032.

At D_p^*=5, the corresponding U_T/U_∞ for the selected bubble regimes are 0.91 (spherical bubble), 0.89 (oblate ellipsoidal or wobbling bubble) and 0.84 (oblate ellipsoidal cap bubble). It is also observed that the increase in the pipe diameters displays larger values for U_T/U_∞, up to a certain point (D_p^*=5).

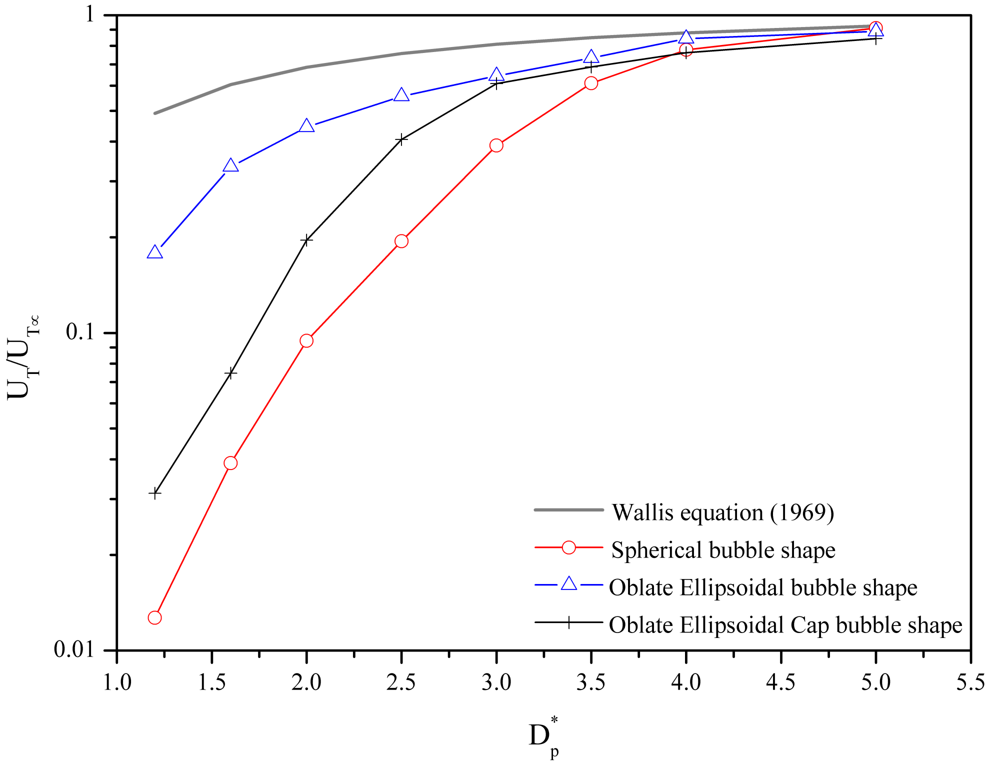

Figure 6.5: Values of the dimensionless terminal bubble velocity for various D_p^*.

At $D_p^* > 5$, the values of U_T/U_∞, increase with very small rate until to achieve the infinite medium velocities. Finally, it can be seen from Figure 6.5 that the U_T/U_∞ presents the largest decrease at $D_p^* < 2.5$ for all the selected bubble regimes, at which the wall effects are significant.

The present simulated terminal velocities were compared with the empirical equation of Wallis (1969):

$$\frac{U_T}{U_\infty} = 1.13\, e^{-\lambda} \tag{6.2}$$

where $\lambda = \frac{1}{D_p^*}$. This correlation is valid for low Morton and high Reynolds systems. For $\lambda \geq 0.125$ the lateral effects are negligible while the correlation is valid for values of $\lambda \leq 0.6$. It is noticed that the predicted dimensionless terminal velocity is in reasonable agreement for the spherical bubble regime at $3.5 \leq D_p^* \leq 5$. In the case of oblate ellipsoidal bubble shape, the curve follows a similar pattern compared to the correlation of Wallis (1969) with a fair agreement, up to a certain point ($D_p^* = 2.5$) .

Similar deviation exhibits the values of the dimensionless terminal velocity for the case of oblate ellipsoidal cap bubble shape. It should be noted that the value of Morton number is higher ($Mo = 1.31$) compared to the other two cases ($Mo = 2.52 \cdot 10^{-11}$), while the value of Reynolds number is small ($Re = 20.4$) which is against to the valid limits of the Wallis correlation for low Mo and high Re numbers systems. However, Bhaga's results support that Eq. 6.2 can be used down to $Re = 10$ regardless of whether skirts are being trailed (Clift et al., 1978).

Figure 6.6 depicts the computed drag coefficient C_D vs. the dimensionless pipe diameter. It is shown that the decrease in the wall distance increases the C_D, while the increase of the wall distance displays small C_D values, approaching to a point of which the C_D is close to a constant value. The values of C_D at $D_p^* = 1.2$ are 8507 (spherical shape), 173.54 (oblate ellipsoidal) and 11130 (oblate ellipsoidal cap). At $D_p^* = 5$, the values of C_D = 0.4, 1.67 and 3.67 correspond to the spherical, oblate ellipsoidal and oblate ellipsoidal cap, respectively.

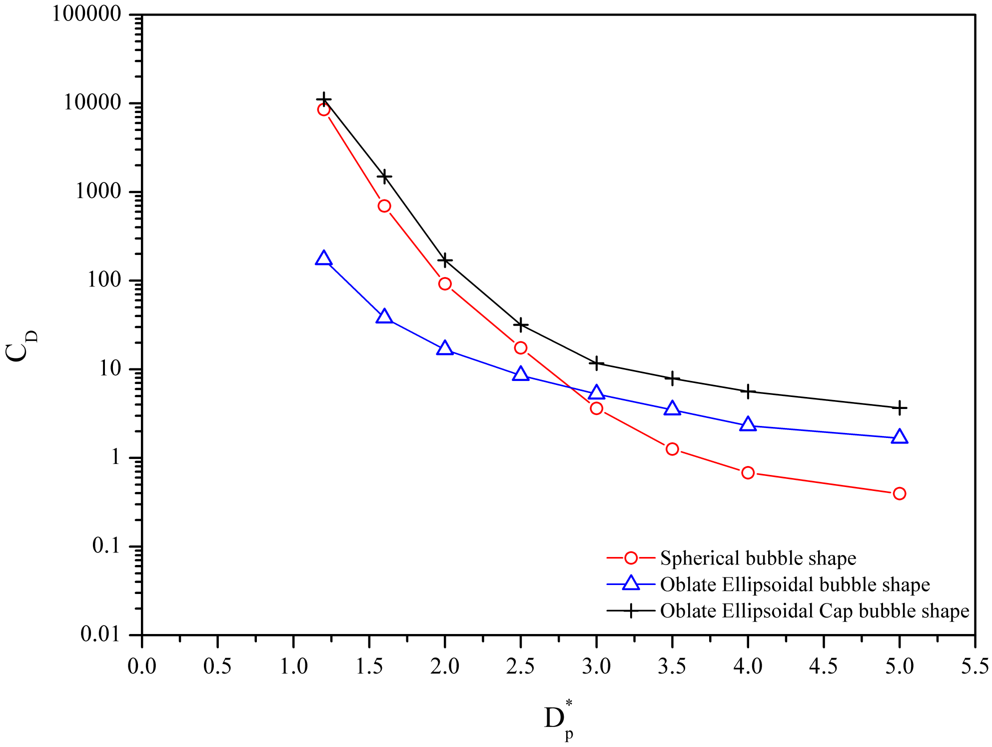

Figure 6.6: Values of the drag coefficient (C_D) for various D_p^*.

In this section, we have also investigated the characteristics of the flow fluid regarding the bubble motion and the wall effects on the bubble. It is observed that the increase of the wall effects leads to squeeze of the bubble shape in the direction of the horizontal axis of the oblate ellipsoidal bubble, as shown in Figures 6.7 (a) and (b) for $D_p^* = 1.2$ and 1.6, respectively.

On the other hand, the increase of the D_p^* leads to the weakness of the wall effects, resulting to the the dominance of the wobbling bubble shape, as shown in Figure 6.7 (h). Figures 6.7 (a)-(d) illustrate the streamlines for the oblate ellipsoidal cap and oblate ellipsoidal bubbles at terminal state and the selected $D_p^* = 2$, 3.5, 4 and 5.

For D_p^* =5, the terminal bubble shape is close to spherical cap with a small indentation at the bottom, as shown in Figure 6.7 (d). In Figure 6.7 (c), it is observed that the bubble shape at D_p^* =4 exhibits to a certain extent the reduction of the indentation at the bottom, while a very small elongation occurs in the axial direction. At $D_p^* = 3.5$ (Figure 6.7 (b)), the bubble shape maintains a similar behaviour as in Figure 6.7 (c), however, a small flattening takes place at the rear of the bubble.

For D_p^* =2, the bubble shape is more elongated, while the bottom of the bubble is getting flatten, as shown in Figure 6.7 (a). All the Figures 6.7 (a)-(d) depict recirculation effects at the rear of the bubble and the vorticity strength varies from the large to small wall distances on the bubble.

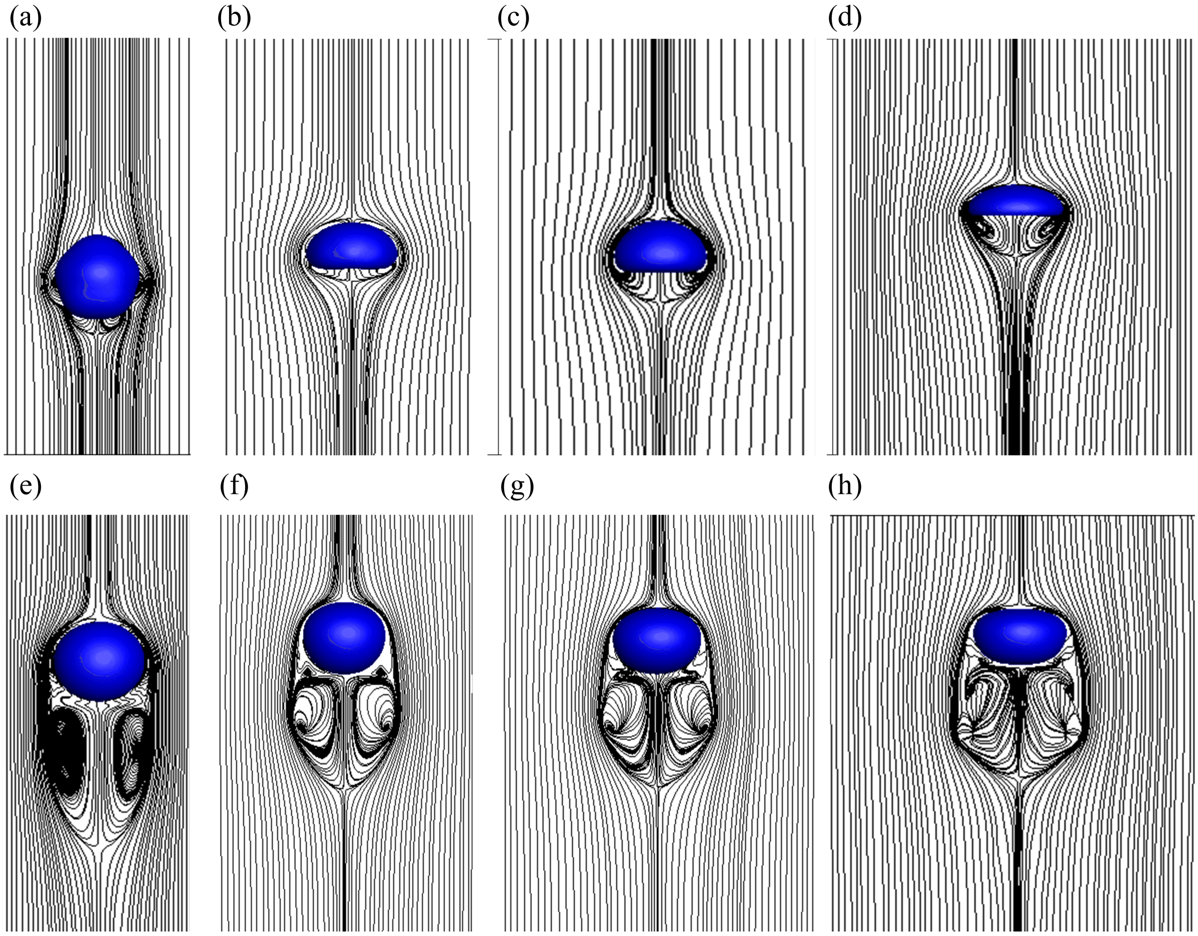

Figure 6.7: Streamlines for oblate ellipsoidal cap regime at (a) D_p^*=2, (b) D_p^*=3.5, (c) D_p^*=4, (d) D_p^*=5 and for oblate ellipsoidal or wobbling regime at (e) D_p^*=2, (f) D_p^*=3.5, (g) D_p^*=4 and (h) D_p^*=5 .

Figures 6.7 (e)-(h) present the streamlines for the oblate ellipsoidal bubble regime. It is seen that the bubble shape becomes almost spherical (Figure 6.7 (e)) and is accompanied with an asymmetry on the right top side surface due to the rectilinear motion of the bubble. Further reduction of D_p^* at 1.6 and 1.2 results in a very small elongation in the axial direction (see Figure 6.2). On the other hand, the increase of D_p^* follows a more ellipsoidal shape for the bubble, as shown in Figure 6.7 (e)-(h).

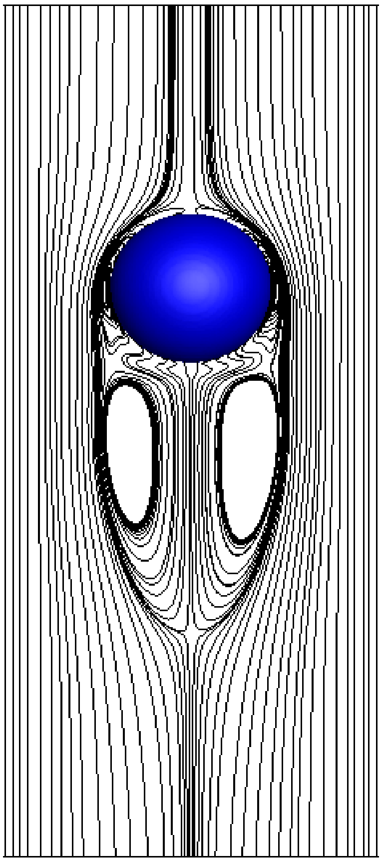

Figure 6.8: Further zooming for case (e) from Figure 6.7.

Similar to the oblate ellipsoidal cap regime, the presence of vortices at the rear of the bubble was also observed for the oblate ellipsoidal regime, as shown in Figure 6.7 (e)-(h). In our case, an important difference between the oblate ellipsoidal cap and oblate ellipsoidal or wobbling bubble shapes is the presence of small left-right asymmetries due to the high Reynolds number ($Re = 1950$ for infinite medium conditions) (see Figure 6.7 (e)-(h)). According to Magnaudet and Mougin (2007) bubbles at large Reynolds number may exhibit path instability, resulting in a helical or zig-zag path. The critical Re number for this phenomenon without the presence of wall effects was found to be just above 200.

In the present study, small asymmetries exist between the two vortices for different pipe diameters in Figure 6.7 (e)-(h) and more detailed (zoom) is shown in Figure 6.8.

This occurs due to the oscillations of the bubble motion and their effect shorten with increasing the lateral wall effects. Sometime these oscillations may be so violent and lead eventually simulation to stop, in particular for the 3-D Front Tracking method without numerical treatment for bubble break up. The reason for that is the very fast deformation rate of the surface grid (Dijkhuizen et al., 2005). However, these problems are not present in VOF method and the current phase-field method, as well as in recent versions of the Front Tracking method (Hua et al., 2008; Dijkhuizen et al., 2010) which incorporate numerical "treatment" for capturing the topological change (Sussman and Smereka, 1997; Hua et al., 2008).

6.3.4 Bubble shape deformation regimes

Figure 6.9 presents the contours for the oblate ellipsoidal bubble at terminal state for $D_p^* = 1.2$, 1.6, 2, 2.5, 3, 3.5, 4 and 5. Similar maps for different bubble regimes have also been provided by Mukundakrishnan et al. (2007) and Clift et al. (1978). These regime maps provide useful information for the bubble shape deformation on the lateral wall effects.

In Figure 6.9, each graph depicts the relationship of terminal Reynolds number and the Eotvos number, as well as the bubble shape for the three selected bubble regimes. Due to the lack of data for the bubble shape for small values of D_p^*, it was selected to compare the current data for $D_p^* = 5$ (Figure 6.9h). The lateral wall effects at $D_p^* = 5$ are very small and can be compared with the terminal bubble shapes for infinite medium conditions.

The terminal bubble shape for the oblate ellipsoidal cap is similar to the experimental terminal bubble shape from the work of Bhaga and Weber (1981) (see Section 5.4.1.6, pg. 113, Fig. 5.31a). In the case of oblate ellipsoidal bubble, the terminal shape was compared to the terminal shapes from the numerical studies of Dijkhuizen et al. (2005) (see Section 5, pg. 6172, Fig. 3), Yu and Fan (2008) (see pg. 273, Fig. 8b) and Hua et al. (2008) (see Section 3.4, pg. 3376, Fig. 15), presenting good agreement. The numerical predictions for the spherical bubble regime again were compared to the terminal bubble shapes from the work of Hua et al. (2008) (see Section 3.4, pg. 3376, Fig. 15), exhibiting very good agreement.

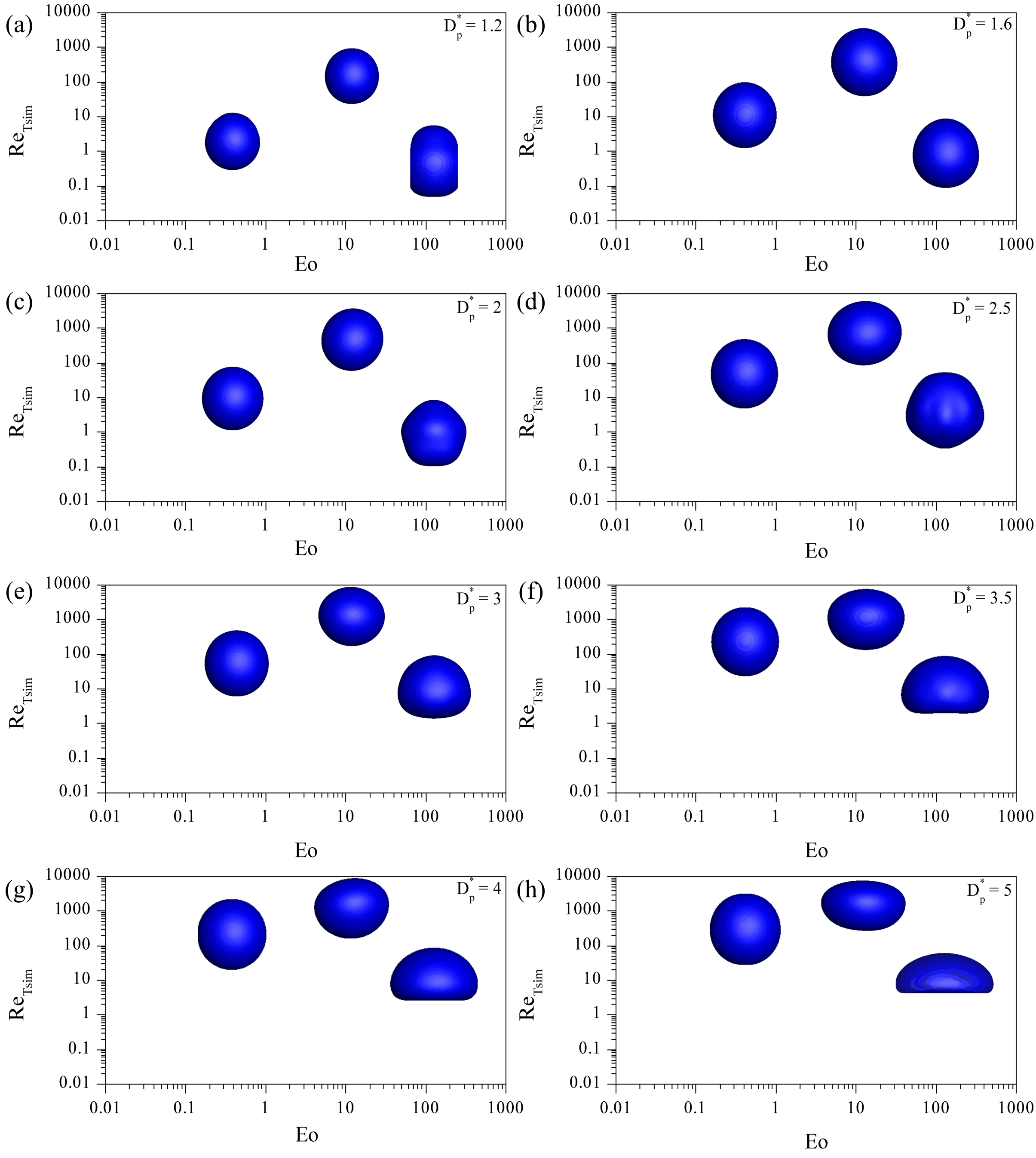

Figure 6.9: Bubble shape regimes for $D_p^* = 1.2$, 1.6, 2, 2.5, 3, 3.5, 4 and 5.

6.4 Chapter summary

In this Chapter, an attempt was made to investigate the wall effects on the rise of a three-dimensional bubble by means of a phase-field method combined with a GCIBM for the reconstruction of the pipe wall.

Three different bubble regimes (spherical, oblate ellipsoidal or wobbling and oblate ellipsoidal cap) and various ratios of the pipe diameter ($D_p^* = 1.2$, 1.6, 2, 2.5, 3, 3.5, 4 and 5). In the present study, a parametric analysis was performed based on the dimensionless number Re, We, Mo and Eo. The flow field was also investigated and illustrated for the aforementioned bubble regimes, as well as bubble regime maps with reference to the relationship of $Re_{T_{sim}}$ and Eo numbers.

The proposed numerical model was validated against the available numerical and experimental data of Mukundakrishnan et al. (2007) and Krishna et al. (1999), presenting satisfactory agreement.

Chapter 7

Dynamics of 3-D Taylor bubbles in viscous liquids

7.1 Introduction

The purpose of the present effort is to investigate the dynamics of three-dimensional Taylor bubbles. A Taylor bubble is characterised as a bullet shape gas or vapor with a length of several time of its diameter and a tailing edge.

The present numerical simulations are focused on the effects of Morton and Eotvos numbers, as well as on the role of density and viscosity ratios in the formation of a Taylor bubble rising in stagnant liquids. A second order ghost cell immersed boundary method combined with a phase-field method were employed for simulating the interfacial region.

7.2 Literature survey

Over the decades, many studies have been devoted to investigating the dynamics of Taylor bubbles in viscous liquids. Classical theoretical studies, such as those of Zukoski (1966), Collins et al. (1978), Bendiksen (1985) and Batchelor (1987) have contributed significantly to the understanding of the mechanisms involved in the formation of a Taylor bubble.

The motion of a Taylor bubble has also been studied experimentally by several scientists and engineers. Some representative experimental studies were performed by Campos and Carvalho (1988), Polonsky et al. (1999b), Nogueira et al. (2006b), Mandal et al. (2008), among others. Herein, the main focus is concentrated on the numerical investigation, as it was selected to be the preferable method for studying the formation of a Taylor bubble in stagnant liquids.

An early attempt to investigate numerically the dynamics of the Taylor bubbles was presented by Mao and Dukler (1990). The set of Navier-Stokes equations for axisymmetric flow, along with the appropriate boundary conditions, have been solved by means of the Finite Difference Method (FDM). A QUICKER scheme was employed to descritise the equations and the solution was obtained using an iterative algorithm for pressure-correction, namely SIMPLE (semi-implicit method for pressure-linked equations). The numerical predictions obtained for the rise velocity were compared with available experimental data, presenting excellent agreement.

Tomiyama et al. (1996) performed numerical simulations to investigate the dynamics of a Taylor bubble in a stagnant liquid using a VOF method. They investigated the effects of Eotvos and Morton numbers on the flow field of a Taylor bubble. The rise velocity and shape deformation of a Taylor bubble were predicted fairly well compared with available experimental data.

Kawaji et al. (1997) conducted axisymmetric simulations to study the flow structure of slug flow using a VOF interface tracking method. They predicted the velocity profile and shape deformation of a Taylor bubble. They concluded that the drag force is decreased as the Taylor bubble is moved laterally, which is of high importance for understanding the effects on the coalescence and acceleration of a Taylor bubble in slug flow.

Bugg et al. (1998) and Bugg and Saad (2002) presented numerical results for the motion of a Taylor bubble rising through stagnant liquids in vertical tubes. They examined the effects on the terminal velocity for different values of the Morton and Eotvos numbers, as well as for the film thickness and the average velocity in film. The numerical results obtained were compared with available experimental data, presenting satisfactory agreement.

Some years later, Son (2001) developed a numerical method for the simulation of incompressible two-phase flows using a level-set (LS) method for the interfacial region. The proposed method was implemented for simulating axisymmetric single Taylor bubble and a train of Taylor bubbles rising in vertical tubes, under the effect of periodic or open boundary conditions. The numerical results predicted fairly well the shape and rise velocity of the Taylor bubble against available data from the literature.

Anglart and Podowski (2002) investigated numerically the dynamics of Taylor bubbles rising in vertical channel using a VOF approach combined with an interface sharpening algorithm. The model was implemented in the general commercial computer program CFX 4.2. They examined the effects of flow conditions in relation to the bubble shape and rise velocity. They also conducted numerical simulations for studying the phenomenon of coalescence between two neighboring bubbles. The numerical results obtained were compared with available experimental data, presenting excellent agreement.

Ndinisa et al. (2005) used the commercial computer program CFX 5.6 from ANSYS in order to study the effects of three different numerical methods for the simulation of the interfacial region of a Taylor bubble rising , namely volume of fluid (VOF), two Euler two-fluid model and a combined model that combines the best features of both models. The two-dimensional numerical results for both methods exhibited good agreement with available experimental data from the literature.

Taha and Cui (2006) performed numerical simulations for the investigation of the dynamics of single Taylor bubbles in vertical tubes. The capturing of interface was obtained by using a VOF method. The proposed model was implemented in the general computer program FLUENT. They predicted the shape, velocity field and wall shear stress in both stagnant and flowing liquids. Numerical simulations were also presented in order to demonstrate the effect of angle of inclination and turbulence effects using a $k-\varepsilon$ model. The numerical predictions obtained were compared with available experimental data from the literature, exhibiting satisfactory agreement.

Zheng et al. (2007) presented numerical simulations for the investigation of the dynamics of slug flow and the mechanism of the slug flow induced CO_2 corrosion using a VOF approach. The examined hydrodynamic characteristics such as the bubble shape, the thickness of falling liquid film, terminal velocity, the wake length and shape, the wall shear stress and the CO_2 corrosion rate. The numerical predictions were compared against experimental data with reasonable agreement. They also found that the wall shear stress, resulting in the corrosion product scale fatigue cracking.

Lu and Prosperetti (2009) conducted axisymmetric numerical simulations for studying the hydrodynamics of Taylor bubbles in a vertical tube, by means of the Finite Volume Method (FVM). They investigated the effect of Eotvos and Morton numbers on the rising velocity of Taylor bubbles. The computational results were compared with available experimental data from the literature, presenting good agreement.

Kang et al. (2010) studied numerically the motion of a Taylor bubble rising in stagnant liquids using a front tracking method. They investigated the effects of the Reynolds number, Froude number, the Weber number, the density ratio, and the viscosity ratio on the hydrodynamics of Taylor bubble (e.g. terminal velocity, wall shear stress and wake length). They found that the effect of density and viscosity ratio is almost negligible. They also concluded that the Archimedes number affects the Taylor bubble shape, terminal velocity, wall shear stress and the thickness of thin liquid film.

Recently, Ramdin and Henkes (2012) performed 2-D and 3-D numerical simulation using a VOF method in the commercial CFD code (FLUENT). They investigated the dynamics of Benjamin and Taylor bubbles which belong to the slug flow regime. The numerical results were compared with the available experimental and analytical data, exhibiting very good agreement.

Unlike the most previous efforts which mainly limited in axisymmetric simulations using VOF and Front Tracking methods for capturing the interface, the present study investigates for first time fully three-dimensional Taylor bubbles rising in stagnant liquids, by using a GCIBM with a phase-field method with large density ratio (e.g. $\frac{\rho_l}{\rho_g} = 1000$). The present method is characterised by superiority for handling the topology changes and omits the ambiguous gas-liquid interface reconstruction in VOF (Kang et al., 2010) or the numerical "treatment" of Front Tracking method for handling topological changes (Sussman and Smereka, 1997; Hua et al., 2008).

A parametric analysis was performed for different properties of fluids and dimensionless parameters relevant to the problem (e.g. Eo, Mo, Re_B) in order to study the gas entrainment at tail and its relation to maximum Taylor bubble sizes, as well as the effects on the terminal shape of 3-D Taylor bubbles.

7.3 Results and discussion

In the present study, a substantial number of simulations was performed to investigate the dynamics of Taylor bubbles in a vertical pipe. A number of fluid properties (e.g. viscosity and density ratio) and dimensionless parameters relevant to the problems (e.g. Re_B, Eo and Mo). Numerical results for the validity of the model were compared with available experimental data from the work of Nogueira et al. (2006b). For all the numerical simulations, a computational domain has been selected, with pipe length $7.5 \cdot D_p$. The pipe diameter D_p and the Taylor Bubble diameter D_{TB} are taken to be equal to 1 and 0.84375, respectively. The length of the Taylor bubble is $2 \cdot D_{TB}$.

A grid of 1640x230x230 with a resolution $\Delta h = 0.0045$ was adopted for all the Taylor bubble simulations. This selection was made in order to ensure the highest available accuracy corresponding to the available computer sources and CPU time from the High Performance Computing (HPC). It should be noted that the present validation test is also a tough test for the validity of the developed GCIBM, because the pipe wall plays an important role to the evolution of the physical phenomenon.

7.3.1 Validation of the model

The current model was validated against the experimental findings reported by Nogueira et al. (2006b). According to their work, a number of experiments were conducted for the investigation of a Taylor bubble rising in stagnant liquid. A vertical tube with 0.032 m internal diameter (D) and 6 m long was selected for the experiments.

In the present study, the model was tested with one of the experiments for stagnant flowing liquid (aqueous glycerol), with reference to the Froude number (Fr) and the liquid film thickness (w). The experimental parameters are $\mu_l = 0.109\ Pas$, $\rho = 1222\ Kg/m^3$, $U_L = 0.000\ m/s$, $U_B = 0.197\ m/s$ and $Re_B = 200$. According to the experimental measurements, the Froude number (Fr) was found to be 0.35 and the liquid film thickness (w) was 0.00327 m.

The computed Froude number was found to be around 0.38. The simulated Froude number presents a deviation of 8.6 % compared to the experimental Froude number (Fr = 0.35) of Nogueira et al. (2006b,a). However, the value of the simulated Froude number is close to the reported values of Froude number which is known as constant "C" and is expressed as (Dumitrescu, 1943):

$$U_{TB} = C(gD)^{1/2} \tag{7.1}$$

where D is the pipe diameter, g the gravitational force and U_{TB} the terminal Taylor bubble velocity. In the literature, there are several reported analytical and experimental values for constant C, such as 0.328 (Davies and Taylor, 1950), 0.351 (Dumitrescu, 1943), 0.345 (White and Beardmore, 1962) 0.303 (Brown, 1965), 0.328 (Laird and Chisholm, 1956), 0.350 (Campos and Carvalho, 1988), and 0.351 (Polonsky et al., 1999b), among others.

The simulated liquid film thickness (w) was also compared with the experimental data of Nogueira et al. (2006b) and the theoretical equation reported by Brown (1965), which is given by the following formula:

$$w = \sqrt[3]{\frac{3\mu_l U_T (R - w)}{2\rho_l g}} \tag{7.2}$$

From Eq. 7.2, the calculated value of w is equal to 0.00319m. The dimensionless liquid film thickness can be obtained by dividing Eq 7.2 with the pipe radius (R = 0.016) according to Llewellin et al. (2012), as well as for the experimental value. As a result, the value of dimensionless film thickness is 0.20 for the theoretical equation and 0.204375 for the experimental measurement. In the present study, the simulated value was found to be equal to 0.185, which is 7.5% and 9.5% less than the theoretical and experimental values, respectively.

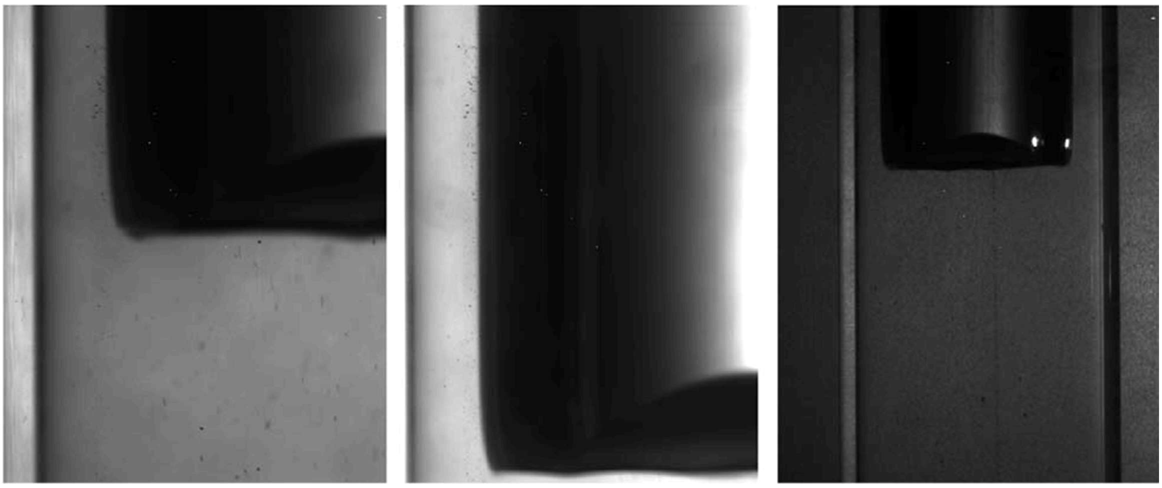

Figure 7.1: Shadow of the bottom of isolated Taylor bubbles rising in a stagnant solution, $Re_B = 200$ (Nogueira et al., 2006b)

Figure 7.1 presents experimental photographs of the bottom of isolated Taylor bubble in a half and full domain, as shown in the work of Nogueira et al. (2006b) for $Re_B = 200$. In Figure 7.2, it is observed that the simulated Taylor bubble captures satisfactory the shadow of the bottom compared with the experimental photographs in Figure 7.1, presenting encouraging agreement.

The difference can be explained mainly by the inadequate grid resolution for the simulation which has also influence on the numerical errors by the FDM and the GCIBM. It should be noted that a 3-D Taylor bubble simulation with the current grid resolution and 64 CPU cores needs more than 1.5 month, and with 128 CPU cores around 20 days to obtain a solution, depending also on the time step (large ratio of density needs small time step). Therefore, a compromise between the grid resolution and the available computer sources is unavoidable.

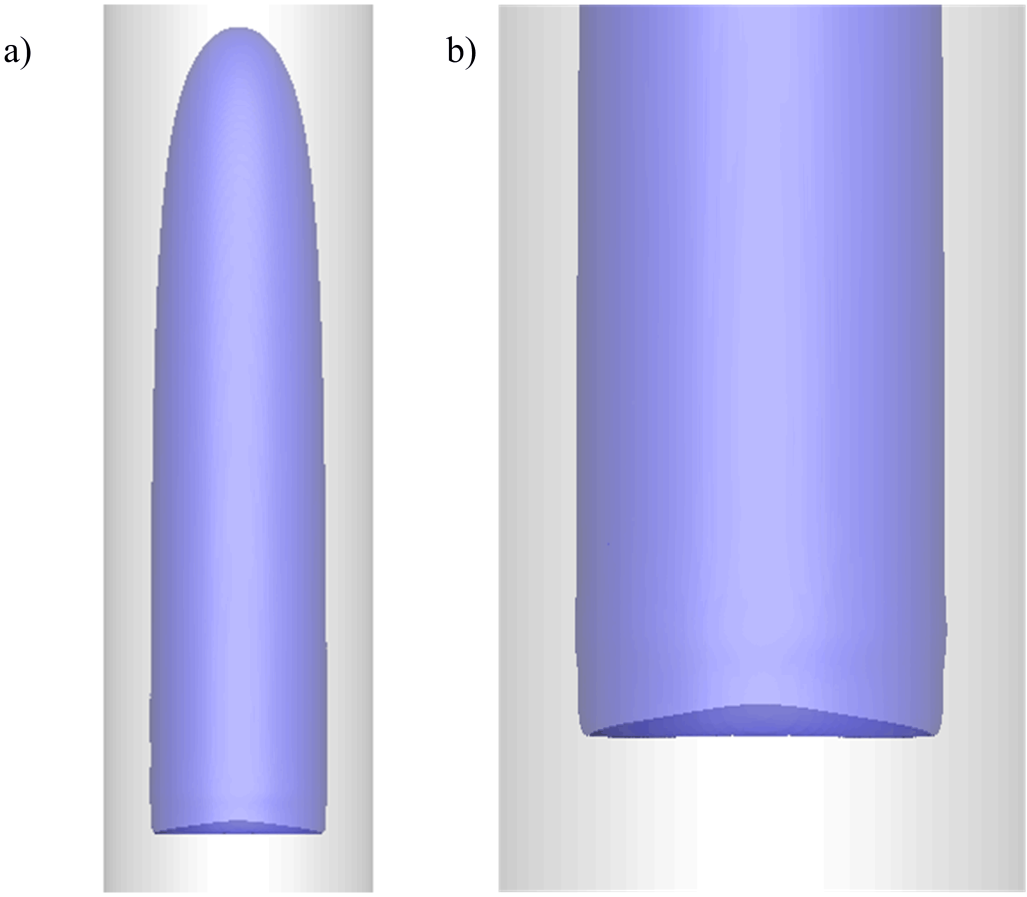

Figure 7.2: Numerical simulation of a Taylor bubble according to the experimental data from the work of Nogueira et al. (2006b) for $Re_B = 200$ and $Ar = 4 \cdot 10^4$: a) Terminal shape of the Taylor bubble and b) the shadow at the bottom of the Taylor bubble.

7.3.2 The role of density and viscosity ratio in the formation of a Taylor bubble

The present section is devoted to investigate numerically the effects of density and viscosity ratio in the formation of a Taylor bubble rising in stagnant liquid through a vertical pipe. A number of selected viscosity and density ratios were adopted for the present numerical simulations.

The values for the selected ratio of density ($\frac{\rho_l}{\rho_g}$) are taken to be equal to 50, 100 and 1000, respectively. The values of the viscosity ratio are taken to be equal to 50 and 100. The other parameters for the numerical simulations are $Re_B = 1910$, $Eo = 7$, $Mo = 2.6 \cdot 10^{-11}$ and $\frac{\mu_l}{\mu_g} = 50$. It should be noted that the value of the Morton number represents the properties of air-water system. It is also important to point out that the viscous effects are not so strong due to the low Morton number (White and Beardmore, 1962; Lu and Prosperetti, 2009).

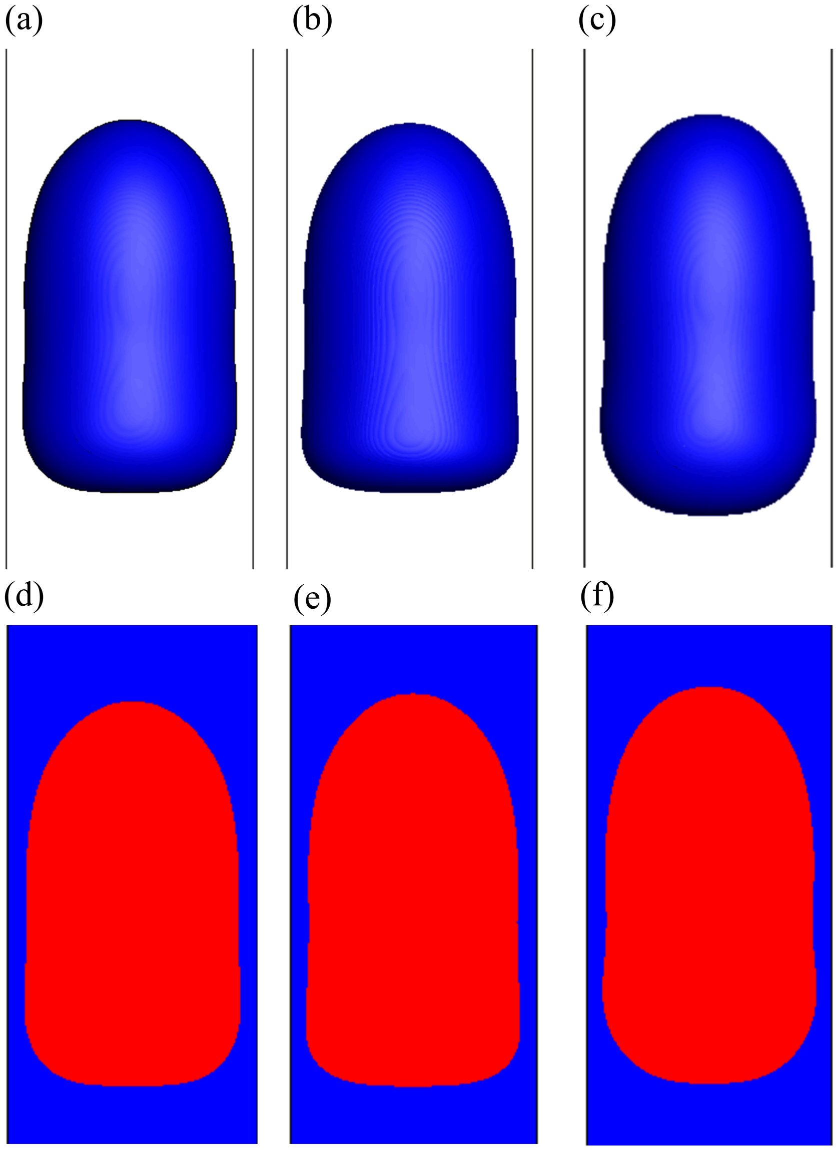

Figure 7.3: Terminal Taylor bubble shapes and cross sections for $Re_B = 1910$, $Eo = 7$, $Mo = 2.6 \cdot 10^{-11}$ and different density ratios: at 50 for (a) and (d), at 100 for (b) and (e), and at 1000 for (c) and (f).

Figure 7.3 presents the Taylor bubble shapes for the selected density ratios along with their cross sections. It is observed that the terminal bubble shapes for density ratio 50 and 100 are slightly different with a little wider sides at the bottom for the case (b). However, the bubble shape for the high density ratio (case c) displays two small bulges (left and right side) near to the bottom due to tail oscillations (weak viscous effects). It is also observed that the tail of the bubble for case (c) appears a curved shape compared to the other two cases (a) and (b) which display a flat tail. It is concluded that the bottom of the Taylor bubble is affected with increasing the density ratio.

The nose of the Taylor bubble maintains a prolate spheroid shape for all the cases without distinguishable differences, as shown in Figure 7.3. The value of the selected density ratio for the specific Morton number does affect the terminal shape of the bubble. However, the high density ratio requires a small time step, $\Delta t = 10^{-4}$ which increases significantly the simulation time.

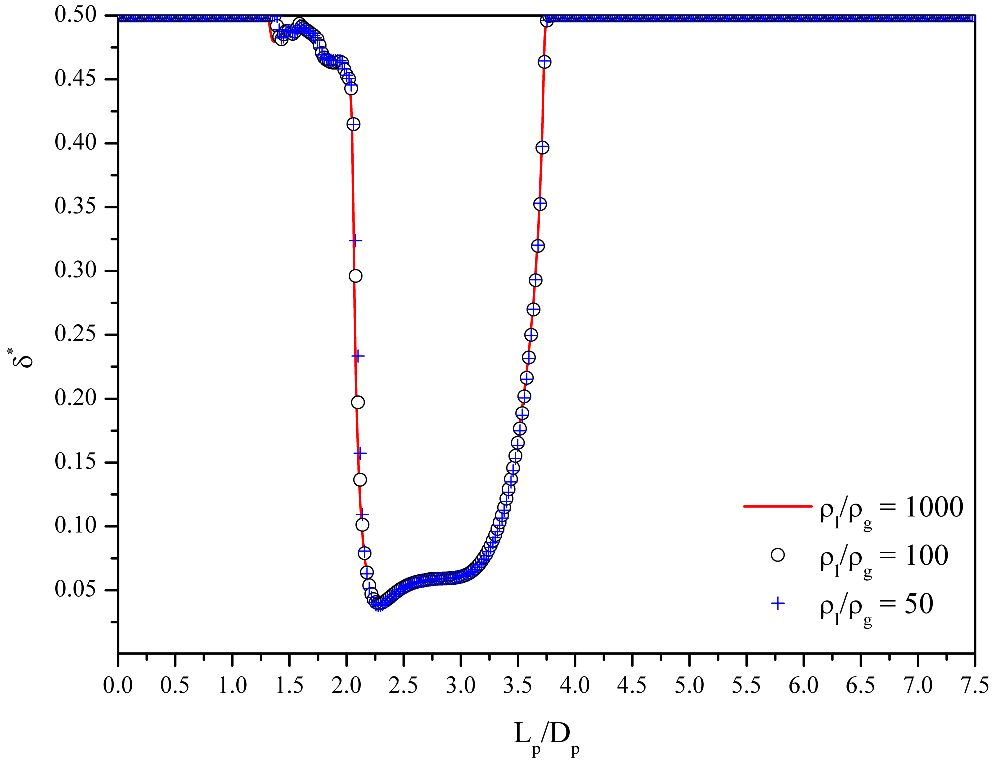

Figure 7.4: Film thickness vs. the pipe length for different density ratios.

Figure 7.4 depicts the film thickness (δ) for the three selected values of density ratio.

It is shown that the difference between the values of density ratio, 50 and 100 are indistinguishable, while for the value 1000 is slightly different only in few parts of the curve. It should be noted that a finer grid might give larger variations between the low and high density ratios regarding the film thickness.

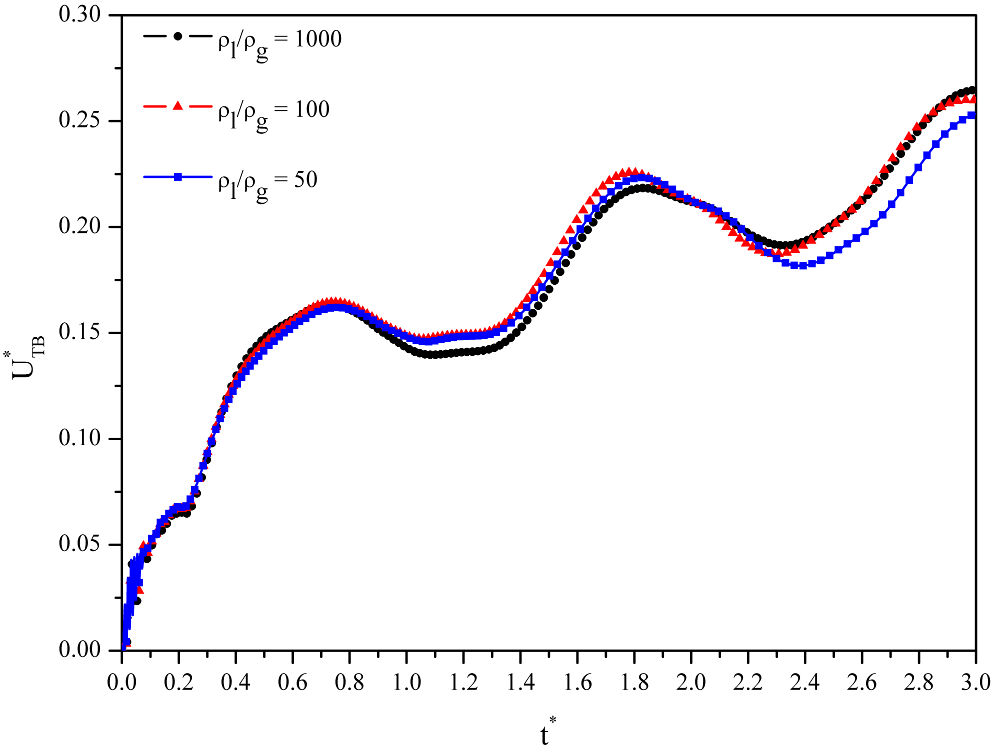

Figure 7.5: Rise velocities of oscillating Taylor bubbles for different density ratios.

As mentioned above, the shape of the Taylor bubble indicates that the bubble tail oscillates periodically due to weak viscous effects (Lu and Prosperetti, 2009). This is also supported by the fluctuated rising dimensionless bubble velocity for the three cases, as shown in Figure 7.5.

In order to investigate the effect of the viscosity ratio on the Taylor bubble shape, two different values were examined, namely 10 and 100. The other parameters of the simulations remain the same as above.

Figure 7.6 illustrates the Taylor bubble shapes for the two different values of the selected viscosity ratio. It can be seen that the viscosity ratio has also influence on the terminal bubble shape at the bottom, similar to the effects of density ratio, as well as to the streamline patterns at the bubble bottom.

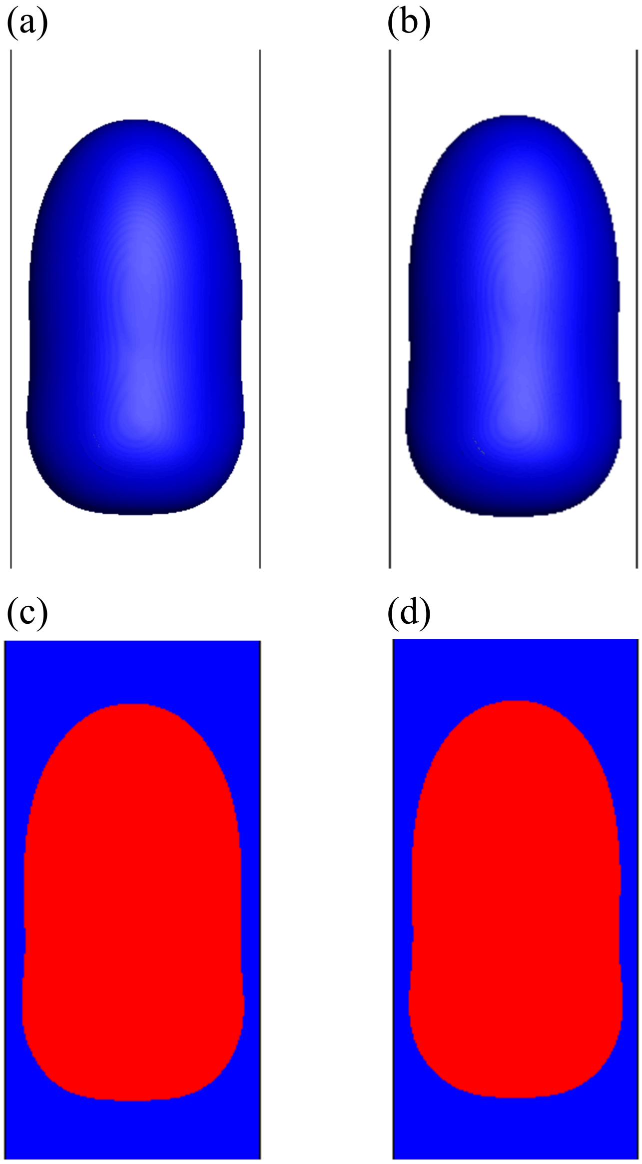

Figure 7.6: Terminal Taylor bubble shapes and cross sections for $Re_B = 1910$, $Eo = 7$, $Mo = 2.6 \cdot 10^{-11}$ and different viscosity ratios: at 10 for (a) and (c) and at 100 for (b) and (d).

In Figure 7.7, it is depicted the relation of the dimensionless film thickness along with the dimensionless pipe length for density ratio 10 and 100. It is shown that the film thickness curve is almost identical without any important change.

It is also observed that the dimensionless velocity is fluctuated during the simulation for the two selected viscosity ratios, as shown in Figure 7.8. This occurs due to the oscillations of the Taylor bubble bottom.

The presence of oscillations has been reported for low-viscosity fluids by Lu and Prosperetti (2009). They used the gravity-capillary theory in order to estimate the oscillations frequency. However, their code did not take into account the topological changes (e.g. break up).

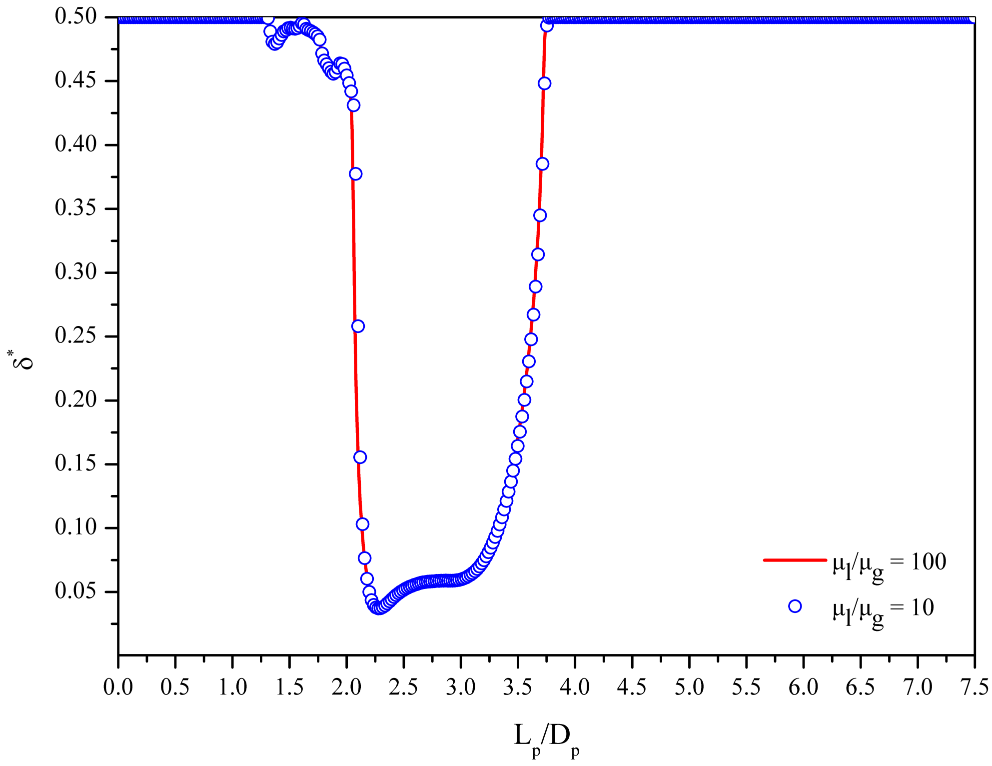

Figure 7.7: Film thickness vs. the pipe length for different viscosity ratios.

This phenomenon has also been studied experimentally for air-water system by Polonsky et al. (1999a). The power spectra of the bubble oscillations were presented for various bubble lengths in stagnant liquid. They concluded that the bottom oscillations of the Taylor bubble depend on the bubble length and their amplitude increases with increasing the Taylor bubble length.

According to the above results, the density and viscosity ratio are taken to be equal to 1000 and 100 for the numerical simulations in the next sections. A time step, $\Delta t = 1.2 \cdot 10^{-4}$ was also used for the following simulations.

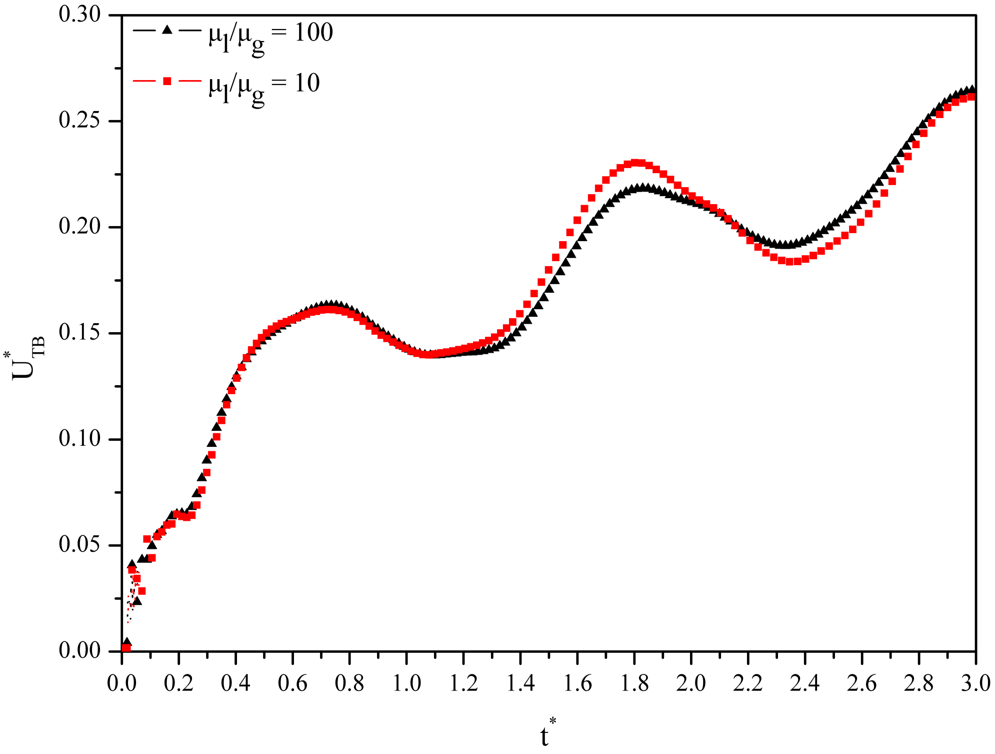

Figure 7.8: Rise velocities of oscillating Taylor bubbles for different viscosity ratios.

7.3.3 The role of Eotvos number in the formation of a Taylor bubble

The Eotvos number expresses the relation between the body forces and surface tension forces. As a result, a high Eotvos number decreases the surface tension effects on the system, while a low Eotvos number is accompanied by the dominance of the surface tension forces.

Many studies have been devoted to identify a critical Eo number at which the surface tension forces are dominant and as a result the Taylor bubble cannot move and remains stuck in the vertical pipe. The criterion for a zero bubble velocity is specified as $Eo = 3.4$ according to the work of White and Beardmore (1962) and in general express for $Eo < 4$ the bubble is not rising. Other researchers have also proposed a value of Eo $=$ 0.58 by Barr (1926), 3.37 by Bretherton (1961), 3.36 by Hattori (1935) and 4 given by Gibson (1913). The phenomenon has also discussed in the work of Viana et al. (2003).

According to the above mentioned values for the critical values Eo number, we have selected two Eo values in order to investigate the phenomenon, namely 3.4 and 4. The other parameters for the simulations are $Mo = 2.6 \cdot 10^{-11}$, $\frac{\mu_l}{\mu_g} = 100$ and $\frac{\rho_l}{\rho_g} = 1000$.

Simulations with $Eo = 3.4$ has also been conducted by Taha and Cui (2006) with VOF and Lu and Prosperetti (2009) with a set of marker points linked by cubic splines. According to the author's knowledge, it is the first time that the present method is used for the simulation of this phenomenon. For both cases of Eo numbers the code crashed after a number of iterations, even with very small time steps (e.g. $10^{-4}, 5 \cdot 10^{-5}$ and 10^{-5}). The bubble motion was prevented by the strong surface tension forces. In order to release the strong surface energy, the bubble tends to stretch its initial shape to spherical structure. As a result, this process leads to the rupture of the thin film at the bottom of the bubble. The failure of calculations for $Eo = 3.4$ is also reported in the numerical study of Lu and Prosperetti (2009).

When the surface tension forces are decreased, the value of Eo increases. Therefore, two additional values of Eo, 7 and 28 are adopted for further investigation at $Mo = 2.6 \cdot 10^{-11}$. From Figure 7.9, it is shown that the streamlines for the two Eo numbers give different patterns and bottom shapes. It is also seen that the configuration of the two main vortices at the bottom with the strongest display for case (b). For case (a), Eo number is four times lower than case (b). Therefore, case (a) is affected by higher resistance of the surrounding fluid compare to case (b), resulting to a lower rising velocity, as shown in Figure 7.11.

Figure 7.10 illustrates cross sections for the two cases in order to notice better the final shape of the Taylor bubbles. For the first case the bubble shape is characterised as a bullet with fatter sides at the bottom, resulting to spherical shape bottom. On the other side, for $Eo = 28$, bubble can be described as a bullet shape with two lateral tail edges (right and left) and in the middle a flat shape at the bottom.

It is also important to note that unlike the fluctuated dimensionless bubble velocity for $Eo = 7$ due to the presence of tail oscillations, the case for $Eo = 28$ does not display oscillations and seems to be more stable, as shown in Figure 7.11. In Figure 7.10, it is

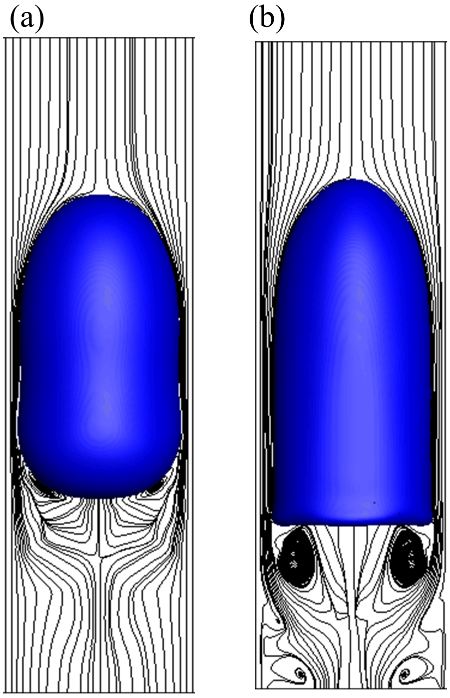

Figure 7.9: Taylor bubble shapes for $Mo = 2.6 \cdot 10^{-11}$, $\frac{\mu_l}{\mu_g} = 100$, $\frac{\rho_l}{\rho_g} = 1000$ and different Eotvos number: (a) Eo = 7 and (b) Eo = 28.

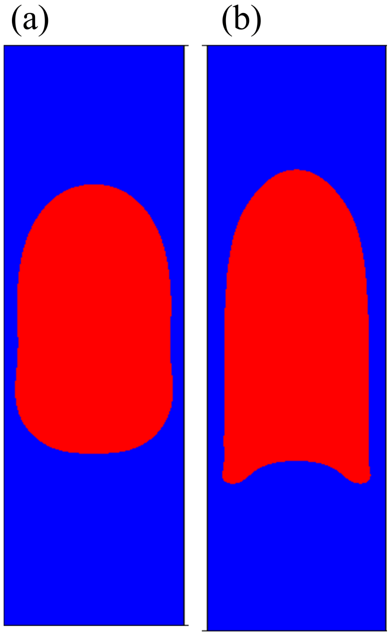

Figure 7.10: Taylor bubble cross sections for $Mo = 2.6 \cdot 10^{-11}$, $\frac{\mu_l}{\mu_g} = 100$, $\frac{\rho_l}{\rho_g} = 1000$ and two Eotvos values: (a) $Eo = 7$ and (b) $Eo = 28$.

also seen that the Eo number affects the determination of tail elongation.

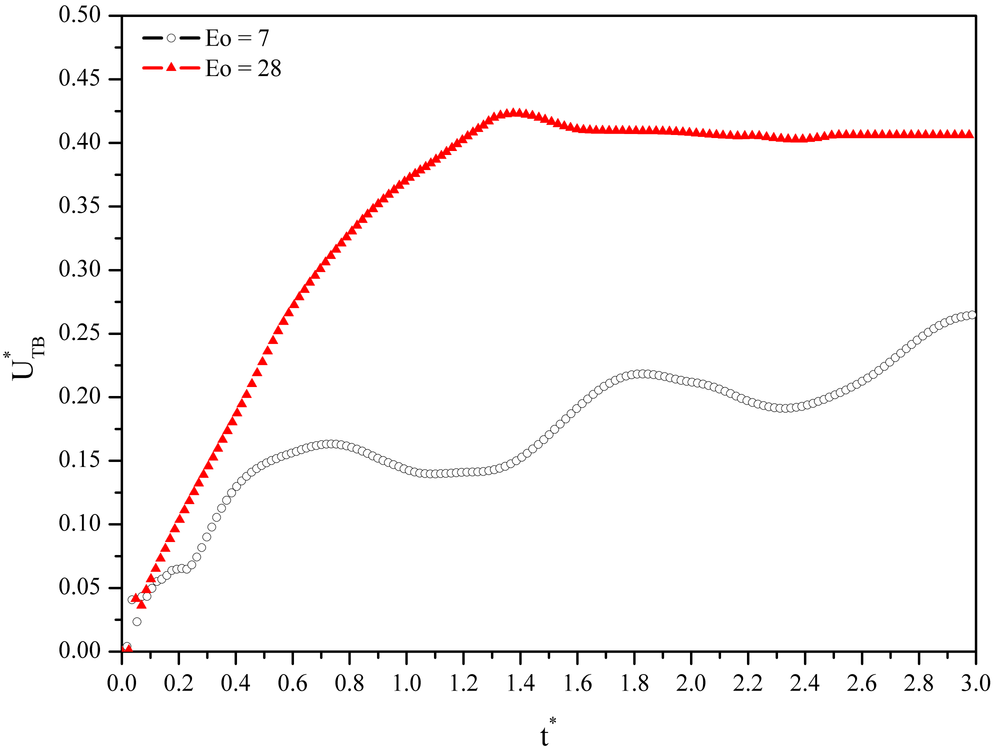

Figure 7.11: Dimensionless bubble velocities for Eo = 7 and 28.

7.3.4 The role of Morton number in the formation of a Taylor bubble

Morton number along with Eotvos number can be used for the characterisation of the bubble or drop shape. In this section, a detailed study is performed for investigating the effects of Morton (Mo). Several cases were examined with the same density ratio of 1000, viscosity ratio of 100 and two Eotvos numbers of 7 and 200. The selected values of Morton number is varied from $O(10^{-11})$ to $O(10^{-4})$.

Figure 7.12 illustrates the terminal shapes of Taylor bubbles for five different values of the dimensionless Morton (Mo) number and Eotvos (Eo) value of 7. From Figure 7.12(a), it is seen that the terminal shape of the Taylor bubble is prolate spheroid shaped with rounded trailing and leading edges. It is also interesting to point out that the length

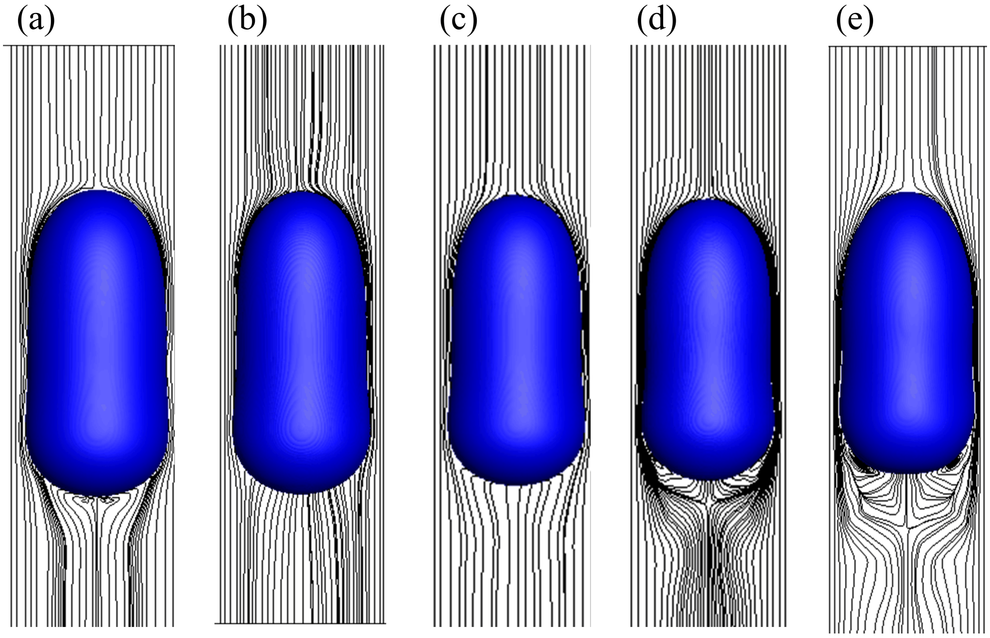

Figure 7.12: Terminal bubble shapes and streamlines for $Eo = 7$ and various values of Mo: (a) $Mo = 10^{-6}$, (b) $Mo = 10^{-7}$, (c) $Mo = 10^{-8}$, (d) $Mo = 10^{-9}$ and (e) $Mo = 2.6 \cdot 10^{-11}$.

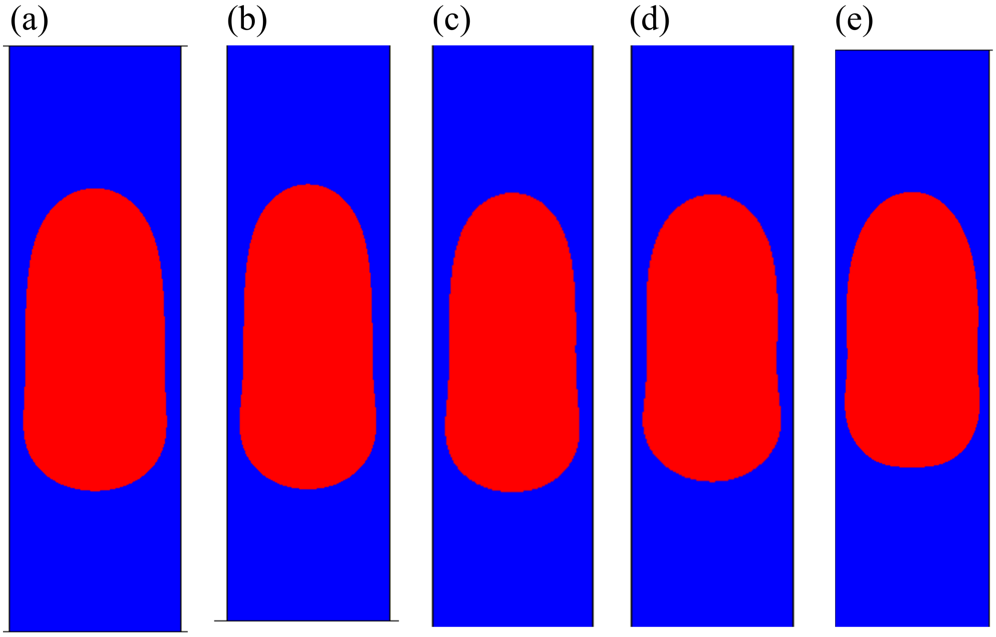

Figure 7.13: Bubble cross sections for $Eo = 7$ and various values of Mo: (a) $Mo = 10^{-6}$, (b) $Mo = 10^{-7}$, (c) $Mo = 10^{-8}$, (d) $Mo = 10^{-9}$ and (e) $Mo = 2.6 \cdot 10^{-11}$.

of the Taylor bubble is the longest, resulting in the thickest liquid film among the other cases.

With the decrease in Morton number, the viscous forces are not too strong. The long shape of the Taylor bubble is reformed from a long and thin shape to a fatter and shorter schema. These topological changes of the Taylor bubble squeeze and bound the thin liquid film into a narrower region, as shown in Figure 7.12 (e).

Figure 7.13 present cross sections of the Taylor bubbles for the five different values of Morton number and the selected Eotvos value of 7. Figures 7.13(a)-(e) also support the previous findings for the terminal shape of the bubble and thin liquid film.

An interesting phenomenon that has been reported in previous studies such as, for example, Lu and Prosperetti (2009) and Polonsky et al. (1999b). From the present numerical predictions, it is found that there is a critical value of Morton number regarding the presence of these oscillations, as shown in Figure 7.14. We do not refer to the initial oscillations for dimensionless time between 0 and 0.4, but for the larger oscillations for $t^* = 0.4 - 3$. The value of Morton number was found to be $\leq 10^{-8}$ for the selected Eotvos value of 7.

Figure 7.14 presents the dimensionless velocity of the Taylor bubbles for the considered cases. It is seen that the bubble velocity for the cases with Mo values of $2.6 \cdot 10^{-11}$, 10^{-9} and 10^{-8} fluctuates, as shown in Figure 7.14. This expresses an indication of bubble oscillations at the bottom. This is also supported by the bubble deformantion at the bottom for different times, as shown in Figure 7.15 and 7.16 at $Mo = 2.6 \cdot 10^{-11}$ and $Mo = 10^{-9}$. In Figure 7.17, it is observed that the deformation of the bubble shape at the botton is very small due to the attenuation of the oscillation effects compared to the previous cases. Below the critical value of $Mo = 10^{-8}$ there is no oscillation effects to the bottom shape of the Taylor bubble.

The second group of simulations for Eotvos number of 200 is comprised by three different values of Morton number, namely 10^{-3}, $2.1 \cdot 10^{-4}$ and $8 \cdot 10^{-6}$. The other parameters of the simulations are the same as above. The motivation of this attempt is the further investigation of unsteady effects on thin liquid film such as, for example,

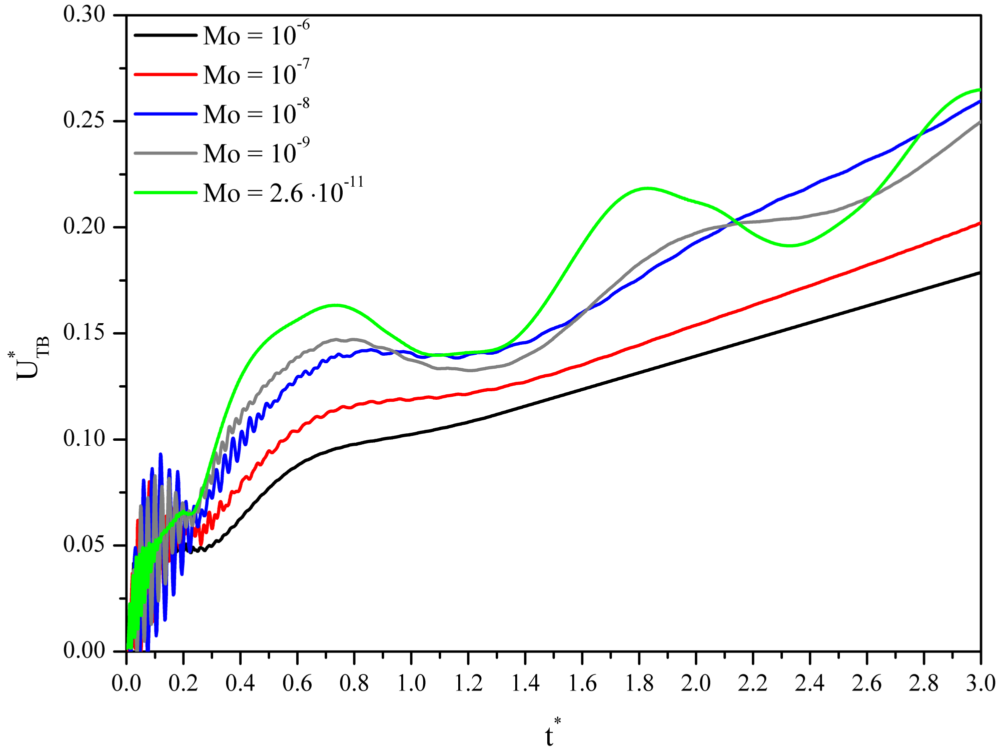

Figure 7.14: Bubble velocity for $Eo = 7$ and various values of Morton number (Mo).

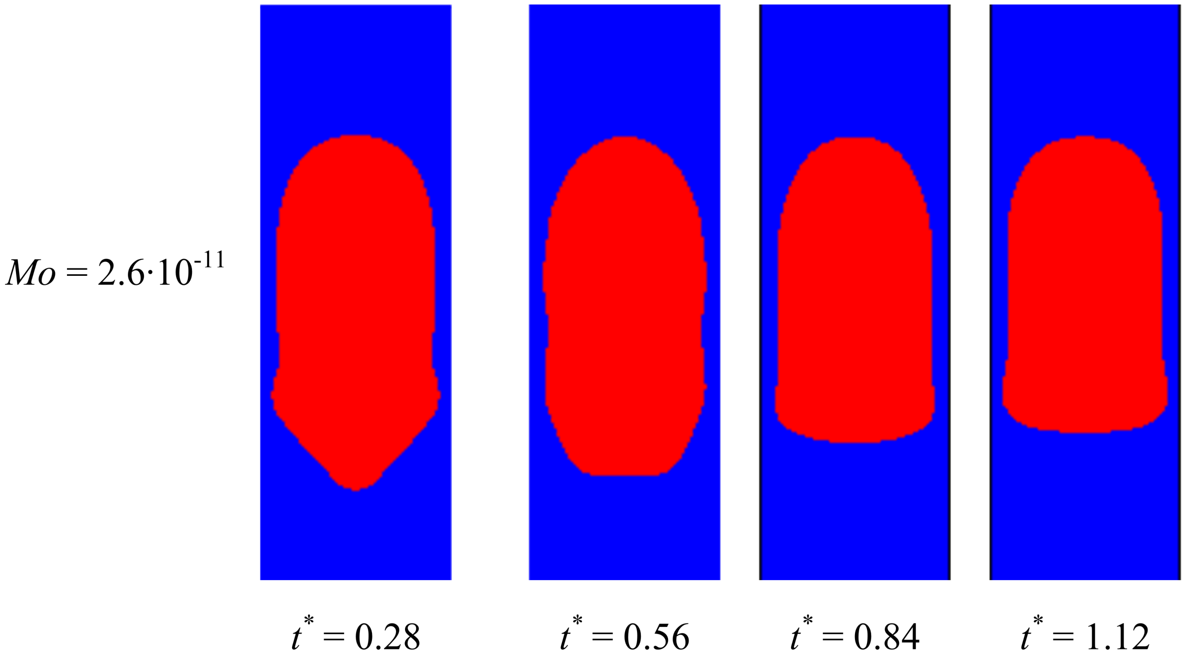

Figure 7.15: Cross section profiles for $Eo = 7$, $Mo = 2.6 \cdot 10^{-11}$ and different times.

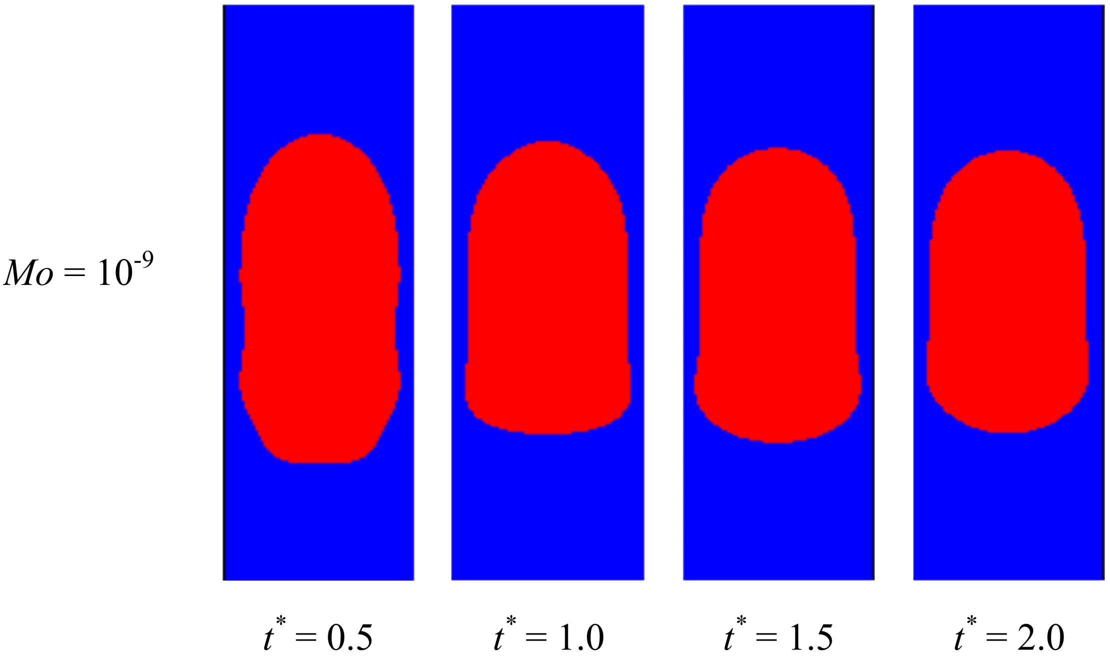

Figure 7.16: Cross section profiles for $Eo = 7$, $Mo = 10^{-9}$ and different times.

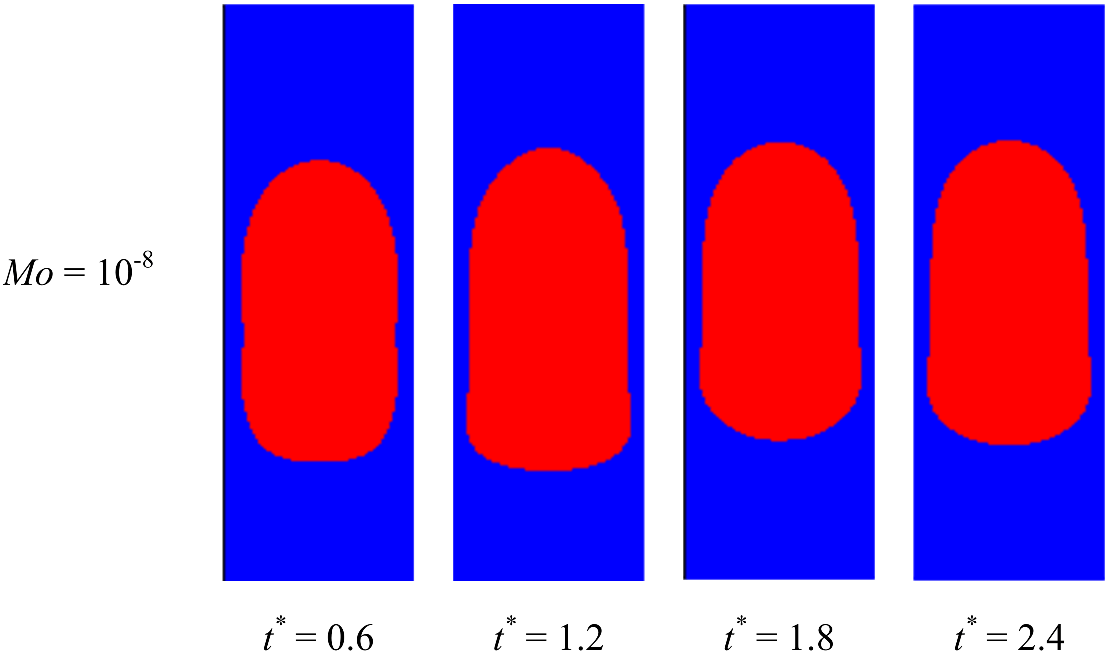

Figure 7.17: Cross section profiles for $Eo = 7$, $Mo = 10^{-8}$ and different times.

appearance of waves at the bubble sides and break up of many small bubbles at the bottom.

It should be noted that the latter case can not be simulated by numerical methods such as the Front Tracking (Kang et al., 2010) or sharp methods using a set of marker points linked by cubic splines, because they cannot handle topological changes (e.g. bubble break up). The present method is characterised by superiority from the aspect of handling the topological changes. However, the present method is not so accurate as the previous methods and demands very fine grid in order to capture the above mentioned phenomena in detail. Therefore, a compromise between the grid resolution and the available computer sources is necessary.

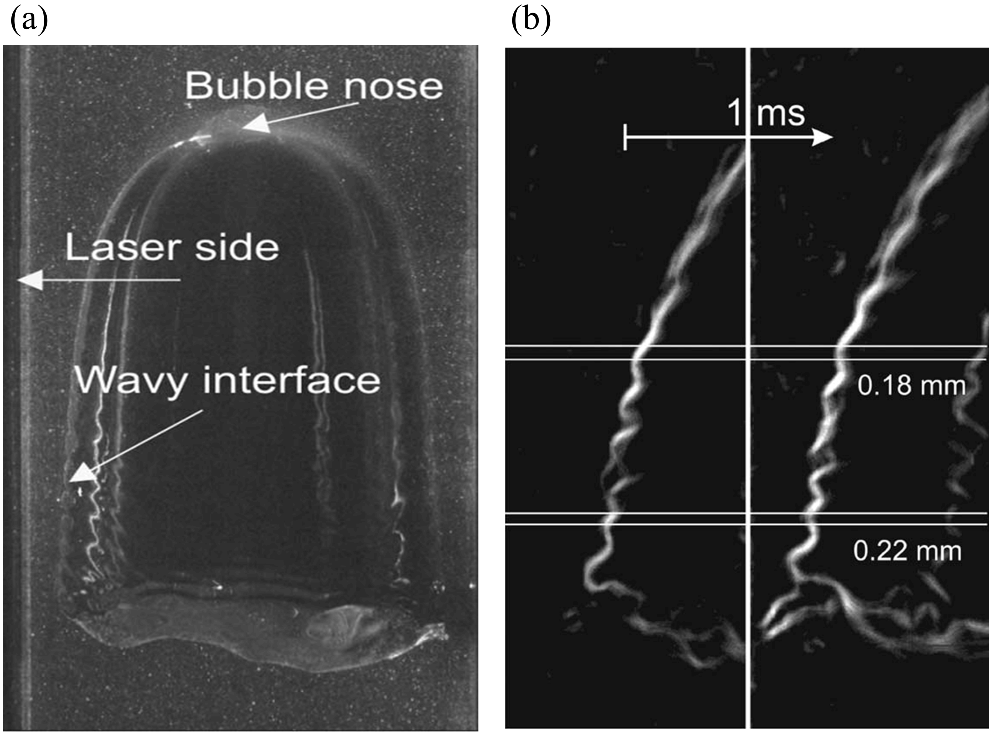

Figure 7.18: (a) Waves on the interface of the Taylor bubble rising in stagnant water in the pipe of D = 26 mm, (b) Pair of images of a Taylor bubble rising in a pipe with D = 44 mm in stagnant water. Horizontal lines mark corresponding individual wave crests, propagating upwards. The Figures adopted from the work of Liberzon et al. (2006).

Polonsky et al. (1999b) and Polonsky et al. (1999a) claimed that while the nose of the Taylor bubble remains constant, the bottom of the bubble presents quasi-periodic oscillations. Similar findings were also reported from Nigmatulin and Bonetto (1997). They found that the surface oscillations express standing capillary waves and their amplitudes increase as the waves become shorter.

Kockx et al. (2005) also studied the disturbance on the surface of a long Taylor bubble in a pipe. They concluded that the presence of the oscillations is related to the entrainment of small gas bubbles from the Taylor bubble in the surrounding fluid.

Liberzon et al. (2006) presented an experimental study regarding the short capillary waves on the surface of air Taylor bubble in water rising in vertical pipes of different diameters (e.g. D = 14, 26, 44 mm) using particle image velocity (PIV) technique. One of their conclusion is that the phenomenon occurs only for sufficient short bubbles only. According to their experiments the generation of waves on the surface of Taylor bubbles is attributed to the bubble bottom oscillations. They also predicated that the wave frequencies at the bubble bottom range from 2 to 12 Hz. The frequencies depend on the bubble diameter, bubble length and the water flow rate. Figure 7.18(a) depicts the presence of capillary waves on the bubble surface, while Figure 7.18(b) illustrates that the waves propagating upwards. Approaching the nose of the bubble the waves become longer due to the variation of the film velocity.

As mentioned above, three different cases were considered for the investigation of unsteady phenomena on the thin film. It is interesting to point out that the decrease of the Morton number causes remarkable changes at the bottom of the Taylor bubbles at $Eo = 200$, as shown in Figures 7.19. It is observed that the tail of the Taylor bubble at $Mo = 10^{-3}$ achieves a dimpled shape, as shown in Figure 7.19(a). The effect of viscous force is strong, as reflected by a large Eo number ($Eo = 200$) and weak surface tension forces.

This case similar to the case (13) from the work of Kang et al. (2010). In their study, the tail of the Taylor bubble presents a further indentation compared to the present results. This can be explained by the inadequate grid resolution and the selected method for simulations the interface (Phase-field) method. Their calculation for the Froude (Fr) number gives a value of 0.33, while the present numerical predictions yield a value around 0.40. According to the following universal correlation of Viana et al. (2003) for $Re_B > 200$:

$$Fr = 0.34/(1 + 3805/Eo^{3.06})^{0.58} \tag{7.3}$$

the estimated value of yields a value of 0.34.

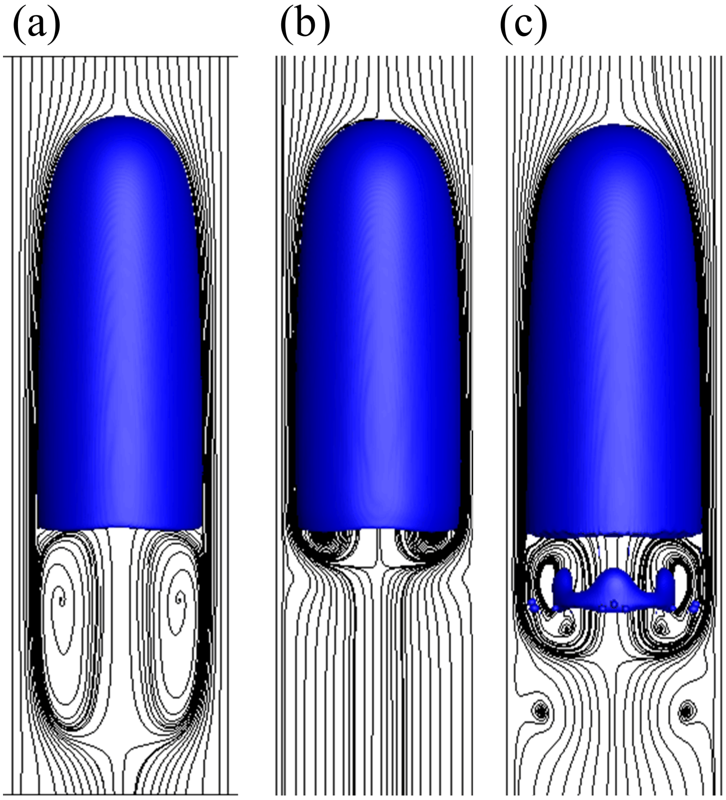

Figure 7.19: Terminal bubble shapes and streamlines for $Eo = 200$ and various values of Mo: (a) $Mo = 10^{-3}$, (b) $Mo = 2.1 \cdot 10^{-4}$ and (c) $Mo = 8 \cdot 10^{-6}$.

With the further decrease of the Morton number ($Mo = 2.1 \cdot 10^{-4}$ the tail of the Taylor bubble develops a gas "skirt" again due to the weak surface tension forces, as shown in Figure 7.20(b). The bottom shape of the bubble presents similarities with the case (14) from the study of Kang et al. (2010). The simulated Fr number was found to be around 0.38, while for the case (14) is again 0.33. The theoretical prediction of the Fr number from the above universal correlation of Viana et al. (2003) is again 0.34.

In Figure 7.20, it is observed that the further decrease of Morton number $Mo = 8{\cdot}10^{-6}$ results in the break up of many small bubbles at the bottom, as shown in Figures 7.19(c) and 7.20(c). It is important to mention that the mechanism of breaking up of many small bubbles from the rear of the Taylor bubble is still not clear. However, a gas entrainment mechanism has been proposed by Delfos et al. (2001) and Kockx et al. (2005). With the decrease of the Morton number, the viscous effects are getting weaker and bubble tail may oscillate. The large values of Eotvos number also affects the surface tension forces which are getting smaller. When a wave on the thin film travels at the surface of the bubble it generates a gravity wave. In order to enclosed the gas (e.g air), the slope of the gravity wave should be large enough and at the same time the surface wave should travel very fast. Then, the gravity wave crest contacts with the next wave on the bubble surface and traps the air.

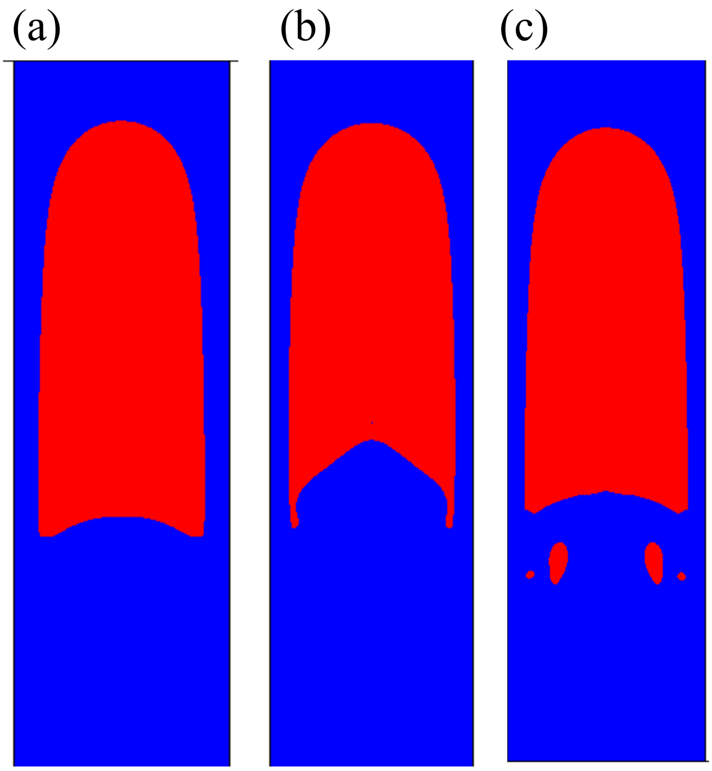

Figure 7.20: Bubble cross sections for $Eo = 200$ and various values of Mo: (a) $Mo = 10^{-3}$, (b) $Mo = 2.1 \cdot 10^{-4}$ and (c) $Mo = 8 \cdot 10^{-6}$.

Figure 7.21 depicts a phase diagram for various values of Morton number versus the Eotvos number with three regions for the bubble tail, namely steady, wavy and unstable (break up). In the diagram, the empty geometrical schemes are numerical data from the work of Lu and Prosperetti (2009), while the filled blue triangles and squares represent the present results.

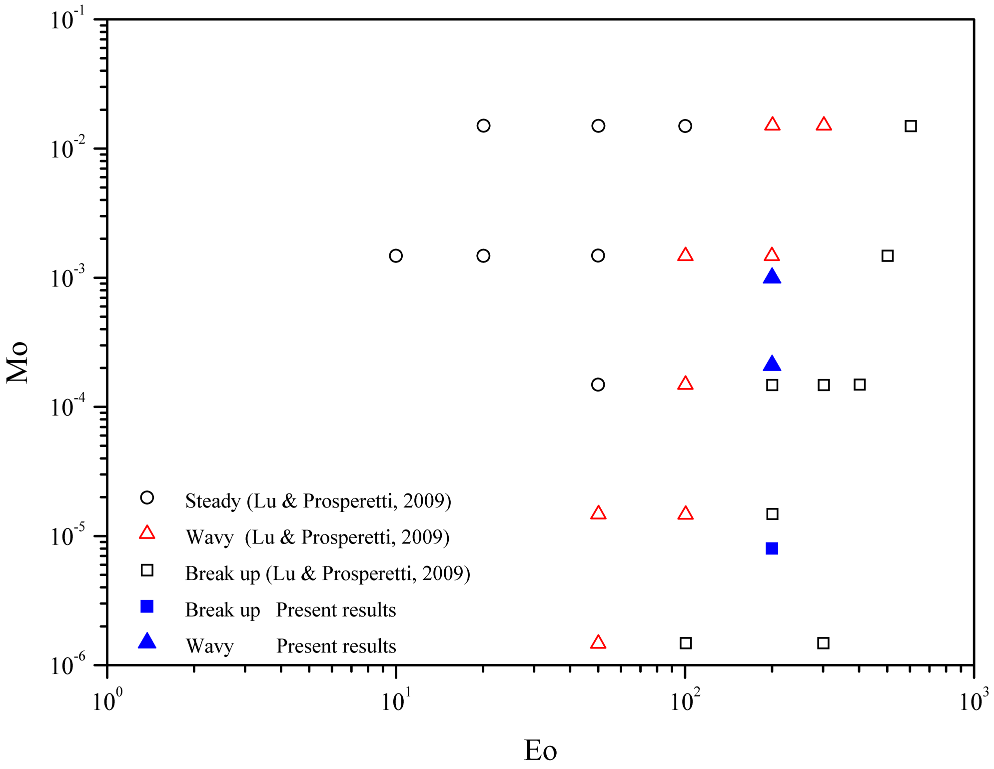

Figure 7.21: Phase diagram of the tail shape in Mo and Eo for a bubble rising in quiescent liquids.

The numerical predictions are in good agreement with the numerical data of Lu and Prosperetti (2009), excluding the case for $Mo = 2.1 \cdot 10^{-4}$. This occurs due to the inadequate grid resolution.

7.4 Chapter summary

In this chapter, an attempt was made to study the dynamics of three-dimensional Taylor bubbles rising in stagnant liquid through a vertical pipe. The numerical method was validated initially against the available experimental and numerical data from the works of Nogueira et al. (2006b) and Kang et al. (2010).

Numerical simulations were conducted for different values of Morton (Mo), Eotvos (Eo), buoyancy Reynolds (Re_B) numbers, density and viscosity ratios in order to investigate the final bubble shape, the gas entrainment at trail, liquid film thickness and rising velocity. The numerical predictions were compared to other numerical data, wherever is possible.

Chapter 8

Conclusions and future directions[1]

8.1 Introduction

In this chapter, the main conclusions arising from the numerical predictions in the present work are summarized and discussed. Future directions and general considerations are also presented, including further development and improvement of the CFD code, implementation of the proposed numerical method for other flow problems. Special attention is also given to the available Direct Numerical Simulation (DNS) and Large Eddy Simulation (LES) techniques for two-phase pipe flows and a brief literature review is also introduced.

8.2 Main findings

8.2.1 Contributions of thesis

The contributions of the present thesis in the fields of Computational Fluid Dynamics and two-phase pipe flows can be summarised in the following five points:

---

[1] The present Chapter contains material from the review paper entitled "Recent advances on the numerical modelling of turbulent flows" by C.D. Argyropoulos and N.C. Markatos in Applied Mathematical Modelling, 39 (2015) 693.

1. A detailed literature review is presented of the available immersed boundary methods and interface and capturing methods with main focus on the ghost-cell immersed boundary method (CGIBM) and phase-field method, respectively.
2. A numerical method based on a combined ghost-cell immersed boundary/phase field technique along with a finite difference method is presented for three-dimensional two-phase pipe flows. The combination of the above methods is implemented for first time.
3. The proposed numerical method is used to investigate the latteral wall effects of a 3-D single bubble in a viscous liquid for different pipe diameters and bubble flow regimes for high and intermediate Reynolds numbers.
4. The dynamics of 3-D Taylors bubbles is examined in vertical pipes for different properties of fluids (e.g. air-water system) and dimensionless parameters relevant to the problem (e.g. Re_B, Eo and Mo). The numerical simulations are also focused on the investigation of unsteady effects on thin liquid film (e.g. waves at the bubble sides and break up for many small bubbles at the bottom).
5. A literature review is also presented of the problems and successes of computing turbulent flow. The review is concerned with methods for turbulent flow computer predictions and their applications, and describes several of them. The successes and problems are demonstrated by listing and briefly discussing several applications of DNS and LES to flows in pipes and free-surface flows. A hard-copy of the review paper can be found in Appendix C.

The next sections outline the main findings of Chapters 5, 6 and 7.

8.2.2 Conclusions of Chapter 5

In Chapter 5, the numerical method along with the developed IBM methods were verified and validated with available numerical and experimental data from the literature. The developed IB algorithms are based on the penalty technique and ghost cell method, respectively. The GCIBM based on the main idea of Tseng and Ferziger (2003). The method was also modified in order to incorporate the appropriate boundary conditions for coupling the Phase-Field, momentum and pressure solvers for two-phase pipe flows. Tseng and Ferziger (2003) used the GCIBM for turbulent single-phase flows, however, the present version exhibits a continuation of the method for handling two-phase pipe flows.

Two classical test cases were selected for the performance evaluation of the IB algorithms, namely single- and two-phase Poiseuille flow. Both algorithms were compared against the analytical solution for the velocity profile corresponding to the single- and two-phase Poiseuille flow, respectively.

The GCIBM presents superior performance compared to the IB algorithm based on the penalty technique regarding the velocity profile for the examined two test cases. In the case of the single-phase Poiseuille flow, the u_{max} % error value ($\Delta h = 0.01$) regarding the velocity profile is 2.11% for the IB algorithm based on the penalty technique and around 0.5% for the GCIBM algorithm. It is also important to mention that the accuracy of the GCIBM algorithm for the specific test case is around to the second order while for the other algorithm the accuracy approaches the first order.

In the case of two-phase Poiseuille flow, again the GCIBM algorithm exhibits better performance compared to the IB algorithm based on the penalty technique. The % error ($\Delta h = 0.005$) for the u_{max} compared to the analytical solution for the GCIBM is 4.79%, while for the other IB algorithm is 5.74%. The accuracy of the GCIBM algorithm is higher than first order corresponding to a slope of about 1.3, while for the IB algorithm based on the penalty technique close to first order.

It is also important to point out that the IBM based on the penalty technique is limited by two main constraints, namely time-step and the value of the user-defined parameter. In order to achieve a converged solution, a small time step is necessary, which increase sufficiently the computational time. The user-defined parameter leads to stability and accuracy problems, especially with small values. A possible solution of the above problem could be the use of a value of C_{IB} (user define parameter, see Section 4.4.1) which compromises the need of approximating solid boundaries and the preservation of the numerical stability at a reasonable computational cost.

The next validation test for the proposed numerical methods was the rise of a single three-dimensional bubble in a vertical pipe. A detailed study has been performed for the appropriate selection of the pipe length and pipe diameter, as well as for the suitable grid resolution. The dimensionless parameter pipe length L_p^* is taken equal to 10, while the dimensionless parameter D_p^* is taken equal to 7. The selection of the grid for the numerical simulation was based on a grid sensitivity analysis among five different grids, 238x175x175, 286x210x210, 358x262x262, 408x300x300 and 476x350x350, respectively.

The results between the last three grids were found to be sufficiently close to each other with deviation of 1.31, 1.24 and 1.09%, respectively, with reference to the terminal Reynolds number. However, the finest grid was selected in order to achieve the highest available accuracy. The selected grid was used for the simulation of four different bubble flow regimes, namely spherical, oblate ellipsoidal, oblate ellipsoidal disk and oblate ellipsoidal cap.

The numerical predictions with reference to the bubble shape and terminal Reynolds number were compared with available experimental data from the works of Bhaga and Weber (1981), Grace (1973) and Clift et al. (1978), presenting very good agreement for the prediction of the bubble shape and satisfactory agreement for the terminal Reynolds number.

The model was tested for the bubble volume conservation by examining the bubble volume percentage error for a spherical and an oblate ellipsoidal bubble. The percentage error is less than 1% for the spherical regime and less than 1.4% for the ellipsoidal bubble, which indicate that the volume of rising bubble is satisfactory conserved.

The numerical method was also tested for the presence of parasitic or spurious currents. A static bubble was selected as a test case for investigating the parasitic currents on the interfacial region. The results indicate that the magnitude of spurious velocity is in the range of 10^{-6}. It is also observed that for $\epsilon = 0.5\Delta h$ displays the minimum value for the spurious velocity, which is also the selected interface thickness for the bubble simulations.

Other test case for the current model is the computation of the drag coefficient for a single rising bubble and comparison with the obtained correlation from the experimental data of Bhaga and Weber (1981). Three numerical simulations were performed with three different Morton numbers, namely $Mo = 5.48 \cdot 10^{-3}$, 0.01 and 0.1. The numerical predictions presented small deviation compared to the correlation of Bhaga and Weber (1981). This behaviour can be explained by the numerical error of the method and the need of a finer grid.

The CFD code was also validated against experimental data from the work of Brereton and Korotney (1991) for the bubble coalescence of two rising bubbles in a vertical pipe and showed good agreement.

8.2.3 Conclusions of Chapter 6

In Chapter 6, an attempt was made to investigate the wall effects on the rise of a three-dimensional bubble, by means of a combined immersed boundary/phase-field method. A GCIBM was employed for the reconstruction of the pipe wall, while a phase-field method was used for the simulation of the interfacial region between the two fluids.

Numerical simulations were performed to investigate the wall effects for three bubble regimes (spherical, oblate ellipsoidal and oblate ellipsoidal cap) and various ratios of the pipe diameters (D_p^*= 1.2, 1.6, 2, 2.5, 3, 3.5, 4 and 5). The numerical results indicate that the presence of the wall effects on the rise of a single bubble for the considered values of D_p^* are significant compared to the infinite medium conditions, which are specified for pipe length $L_p^* \geq 8$ and pipe diameter $D_p^* \geq 6$.

The proposed values of L_p^* and D_p^* for the infinite medium are in agreement with the numerical predictions from the works of Mukundakrishnan et al. (2007) and Hua et al. (2008). A parametric analysis was performed based on the dimensionless numbers Re, We, Mo and Eo. The ratio of density and viscosity was selected to be equal to $\frac{\rho_l}{\rho_g} = 1000$ and $\frac{\mu_l}{\mu_g} = 100$. It should be noted that the value of $Mo = 2.52 \cdot 10^{-11}$ for the spherical and oblate ellipsoidal or wobbling regime represents fluid properties for air-water system, while for the oblate ellipsoidal cap the value of Mo selected to be equal to 116. The simulations of air-water system are characterised by great complexity due to the instabilities at the interface and the need of small time step ($10^{-5} - 10^{-6}$) for the convergence, as well as high demand of fine grid resolution.

The numerical results predicted very good the terminal bubble shapes for the spherical, oblate ellipsoidal and oblate ellipsoidal cap bubble regimes. The results regarding the terminal bubble shape at $D_p^* = 5$ are also in very good agreement with similar numerical studies from the literature for infinite medium conditions. The predicted terminal velocities, the values of terminal Re and We numbers decrease with the increase of the lateral wall effects, while increase with increasing the wall distance on the bubble up to reaching the infinite medium conditions (negligible wall effects).

The flow field was also investigated and illustrated for the aforementioned bubble regimes. It is concluded that the strength of vortices decrease with small values of the pipe diameter. It is also observed that the vortices for the oblate ellipsoidal present a small asymmetry due to the oscillations of the zig-zag bubble motion, which characterises air bubbles in water. As a result, the numerical method is capable to handle these type of flows with satisfactory accuracy for bubble flows with high Reynolds numbers. However, for flows with $Re > 2000$ the accuracy of method is lower and is dependent on the grid resolution. Therefore, the use of an adaptive grid refinement method for very high Reynolds number is necessary, in order to obtain high accuracy for the interfacial region.

Bubble regimes maps with reference to $Re_{T_{sim}}$ and Eo numbers for different wall distances were also illustrated. These regime maps provide useful information for the bubble shape deformation on the lateral wall effects.

The proposed numerical model was compared with the available numerical and experimental data of Mukundakrishnan et al. (2007) and Krishna et al. (1999), exhibiting encouraging agreement.

8.2.4 Conclusions of Chapter 7

In this Chapter, a combined immersed boundary/phase-field method was used for investigating the dynamics of Taylor bubbles rising in stagnant liquids through vertical pipes. The mathematical model was validated with available experimental and numerical data from the works of Nogueira et al. (2006b) and Kang et al. (2010), exhibiting satisfactory agreement. The proposed numerical method was used in order to investigate the effects of viscosity and density ratio, Eotvos and Morton numbers, on the creation of a three dimensional Taylor bubble rising in vertical pipe.

Numerical predictions indicate that the density and viscosity ratio have significant effects on the tail shape of the bubble, especially for high density ratio (e.g. $\frac{\rho_l}{\rho_g} = 1000$).

The role of Eotvos number is significant regarding the elongation of the tail bubble and the wake strength. As a result, the increase of Eo number results to decrease of the surface tension of the bubble. All the considered Taylor bubbles maintain a well defined spherical nose and retains its shape during the simulation.

Numerical simulations were also performed for studying the dominant role of the surface tension forces for a Taylor bubble in a vertical pipe. Two values of Eotvos number were examined, namely 3.4 and 4. For both cases of Eo number the code crash and the calculations failed, even with very small time step. The bubble motion was prevented by the strong surface tension forces. Subsequently, two additional values of Eo, 7 and 28 were selected for further study at $Mo = 2.6 \cdot 10{-}11$. In the case of $Eo = 7$, there was presence of oscillations at the bottom of the bubble.

The role of Morton number was also investigated for various values ranging from $O(10^{-11})$ to $O(10^{-4})$ with two Eo numbers of 7 and 200. The terminal shape for $Eo = 7$ is characterised as prolate spheroidal shaped with rounded trailing and leading edges. With the decrease in Mo number, the viscous forces are not too strong. As a result, the long shape of the Taylor bubble is reformed from a long and thin shape to a fatter and shorter structure. This behaviour is accompanied by squeezing and bounding the thin liquid film into a narrower region.

It is also found that there is a critical value of Mo number regarding the presence of these oscillations. The value of Morton number is $\leq 10{-}8$ for $Eo = 7$.

Numerical simulations were also conducted for the investigation of the unsteady effects on thin liquid film such as the appearance of waves at the bubble sides and break up of many small bubbles at the bottom. The numerical method presented good performance for the aforementioned phenomena, even if the current grid resolution was not fine enough. A compromise between the grid resolution and the available computer sources was unavoidable.

The numerical predictions were compared with numerical data from the works of Kang et al. (2010) and Lu and Prosperetti (2009), exhibiting encouraging agreement.

8.3 Future directions and general considerations

In the present study, special attention is given to the future applications of the current methodology but also for the further development of the CFD code. In the next sections, are presented applications of the numerical code for the dynamic investigation of several physical phenomena such as drops, bubble swarms and interfacial waves in core annular flows. General consideration are also discussed for the turbulence modelling of single- and two-phase flows, by means of LES and DNS techniques.

8.3.1 Improvement and further development of the CFD code

The existing CFD code has already been parallelised with Open Multi-Processing (OMP) which is inefficient when a large number of processors is used. Therefore, for the investigation of a rising Taylor bubble in a vertical pipe and in general for three-dimensional flow problems, the present CFD code was extended with a Message Passing Interface (MPI) to accommodate the increasing complexity of calculations. However, the sustained performance (actual scaling) of the CFD code is below the ideal scaling which is an indication for further improvement of the scalability of the CFD code. Scalability stands for the ability of a parallel system to demonstrate the increase of the performance in parallel speed up with additional number of cores.

An alternative to increase the scalability of the present CFD code could be the implementation of Hybrid programming. A Hybrid scheme is characterised as the combination of OMP and MPI. Thus, OMP (shared memory) is used inside of the symmetric multiprocessor (SMP) nodes, while MPI (distributed memory) is used between the nodes via node interconnection. In the present CFD code, the pressure solver is responsible for the poor performance of the code and also affects the parallelization process for the Navier-Stokes. This is responsible for the delay because it needs the most time (more iterations) among all the solvers of the CFD code in order to achieve converged solution.

More specifically, for the cases of DNS of two-phase flows the problem is focused on the performance of the scalable Poisson solver combined with a preconditioner in order to significantly increase the number of CPUs the solver can efficiently use. In these cases, the modern architectures of HPC motivate the use of two-level Hybrid MPI and OMP parallelization. In this study, the numerical solver is simple and based on the Gauss-Seidel Successive Over Relaxation (SOR) method without preconditioner. However, the introduction and testing of the appropriate preconditioner is not a trivial case and needs a lot of effort in order to increase the performance of solver (e.g. less iterations, faster convergence), as well as the performance of the parallelization process of the CFD code.

Further improvement could be achieved by implementing a multigrid algorithm in the existing CFD code. The main idea behind the multigrid algorithms is the convergence acceleration of an iterative method for a coarse problem and then the obtained solution is interpolated to the fine grid in order to correct the fine grid approximation. A multigrid algorithm comprises the three following steps, namely smoothing, restriction and interpolation or prolongation. More details for the multigrid methods and their implementation can be found in the textbook by Wesseling (1992). Multigrid algorithms present very good performance for symmetric systems. They can also be adopted for the solution of many sparse and realistic systems with high accuracy in a fixed number of iterations.

An increase of the current accuracy of the CFD code can be achieved by replacing the first order in time Euler numerical scheme with a third-order Runge-Kutta scheme. This upgrade will satisfy the appropriate accuracy for problems involving flows with turbulence because the Euler scheme is unstable for turbulent flows and as a result needs small time step (Fishpool and Leschziner, 2009). Another alternative is the implementation of an adaptive grid refinement which will be able to ensure much better accuracy for the simulation of the interfacial region compared to the adopted Cartesian grid.

8.3.2 Implementation of the present numerical method for the investigation of other flow problems

During the author's PhD studies a substantial number of numerical simulations was performed to investigate the dynamics of droplets, bubble swarms and interfacial waves in core annular flows (CAF) in pipes. The main goal of these simulations was initially to examine the capability of the numerical code to handle this type of flow problems and to comprise the base for the extension of the numerical code for future applications.

The numerical code was shown to be capable of simulating the aforementioned problems with good agreement against available qualitative data for the topological changes of the interface, wherever possible. However, limitations in computing resources and lack of the desired performance of the numerical code to handle many CPU nodes efficiently did not allow the further investigation of the above problems, in particular for the cases of bubble swarms and interfacial waves in pipes.

8.3.2.1 Drop dynamics

Figure 8.1 illustrates the shape deformation and the velocity vectors of a three-dimensional drop in a horizontal pipe. The characteristic parameters for the present numerical simulations are: $Re_p = 40$, $Ca = 0.5$, $r_v = 0.1$, $r_d = 1$ and $Eo = 0.001$.

The initial numerical predictions for the drop terminal shape are in very good agreement with the numerical predictions from the work of Coulliette and Pozrikidis (1998) (see Figures 8(a)-(b) and 13(a)-(b)), as well as to available micro-photographs of red blood circulating in the mesentery of a dog (Fung, 1969) and travelling in capillary tube (Gaehtgens, 1980). Hence, the obtained initial results indicate the capability of the proposed method to investigate the individual drop motion under the effect of different parameters such as the Reynolds number, Eotvos number, ratio viscosity, ratio density, among others.

The study of drop dynamics is of great importance for many physical problems (e.g. oil recovery, blood flow) and could be one of the future directions for further research with the current numerical method in the field of micro-hydrodynamics and in particular for the tank-treating motion of the red-blood-cell membrane (Basu et al., 2011).

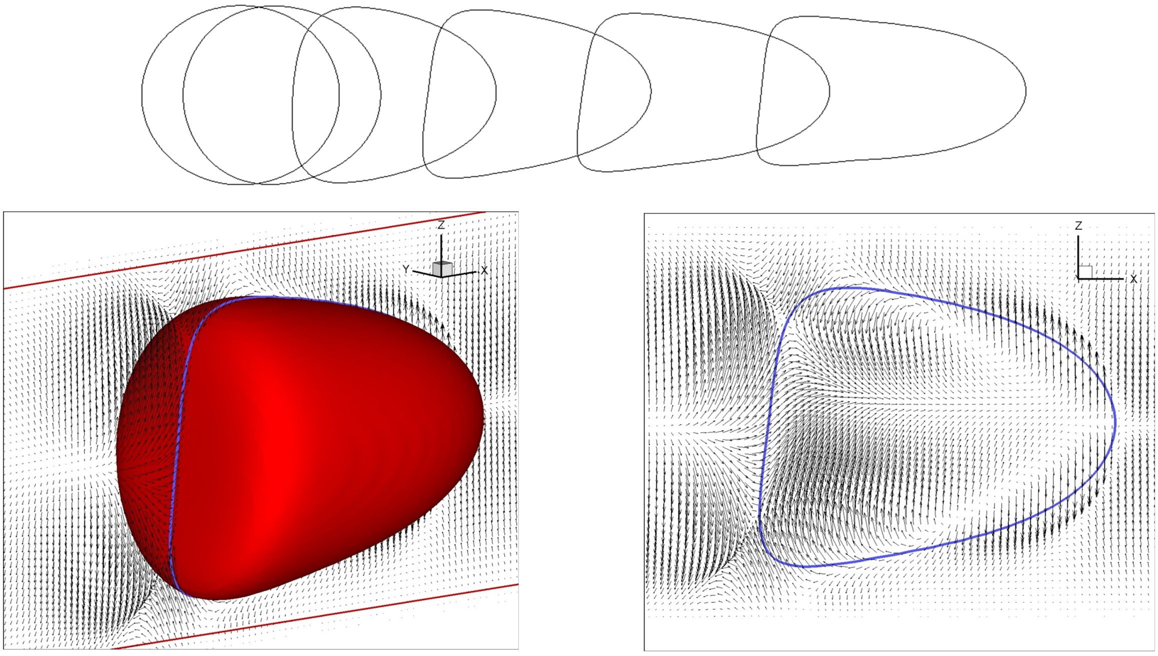

Figure 8.1: Shape deformation of a drop in a horizontal pipe for $Re_p = 40$, $Ca = 0.5$, $r_v = 0.1$, $r_d = 1$ and $Eo = 0.001$.

8.3.2.2 Bubble swarms

Another interesting physical problem for investigating with the present numerical method is the dynamics of the bubble swarms. Dynamics of bubble flows is very important in order to control the efficiency and the hydrodynamics in bubble columns or chemical and biological reactors (Roghair et al., 2011; Stewart, 1995). This type of flows is difficult to simulate due to the high surface tension (e.g. air-water system), high Reynolds numbers, presence of parasitic currents and mass loss.

It is also known that the bubble swarm flow is dependent on the Morton number for distinguishing the transition from “coalescing” to “non-coalescing” between “low-Mo” and “high-Mo” liquids, a suggested value of $Mo = 4 \cdot 10^{-4}$ was proposed by (Stewart, 1995) for the transition, as well as by many others.

Initial numerical results showed that the present method is capable of handling this type of flows. However, there is high demand of computational resources and time in order to take even some results after some thousands of iterations due to the very small time step $\Delta t = 4 \cdot 10^{-5}$. The selected parameters for the simulation are $Eo = 1.2$, $Mo = 2.52 \cdot 10^{-11}$, $\frac{\rho_l}{\rho_g} = 1000$ and $\frac{\mu_l}{\mu_g} = 100$. A fine grid of 500x260x260 and a number of 30 bubbles were also selected for the present simulation. It is important to mention that the grid resolution affects the capture of the bubble coalescence. Therefore, there is a need for fine grid resolution. The current resolution is sufficient for capturing the coalescence of bubble swarms, as shown in Figure 8.2.

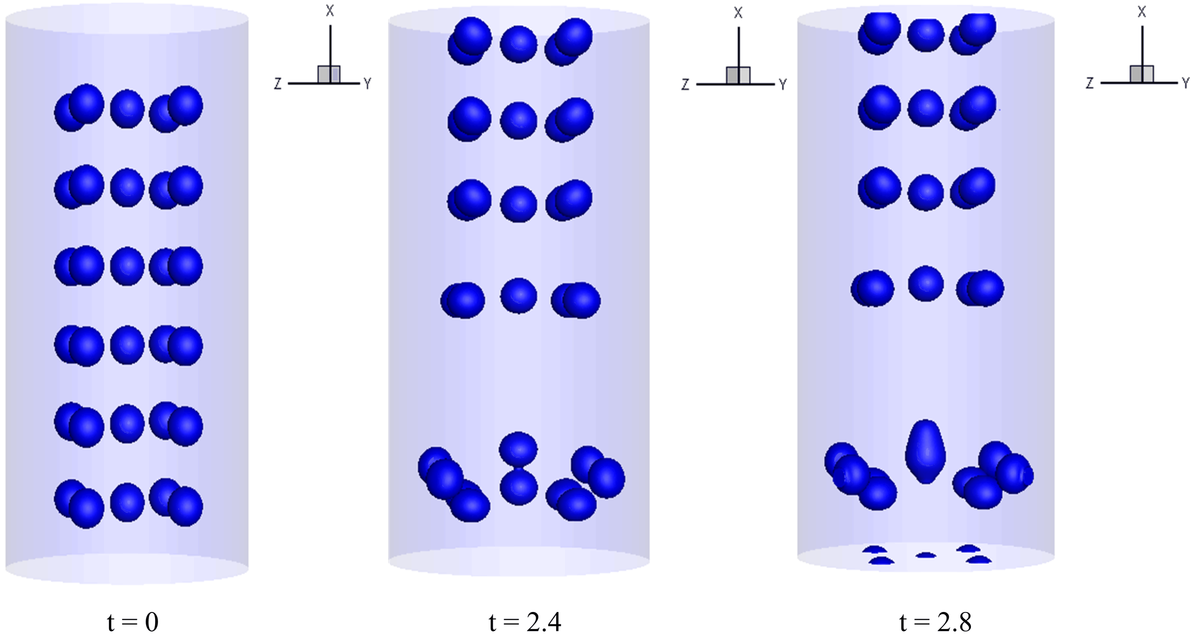

Figure 8.2: Different time frames of a bubble swarm simulation for $Eo = 1.2$, $Mo = 2.52 \cdot 10^{-11}$.

It should be noted that the Morton number is very small and it is expected multiple coalescence phenomena and mergers of the bubble array in a swarm, as previously mentioned. Figure 8.2 illustrates time frames of the bubble swarm simulation for the ellipsoidal regime which lead to coalescence all the bubble swarms at the end of the simulation. However, in the current case only an initial part of the simulation was presented. In Figure 8.2 (b) and (c), it can be seen the initial and intermediate stages of the coalescence between two bubbles of the bubble swarm at different time frames. The obtained numerical results are in good agreement with quantitative experimental and numerical data from the works of Stewart (1995) and Smolianski et al. (2008), respectively.

The current methodology looks promising for future simulations regarding the investigation of the drag force and the interaction between the bubbles of the bubble swarms.

8.3.2.3 Interfacial waves in core annular flows

Initial results for the investigation of interfacial waves in annular-core flow (CAF) are also presented. CAF is attractive option for heating or diluting the oil. In lubricating CAF the core (oil) is surrounded by less viscous annulus (water). It has been observed by many scientists that the waves on the oil/water interface determine the stability of the flow.

Numerical simulations of interfacial waves were performed for a less viscous core surrounded by more viscous annulus. Interfacial waves were simulated for investigating the propagating waves and the type of the waves (e.g. bamboo, snake, corkscrew, etc.). Future numerical simulations for interface waves in core annular flow will be useful to performed in order to identify flow patterns and the effects of gravity acceleration in the wave formation.

Figure 8.3 presents the formation of interfacial waves for $Re_p = 20$, $r_v = 0.1$, $r_d = 1$ and $Ca = 0.5$. According to the author's knowledge this is the first application of 3-D simulations for interfacial waves in CAF using an immersed boundary/phase-field method. However, the limitations of computing resources and the high demands for CPU time did not allow the further investigation of the physical phenomenon with the current version of the CFD code.

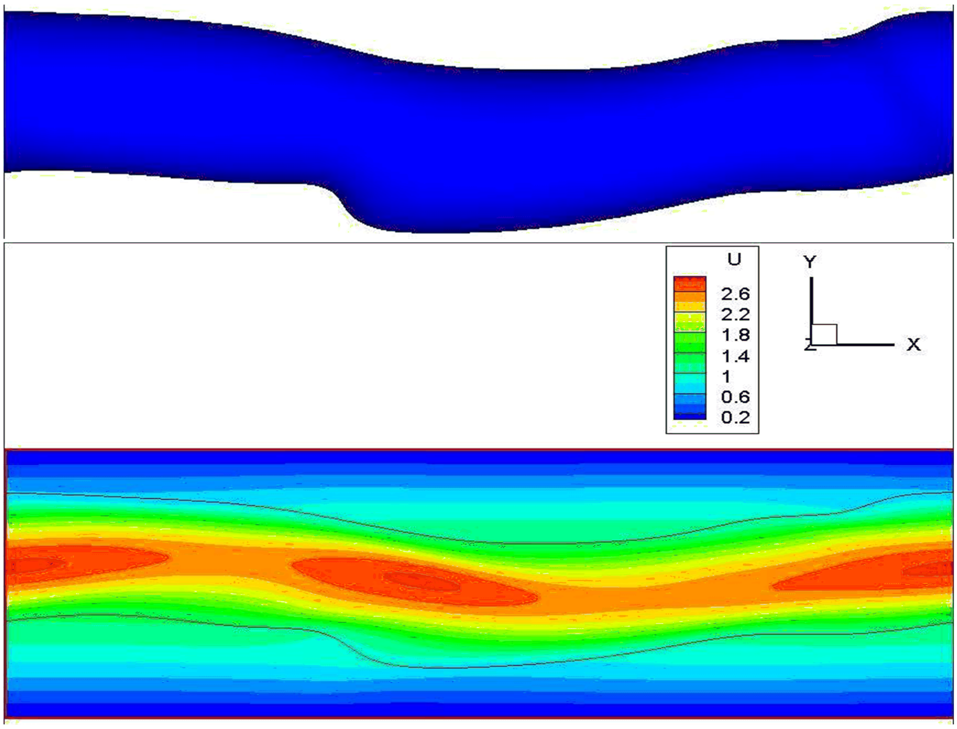

Figure 8.3: Formation of interfacial waves in horizontal pipe for $Re_p = 20$ and $Ca = 0.5$.

8.3.3 Applications of DNS and LES to flows in pipes

Solutions of turbulent flow problems can be obtained by using various analytical or numerical approaches, with different level of accuracy in each case. Among the latter approaches, the Direct Numerical Simulation (DNS) has made a significant contribution in turbulence research over the last decades (Moin and Mahesh, 1998), as it involves the numerical solution of the above full three-dimensional, time-dependent NavierStokes equations without the need of any turbulence model. DNS is indeed useful for the investigation of turbulence mechanisms, the improvement and development of turbulence models and for assessing two-point closure theories.

Another modelling approach, promising to be more accurate and of wider applicability than Reynolds-Averaged Navier Stokes (RANS) and less computationally demanding than DNS, is the Large Eddy Simulation (LES) approach. In LES of turbulence, the important large scales are fully resolved whilst the small sub-grid scales are modelled.

Wall resolving LES is a method that near to the wall, where the energy spectrum is made up of anisotropic currents, performs a direct numerical simulation; away from the wall isotropic currents make up a large fraction of the energy spectrum and are modelled by the use of sub-grid scale (SGS) model. Therefore, the mesh pitch away from the walls may be greater and computational time is shorter than required by direct numerical simulation. Hence, LES is only meaningful on a refined grid; on a regular grid fine enough to resolve wall currents the sub-grid scale model is unnecessary.

The required resolution of a wall-bounded resolved LES should be sufficient in order to resolve the wall layer according to Piomelli (2001). More specifically, $\Delta x^+ \approx 50 - 150, \Delta z^+ \approx 15 - 40$ and the first point in the wall normal direction is at $y^+ < 1$. However, with the help of the appropriate wall model required resolution can be adjusted to $\Delta x^+ \approx 100 - 160, \Delta z^+ \approx 100 - 300$ and the first point in the wall-normal direction should be at $y^+ = 30 - 150$ (Piomelli, 2001). More details for wall modelling may be found in the review paper by Piomelli and Balaras (2002).

LES on turbulent two-phase channel flows with flat interface combined with Van Driest damping wall functions is an ordinary approach for the investigation of this type of problems. However, this approach is not preferable for LES of turbulent two-phase pipe flows, by means of a phase-field method for the interface, because of the following obstacles: a) Cahn-Hilliard equation is difficult to solve on a stretched grid, b) Stretched grid is static and therefore only suitable for simulations where interface is stationary, c) Stretched grid is refined only in one direction and therefore is not suitable for simulations where large waves are developed in the interface.

Adaptive grid refinement can be used to overcome the above mentioned obstacles, but requires enormous amounts of computing sources especially for three-dimensional simulations. In the present numerical code the Euler scheme is the selected time discretisation scheme which can be used for the present type of problems (laminar flows) without any issue. However, the Euler scheme is unstable for turbulent flow (needs very small time step) and should be replaced by a 3rd order Runge-Kutta scheme. More details can be found in the work of (Fishpool and Leschziner, 2009).

Another issue is the selection of the appropriate pipe length for obtaining the minimum amount of turbulence statistics. For a turbulent single-phase pipe flow, the literature recommends a minimum length of 5 pipe diameters (D). Experimental evidence indicates that for turbulent two-phase pipe flow a larger domain (e.g. $7-10\,D$) will be required in order to obtain high quality statistics. However, the larger pipe domain requires larger number of grid nodes and as a result there is a high demand for computing sources and post-processing for large data files.

Due to space limitations, the interested reader is directed to the recent review paper by Argyropoulos and Markatos (2015). This paper reviews the problem and successes of computing turbulent flows. The review is primarily concerned with the most recent methods for such computer predictions. The successes and problems are demonstrated by listing and briefly discussing several applications of DNS and LES to flows in pipes and free-surface flows. The relevant material is certainly to much to be presented in a single section. For this reason, only the Table 8.1 and 8.2 with previous studies in DNS and LES of turbulent single-phase pipe flows are presented. To the author's best knowledge two-phase pipe LES and DNS studies are not available except for the recent work of Lakehal (2010). He performed Large Eddy Interface Simulation (LEIS) for modelling the slug formation of a two-phase pipe flow and the emergency core cooling (ECC). A BFC grid with block-mesh refinement (BMR) was adopted for the computational domain and a level set method for the interfacial region. The numerical results were compared with analytical and experimental data, predicting the slug speed (tail and centre) with reasonable accuracy.

Some important DNS and LES works involving turbulent flows with free surfaces, with and without shear can be found in the recent review by Argyropoulos and Markatos (2015).

The LES approach appears, from the given referenced that describe its applications, to have reached maturity. However, further work is required to improve the characteristics of the method for more types of turbulent flow, in particular for complex industrial flows. There are still challenges facing LES of turbulence such as the development of advanced sub-grid scale models, high-order discretization techniques for eliminating the numerical errors, implementation on unstructured grids, control of the numerical errors, interaction with other physical mechanisms and a “simple” wall stress model for wall-bounded complex flows. LES is currently the most accurate method available for practical computations and its use is expected to rise fast over the next few years.

The continuing progress of computer-hardware development is promising for DNS, in the near future, with major improvements expected in statistical samples and in considering a variety of several physical parameters, for better understanding of the turbulence nature. DNS is obviously the method that provides the most precise and detailed description of turbulence but it is still out of reach of the available everyday computer power, i.e. it cannot be used for everyday engineering design. It is, however, even today very useful as it serves as a “test” of the other model predictions and of any new ideas on turbulence calculations. Until it becomes also a practical tool the author recommends the use of “two-fluid” models (Argyropoulos and Markatos, 2015) that appear very promising (but need further refinement), and LES along with its derivatives and the hybrid methods that have already reached maturity.

Table 8.1: Previous studies in DNS of turbulent single-phase pipe flows.

References	Mesh	Re_b	Geometry	Method
Nikitin (1994)	43x64x43	2000-4000	Straight pipe	FDM + SM
Eggels et al. (1994)	96x128x256	5300	Straight pipe	FVM
Zhang et al. (1994)	75x128x128	2500,4000	Straight pipe	SM
Loulou et al. (1997)	72x160x192	5600	Straight pipe	B-spline spectra
Orlandi and Fatica (1997)	128x96x257	4900	Rotating pipe	FDM
Orlandi and Ebstein (2000)	129x96x193	4900	Rotating pipe	FDM
Schmidt et al. (2001)	Cyl:150 elements Car: 64 elements	4910	Straight pipe	SEM
Wagner et al. (2001)	70x240x486	10300	Straight pipe	FVM
Fukagata and Kasagi (2002)	96x128x256	5300	Straight pipe	FDM
Veenman (2004)	152x256x394	10300	Straight pipe	SM
Nikitin and Yakhot (2005)	200x160x256	6000	Elliptical pipe	FDM
Voronova and Nikitin (2006)	32x256x64	4000	Elliptical pipe	FDM
Voronova and Nikitin (2007)	48x256x128	6000	Elliptical pipe	FDM
Wu and Moin (2008)	300x1024x1048	44000	Straight pipe	FDM
Boersma (2011)	430x512x1024	24500, 61000	Straight pipe	SM + FDM
Wu et al. (2012)	256x1024x2048	24580	Straight pipe	FDM
Khoury et al. (2013)[2]	18.67×10^6, 121.4×10^6, 4374×10^6, 2.184×10^9	5300, 11700, 19000, 37700	Straight pipe	SEM

FDM: Finite Difference Method; FVM: Finite Volume Method; SM: Spectral Method; SEM: Spectral Element Method; Car: for Cartesian coordinates; Cyl: for Cylindrical coordinates; Re_b: Reynolds number based on bulk-mean velocity and pipe diameter of the pipe.

---

[2] Number of grid points for each considered Re_b, respectively

Table 8.2: Previous studies in LES of turbulent single-phase pipe flows.

References	Mesh	Re_b	Geometry	SGS model	Method
Unger and Friedrich (1991)	96x128x256	50000	Straight pipe	Smagorinsky	FVM
Eggels et al. (1993)	96x128x256	59500	Rotating pipe	Smagorinsky	FVM
Boersma and Nieuwstadt (1996)	40x114x200	20000	Curved pipe	Smagorinsky	FVM
Yang (2000)	192x64x128	20000	Rotating pipe	Smagorinsky Dynamic	FVM
Rudman and Blackburn (1999)	Car:192	36700	Straight pipe	Smagorinsky	SEM
Schmidt et al. (2001)	Cyl:80 Car:105	16000	Straight pipe	Smagorinsky	SEM
Feiz et al. (2003)	65x39x65	4900, 7400	Rotating pipe	Smagorinsky Dynamic	FDM
Jordan (2003)	64x141x401	8000	Pipe roughened ($p/k = 5$)	Dynamic	FDM
Vijiapurapu and Cui (2004)	64x96x64	5000, 30000	Straight pipe	Smagorinsky Dynamic	FDM
Vijiapurapu and Cui (2010)	96x128x128	100000	Pipe roughened ($p/k = 2, 5, 10$)	Dynamic	FVM
Jung and Chung (2012)	128x256x256	7000- 36000	Straight pipe	Dynamic	FDM

FDM: Finite Difference Method; FVM: Finite Volume Method; SEM: Spectral Element Method; Car:elements for Cartesian coordinates; Cyl: elements for Cylindrical coordinates; Re_b: Reynolds number based on bulk-mean velocity and pipe diameter of the pipe; p/k: ratio of rib periodicity where p is the distance between two successive ribs and k is the rib height.

Bibliography

Ahn, H. T. and Shashkov, M. (2009). Adaptive moment-of-fluid method. *Journal of Computational Physics*, 228(8):2792–2821.

Amsden, A. A. and Harlow, F. H. (1970). The smac method: A numerical technique for calculating incompressible fluid flow. Technical report, Los Alamos Scientific Laboratory, LA-4370.

Anderson, D., McFadden, G., and Wheeler, A. (1998). Diffuse-interface methods in fluid mechanics. *Annual Review of Fluid Mechanics*, 30:139–165.

Anglart, H. and Podowski, M. (2002). Fluid mechanics of taylor bubbles and slug flows in vertical channels. *Nuclear Science and Engineering*, 140:165–171.

Angot, P., Bruneau, C.-H., and Fabrie, P. (1999). A penalization method to take into account obstacles in incompressible viscous flows. *Numerische Mathematik*, 81(4):497–520.

Argyropoulos, C. and Markatos, N. (2015). Recent advances on the numerical modelling of turbulent flows. *Applied Mathematical Modelling*, 39(2):693–732.

Argyropoulos, C. D. (2011). Numerical simulations of turbulent two-phase pipe flows. Mphil report, MPhil Report, Department of Chemical Engineering, Imperial College London, UK, pp: 1-75.

Ashgriz, N. and Poo, J. Y. (1991). Flair: Flux line-segment model for advection and interface reconstruction. *Journal of Computational Physics*, 93(2):449–468.

Aulisa, E., Manservisi, S., Scardovelli, R., and Zaleski, S. (2003). A geometrical area-preserving volume-of-fluid advection method. *Journal of Computational Physics*, 192(1):355–364.

Azzopardi, B. (2006). *Gas-liquid flows*. New York: Begell House.

Badalassi, V. E., Ceniceros, H. D., and Banerjee, S. (2003). Computation of multiphase systems with phase field models. *Journal of Computational Physics*, 190(2):371–397.

Balaras, E. (2004). Modeling complex boundaries using an external force field on fixed cartesian grids in large-eddy simulations. *Computers and Fluids*, 33(3):375–404.

Bandringa, H. (2010). Immersed boundary methods, Master thesis,.

Barr, G. (1926). The air-bubble viscometer. *The London, Edinburgh, and Dublin Philosophical Magazine and Journal of Science*, 1(2):395–405.

Bashforth, F. and Adams, J. (1883). *An attempt to test the theories of capillary action by comparing the theoretical and measured forms of drops of fluid, with an explanation of the method of integration employed in constructing the tables which give the theoretical forms of such drops*. Cambridge University Press, Cambridge, UK.

Basu, H., Dharmadhikari, A., Dharmadhikari, J., Sharma, S., and Mathur, D. (2011). Tank treading of optically trapped red blood cells in shear flow. *Biophysical Journal*, 101(7):1604–1612.

Batchelor, G. K. (1987). The stability of a large gas bubble rising through liquid. *Journal of Fluid Mechanics*, 184:399–422.

Batty, C., Bertails, F., and Bridson, R. (2007). A fast variational framework for accurate solid-fluid coupling. *ACM Transactions on Graphics*, 26(3):100.

Bendiksen, K. H. (1985). On the motion of long bubbles in vertical tubes. *International Journal of Multiphase Flow*, 11(6):797–812.

Berthelsen, P. A. and Faltinsen, O. M. (2008). A local directional ghost cell approach for incompressible viscous flow problems with irregular boundaries. *Journal of Computational Physics*, 227(9):4354–4397.

Beyer, R. P. and Leveque, R. J. (1992). Analysis of a one-dimensional model for the immersed boundary method. *SIAM Journal on Numerical Analysis*, 29(2):332–364.

Bhaga, D. and Weber, M. E. (1981). Bubbles in viscous liquids: shapes, wakes and velocities. *Journal of Fluid Mechanics*, 105:61–85.

Biben, T., Kassner, K., and Misbah, C. (2005). Phase-field approach to three-dimensional vesicle dynamics. *Physical Review E*, 72(4):041921.

Boersma, B. J. (2011). Direct numerical simulation of turbulent pipe flow up to a reynolds number of 61,000. *Journal of Physics: Conference Series*, 318(4):042045.

Boersma, B. J. and Nieuwstadt, F. T. M. (1996). Large-eddy simulation of turbulent flow in a curved pipe. *Journal of Fluids Engineering*, 118(2):248–254.

Bonometti, T. and Magnaudet, J. (2007). An interface-capturing method for incompressible two-phase flows. validation and application to bubble dynamics. *International Journal of Multiphase Flow*, 33:109–133.

Borcia, R. and Bestehorn, M. (2003). Phase-field model for marangoni convection in liquid-gas systems with a deformable interface. *Physical Review E*, 67(6):066307.

Boris, J. P. and Book, D. L. (1973). Flux-corrected transport. i. shasta, a fluid transport algorithm that works. *Journal of Computational Physics*, 11:38–69.

Bourlioux, A. (1995). A coupled level-set volume-of-fluid algorithm for tracking material interfaces. In *Proceedings of 6th International Symposium on Computational Fluid Dynamics, Lake Tahoe, CA*, pages 15–22.

Brackbill, J., Kothe, D., and Zemach, C. (1992). A continuum method for modeling surface tension. *Journal of Computational Physics*, 100:335–354.

Bramble, J. and King, J. (1996). A finite element method for interface problems in domains with smooth boundaries and interfaces. *Advances in Computational Mathematics*, 6:109–138.

Bratland, O. (2009). *Pipe flow 1: Single-phase flow assurance.*

Bratland, O. (2010). *Pipe flow 2: Multi-phase flow assurance.*

Bray, A. (1994). Theory of phase-ordering kinetics. *Advances in Physics*, 43:357–459.

Brennen, E. (2005). *Fundamentals of Multiphase Flows.* Cambridge University Press.

Brereton, G. and Korotney, D. (1991). Coaxial and oblique coalescence of two rising bubbles. In *Sahin, L., Tryggvason, G. (Eds.), Dynamics of Bubbles and Vortices Near a Free Surface, AMD-vol. 119 ASME, New York.*

Bretherton, F. P. (1961). The motion of long bubbles in tubes. *Journal of Fluid Mechanics*, 10:166–188.

Briscolini, M. and Santangelo, P. (1989). Development of the mask method for incompressible unsteady flows. *Journal of Computational Physics*, 84:57–75.

Brown, R. A. S. (1965). The mechanics of large gas bubbles in tubes: I. bubble velocities in stagnant liquids. *The Canadian Journal of Chemical Engineering*, 43(5):217–223.

Bugg, J., Mack, K., and Rezkallah, K. (1998). A numerical model of taylor bubbles rising through stagnant liquids in vertical tubes. *International Journal of Multiphase Flow*, 24:271–281.

Bugg, J. and Saad, G. (2002). The velocity field around a taylor bubble rising in a stagnant viscous fluid: numerical and experimental results. *International Journal of Multiphase Flow*, 28:791–803.

Cahn, J. W. and Hilliard, J. E. (1958). Free energy of a nonuniform system. i. interfacial free energy. *The Journal of Chemical Physics*, 28:258–267.

Campos, J. B. L. M. and Carvalho, J. R. F. G. D. (1988). An experimental study of the wake of gas slugs rising in liquids. *Journal of Fluid Mechanics*, 196:27–37.

Cavanagh, D. P. and Eckmann, D. M. (1999). Interfacial dynamics of stationary gas bubbles in flows in inclined tubes. *Journal of Fluid Mechanics*, 398:225–244.

Cervone, A., Manservisi, S., Scardovelli, R., and Zaleski, S. (2009). A geometrical predictor-corrector advection scheme and its application to the volume fraction function. *Journal of Computational Physics*, 228:406–419.

Chakraborty, I., Biswas, G., and Ghoshdastidar, P. (2013). A coupled level-set and volume-of-fluid method for the buoyant rise of gas bubbles in liquids. *International Journal of Heat and Mass Transfer*, 58:240–259.

Chang, Y., Hou, T., Merriman, B., and Osher, S. (1996). A level set formulation of eulerian interface capturing methods for incompressible fluid flows. *Journal of Computational Physics*, 124:449–464.

Chen, L., Garimella, S. V., Reizes, J. A., and Leonardi, E. E. (1999). The development of a bubble rising in a viscous liquid. *Journal of Fluid Mechanics*, 387:61–96.

Chen, S., Johnson, D. B., and Raad, P. E. (1991). *The surface marker method, in Computational Modeling of Free and Moving Boundary Problems, Vol. 1,*. De Gruyter, New York.

Chen, S., Johnson, D. B., Raad, P. E., and Fadda, D. (1997). The surface marker and micro cell method. *International Journal for Numerical Methods in Fluids*, 25:749–778.

Choi, J.-I., Oberoi, R. C., Edwards, J. R., and Rosati, J. A. (2007). An immersed boundary method for complex incompressible flows. *Journal of Computational Physics*, 224(2):757–784.

Chorin, A. J. (1967). A numerical method for solving incompressible viscous flow problems. *Journal of Computational Physics*, 2:12–26.

Chorin, A. J. (1968). Numerical solution of the navier-stokes equations. *Mathematics of Computation*, 22:745–762.

Chorin, A. J. (1980). Flame advection and propagation algorithms. *Journal of Computational Physics*, 35:1–11.

Clarke, D. K., Salas, M., and Hassan, H. (1986). Euler calculations for multielement airfoils using cartesian grids. *AIAA Journal*, 24:353–358.

Clift, R., Grace, J., and M.E., W. (1978). *Bubbles, Drops, and Particles.* Academic, New York,.

Collins, R., Moraes, F. F. D., Davidson, J. F., and Harrison, D. (1978). The motion of a large gas bubble rising through liquid flowing in a tube. *Journal of Fluid Mechanics*, 89:497–514.

Coulliette, C. and Pozrikidis, C. (1998). Motion of an array of drops through a cylindrical tube. *Journal of Fluid Mechanics*, 358:1–28.

Coutanceau, M. and Thizon, P. (1981). Wall effect on the bubble behaviour in highly viscous liquids. *Journal of Fluid Mechanics*, 107:339–373.

Crank, J. and Nicolson, P. (1947). A practical method for numerical evaluation of solutions of partial differential equations of the heat-conduction type. *Mathematical Proceedings of the Cambridge Philosophical Society*, 43:50–67.

Davies, R. M. and Taylor, G. (1950). The mechanics of large bubbles rising through extended liquids and through liquids in tubes. *Proceedings of the Royal Society of London. Series A. Mathematical and Physical Sciences*, 200:375–390.

Delfos, R., Rops, C. M., Kockx, J. P., and Nieuwstadt, F. T. M. (2001). Measurement of the recoalescence flux into the rear of a taylor bubble. *Physics of Fluids*, 13:1141–1150.

Dijkhuizen, W., Roghair, I., Annaland, M. V. S., and Kuipers, J. A. M. (2010). Dns of gas bubbles behaviour using an improved 3d front tracking model-model development. *Chemical Engineering Science*, 65:1427–1437.

Dijkhuizen, W., van den Hengel, E. I. V., Deen, N. G., van Sint Annaland, M., and Kuipers, J. A. M. (2005). Numerical investigation of closures for interface forces acting on single air-bubbles in water using volume of fluid and front tracking models. *Chemical Engineering Science*, 60:6169–6175.

Ding, H., Spelt, P. D. M., and Shu, C. (2007). Diffuse interface model for incompressible two-phase flows with large density ratios. *Journal of Computational Physics*, 226:2078–2095.

Dukler, A. and Taitel, W. (1986). *Flow pattern transitions in gas-liquid systems: Measurements and modelling.* Hemisphere Publishing Corporation.

Dumitrescu, D. T. (1943). Stromung an einer luftblase im senkrechten rohr. *ZAMM - Journal of Applied Mathematics and Mechanics*, 23:139–149.

Dyadechko, V. and Shashkov, M. (2005). Moment-of-fluid interface reconstruction. Technical report, Los Alamos National Laboratory.

Eggels, J. G. M., Unger, F., Weiss, M. H., Westerweel, J., Adrian, R. J., Friedrich, R., and Nieuwstadt, F. T. M. (1994). Fully developed turbulent pipe flow: a comparison between direct numerical simulation and experiment. *Journal of Fluid Mechanics*, 268:175–210.

Eggels, J. G. M., Westerweel, J., Nieuwstadt, F. T. M., and Adrian, R. J. (1993). Direct numerical simulation of turbulent pipe flow. *Applied Scientific Research*, 51:319–324.

Enright, D., Fedkiw, R., Ferziger, J., and Mitchell, I. (2002). A hybrid particle level set method for improved interface capturing. *Journal of Computational Physics*, 183:83–116.

Fadlun, E. A., Verzicco, R., Orlandi, P., and Mohd-Yusof, J. (2000). Combined immersed-boundary finite-difference methods for three-dimensional complex flow simulations. *Journal of Computational Physics*, 161:35–60.

Feiz, A. A., Ould-Rouis, M., and Lauriat, G. (2003). Large eddy simulation of turbulent flow in a rotating pipe. *International Journal of Heat and Fluid Flow*, 24:412–420.

Fishpool, G. and Leschziner, M. (2009). Stability bounds for explicit fractional-step schemes for the navier-stokes equations at high reynolds number. *Computers and Fluids*, 38:1289–1298.

Francois, M. M., Cummins, S. J., Dendy, E. D., Kothe, D. B., Sicilian, J. M., and Williams, M. W. (2006). A balanced-force algorithm for continuous and sharp interfacial surface tension models within a volume tracking framework. *Journal of Computational Physics*, 213:141–173.

Frank, X., Funfschilling, D., Midoux, N., Euml, L., and Li, H. Z. (2006). Bubbles in a viscous liquid: lattice boltzmann simulation and experimental validation. *Journal of Fluid Mechanics*, 546:113–122.

Fukagata, K. and Kasagi, N. (2002). Highly energy-conservative finite difference method for the cylindrical coordinate system. *Journal of Computational Physics*, 181:478–498.

Fung, Y. (1969). Blood flow in the capillary bed. *Journal of Biomechanics*, 2:353–372.

Gaehtgens, P. (1980). Flow of blood through narrow capillaries: rheological mechanisms determining capillary hematocrit and apparent viscosity. *Biorheology*, 17:183–189.

Gao, T., Tseng, Y.-H., and Lu, X.-Y. (2007). An improved hybrid cartesian/immersed boundary method for fluid-solid flows. *International Journal for Numerical Methods in Fluids*, 55:1189–1211.

Ge, L. and Sotiropoulos, F. (2007). A numerical method for solving the 3d unsteady incompressible navier-stokes equations in curvilinear domains with complex immersed boundaries. *Journal of Computational Physics*, 225:1782–1809.

Gibson, A. (1913). On the motion of long air-bubbles in a vertical tube. *Philosophical Magazine Series 6*, 26:952–965.

Gilmanov, A. and Sotiropoulos, F. (2005). A hybrid cartesian/immersed boundary method for simulating flows with 3d, geometrically complex, moving bodies. *Journal of Computational Physics*, 207:457–492.

Gilmanov, A., Sotiropoulos, F., and Balaras, E. (2003). A general reconstruction algorithm for simulating flows with complex 3d immersed boundaries on cartesian grids. *Journal of Computational Physics*, 191:660–669.

Glimm, J., Grove, J., Li, X., Shyue, K., Zeng, Y., and Zhang, Q. (1998). Three-dimensional front tracking. *SIAM Journal on Scientific Computing*, 19:703–727.

Glimm, J., Li, X. L., Liu, Y., and Zhao, N. (2001). Conservative front tracking and level set algorithms. *Proceedings of the National Academy of Sciences*, 98:14198–14201.

Glimm, J., Marchesin, D., and McBryan, O. (1981). A numerical method for two phase flow with an unstable interface. *Journal of Computational Physics*, 39:179–200.

Glimm, J., McBryan, O., Menikoff, R., and Sharp, D. H. (1986). Front tracking applied to rayleigh-taylor instability. *SIAM Journal on Scientific and Statistical Computing*, 7:230–251.

Goldstein, D., Handler, R., and Sirovich, L. (1993). Modeling a no-slip flow boundary with an external force field. *Journal of Computational Physics*, 105:354–366.

Gopala, V. R. and van Wachem, B. G. (2008). Volume of fluid methods for immiscible-fluid and free-surface flows. *Chemical Engineering Journal*, 141:204–221.

Grace, J. (1973). Shapes and velocities of bubbles rising in infinite liquids. *Transactions of the Institution of Chemical Engineering*, 51:116–120.

Gurtin, M., Polignone, D., and Vinals, J. (1996). Two-phase binary fluids and immiscible fluids described by an order parameter. *Mathematical Models and Methods in Applied Sciences*, 6:815–831.

Harlow, F. H. and Welch, J. E. (1965). Numerical calculation of time-dependent viscous incompressible flow of fluid with free surface. *Physics of Fluids*, 8:2182–2189.

Harmathy, T. Z. (1960). Velocity of large drops and bubbles in media of infinite or restricted extent. *AIChE Journal*, 6:281–288.

Harvie, D., Davidson, M., and Rudman, M. (2006). An analysis of parasitic current generation in volume of fluid simulations. *Applied Mathematical Modelling*, 30:1056–1066.

Hattori, S. (1935). On the motion of a cylindrical bubble in a tube and its application to the measurement of the surface tension of a liquid. *Report of the Aeronautical Research Institute, Tokyo Imperial University*, 9:159–193.

Hewitt, G. (1982). *Handbook of multiphase systems.* Hemisphere Publishing Corporation, New York.

Hirt, C. W. and Nichols, B. D. (1981). Volume of fluid vof method for the dynamics of free boundaries. *Journal of Computational Physics*, 39:201–225.

Hnat, J. G. and Buckmaster, J. D. (1976). Spherical cap bubbles and skirt formation. *Physics of Fluids*, 19:182–194.

Hohenberg, P. C. and Halperin, B. I. (1977). Theory of dynamic critical phenomena. *Reviews of Modern Physics*, 49:435–479.

Hua, J. and Lou, J. (2007). Numerical simulation of bubble rising in viscous liquid. *Journal of Computational Physics*, 222:769–795.

Hua, J., Stene, J. F., and Lin, P. (2008). Numerical simulation of 3d bubbles rising in viscous liquids using a front tracking method. *Journal of Computational Physics*, 227:3358–3382.

Hyman, J. M. (1984). Numerical methods for tracking interfaces. *Physica D: Nonlinear Phenomena*, 12:396–407.

Iaccarino, G. and Verzicco, R. (2003). Immersed boundary technique for turbulent flow simulations. *Applied Mechanics Reviews*, 56:331–347.

Ikeno, T. and Kajishima, T. (2007). Finite-difference immersed boundary method consistent with wall conditions for incompressible turbulent flow simulations. *Journal of Computational Physics*, 226:1485–1508.

Ishii, M. and Takashi, H. (2010). *Thermo-fluid dynamics of two-phase flow.* 2nd Edition, Berlin: Springer-Verlag.

Jacqmin, D. (1999). Calculation of two-phase navier-stokes flows using phase-field modeling. *Journal of Computational Physics*, 155:96–127.

Jacqmin, D. (2000). Contact-line dynamics of a diffuse fluid interface. *Journal of Fluid Mechanics*, 402:57–88.

Jamet, D., Torres, D., and Brackbill, J. (2002). On the theory and computation of surface tension: The elimination of parasitic currents through energy conservation in the second-gradient method. *Journal of Computational Physics*, 182:262–276.

Jasnow, D. and Vinals, J. (1996). Coarse-grained description of thermo-capillary flow. *Physics of Fluids*, 8:660–669.

Jemison, M., Loch, E., Sussman, M., Shashkov, M., Arienti, M., Ohta, M., and Wang, Y. (2013). A coupled level set-moment of fluid method for incompressible two-phase flows. *Journal of Scientific Computing*, 54:454–491.

Jiang, G.-S. and Shu, C.-W. (1996). Efficient implementation of weighted ENO schemes. *Journal of Computational Physics*, 126:202–228.

Jordan, S. A. (2003). The turbulent character and pressure loss produced by periodic symmetric ribs in a circular duct. *International Journal of Heat and Fluid Flow*, 24:795–806.

Jung, S. Y. and Chung, Y. M. (2012). Large-eddy simulation of accelerated turbulent flow in a circular pipe. *International Journal of Heat and Fluid Flow*, 33:1–8.

Kang, C.-W., Quan, S., and Lou, J. (2010). Numerical study of a taylor bubble rising in stagnant liquids. *Physical Review E*, 81:066308.

Kang, S., Iaccarino, G., and Ham, F. (2009). Dns of buoyancy-dominated turbulent flows on a bluff body using the immersed boundary method. *Journal of Computational Physics*, 228:3189–3208.

Kawaji, M., DeJesus, J., and Tudose, G. (1997). Investigation of flow structures in vertical slug flow. *Nuclear Engineering and Design*, 175:37–48.

Khadra, K., Angot, P., Parneix, S., and Caltagirone, J.-P. (2000). Fictitious domain approach for numerical modelling of navier-stokes equations. *International Journal for Numerical Methods in Fluids*, 34:651–684.

Khoury, G. K., Schlatter, P., Noorani, A., Fischer, P., Brethouwer, G., and Johansson, A. (2013). Direct numerical simulation of turbulent pipe flow at moderately high reynolds numbers. *Flow, Turbulence and Combustion*, 91:475–495.

Kim, H. J., Figueroa, C. A., Hughes, T. J. R., Jansen, K. E., and Taylor, C. A. (2009). Augmented lagrangian method for constraining the shape of velocity profiles at outlet boundaries for three-dimensional finite element simulations of blood flow. *Computer Methods in Applied Mechanics and Engineering*, 198:3551–3566.

Kim, J. (2007). A numerical method for the cahn-hilliard equation with a variable mobility. *Communications in Nonlinear Science and Numerical Simulation*, 12:1560–1571.

Kim, J. (2012). Phase field models for multi-component fluid flows. *Communications in Computational Physics*, 12:613–661.

Kockx, J., Nieuwstadt, F., Oliemans, R., and Delfos, R. (2005). Gas entrainment by a liquid film falling around a stationary taylor bubble in a vertical tube. *International Journal of Multiphase Flow*, 31:1–24.

Kothe, D., Rider, W., Mosso, S., Brock, J., and Hochstein, J. (1996). Volume tracking of interfaces having surface tension in two and three dimensions. In *Aerospace Sciences Meetings*. AIAA.

Krishna, R. and Baten, J. M. v. (1999). Simulating the motion of gas bubbles in a liquid. *Nature*, 398:208–208.

Krishna, R., Urseanu, M., van Baten, J., and Ellenberger, J. (1999). Rise velocity of a swarm of large gas bubbles in liquids. *Chemical Engineering Science*, 54:171–183.

Lafaurie, B., Nardone, C., Scardovelli, R., Zaleski, S., and Zanetti, G. (1994). Modelling merging and fragmentation in multiphase flows with surfer. *Journal of Computational Physics*, 113:134–147.

Lai, M.-C. and Peskin, C. S. (2000). An immersed boundary method with formal second-order accuracy and reduced numerical viscosity. *Journal of Computational Physics*, 160:705–719.

Laird, A. D. K. and Chisholm, D. (1956). Pressure and forces along cylindrical bubbles in a vertical tube. *Industrial and Engineering Chemistry*, 48:1361–1364.

Lakehal, D. (2010). Leis for the prediction of turbulent multifluid flows applied to thermal-hydraulics applications. *Nuclear Engineering and Design*, 240:2096–2106.

Langer, J. S., Bar-on, M., and Miller, H. D. (1975). New computational method in the theory of spinodal decomposition. *Physics Review A*, 11:1417–1429.

Li, Z. and Lai, M.-C. (2001). The immersed interface method for the navier-stokes equations with singular forces. *Journal of Computational Physics*, 171:822–842.

Liberzon, D., Shemer, L., and Barnea, D. (2006). Upward-propagating capillary waves on the surface of short taylor bubbles. *Physics of Fluids (1994-present)*, 18:048103.

Llewellin, E. W., Del Bello, E., Taddeucci, J., Scarlato, P., and Lane, S. J. (2012). The thickness of the falling film of liquid around a taylor bubble. *Proceedings of the Royal Society of London A: Mathematical, Physical and Engineering Sciences.*

Loulou, P., Moser, R., Mansour, N., and Cantwell, B. (1997). Direct simulations of incompressible pipe flow using a b-spline spectral method. Technical report, NASA, pp. 1-138.

Lowengrub, J. and Truskinovsky, L. (1998). Quasi-incompressible cahn-hilliard fluids and topological transitions. *Proceedings of the Royal Society of London. Series A: Mathematical, Physical and Engineering Sciences*, 454(1978):2617–2654.

Lu, X. and Prosperetti, A. (2009). A numerical study of taylor bubbles. *Industrial & Engineering Chemistry Research*, 48:242–252.

Magnaudet, J. and Mougin, G. (2007). Wake instability of a fixed spheroidal bubble. *Journal of Fluid Mechanics*, 572:311–337.

Majumdar, J., Iaccarino, G., and Durbin, P. (2001). Rans solver with adaptive structural boundary non-conforming grids. Technical report, Center for Turbulence Research Annual Research Briefs, pp. 353-366.

Mandal, T. K., Das, G., and Das, P. K. (2008). Motion of taylor bubbles and taylor drops in liquid-liquid systems. *Industrial and Engineering Chemistry Research*, 47:7048–7057.

Mao, Z.-S. and Dukler, A. (1990). The motion of taylor bubbles in vertical tubes. i. a numerical simulation for the shape and rise velocity of taylor bubbles in stagnant and flowing liquid. *Journal of Computational Physics*, 91:132–160.

Mark, A. and van Wachem, B. G. (2008). Derivation and validation of a novel implicit second-order accurate immersed boundary method. *Journal of Computational Physics*, 227:6660–6680.

Menard, T., Tanguy, S., and Berlemont, A. (2007). Coupling level set/ vof /ghost fluid methods: Validation and application to 3d simulation of the primary break-up of a liquid jet. *International Journal of Multiphase Flow*, 33:510–524.

Mendelson, H. D. (1967). The prediction of bubble terminal velocities from wave theory. *AIChE Journal*, 13:250–253.

Mittal, R., Bonilla, C., and Udaykumar, H. (2003). Cartesian grid methods for simulating flows with moving boundaries. In *Computational Methods and Experimental Measurements XI*.

Mittal, R., Dong, H., Bozkurttas, M., Najjar, F. M., Vargas, A., and von Loebbecke, A. (2008). A versatile sharp interface immersed boundary method for incompressible flows with complex boundaries. *Journal of Computational Physics*, 227:4825–4852.

Mittal, R. and Iaccarino, G. (2005). Immersed boundary methods. *Annual Review of Fluid Mechanics*, 37:239–261.

Mittal, R., Seshadri, V., and Udaykumar, H. S. (2004). Flutter, tumble and vortex induced autorotation. *Theoretical and Computational Fluid Dynamics*, 17:165–170.

Mohd-Yusof, J. (1997). Combined immersed-boundary/b-spline methods for simulations of flow in complex geometries. Technical report, CTR Annual Research Briefs, Center for Turbulence Research, NASA Ames/Stanford University, pp: 317-327.

Moin, P. (2010). *Fundamentals of engineering numerical analysis*. Cambridge University Press.

Moin, P. and Mahesh, K. (1998). Direct numerical simulation: A tool in turbulence research. *Annual Review of Fluid Mechanics*, 30:539–578.

Moore, D. W. (1959). The rise of a gas bubble in a viscous liquid. *Journal of Fluid Mechanics*, 6:113–130.

Mukundakrishnan, K., Quan, S., Eckmann, D. M., and Ayyaswamy, P. S. (2007). Numerical study of wall effects on buoyant gas-bubble rise in a liquid-filled finite cylinder. *Physical Review E*, 76:036308.

Ndinisa, N., Wiley, D., and Fletcher, D. (2005). Computational fluid dynamics simulations of taylor bubbles in tubular membranes: Model validation and application to laminar flow systems. *Chemical Engineering Research and Design*, 83:40–49.

Nigmatulin, T. and Bonetto, F. (1997). Shape of taylor bubbles in vertical tubes. *International Communications in Heat and Mass Transfer*, 24:1177–1185.

Nikitin, N. (1994). Direct numerical modelin of three-dimensional turbulent flows in pipes of circular cross section. *Fluid Dynamics*, 29:749–758.

Nikitin, N. and Yakhot, A. (2005). Direct numerical simulation of turbulent flow in elliptical ducts. *Journal of Fluid Mechanics*, 532:141–164.

Nochetto, R., Paolini, M., and Verdi, C. (1996). A dynamic mesh algorithm for curvature dependent evolving interfaces. *Journal of Computational Physics*, 123:296–310.

Nogueira, S., Riethmuler, M., Campos, J., and Pinto, A. (2006a). Flow in the nose region and annular film around a taylor bubble rising through vertical columns of stagnant and flowing newtonian liquids. *Chemical Engineering Science*, 61:845–857.

Nogueira, S., Riethmuller, M., Campos, J., and Pinto, A. (2006b). Flow patterns in the wake of a taylor bubble rising through vertical columns of stagnant and flowing newtonian liquids: An experimental study. *Chemical Engineering Science*, 61:7199–7212.

Noh, W. and Woodward, P. (1976). Slic (simple line interface calculation). In van de Vooren, A. and Zandbergen, P., editors, *5th International Conference Fluid Dynamics*, volume 59, pages 330–340. Springer-Verlag.

Oono, Y. and Puri, S. (1988). Study of phase-separation dynamics by use of cell dynamical systems. i. modeling. *Physical Review A*, 38:434–453.

Orlandi, P. and Ebstein, D. (2000). Turbulent budgets in rotating pipes by dns. *International Journal of Heat and Fluid Flow*, 21:499–505.

Orlandi, P. and Fatica, M. (1997). Direct simulations of turbulent flow in a pipe rotating about its axis. *Journal of Fluid Mechanics*, 343:43–72.

Osher, S. and Fedkiw, R. P. (2001). Level set methods: An overview and some recent results. *Journal of Computational Physics*, 169:463–502.

Osher, S. and Sethian, J. A. (1988). Fronts propagating with curvature-dependent speed: Algorithms based on hamilton-jacobi formulations. *Journal of Computational Physics*, 79:12–49.

Pan, D. and Shen, T.-T. (2009). Computation of incompressible flows with immersed bodies by a simple ghost cell method. *International Journal for Numerical Methods in Fluids*, 60:1378–1401.

Peskin, C. S. (1972). *Flow patterns around heart valves: A digital computer method for solving the equation of motion.* PhD thesis, Albert Einstein College of Medicine, Univ. Microfilms. 378:72-30.

Peskin, C. S. (1977). Numerical analysis of blood flow in the heart. *Journal of Computational Physics*, 25:220–252.

Peskin, C. S. (1982). The fluid dynamics of heart valves: Experimental, theoretical, and computational methods. *Annual Review of Fluid Mechanics*, 14:235–259.

Peskin, C. S. (2002). The immersed boundary method. *Acta Numerica*, 11:479–517.

Piomelli, U. (2001). Large-eddy and direct simulation of turbulent flows. In *9th Conference annuelle de la Societe Canadienne de CFD.*

Piomelli, U. and Balaras, E. (2002). Wall-layer models for large-eddy simulations. *Annual Review of Fluid Mechanics*, 34:349–374.

Polonsky, S., Barnea, D., and Shemer, L. (1999a). Averaged and time-dependent characteristics of the motion of an elongated bubble in a vertical pipe. *International Journal of Multiphase Flow*, 25:795–812.

Polonsky, S., Shemer, L., and Barnea, D. (1999b). The relation between the taylor bubble motion and the velocity field ahead of it. *International Journal of Multiphase Flow*, 25(6-7):957–975.

Popinet, S. (2009). An accurate adaptive solver for surface-tension-driven interfacial flows. *Journal of Computational Physics*, 228:5838–5866.

Popinet, S. and Zaleski, S. (1999). A front-tracking algorithm for accurate representation of surface tension. *International Journal for Numerical Methods in Fluids*, 30:775–793.

Press, W., Teukolsky, S., Vetterling, W., and Flannery, B. P. (2007). *Numerical Recipes: The art of scientific computing.* 3rd edition, Cambridge University Press.

Puckett, E. and Saltzman, J. (1992). A 3d adaptive mesh refinement algorithm for multimaterial gas dynamics. *Physica D: Nonlinear Phenomena*, 60:84–93.

Qin, R. S. and Bhadeshia, H. K. (2010). Phase field method. *Materials Science and Technology*, 26:803–811.

Ramdin, M. and Henkes, R. (2012). Computational fluid dynamics modeling of benjamin and taylor bubbles in two-phase flow in pipes. *Journal of Fluids Engineering*, 134:041303.

Rider, W. J. and Kothe, D. B. (1998). Reconstructing volume tracking. *Journal of Computational Physics*, 141:112–152.

Roghair, I., Lau, Y. M., Deen, N. G., Slagter, H. M., Baltussen, M. W., Van Sint Annaland, M., and Kuipers, J. A. M. (2011). On the drag force of bubbles in bubble swarms at intermediate and high reynolds numbers. *Chemical Engineering Science*, 66:3204–3211.

Rudman, M. (1997). Volume-tracking methods for interfacial flow calculations. *International Journal for Numerical Methods in Fluids*, 24:671–691.

Rudman, M. and Blackburn, H. M. (1999). Large eddy simulation of turbulence pipe flow. In *In Proceedings of the 2nd International Conference on CFD in the Minerals and Process Industries, CSIRO*, pages 503–508.

Saiki, E. M. and Biringen, S. (1996). Numerical simulation of a cylinder in uniform flow: Application of a virtual boundary method. *Journal of Computational Physics*, 123:450–465.

Scardovelli, R. and Zaleski, S. (1999). Direct numerical simulation of free-surface and interfacial flow. *Annual Review of Fluid Mechanics*, 31:567–603.

Schmidt, S., Mclver, D. M., Blackburn, H., Rudman, M., and Nathan, G. (2001). Spectral element based simulation of turbulent pipe flow. In *Proceeding 14th Australasian Fluid Mechanics Conference*.

Seppecher, P. (1996). Moving contact lines in the cahn-hilliard theory. *International Journal of Engineering Science*, 34:977–992.

Sethian, J. (1999). *Level set methods and fast marching methods.* 2nd Edition, Cambridge University Press.

Sethian, J. and Smereka, P. (2003). Level set methods for fluid interfaces. *Annual Review of Fluid Mechanics*, 35:341–372.

Sethian, J. A. and Straint, J. (1992). Crystal growth and dendritic solidification. *Journal of Computational Physics*, 98:231–253.

Shinn, A., Goodwin, M., and Vanka, S. (2009). Immersed boundary computations of shear- and buoyancy-driven flows in complex enclosures. *International Journal of Heat and Mass Transfer*, 52(17-18):4082–4089.

Shu, C. (2009). High order weighted essentially nonoscillatory schemes for convection dominated problems. *SIAM Review*, 51:82–126.

Smolianski, A., Haario, H., and Luukka, P. (2008). Numerical study of dynamics of single bubbles and bubble swarms. *Applied Mathematical Modelling*, 32:641–659.

Son, G. (2001). A numerical method for incompressible two-phase flows with open or periodic boundaries. *Numerical Heat Transfer, Part B: Fundamentals*, 39:45–60.

Son, G. (2003). Efficient implementation of a coupled level-set and volume of fluid method for three-dimensional incompressible two-phase flows. *Numerical Heat Transfer, Part B: Fundamentals*, 43:549–565.

Starovoitov, V. N. (1994). Model of the motion of a two-component liquid with allowance of capillary forces. *Journal of Applied Mechanics and Technical Physics*, 35:891–897.

Stewart, C. (1995). Bubble interaction in low-viscosity liquids. *International Journal of Multiphase Flow*, 21:1037–1046.

Stockie, J. M. and Wetton, B. R. (1999). Analysis of stiffness in the immersed boundary method and implications for time-stepping schemes. *Journal of Computational Physics*, 154:41–64.

Sussman, M. (2003). A second order coupled level set and volume-of-fluid method for computing growth and collapse of vapor bubbles. *Journal of Computational Physics*, 187:110–136.

Sussman, M., Almgren, A. S., Bell, J. B., Colella, P., Howell, L. H., and Welcome, M. L. (1999). An adaptive level set approach for incompressible two-phase flows. *Journal of Computational Physics*, 148:81–124.

Sussman, M. and Fatemi, E. (1999). An efficient, interface-preserving level set redistancing algorithm and its application to interfacial incompressible fluid flow. *SIAM Journal on Scientific Computing*, 20:1165–191.

Sussman, M. and Puckett, E. G. (2000). A coupled level set and volume-of-fluid method for computing 3D and axisymmetric incompressible two-phase flows. *Journal of Computational Physics*, 162:301–337.

Sussman, M. and Smereka, P. (1997). Axisymmetric free boundary problems. *Journal of Fluid Mechanics*, 341:269–294.

Sussman, M., Smereka, P., and Osher, S. (1994). A level set approach for computing solutions to incompressible two-phase flow. *Journal of Computational Physics*, 114:146–159.

Taha, T. and Cui, Z. (2006). Cfd modelling of slug flow in vertical tubes. *Chemical Engineering Science*, 61:676–687.

Takemura, F. and Magnaudet, J. (2003). The transverse force on clean and contaminated bubbles rising near a vertical wall at moderate reynolds number. *Journal of Fluid Mechanics*, 495:235–253.

Takewaki, H. and Yabe, T. (1987). The cubic-interpolated pseudo particle (cip) method: application to nonlinear and multi-dimensional hyperbolic equations. *Journal of Computational Physics*, 70:355–372.

Taylor, T. D. and Acrivos, A. (1964). On the deformation and drag of a falling viscous drop at low reynolds number. *Journal of Fluid Mechanics*, 18:466–476.

Temam, R. (1968). Une mthode d'approximation des solutions des quations navier-stokes. *Bulletin de la Socit Mathmatique de France*, 98:115–152.

Tomiyama, A., Sou, A., and Sakaguchi, T. (1996). Numerical simulation of a taylor bubble in a stagnant liquid inside a vertical pipe. *JSME International Journal Series B*, 39:517–524.

Tryggvason, G., Bunner, B., Esmaeeli, A., Juric, D., Al-Rawahi, N., Tauber, W., Han, J., Nas, S., and Jan, Y. J. (2001). A front-tracking method for the computations of multiphase flow. *Journal of Computational Physics*, 169:708–759.

Tseng, Y.-H. and Ferziger, J. H. (2003). A ghost-cell immersed boundary method for flow in complex geometry. *Journal of Computational Physics*, 192:593–623.

Tu, C. and Peskin, C. S. (1992). Stability and instability in the computations of flows with moving immersed boundaries: A comparison of three methods. *SIAM Journal on Scientific and Statistical Computing*, 13:1361–1376.

Ubbink, O. (1997). *Numerical prediction of two fluid systems with sharp interfaces*. PhD thesis, Imperial College of Science, Technology and Medicine.

Udaykumar, H. S., Mittal, R., Rampunggoon, P., and Khanna, A. (2001). A sharp interface cartesian grid method for simulating flows with complex moving boundaries. *Journal of Computational Physics*, 174:345–380.

Unger, F. and Friedrich, R. (1991). Large eddy simulation of fully-developed turbulent pipe flow. In *Proceedings 8th symposium on turbulent shear flows*, pages 19–3–1–19–3–6.

Uno, S. and Kintner, R. C. (1956). Effect of wall proximity on the rate of rise of single air bubbles in a quiescent liquid. *AIChE Journal*, 2:420–425.

Unverdi, S. O. and Tryggvason, G. (1992a). Computations of multi-fluid flows. *Physica D: Nonlinear Phenomena*, 60:70–83.

Unverdi, S. O. and Tryggvason, G. (1992b). A front-tracking method for viscous, incompressible, multi-fluid flows. *Journal of Computational Physics*, 100:25–37.

Van der Waals, J. D. (1979). The thermodynamic theory of capillarity under the hypothesis of a continuous variation of density. *Journal of Statistical Physics*, 20:200–244.

Van Sint Annaland, M., Deen, N., and Kuipers, J. (2005). Numerical simulation of gas bubbles behaviour using a three-dimensional volume of fluid method. *Chemical Engineering Science*, 60:2999–3011.

Van Sint Annaland, M., Dijkhuizen, W., Deen, N. G., and Kuipers, J. A. M. (2006). Numerical simulation of behavior of gas bubbles using a 3-d front-tracking method. *AIChE Journal*, 52:99–110.

Van Wachem, B. G. M. and Schouten, J. C. (2002). Experimental validation of 3-d lagrangian vof model: Bubble shape and rise velocity. *AIChE Journal*, 48:2744–2753.

Veenman (2004). *Statistical analysis of turbulent pipe flow: numerical approach*. PhD thesis, Faculty of Mechanical Engineering, Eindhoven University of Technology, Eindhoven.

Verzicco, R., Iaccarino, G., M., F., and Orlandi, P. (2000). Flow in an impeller stirred tank using an immersed boundary method. Technical report, NASA Ames Research Center/Stanford University Center for Turbulence Research, Stanford.

Viana, F., Pardo, R., Yanez, R., Trallero, J. L., and Joseph, D. D. (2003). Universal correlation for the rise velocity of long gas bubbles in round pipes. *Journal of Fluid Mechanics*, 494:379–398.

Vijiapurapu, S. and Cui, J. (2004). Large eddy simulation of fully developed turbulent pipe flow. *ASME Conference Proceedings*, 2004:675–679.

Vijiapurapu, S. and Cui, J. (2010). Performance of turbulence models for flows through rough pipes. *Applied Mathematical Modelling*, 34:1458–1466.

Voronova, T. and Nikitin, N. (2006). Direct numerical simulation of the turbulent flow in an elliptical pipe. *Computational Mathematics and Mathematical Physics*, 46:1378–1386.

Voronova, T. and Nikitin, N. (2007). Results of direct numerical simulation of turbulent flow in a pipe of elliptical cross-section. *Fluid Dynamics*, 42:201–211.

Wagner, C., Huttl, T., and Friedrich, R. (2001). Low-reynolds-number effects derived from direct numerical simulations of turbulent pipe flow. *Computers and Fluids*, 30:581–590.

Wallis, G. (1969). *One-dimensional two-phase flow.* McGraw-Hill, New York.

Wang, Y., Simakhina, S., and Sussman, M. (2012). A hybrid level set-volume constraint method for incompressible two-phase flow. *Journal of Computational Physics*, 231:6438–6471.

Wegener, P. P. and Parlange, J. Y. (1973). Spherical-cap bubbles. *Annual Review of Fluid Mechanics*, 5:79–100.

Wesseling, P. (1992). *An Introduction to Multigrid Methods.* Wiley-Blackwell.

Whalley, P. (1987). *Boiling, condensetion and gas-Liquid flow.* Oxford Science Publications.

White, E. and Beardmore, R. (1962). The velocity of rise of single cylindrical air bubbles through liquids contained in vertical tubes. *Chemical Engineering Science*, 17:351–361.

Wu, X., Baltzer, J. R., and Adrian, R. J. (2012). Direct numerical simulation of a 30r long turbulent pipe flow at r+= 685: large- and very large-scale motions. *Journal of Fluid Mechanics*, 698:235–281.

Wu, X. and Moin, P. (2008). A direct numerical simulation study on the mean velocity characteristics in turbulent pipe flow. *Journal of Fluid Mechanics*, 608:81–112.

Xu, S. and Wang, Z. J. (2006). An immersed interface method for simulating the interaction of a fluid with moving boundaries. *Journal of Computational Physics*, 216:454–493.

Yamada, T. and Matsui, K. (2008). Characteristic Galerkin finite element method with marker particle integration for metal forming. In *8th. World Congress on Computational Mechanics (WCCM8).*

Yang, Z. (2000). Large eddy simulation of fully developed turbulent flow in a rotating pipe. *International Journal for Numerical Methods in Fluids*, 33(5):681–694–.

Ye, T., Mittal, R., Udaykumar, H. S., and Shyy, W. (1999). An accurate cartesian grid method for viscous incompressible flows with complex immersed boundaries. *Journal of Computational Physics*, 156:209–240.

Yeoh, G. and Tu, J. (2010). *Computational techniques for multiphase flows.* Butterworth - Heinemann.

Youngs, D. (1982). *Time-dependent multi-material flow with large fluid distortion.* Numerical Methods for Fluid Dynamics, Academic Press, New York.

Yu, Z. and Fan, L.-S. (2008). Direct simulation of the buoyant rise of bubbles in infinite liquid using level set method. *The Canadian Journal of Chemical Engineering*, 86:267–275.

Yue, P., Feng, J. J., Liu, C., and Shen, J. (2004). A diffuse-interface method for simulating two-phase flows of complex fluids. *Journal of Fluid Mechanics*, 515:293–317.

Zalesak, S. T. (1979). Fully multidimensional flux-corrected transport algorithms for fluids. *Journal of Computational Physics*, 31:335–362.

Zhang, J. and Jackson, T. L. (2009). A high-order incompressible flow solver with weno. *Journal of Computational Physics*, 228:2426–2442.

Zhang, Y., Chandi, A., Tomboulides, A., and Orszag, S. (1994). Simulation of pipe flow. In *AGARD Conference Proceedings on Applications of Direct and Large Eddy Simulations to Transition and Turbulence.*

Zheng, D., He, X., and Che, D. (2007). Cfd simulations of hydrodynamic characteristics in a gas-liquid vertical upward slug flow. *International Journal of Heat and Mass Transfer*, 50:4151–4165.

Zukoski, E. E. (1966). Influence of viscosity, surface tension, and inclination angle on motion of long bubbles in closed tubes. *Journal of Fluid Mechanics*, 25:821–837.

Appendix A

Non-dimensional analysis

A.1 Dimensionless variables and parameters

The dimensionless variables and parameters can be defined as:

$$u^* \equiv \frac{u}{u_c}, \qquad t^* \equiv t\frac{u_c}{L_c}, \qquad x^* \equiv \frac{x_c}{L_c}, \qquad p^* \equiv \frac{p}{\rho_A u_c^2}$$

$$M^* \equiv \frac{M}{M_c}, \qquad \phi^* \equiv \frac{\phi}{\phi_c}, \qquad g^* \equiv \frac{g}{g_c}, \qquad \nabla^* \equiv L_c^{-1}\nabla$$

where L_c is the characteristic length scale, u_c the characteristic velocity, u is the velocity, t is the time, p is the pressure, M is the mobility, M_c is the characteristic mobility, ϕ is the chemical potential, ϕ_c is the characteristic chemical potential, g is the gravitational acceleration and g_c is the characteristic gravitational acceleration.

The dimensionless form for the viscosity and density is:

$$\rho^* \equiv \frac{\rho}{\rho_A} = (1-C) + r_d C, \qquad \mu^* \equiv \frac{\mu}{\mu_A} = (1-C) + r_v C$$

where C is the volume fraction, ρ_A is the density of fluid A, μ_A is the viscosity of fluid A, r_d is the ratio of density and r_v is the ratio of viscosity.

Additional dimensionless parameters are the Reynolds number, the Peclet number, the Bond number, the Capillary number and Weber number, respectively.

$$Re_c \equiv \frac{\rho_A u_c L_c}{\mu_A}, \quad Pe_c \equiv \frac{L_c u_c}{M_c \phi_c}, \quad Eo \equiv \frac{\rho_A g L_c^2}{\sigma}, \quad Ca_c \equiv \mu_A \frac{u_c}{\sigma}, \quad Fr_c \equiv \frac{u_c}{\sqrt{g L_c}}$$

A.2 Derivation of the dimensionless governing equations

A.2.1 Cahn-Hilliard equation

Cahn-Hilliard equation:

$$\frac{\partial C}{\partial t} + \mathbf{u}\cdot\nabla C - \nabla\cdot(M\nabla\phi) = 0 \tag{A.1}$$

The non-dimensional Cahn-Hilliard equation can be given in dimensionless form, multiplying by $L_c u_c^{-1}$:

$$\begin{aligned}
L_c u_c^{-1}\frac{\partial C}{\partial t} + L_c u_c^{-1}\mathbf{u}\cdot\nabla C - L_c u_c^{-1}\nabla\cdot(M\nabla\phi) = 0 \Leftrightarrow\\
L_c u_c^{-1}\frac{\partial C}{\partial(L_c u_c^{-1} t^*)} + L_c u_c^{-1}\nabla^* L_c^{-1}(u^* u_c C) - L_c u_c^{-1}\nabla^* L_c^{-1}(M^* M_c \nabla^* L_c^{-1}\phi^*\phi_c) = 0 \Leftrightarrow\\
\frac{\partial C^*}{\partial t^*} + u^*\cdot\nabla^* C - M_c\phi_c L_c^{-1} u_c^{-1}\nabla^*(M^*\nabla^*\phi^*) = 0 \Leftrightarrow\\
\frac{\partial C^*}{\partial t^*} + u^*\cdot\nabla^* C - Pe_c^{-1}\nabla^*(M^*\nabla^*\phi^*) = 0
\end{aligned} \tag{A.2}$$

A.2.2 Continuity equation

Continuity equation:

$$\nabla\cdot\mathbf{u} = 0 \tag{A.3}$$

The non-dimensional continuity equation can be expressed in dimensionless form, multiplying by $L_c u_c^{-1}$:

$$\begin{aligned}
L_c u_c^{-1}\nabla^* L_c^{-1} u^* u_c = 0 \Leftrightarrow\\
\nabla^*\cdot\mathbf{u}^* = 0
\end{aligned} \tag{A.4}$$

A.2.3 Navier-Stokes equations

Navier-Stokes equations:

$$\underbrace{\rho\left(\frac{\partial\mathbf{u}}{\partial t} + \mathbf{u}\cdot\nabla\mathbf{u}\right)}_{(1)} = \underbrace{-\nabla p}_{(2)} + \underbrace{\nabla\cdot[\mu(\nabla\mathbf{u}+\nabla\mathbf{u}^T)]}_{(3)} + \underbrace{\phi\nabla C}_{(4)} + \underbrace{\rho\mathbf{g}}_{(5)} \tag{A.5}$$

The above equation can be expressed in dimensionless form, multiplying by $L_c\rho^{-1}u_c^{-2}$ each term individually.

Inertia (per volume) term (1):

$$L_c\rho^{-1}u_c^{-2}\underbrace{\rho\left(\frac{\partial \mathbf{u}}{\partial t}+\mathbf{u}\cdot\nabla\mathbf{u}\right)}_{(1)} = L_c u_c^{-2}\left(\frac{\partial(u^* u_c)}{\partial(t^* L_c u_c^{-1})}\right) + L_c u_c^{-2} u^* u_c \cdot \nabla^* L_c^{-1} u^* u_c \quad \Leftrightarrow$$

$$L_c\rho^{-1}u_c^{-2}\underbrace{\rho\left(\frac{\partial \mathbf{u}}{\partial t}+\mathbf{u}\cdot\nabla\mathbf{u}\right)}_{(1)} = \frac{\partial \mathbf{u}^*}{\partial t^*} + \mathbf{u}^*\cdot\nabla^*\mathbf{u}^* \tag{A.6}$$

Pressure gradient term (2):

$$-L_c\rho^{-1}u_p^{-2}\underbrace{-\nabla p}_{(2)} = -L_c\rho^{-1}u_p^{-2}\nabla^* L_c^{-1} p^*\rho_A u_p^2 = -(\rho^*\rho_A)^{-1}\rho_A\nabla^* p^* = \frac{1}{\rho^*}\nabla^* p^* \quad \Leftrightarrow$$

$$-L_c\rho^{-1}u_p^{-2}\underbrace{-\nabla p}_{(2)} = \frac{1}{\rho^*}\nabla^* p^* \tag{A.7}$$

Viscosity term (3):

$$L_c\rho^{-1}u_c^{-2}\underbrace{\nabla\cdot[\mu(\nabla\mathbf{u}+\nabla\mathbf{u}^T)]}_{(3)} = L_c\rho^{-1}u_c^{-2}\nabla^* L_c^{-1}[\mu^*\mu_A(\nabla^* L_c^{-1}u^* u_c + \nabla^* L_c^{-1}u^{*T}u_c^T)] \quad \Leftrightarrow$$

$$L_c\rho^{-1}u_c^{-2}\underbrace{\nabla\cdot[\mu(\nabla\mathbf{u}+\nabla\mathbf{u}^T)]}_{(3)} = \nabla^* L_c^{-1} L_c(\rho^*\rho_A)^{-1}u_c^{-2}[\mu^*\mu_A(L_c^{-1}u_c\nabla^* u^* + L_c^{-1}u_c^T\nabla^* u^{*T})] \quad \Leftrightarrow$$

$$L_c\rho^{-1}u_c^{-2}\underbrace{\nabla\cdot[\mu(\nabla\mathbf{u}+\nabla\mathbf{u}^T)]}_{(3)} = \nabla^*\frac{1}{\rho^*}\rho_A^{-1}u_c^{-2}\mu^*\mu_A L_c^{-1}(u_c\nabla^* u^* + u_c^T\nabla^* u^{*T}) \quad \Leftrightarrow$$

$$L_c\rho^{-1}u_c^{-2}\underbrace{\nabla\cdot[\mu(\nabla\mathbf{u}+\nabla\mathbf{u}^T)]}_{(3)} = \rho^{*-1}\rho_A^{-1}u_c^{-2}\mu^*\mu_A L_c^{-1}\nabla^*(u_c\nabla^* u^* + u_c^T\nabla^* u^{*T}) \quad \Leftrightarrow$$

$$L_c\rho^{-1}u_c^{-2}\underbrace{\nabla\cdot[\mu(\nabla\mathbf{u}+\nabla\mathbf{u}^T)]}_{(3)} = \frac{\mu^*}{\rho^*}\mu_A\rho_A^{-1}u_c^{-1}L_c^{-1}u_c^{-1}(u_c\nabla^* u^* + u_c^T\nabla^* u^{*T}) \quad \Leftrightarrow$$

$$L_c\rho^{-1}u_c^{-2}\underbrace{\nabla\cdot[\mu(\nabla\mathbf{u}+\nabla\mathbf{u}^T)]}_{(3)} = \frac{\mu^*}{\rho^*}Re_c^{-1}u_c^{-1}(u_c\nabla^* u^* + u_c^T\nabla^* u^{*T}) \quad \Leftrightarrow$$

$$L_c\rho^{-1}u_c^{-2}\underbrace{\nabla\cdot[\mu(\nabla\mathbf{u}+\nabla\mathbf{u}^T)]}_{(3)} = \frac{1}{\rho^*}Re_c^{-1}(\mu^*(\nabla^*\mathbf{u}^* + \nabla^*\mathbf{u}^{*T})) \tag{A.8}$$

Surface tension term (4):

$$L_c\rho^{-1}u_c^{-2}\underbrace{\phi\nabla C}_{(4)} = L_c\rho^{-1}u_c^{-2}[-6\sqrt{2}\varepsilon\sigma\nabla^{*2}L_c^{-2}C + 6\sqrt{2}\varepsilon^{-1}\sigma\psi'(C)]L_c^{-1}\nabla^* C \quad \Leftrightarrow$$

$$L_c\rho^{-1}u_c^{-2}\underbrace{\phi\nabla C}_{(4)} = L_c\rho^{-1}u_c^{-2}[-6\sqrt{2}\varepsilon\sigma L_c^{-2}\nabla^{*2}C + 6\sqrt{2}\varepsilon^{-1}\sigma\psi'(C)]L_c^{-1}\nabla^* C \quad \Leftrightarrow$$

$$L_c\rho^{-1}u_c^{-2}\underbrace{\phi\nabla C}_{(4)} = L_c\rho^{-1}u_c^{-2}[-6\sqrt{2}Cn\sigma L_c^{-1}\nabla^{*2}C + 6\sqrt{2}\varepsilon^{-1}\sigma\psi'(C)]L_c^{-1}\nabla^* C \quad \Leftrightarrow$$

$$L_c\rho^{-1}u_c^{-2}\underbrace{\phi\nabla C}_{(4)} = \rho^{-1}u_c^{-2}[-6\sqrt{2}Cn\sigma\nabla^{*2}C + 6\sqrt{2}\varepsilon^{-1}L_c\sigma\psi'(C)]L_c^{-1}\nabla^* C \quad \Leftrightarrow$$

$$L_c\rho^{-1}u_c^{-2}\underbrace{\phi\nabla C}_{(4)} = \rho^{-1}u_c^{-2}[-6\sqrt{2}Cn\sigma\nabla^{*2}C + 6\sqrt{2}Cn^{-1}\sigma\psi'(C)]L_c^{-1}\nabla^* C \quad \Leftrightarrow$$

$$L_c\rho^{-1}u_c^{-2}\underbrace{\phi\nabla C}_{(4)} = L_c^{-1}\rho_A^{-1}\rho^{*-1}u_c^{-1}u_c^{-1}\mu_A\mu_A^{-1}[-6\sqrt{2}Cn\sigma\nabla^{*2}C + 6\sqrt{2}Cn^{-1}\sigma\psi'(C)]\nabla^* C \quad \Leftrightarrow$$

$$L_c\rho^{-1}u_p^{-2}\underbrace{\phi\nabla C}_{(4)} = Re_c^{-1}\rho^{*-1}u_c^{-1}\mu_A^{-1}\sigma[-6\sqrt{2}Cn\nabla^{*2}C + 6\sqrt{2}Cn^{-1}\psi'(C)]\nabla^* C \quad \Leftrightarrow$$

$$L_c\rho^{-1}u_p^{-2}\underbrace{\phi\nabla C}_{(4)} = \frac{1}{\rho^*}Re_c^{-1}Ca_c^{-1}[-6\sqrt{2}Cn\nabla^{*2}C + 6\sqrt{2}Cn^{-1}\psi'(C)]\nabla^* C \quad \Leftrightarrow$$

$$L_c\rho^{-1}u_c^{-2}\underbrace{\phi\nabla C}_{(4)} = \frac{1}{\rho^*}Re_c^{-1}Ca_c^{-1}\phi^*\nabla^* C \tag{A.9}$$

In the present study for gravity driven flow the term $Re_c^{-1}Ca_c^{-1}$ is replaced by the Eo^{-1}.

Gravity acceleration term (5):

$$L_c\rho^{-1}u_c^{-2}\rho\mathbf{g} = L_c\rho^{-1}u_c^{-2}\rho g^* g_c \quad \Leftrightarrow$$

$$L_c\rho^{-1}u_c^{-2}\rho\mathbf{g} = L_c u_c^{-2} g^* g_c \quad \Leftrightarrow$$

$$L_c\rho^{-1}u_c^{-2}\rho\mathbf{g} = \frac{1}{Fr_c^2}g^* \quad \Leftrightarrow$$

$$L_c\rho^{-1}u_c^{-2}\rho\mathbf{g} = \frac{1}{Fr_c^2}g^* \tag{A.10}$$

Appendix B

Analytical solutions for pipe flows

B.1 Laminar single-phase Poiseuille flow

The governing equations for a steady state laminar pipe flow can be derived from the Navier-Stokes equations in cylindrical polar coordinates as follows:

Continuity equation:

$$\frac{\partial \rho}{\partial t} + \frac{1}{r}\frac{\partial}{\partial r}(\rho r u_r) + \frac{1}{r}\frac{\partial}{\partial \theta}(\rho u_\theta) + \frac{\partial}{\partial z}(\rho u_z) = 0 \tag{B.1}$$

Momentum equations:

r-component:

$$\begin{aligned}\rho\left(\frac{\partial u_r}{\partial t} + u_r\frac{\partial u_r}{\partial r} + \frac{u_\theta}{r}\frac{\partial u_r}{\partial \theta} + u_z\frac{\partial u_z}{\partial z} - \frac{{u_\theta}^2}{r}\right) &= \\ = -\frac{\partial p}{\partial r} + \mu\left(\frac{\partial}{\partial r}\left(\frac{1}{r}\frac{\partial}{\partial r}(r u_r)\right) + \frac{1}{r^2}\frac{\partial^2 u_r}{\partial \theta^2} - \frac{2}{r^2}\frac{\partial u_\theta}{\partial \theta} + \frac{\partial^2 u_r}{\partial z^2}\right) &+ \rho g_r\end{aligned} \tag{B.2}$$

θ-component:

$$\begin{aligned}\rho\left(\frac{\partial u_\theta}{\partial t} + u_r\frac{\partial u_\theta}{\partial r} + \frac{u_\theta}{r}\frac{\partial u_\theta}{\partial \theta} + \frac{u_r u_\theta}{r} + u_z\frac{\partial u_\theta}{\partial z}\right) &= \\ = -\frac{1}{r}\frac{\partial p}{\partial \theta} + \mu\left(\frac{\partial}{\partial r}\left(\frac{1}{r}\frac{\partial}{\partial r}(r u_\theta)\right) + \frac{1}{r^2}\frac{\partial^2 u_\theta}{\partial \theta^2} + \frac{2}{r^2}\frac{\partial u_r}{\partial \theta} + \frac{\partial^2 u_\theta}{\partial z^2}\right) &+ \rho g_\theta\end{aligned} \tag{B.3}$$

z-component:

$$\rho\left(\frac{\partial u_z}{\partial t}+u_r\frac{\partial u_z}{\partial r}+\frac{u_\theta}{r}\frac{\partial u_z}{\partial \theta}+u_z\frac{\partial u_\theta}{\partial z}\right)= \\ =-\frac{\partial p}{\partial z}+\mu\left(\frac{1}{r}\frac{\partial}{\partial r}\left(r\frac{\partial u_z}{\partial r}\right)+\frac{1}{r^2}\frac{\partial^2 u_z}{\partial \theta^2}+\frac{\partial^2 u_z}{\partial z^2}\right)+\rho g_z \quad \text{(B.4)}$$

According to the following set of assumptions for incompressible flow:

- The flow is steady,

$$\frac{\partial \rho}{\partial t}=0 \quad \text{(B.5)}$$

- The radical and swirl components of the fluid velocity are zero,

$$u_r=u_\theta=0 \quad \text{(B.6)}$$

- The pressure gradient is constant,

$$\frac{\partial p}{\partial z}=const. \quad \text{(B.7)}$$

- The flow is axisymmetric,

$$\frac{\partial \mathbf{u}}{\partial \theta}=0 \quad \text{(B.8)}$$

- The gravity is zero,

$$g_r=g_\theta=g_z=0 \quad \text{(B.9)}$$

From the aforementioned assumptions, the continuity equation (B.1) becomes,

$$\frac{\partial u_z}{\partial z}=0 \quad \text{(B.10)}$$

and with Eq.(B.10) and the axisymmetric hypothesis Eq.(B.8), we deduce that,

$$u_z=u_z(r,t) \quad \text{(B.11)}$$

Moreover, the Navier-Stokes Eqs.(B.2)-(B.4) are simplified to:

r-component:

$$\frac{\partial p}{\partial r}=0 \quad \text{(B.12)}$$

θ-component:

$$-\frac{1}{r}\frac{\partial p}{\partial \theta} = 0 \tag{B.13}$$

z-component:

$$-\frac{\partial p}{\partial z} + \mu\frac{1}{r}\frac{\partial}{\partial r}\left(r\frac{du_z}{dr}\right) = 0 \tag{B.14}$$

Eq.(B.14) is an ordinary differential equation (ODE), with general solution for u_z is:

$$u_z(r) = -\frac{1}{4\mu}\left(\frac{\partial p}{\partial z}\right)r^2 + c_1 \ln r + c_2 \tag{B.15}$$

The constants c_1 and c_2 of the general solution of ODE Eq.(B.15) can be calculated by the boundary conditions of the flow problem. Therefore, the appropriate boundary conditions are expressed as:

- The velocity, $u_z = u_{max}$ at $r = 0$, which means $\dfrac{du_z}{dr} = 0$.
- At the wall of the pipe, $u_z = 0$ at $r = R$.

By applying the boundary conditions to Eq.(B.15), we have:
Boundary Condition (1): $\left.\dfrac{du_z}{dr}\right|_{(r=0)} = 0$. Hence the derivative for Eq.(B.15) gives:

$$\begin{aligned}\frac{d}{dr}\left(\frac{1}{4\mu_A}\frac{\partial p}{\partial z}r^2 + c_1 \ln r + c_2\right) &= 0 \Leftrightarrow \\ \frac{1}{2\mu_A}\frac{\partial p}{\partial z}r + c_1\frac{1}{r} &= 0 \Leftrightarrow \\ c_1 &= 0 \end{aligned} \tag{B.16}$$

A solution is possibly, only if $c_1 = 0$.
Boundary Condition (2): $u_z = 0$ at $r = R$ (no slip condition). Accordingly for Eq.(B.15):

$$0 = -\frac{1}{4\mu}\left(\frac{\partial p}{\partial z}\right)R^2 + c_1 \ln r + c_2 \tag{B.17}$$

Substitution of Eq.(B.16) to Eq.(B.17) yields:

$$c_2 = -\frac{1}{4\mu}\frac{\partial p}{\partial z}R^2 \tag{B.18}$$

If we replace the values of constants c_1 and c_2 in the initial Eq.(B.15), we get

$$u_z(r) = -\frac{1}{4\mu}\frac{\partial p}{\partial z}R^2\left(1 - \frac{r^2}{R^2}\right) \tag{B.19}$$

Eq.(B.19) represents a parabolic velocity profile for laminar pipe flow. For the derivation of the dimensionless form of Eq.(B.19), it is necessary to introduce the following normalizations:

$$u_z^* = \frac{u_z}{U_p} \qquad\qquad Re_p = \frac{\rho \cdot U_p \cdot 2R}{\mu}$$

$$U_p = \sqrt{\frac{\partial p}{\partial z}\frac{2R}{\rho}} \Rightarrow \frac{\partial p}{\partial z} = -\frac{\rho U_p^2}{2R}$$

where U_p and *2R* are the velocity-scale and length scale, respectively. Eq.(B.19) then becomes:

$$\begin{aligned} u_z^* &= -\frac{1}{4\mu}\left(-\frac{\rho U_p^2}{2R}\right)U_p^{-1}R^2\left(1-\frac{r^2}{R^2}\right) \Leftrightarrow \\ u_z^* &= \frac{1}{4\mu}\left(\frac{\rho U_p}{2R}\right)R^2\left(1-\frac{r^2}{R^2}\right) \Leftrightarrow \\ u_z^* &= \frac{1}{4}\frac{Re_p}{4R^2}R^2\left(1-\frac{r^2}{R^2}\right) \Leftrightarrow \\ u_z^* &= \frac{Re_p}{16}\left(1-\frac{r^2}{R^2}\right) \end{aligned} \tag{B.20}$$

Eq.(B.20) expresses the analytical profile for a steady state laminar pipe flow in dimensionless form.

B.2 Laminar two-phase annular pipe flow

According to the general solution of the ODE (Eq.(B.14)), we write Eq.(B.15) with respect to μ_A and μ_B,

$$u_z = -\frac{1}{4\mu_A}\left(\frac{\partial p}{\partial z}\right)r^2 + c_1 \ln r + c_2, \qquad if \quad 0 \le r \le kR \tag{B.21}$$

$$u_z = -\frac{1}{4\mu_B}\left(\frac{\partial p}{\partial z}\right)r^2 + c_3 \ln r + c_4, \qquad if \quad kR \le r \le R \tag{B.22}$$

Similar to the single-phase case above, the constants c_1, c_2, c_3 *and* c_4 can be calculated by the appropriate boundary conditions of the flow problem. The boundary conditions are specified as follows:

Boundary condition (1): $u_z = 0$ at $r = R$. Accordingly for Eq.(B.22):

$$0 = -\frac{1}{4\mu_B}\left(\frac{\partial p}{\partial z}\right)R^2 + c_3 \ln r + c_4 \tag{B.23}$$

Boundary condition (2): $\left.\frac{\partial u_z}{\partial r}\right|_{(r=0)} = 0$. Hence the derivative for Eq.(B.21) gives:

$$\begin{aligned} \frac{d}{dr}\left(\frac{1}{4\mu_A}\frac{\partial p}{\partial z}r^2 + c_1 \ln r + c_2\right) &= 0 \Leftrightarrow \\ 2\frac{1}{4\mu_A}\frac{\partial p}{\partial z}r + c_1\frac{1}{r} &= 0 \Leftrightarrow \\ c_1 &= 0 \end{aligned} \tag{B.24}$$

Boundary condition (3): $\mu_A \left.\frac{\partial u_z}{\partial r}\right|_A = \mu_B \left.\frac{\partial u_z}{\partial r}\right|_B$

$$\begin{aligned} \mu_A \left.\frac{\partial u_z}{\partial r}\right|_A &= \mu_B \left.\frac{\partial u_z}{\partial r}\right|_B \Leftrightarrow \\ \mu_A\left(\frac{1}{4\mu_A}\frac{\partial p}{\partial z}2r + c_1\frac{1}{r}\right) &= \mu_B\left(\frac{1}{4\mu_B}\frac{\partial p}{\partial z}2r + c_3\frac{1}{r}\right) \Leftrightarrow \\ \frac{1}{4}\frac{\partial p}{\partial z}2r + c_1\frac{\mu_A}{r} &= \frac{1}{4}\frac{\partial p}{\partial z}2r + c_3\frac{\mu_B}{r} \Leftrightarrow \\ c_1 &= \frac{\mu_B}{\mu_A}c_3 \Leftrightarrow \\ c_3 &= 0 \end{aligned} \tag{B.25}$$

Boundary condition (4): $\frac{1}{4\mu_A}\frac{\partial p}{\partial z}k^2R^2 + c_2 = \frac{1}{4\mu_B}\frac{\partial p}{\partial z}k^2R^2 + c_4$

$$\begin{aligned} \frac{1}{4\mu_A}\frac{\partial p}{\partial z}k^2R^2 + c_2 &= \frac{1}{4\mu_B}\frac{\partial p}{\partial z}k^2R^2 + c_4 \Leftrightarrow \\ c_2 &= \frac{1}{4\mu_B}\frac{\partial p}{\partial z}k^2R^2 - \frac{1}{4\mu_A}\frac{\partial p}{\partial z}k^2R^2 + c_4 \Leftrightarrow \\ c_2 &= \frac{1}{4}\frac{\partial p}{\partial z}k^2R^2\left(\frac{1}{\mu_B} - \frac{1}{\mu_A}\right) + c_4 \end{aligned} \tag{B.26}$$

Eq.(B.23) according to Eq.(B.25) takes the form:

$$c_4 = -\frac{1}{4\mu_B}\frac{\partial p}{\partial z}R^2 \tag{B.27}$$

Then the combination of Eq.(B.26) with Eq.(B.27) yields:

$$\begin{aligned} c_2 &= \frac{1}{4}\frac{\partial p}{\partial z}k^2R^2\left(\frac{1}{\mu_B}-\frac{1}{\mu_A}\right)-\frac{1}{4\mu_B}\frac{\partial p}{\partial z}R^2 \Leftrightarrow \\ c_2 &= \frac{1}{4}\frac{\partial p}{\partial z}R^2\left(k^2\left(\frac{1}{\mu_B}-\frac{1}{\mu_A}\right)-\frac{1}{\mu_B}\right) \end{aligned} \tag{B.28}$$

From the above Eqs.(B.24),(B.25),(B.28), the Eqs.(B.21) and (B.22), respectively, give:

$$u_z = \frac{1}{4\mu_A}\frac{\partial p}{\partial z}r^2+\frac{1}{4}\frac{\partial p}{\partial z}R^2\left(k^2\left(\frac{1}{\mu_B}-\frac{1}{\mu_A}\right)-\frac{1}{\mu_B}\right), \qquad if \quad 0 \le r \le kR \tag{B.29}$$

$$u_z = \frac{1}{4\mu_B}\frac{\partial p}{\partial z}r^2-\frac{1}{4\mu_B}\frac{\partial p}{\partial z}R^2, \qquad if \quad kR \le r \le R \tag{B.30}$$

Then, it is introduced the following normalizations (critical velocity and *Re* number) in order to derive the dimensionless form of the above equations. Thus, we have:

$$U_p = \sqrt{\frac{\partial p}{\partial z}\frac{2R}{\rho_A}} \Rightarrow \frac{\partial p}{\partial z} = -\frac{\rho_A U_p^2}{2R}$$

$$u_z^* = \frac{u_z}{U_p} \qquad\qquad Re_p = \frac{\rho_A \cdot U_p \cdot 2R}{\mu_A}$$

such that

$$\begin{aligned} u_z^* &= -\frac{1}{4\mu_A}U_p^{-1}\frac{\rho_A U_p^2}{2R}r^2-\frac{1}{4}\mu_A\frac{\rho_A U_p^2}{2R}U_p^{-1}R^2\left(k^2\frac{1}{\mu_A}\left(\frac{\mu_A}{\mu_B}-1\right)-\frac{1}{\mu_A}\frac{\mu_A}{\mu_B}\right) \Leftrightarrow \\ u_z^* &= -\frac{1}{16}\frac{Re_p}{R^2}r^2-\frac{1}{16}\frac{Re_p}{R^2}\mu_A R^2\left(k^2\frac{1}{\mu_A}\left(\frac{\mu_A}{\mu_B}-1\right)-\frac{1}{\mu_A}\frac{\mu_A}{\mu_B}\right) \Leftrightarrow \\ u_z^* &= -\frac{Re_p}{16}\frac{r^2}{R^2}-\frac{Re_p}{16}\left(k^2\left(\frac{\mu_A}{\mu_B}-1\right)-\frac{\mu_A}{\mu_B}\right), \qquad if \quad 0 \le r \le kR \end{aligned} \tag{B.31}$$

Similarly, for Eq.(B.22) the dimensionless form is given by:

$$\begin{aligned} u_z^* &= -\frac{1}{4\mu_B}{U_p}^{-1}\frac{\rho_A {U_p}^2}{2R}r^2+\frac{1}{4\mu_B}{U_p}^{-1}\frac{\rho_A {U_c}^2}{2R}R^2 \Leftrightarrow \\ u_z^* &= -\frac{1}{4\mu_B}\frac{Re_p\mu_A}{4R^2}r^2+\frac{1}{4\mu_B}\frac{Re_p\mu_A}{4R^2}R^2 \Leftrightarrow \\ u_z^* &= -\frac{\mu_A}{16\mu_B}\frac{Re_p}{R^2}r^2+\frac{\mu_A}{16\mu_B}Re_p \Leftrightarrow \\ u_z^* &= \frac{Re_p}{16}\frac{\mu_A}{\mu_B}\left(1-\frac{r^2}{R^2}\right), \qquad if \quad kR \le r \le R \end{aligned} \tag{B.32}$$

Finally, Eqs.(B.31) and (B.32) give the velocity profile for two-phase annular flow.

Appendix C

Review paper

Recent advances on the numerical modelling of turbulent flows by C.D. Argyropoulos and N.C. Markatos